Selim Gürgen *Editor*

Shear Thickening Fluid

Case Studies in Engineering

Springer

Shear Thickening Fluid

Selim Gürgen
Editor

Shear Thickening Fluid

Case Studies in Engineering

Springer

Editor
Selim Gürgen
Department of Aeronautical Engineering
Eskişehir Osmangazi University
Eskişehir, Turkey

ISBN 978-3-031-35520-2 ISBN 978-3-031-35521-9 (eBook)
https://doi.org/10.1007/978-3-031-35521-9

This Springer imprint is published by the registered company Springer Nature Switzerland AG
The registered company address is: Gewerbestrasse 11, 6330 Cham, Switzerland

Preface

The book *Shear Thickening Fluid: Case Studies in Engineering* provides a set of case studies from Shear Thickening Fluid (STF)-based engineering applications. Engineers, researchers, and scientists benefit from this book to understand the adaptive behavior of STF in different engineering applications. The main STF areas are protective structures, energy-absorbing applications, vibration-damping devices, multi-functional systems, and surface finishing operations. These applications are described by providing various case studies. STF is adapted to different engineering designs to take advantage of smart behavior of this fluid. The content will help readers understand STF usage through several case studies in various engineering applications.

Department of Aeronautical Engineering, Eskişehir Osmangazi University, Eskişehir, Turkey

Selim Gürgen

Contents

About the Editor

Selim Gürgen Ph.D. is an Associate Professor at the Department of Aeronautical Engineering, Eskişehir Osmangazi University and the Director of Eskişehir Vocational School. He received his B.Sc. and M.Sc. degrees in Mechanical Engineering from Gazi University and Middle East Technical University, respectively, and his Ph.D. in Mechanical Engineering from Eskişehir Osmangazi University. He was a Visiting Researcher at the University of Wollongong, Australia, for a project on smart materials. He was at the University of Aveiro, Portugal, on natural composites and worked as a Researcher at the School of Transportation at Anadolu University for 4 years. Before his academic life, he worked as a manufacturing engineer in a joint venture of KMWE-Dutch Aero, the Netherlands, for 3 years. Dr. Gürgen has contributed to several industrial and research projects in collaboration with major organizations such as Fiat Automobiles, Turkish Aerospace Industries (TAI), and the Turkish Air Force. His projects were funded by the Scientific and Technological Research Council of Turkey (TÜBİTAK) and the European Union (EU). He has many publications in refereed international journals and conferences. He serves as an editorial member for several international journals. His primary area of research is material science, in particular smart fluids and their applications in defense and aerospace applications. His Ph.D. studies were on shear thickening fluid (STF), and many of his projects and publications focus on STF and its applications.

Chapter 1
Development of Shear Thickening Fluid Based Polishing Slurries

Abdullah Sert, Selim Gürgen, and Melih Cemal Kuşhan

1.1 Introduction

STF rheology provides a unique characteristic for scientists, researchers, and engineers. This smart material shows a drastic increase in its viscosity under loading. The viscosity quickly turns back to the initial condition just after the removal of the loading from the medium. Hence, the reversible behavior in viscosity attracts much attention for designing novel applications. Knowing that STF has been adapted to various fields such as protective structures [1–6], anti-vibration applications [7–12], manufacturing operations [13, 14], and multifunctional systems [15–21]. In recent years, STF has been used in surface finishing operations. The carrier fluids in polishing slurries are replaced with STF and an adaptive stiffness is gained in the slurries. According to the previous studies [22–25], STF is a promising material for surface finishing operations.

The STF based polishing method has some advantages over the traditional methods such as eliminating deep scratches, abrasive plunges, sudden force jump etc. Moreover, process time can be reduced by submerging the workpiece into STF based slurry and thereby enabling a simultaneous processing for multiple surfaces. In addition, difficult-to-access areas such as internal surfaces in the parts can be processed by flowing the STF. Beside the traditional polishing operations, STF has some advantages over the advanced surface finishing processes such as magnetorheological polishing. Similar to STF based processing, magnetorheological polishing method benefits from the stiffened liquid medium to hold the abrasive particles tightly during the material removal process. To increase the stiffness in the

A. Sert
Department of Mechanical Engineering, Eskişehir Osmangazi University, Eskişehir, Turkey

S. Gürgen (✉) · M. C. Kuşhan
Department of Aeronautical Engineering, Eskişehir Osmangazi University, Eskişehir, Turkey
e-mail: sgurgen@ogu.edu.tr

S. Gürgen (ed.), *Shear Thickening Fluid*, https://doi.org/10.1007/978-3-031-35521-9_1

carrier liquid, magnetic particles are suspended in the liquid. An external magnetic field is applied to the liquid to closely pack the magnetic particles in an orientation and thereby increasing the suspension stiffness. Abrasive particles are firmly held between the oriented magnetic particles so that the magnetorheological slurry flows on the workpiece to remove the asperities on the surface. A magnetic field is the essential source to conduct the process, and therefore, a high cost magnetic field generator and an additional power consumption are required for magnetorheological polishing process. On the other hand, the main advantage in the STF polishing technique is that no external excitation is needed to adjust the suspension stiffness. Stiffness control in STF based slurry is only dependent on the shear rate, which can be adjusted by the flowing speed of STF on the workpiece surface. In brief, STF based polishing is a highly simple technique for controlling the process parameters and surface quality.

Regarding the STF based polishing, the first attempt was a patent application by a research group from the University of Sydney in 2013 [26]. Then the system was investigated by some researchers. Li et al. [22] investigated a polishing operation in an STF based slurry. Material removal process was analyzed in the light of shear thickening rheology. Based on the STF rheology, an analytical model was proposed for material removal rate, and the model was verified by a set of polishing experiments. The model shows a good correlation with the experiments that the maximum difference was only 6.12% in terms of material removal rate. In addition, a parametric study was carried out in this work for a better understanding of the process. Polishing speed, abrasive particle size, and abrasive loading were varied in the experiments so that the role of each parameter was discussed in detail. In the STF based polishing of a die steel, an initial surface roughness of Ra 105.95 nm was lowered to Ra 5.1 nm in a processing period of 30 min. The material removal rate of the workpiece reached to 13.69 μm/h, which is quite a good rate in comparison with the current polishing techniques. In another study [23], a comprehensive surface roughness model was proposed for STF based polishing operations based on the hardness of workpiece, shear thickening rheology, and plastic indentation on abrasive wear theory. Furthermore, abrasive particle size to colloidal particle size ratio was considered in the model. A set of polishing tests was carried out to validate this analytical model. According to the test results, the variation in the model was about 12%, which is an acceptable rate for such a complicated process. The study was conducted with an STF having multi-hydroxyl polymer colloidal particles distributed in a dispersant while using spherical aluminum oxide particles as the abrasive phase. Furthermore, a die steel of Cr12Mo1V1 was used as the workpiece in the experiments. Despite the good correlations between the analytical model and the test results, the authors stated that the model needs a modification based on the material properties to predict brittle material processing results. Nguyen et al. [27] proposed the STF based polishing technique for gears, which have complex geometrical designs including difficult-to-access areas. A case study was carried out by using a spur gear made from an alloy steel JIS-SCM435. The optimum process parameters were found for an STF based slurry based on multi-hydroxyl polymer colloidal and abrasive diamond particles. The optimization procedure was conducted for the input

parameters of polishing speed, gear inclination angle, and gear/tank wall gap. The pressure levels were investigated on the gear surfaces during the processing and thereby correlating with the shear thickening rheology. According to the results, the surface roughness was reduced to Ra 13 nm at the maximum pressure areas for the optimum process parameters. It was concluded that a product based design is important to effectively benefit from the STF based polishing process. Shao et al. [28] discussed the drawbacks in the traditional polishing of concave surfaces as such in the turbine blades. For this reason, STF based polishing was suggested for turbine blades since these products have highly complicated concave surfaces. Various process parameters such as polishing angle, polishing speed, pH value of slurry, etc. were considered in the study. The process was set up for a turbine blade made from a high-temperature resistant nickel alloy. By optimizing the process parameters, the initial roughness of Ra 72.3 nm was reduced to Ra 4.2 nm after a quick processing. The authors noted that STF based slurries exhibit high material removal rates and provide short processing times even for the difficult-to-process materials. A similar work for curved surfaces was carried out in another research [29]. A bar made from a bearing steel was polished in an STF slurry. The roughness of the outer surface was reduced from Ra 105.95 nm to Ra 6.99 nm after 1-hour processing. Lyu et al. [30] proposed the STF based slurries for sharpening the carbide inserts. The effects of polishing speed, abrasive particle size, abrasive particle loading, and inclination angle were investigated in a set of polishing experiments. Product-specific operational designs are suggested due to the complicated geometries of the carbide inserts. For the considered carbide inserts, the surface roughness was lowered from Ra 121.8 nm to Ra 7.1 nm after a 15-min processing. Scanning electron images proved that surface topographies are greatly improved after the STF based polishing operations. According to the results, STF based polishing technique is a promising and feasible method both for complicated geometries and refractory materials. The same research team used lithium tantalite substrates, which are very brittle and low fracture toughness materials, in an STF based polishing operation [31]. The efficiency of the STF processing was also observed for the materials requiring gentle finishing. Difficult-to-process materials are good application fields for STF slurries because these materials need advanced polishing systems for effective processing. In recent works [32, 33], workpieces made from quartz glass and zirconia were investigated in the STF based polishing operations. Despite the challenging material removal characteristics in these materials, good surface qualities are achieved by using STF slurries in the operations. Mirror finishing surfaces are obtained after carefully optimized processes. In addition, high material removal rates are observed in the operations.

This chapter presents a work regarding the role of shear thickening rheology on polishing operation. For this purpose, two polishing slurries were prepared based on (i) a Newtonian fluid and (ii) a non-Newtonian fluid. In the Newtonian fluid based slurry, polyethylene glycol (PEG) was used as the carrier liquid for the abrasive silicon carbide (SiC) particles. The non-Newtonian fluid was an STF, which was synthesized by distributing fumed silica particles in PEG. Similar to the Newtonian case, SiC particles were included as the abrasive phase in the STF. A WC-Co specimen was subjected to polishing operations by using both slurries. After the

operations, surface roughness and surface topography results were evaluated. The results show that there is a clear difference between the polishing slurries. The Newtonian based slurry leads to a very slight improvement in the surface quality, while the STF based slurry greatly enhances the surface finish in the specimen.

1.2 Experimental Details

In order to prepare an STF, nano-size fumed silica was distributed in a 200 g/mol PEG. The loading ratio of the silica was 20 wt% in the suspension. A high-speed homogenizer was used for 1 hour to homogeneously distribute the silica particles. As the abrasive phase, SiC powder with the average particle size of 1 μm was included in the STF. The SiC amount was 45 wt% in the polishing slurry. In order to understand the shear thickening effect on the polishing process, another slurry was prepared by distributing 45 wt% SiC particles in PEG, which is a Newtonian fluid that shows constant viscosity under increasing shear rate unlike shear thickening rheology. Table 1.1 shows the details of the polishing cases.

Polishing tests were carried out in a Struers TegraPol abrasive system for an 8-mm-diameter WC-Co bar. A polishing pad was wetted with 15 ml of the fabricated slurries prior to the tests. The pad was rotated at 150 rpm while applying 15 N at the polishing interface during the tests. The initial roughness of the specimen surface was prepared in a grinding process using a 220 mesh wheel just before the polishing tests. The initial roughness was kept constant at Ra 0.12 μm. Surface roughness profiles and surface topographies were evaluated after the polishing tests.

1.3 Results and Discussion

Figure 1.1 shows the surface roughness profiles for the unpolished, PEG/SiC polished, and STF/SiC polished specimens. From the charts, it is clearly seen that the unpolished surface, which is the initial surface condition for the polishing tests, includes sharp peaks and deep valleys. This surface was obtained after a grinding process just to set a standard surface before the polishing tests. On the other hand, the surface after the polishing with the PEG/SiC slurry includes somehow suppressed peaks and valleys on the surface. Despite a reduced roughness in average, the surface is quite rough after the PEG/SiC polishing. Regarding the STF/SiC slurry, it can be mentioned that there is an obvious improvement in the surface finish. The STF/SiC

Table 1.1 Details of the polishing tests

Slurry	Content
PEG/SiC	45 wt% SiC particles in PEG and SiC suspension
STF/SiC	45 wt% SiC particles in STF and SiC suspension

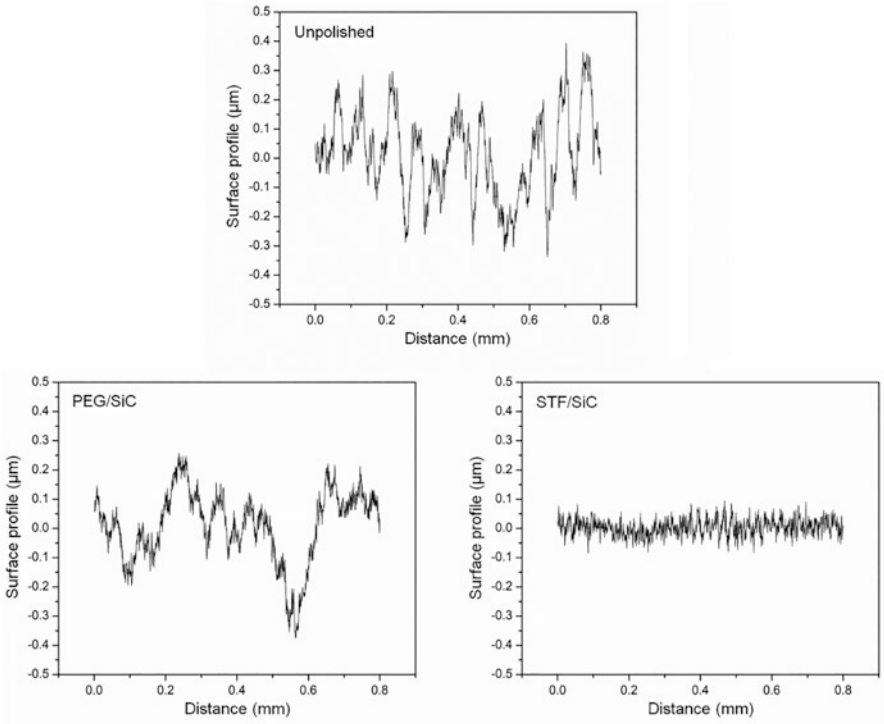

Fig. 1.1 Surface roughness profiles for the specimens

slurry provides a strong mechanism for removing sharp peaks and deep valleys on the specimen surface. According to the surface profile, the variation of the surface profile is limited in a very narrow band after the STF/SiC process. Considering the surface roughness measurements, the initial roughness of Ra 0.12 µm is reduced to Ra 0.09 µm after the polishing operation with the PEG/SiC slurry, while it shows a further reduction to Ra 0.02 µm by the effect of the STF/SiC slurry.

Figure 1.2 shows the surface micrographs for the specimens. According to the initial case micrograph, there is a rough surface including deep and random scratches on the specimen. Because the specimen preparation procedure was completed by using a 220 mesh sandpaper, which corresponds to an average abrasive size of about 60 µm, deep scratches are quite common on the surface. After the polishing test with the PEG/SiC slurry, there is a smoothening process clearly identified on the surface. Comparing the unpolished and the PEG/SiC surfaces, it can be stated that the PEG/SiC operation removes the slight scratches on the surface; however, deep scratches are still visible on the micrograph. On the other side, the STF/SiC polishing leads to a very smooth surface by removing the deep scratches effectively. For this reason, surface roughness is significantly suppressed by the effect of the STF/SiC slurry.

Figure 1.3 shows the surface topographies for the specimens based on the micrographs. The surface topography images support both the surface profiles and

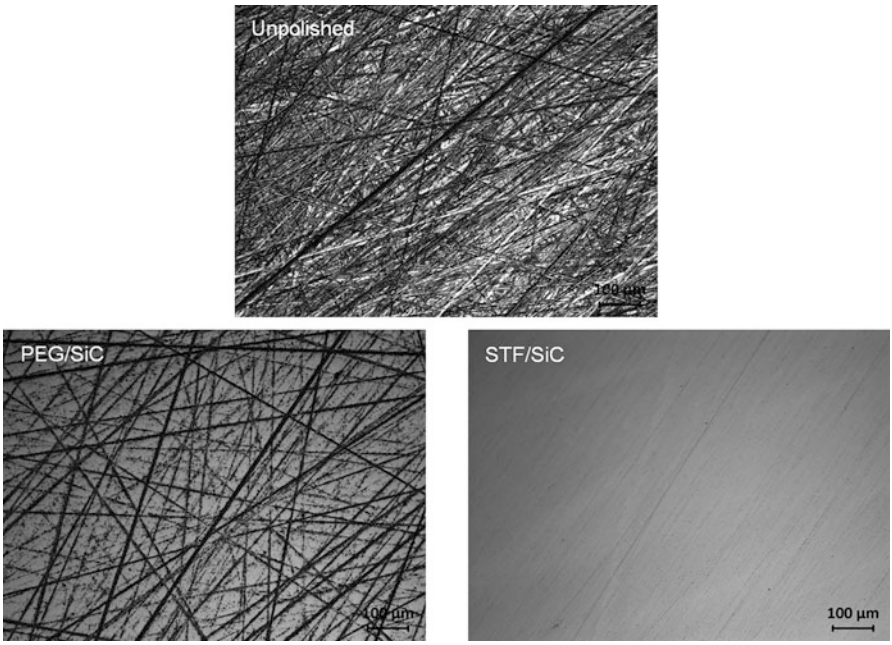

Fig. 1.2 Surface micrographs for the specimens

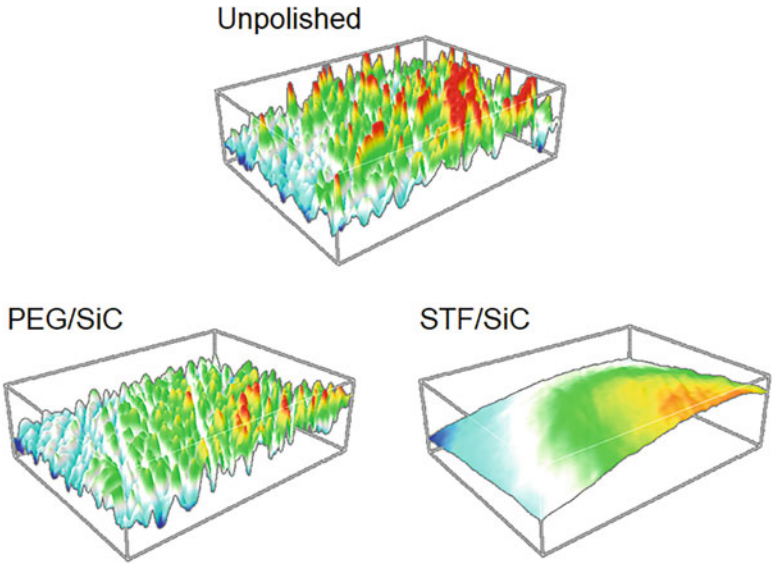

Fig. 1.3 Surface topographies for the specimens

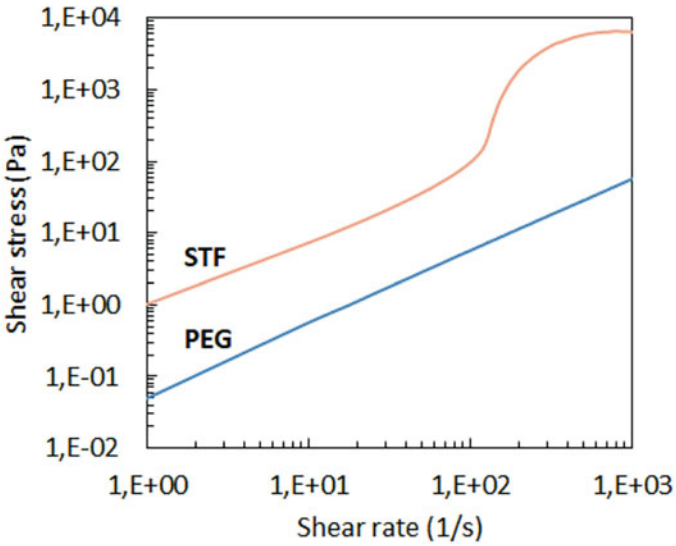

Fig. 1.4 Stress development in PEG and STF [34]. (Reprinted by permission from Springer)

micrographs. The initial surface condition includes several spiky profiles that yield a heavy roughness on the surface. The PEG/SiC slurry shows an effective polishing process for the surface, thereby removing the sharp peaks. A slight reduction is obviously seen in the spiky profile. Despite this effect, a real polishing process is observed in the STF/SiC case. The peaks and valleys are removed to a great extent by the effect of STF/SiC slurry.

Regarding the polishing results, it can be stated that shear thickening rheology has a considerable effect on the polishing process. PEG is a Newtonian fluid, and the carbide abrasives in this fluid do not produce an effective material removal mechanism. On the other hand, the same abrasives provide an enhanced material removal process in a non-Newtonian fluid. This difference can be explained by the material removal mechanism in polishing operations. In the polishing operations, abrasive particles contact the specimen surface and thereby apply a cutting force during the relative motion with the surface. The polishing pad supports the abrasive particles to provide material removal from the surface; however, the fluffy nature of the polishing pads makes the abrasive particles embedded into the pad. On the other hand, liquid medium within the slurries supports the abrasives to realize the material removal. In the PEG/SiC slurry, the stresses developed in the liquid remain at lower levels due to the Newtonian characteristics. However, the stresses drastically increase by the effect of viscosity jump in the STF/SiC slurry. Figure 1.4 shows the stress development in the PEG and STF samples. It can be clearly seen that STF shows higher stresses than PEG before the shear thickening point. At this phase, this difference is associated with the increased density due to the solid particle doping in STF. Beyond the shear thickening point, stresses show a quick jump in STF while PEG has a stable increase. For this reason, STF can withstand higher cutting forces

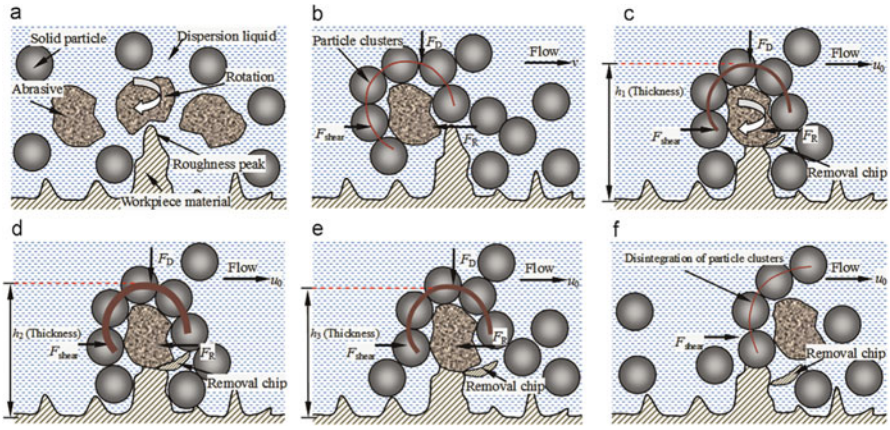

Fig. 1.5 Microstructural description of polishing process in STF slurry [22]. (Reprinted by permission from Elsevier)

during polishing in comparison with PEG in slurry. Consequently, the abrasive particles exhibit an increased material removal mechanism in the operation.

The stress bearing capacity of the slurry is completely dependent on the shear thickening rheology. As suggested by the previous works [35–39], solid particles (fumed silica particles in this work) in STF generate small particle clusters at low shear rates. These clusters get bigger by the effect of hydrodynamic forces acting on the solid particles. As shear rate increases in the medium, particle-to-particle contacts prevail over the field, thereby extending the particle clusters in the mixture. The clusters form chain-like elongations in the suspension. The stresses show a further increase up to a peak point during the clustering process. Beyond the peak point, the particle networks in the suspension cannot bear the developed stresses, and therefore, a structural breakdown is observed. Knowing this microstructural evolution in shear thickening phenomenon, it can be mentioned that STF polishing is effectively carried out at the thickening phase. Figure 1.5 shows the microstructural description of the polishing process in STF slurries. At the shear rates lower than the shear thickening point, the mixture behaves as a Newtonian fluid, and the distributed phases both solid particles and abrasives randomly move in the suspension. A rapid increase is observed in the viscosity upon shearing the suspension above the critical shear rate [40]. The mixture introduces to the shear thickening phase, thereby forming particle clusters by the effect of growing hydrodynamic forces [41]. During this process, abrasives are surrounded and firmly held by the particle clusters in the flow field. When the abrasives contact the specimen surface, material removal is realized by the effect of sharp edges of the abrasive particles. The cutting forces generated during material removal are compensated by the support of surrounding clusters. An adaptive material removal process is observed at the abrasive and specimen interface because higher cutting forces are met due to the growing stresses in the suspension when the shear rate increases to further levels. The STF acts as a

backing material for the abrasive particles, thereby providing a stiffened matrix for them to realize the material removal [22]. In addition to this effect, STF prevents the specimen surface from the abrasive plunges by providing a flexible backing support for the abrasive particles.

1.4 Conclusions

The adaptive rheology of STF has been used in different engineering applications for two decades. This works presents a novel approach to STF for polishing operations. The changeable stiffness in STF is efficiently adapted to polishing process. Comparing to a Newtonian polishing slurry, non-Newtonian behavior of STF based slurry provides enhanced material removal mechanism in the polishing. This is attributed to the high stresses developed in the suspension during the shear thickening phase. Higher cutting forces can be compensated by the effect of high level suspension stresses, thereby enhancing the material removal from the specimen surface. For this reason, the asperities on the workpiece are effectively flattened out, and thus, a smoother surface finish is achieved in the STF based polishing operation. This study shows that STF is a good candidate for the carrier liquid of polishing suspensions. Shear depended stiffness in STF provides an opportunity for tailoring the material removal rate from the workpiece. In addition to the enhanced material removal properties, STF based polishing does not require an additional equipment for tuning the stiffness as such in the magnetorheological polishing. STF is a promising material for designing precise surface finishing operations, and therefore, it can be adapted to the polishing of refractory materials.

Acknowledgments This work is supported by the Research Fund of Eskişehir Osmangazi University, Project #FOA-2022-2380.

References

1. Gürgen S, Kuşhan MC. The stab resistance of fabrics impregnated with shear thickening fluids including various particle size of additives. Compos Part Appl Sci Manuf. 2017;94:50–60.
2. Gürgen S, Kuşhan MC. The ballistic performance of aramid based fabrics impregnated with multi-phase shear thickening fluids. Polym Test. 2017;64:296–306.
3. Gürgen S, Kuşhan MC. The effect of silicon carbide additives on the stab resistance of shear thickening fluid treated fabrics. Mech Adv Mater Struct. 2017;24(16):1381–90.
4. Gürgen S. An investigation on composite laminates including shear thickening fluid under stab condition. J Compos Mater. 2019;53(8):1111–22.
5. Majumdar A, Butola BS, Srivastava A. An analysis of deformation and energy absorption modes of shear thickening fluid treated Kevlar fabrics as soft body Armour materials. Mater Des. 2013;51:148–53.

6. Majumdar A, Butola BS, Srivastava A. Development of soft composite materials with improved impact resistance using Kevlar fabric and nano-silica based shear thickening fluid. Mater Des 1980–2015. 2014;54:295–300.
7. Gürgen S, Sofuoğlu MA. Experimental investigation on vibration characteristics of shear thickening fluid filled CFRP tubes. Compos Struct. 2019;226:111236.
8. Gürgen S, Sofuoğlu MA. Vibration attenuation of sandwich structures filled with shear thickening fluids. Compos Part B Eng. 2020;186:107831.
9. Gürgen S, Sofuoğlu MA. Smart polymer integrated cork composites for enhanced vibration damping properties. Compos Struct. 2021;258:113200.
10. Fischer C, Braun SA, Bourban PE, Michaud V, Plummer CJG, Månson JAE. Dynamic properties of sandwich structures with integrated shear-thickening fluids. Smart Mater Struct. 2006;15(5):1467–75.
11. Iyer SS, Vedad-Ghavami R, Lee H, Liger M, Kavehpour HP, Candler RN. Nonlinear damping for vibration isolation of microsystems using shear thickening fluid. Appl Phys Lett. 2013;102 (25):251902.
12. Neagu RC, Bourban PE, Månson JAE. Micromechanics and damping properties of composites integrating shear thickening fluids. Compos Sci Technol. 2009;69(3–4):515–22.
13. Yuan X, Wang S, Mao X, Liu H, Liang Z, Guo Q, et al. Forced vibration mechanism and suppression method for thin-walled workpiece milling. Int J Mech Sci. 2022;230:107553.
14. Gürgen S, Sofuoğlu MA. Integration of shear thickening fluid into cutting tools for improved turning operations. J Manuf Process. 2020;56:1146–54.
15. Liu B, Du C, Deng H, Fu Y, Guo F, Song L, et al. Study on the shear thickening mechanism of multifunctional shear thickening gel and its energy dissipation under impact load. Polymer. 2022;247:124800.
16. Liu B, Du C, Wang L, Fu Y, Song L. The rheological properties of multifunctional shear thickening materials and their application in vehicle shock absorbers. Smart Mater Struct. 2021;30(8):085028.
17. Zhang X, Li TT, Peng HK, Lou CW, Lin JH. Enhanced sandwich structure composite with shear thickening fluid and thermoplastic polyurethanes for high-performance stab resistance. Compos Struct. 2022;280:114930.
18. Wu X, Xiao K, Yin Q, Zhong F, Huang C. Experimental study on dynamic compressive behaviour of sandwich panel with shear thickening fluid filled pyramidal lattice truss core. Int J Mech Sci. 2018;138–139:467–75.
19. Pinto F, Meo M. Design and manufacturing of a novel shear thickening fluid composite (STFC) with enhanced out-of-plane properties and damage suppression. Appl Compos Mater. 2017;24 (3):643–60.
20. Li W, Nakano M, Tian T, Totsuka A, Sato C. Viscoelastic properties of MR shear thickening fluids. J Fluid Sci Technol. 2014;9(2):JFST0019.
21. Peng GR, Li W, Tian TF, Ding J, Nakano M. Experimental and modeling study of viscoelastic behaviors of magneto-rheological shear thickening fluids. Korea-Aust Rheol J. 2014;26(2): 149–58.
22. Li M, Lyu B, Yuan J, Dong C, Dai W. Shear-thickening polishing method. Int J Mach Tools Manuf. 2015;94:88–99.
23. Li M, Lyu B, Yuan J, Yao W, Zhou F, Zhong M. Evolution and equivalent control law of surface roughness in shear-thickening polishing. Int J Mach Tools Manuf. 2016;108:113–26.
24. Span J, Koshy P, Klocke F, Müller S, Coelho R. Dynamic jamming in dense suspensions: Surface finishing and edge honing applications. CIRP Ann. 2017;66(1):321–4.
25. Gürgen S, Sert A. Polishing operation of a steel bar in a shear thickening fluid medium. Compos Part B Eng. 2019;175:107127.
26. Chang L, Friedrich K, Ye L. Methods, systems and compositions for polishing. 2013; WO2013016779 A1.

27. Nguyen DN, Dao TP, Prakash C, Singh S, Pramanik A, Krolczyk G, et al. Machining parameter optimization in shear thickening polishing of gear surfaces. J Mater Res Technol. 2020;9(3): 5112–26.
28. Shao Q, Lyu B, Yuan J, Wang X, Ke M, Zhao P. Shear thickening polishing of the concave surface of high-temperature nickel-based alloy turbine blade. J Mater Res Technol. 2021;11:72–84.
29. Lyu B, Dong C, Yuan J, Sun L, Li M, Dai W. Experimental study on shear thickening polishing method for curved surface. Int J Nanomanufact. 2017;13(1):81.
30. Lyu BH, He QK, Chen SH, Shao Q, Chen Y, Geng ZY. Experimental study on shear thickening polishing of cemented carbide insert with complex shape. Int J Adv Manuf Technol. 2019;103 (1–4):585–95.
31. Lyu BH, Shao Q, Hang W, Chen SH, He QK, Yuan JL. Shear thickening polishing of black lithium tantalite substrate. Int J Precis Eng Manuf. 2020;21(9):1663–75.
32. Shao Q, Duan S, Fu L, Lyu B, Zhao P, Yuan J. Shear thickening polishing of quartz glass. Micromachines. 2021;12(8):956.
33. Li M, Huang Z, Dong T, Tang C, Lyu B, Yuan J. Surface quality of zirconia (ZrO2) parts in shear-thickening high-efficiency polishing. Procedia CIRP. 2018;77:143–6.
34. Gürgen S, Fernandes FAO, de Sousa RJA, Kuşhan MC. Development of eco-friendly shock-absorbing Cork composites enhanced by a non-Newtonian fluid. Appl Compos Mater. 2021;28 (1):165–79.
35. Mari R, Seto R, Morris JF, Denn MM. Shear thickening, frictionless and frictional rheologies in non-Brownian suspensions. J Rheol. 2014;58(6):1693–724.
36. Raghavan SR, Khan SA. Shear-thickening response of Fumed silica suspensions under steady and oscillatory shear. J Colloid Interface Sci. 1997;185(1):57–67.
37. Gürgen S, Kuşhan MC, Li W. Shear thickening fluids in protective applications: A review. Prog Polym Sci. 2017;75:48–72.
38. Gürgen S, Kuşhan MC, Li W. The effect of carbide particle additives on rheology of shear thickening fluids. Korea-Aust Rheol J. 2016;28(2):121–8.
39. Gürgen S, Li W, Kuşhan MC. The rheology of shear thickening fluids with various ceramic particle additives. Mater Des. 2016;104:312–9.
40. Galindo-Rosales FJ, Rubio-Hernández FJ, Sevilla A, Ewoldt RH. How Dr. Malcom M. Cross may have tackled the development of "An apparent viscosity function for shear thickening fluids.". J Non-Newton Fluid Mech. 2011;166(23–24):1421–4.
41. Wagner NJ, Brady JF. Shear thickening in colloidal dispersions. Phys Today. 2009;62(10): 27–32.

Chapter 2
Conductive Shear Thickening Fluids for Multifunctional Purposes

Mohammad Rauf Sheikhi, Mahdi Hasanzadeh, and Selim Gürgen

2.1 Introduction

Shear thickening is a non-Newtonian phenomenon in which the stress needed to shear a fluid grows more quickly than linearly with the shear rate. Discontinuous shear thickening, which occurs when the stress abruptly increases with increased shear rate and results in a solid-like behavior, is a particularly dramatic variation that many concentrated suspensions of particles experience [1, 2].

Shear thickening fluids (STFs) are innovative materials with rate-sensitive properties. STFs are relatively soft and fluidic in the absence of external stimulation. When exposed to a high-speed loading, these materials get stiffer in reaction to external stresses. When the stress is removed, the materials turn back to their original fluidic texture. Because of its unique mechanical capabilities, this type of intelligent materials has prompted widespread attention with a key study focusing on shear thickening mechanism, performance, model, and application [3, 4].

Shear thickening effect was first discovered in the 1960s [5]. Interestingly, this phenomenon was initially defined as a problem in many industrial processes such as mixing and coating, for instance, as it hinders the fluid to flow, consequently leading

M. R. Sheikhi
Key Laboratory of Traffic Safety on Track of Ministry of Education, School of Traffic & Transportation Engineering, Central South University, Changsha, Hunan, China

State Key Laboratory for Strength and Vibration of Mechanical Structures, Shaanxi ERC of NDT and Structural Integrity Evaluation, School of Aerospace Engineering, Xi'an Jiaotong University, Xi'an, China

M. Hasanzadeh (✉)
Department of Textile Engineering, Yazd University, Yazd, Iran
e-mail: m.hasanzadeh@yazd.ac.ir

S. Gürgen
Department of Aeronautical Engineering, Eskişehir Osmangazi University, Eskişehir, Turkey

S. Gürgen (ed.), *Shear Thickening Fluid*, https://doi.org/10.1007/978-3-031-35521-9_2

to uneven coating on surfaces, blockage of crude oil in pipelines, overloading of blenders at high speeds, and mostly failure of the equipment. Shear thickening effect has attracted little or no attention by the researchers because it is not conducive to industrial production. With the rise of nanotechnology during the mid-1990s, a novel STF was successfully fabricated, which has attracted much attention for different kinds of applications. The unique characteristics of the STF have been used to develop smart materials and structures more recently. For instance, STFs have been used in conjunction with high-performance fabrics to create novel, thin, flexible, affordable materials that have comparable or even superior ballistic, stab, and puncture protective qualities than the current protective materials [6–9]. Recently, there has been a lot of interest in improving the impact resistance of textile structures by impregnating the fabrics with STFs [10]. The absorption of the shock waves from earthquakes or severe wind conditions and the integration of STF within the damper systems are other applications of STFs that have been recently investigated [11, 12]. In structural components, STFs are suggested to improve the vibration and damage resistance of whole systems. Moreover, they could restrict the movement of shoulders, knees, elbows, ankles, and hips to prevent them from sudden accelerations [3].

Shear thickening behavior is observed in various suspensions including starch dispersions, silica suspended ethylene glycol (EG), polyvinylchloride in dioctylphthalate, kaolin clay in glycerol, poly (methyl methacrylate) (PMMA) in PEG, fumed silica in propylene glycol, silica suspended PEG, multiwalled carbon nanotubes (MWCNTs) in polypropylene glycol (PPG), and silica particles in ionic liquids. Among them, the suspension of silica particles in PEG has been widely investigated, analyzed, and more often reported in the literature on STF.

As for C-STFs, both rheology and electrical properties are sensitive to the chain-like particle formations and doping. The change in electrical resistance of C-STF during the shear thickening process can be collected as a signature for detecting the working conditions in applications. Therefore, developing a kind of C-STFs and investigating their shear-dependent electrical properties are necessary. This chapter focuses on the classification and mechanism of STFs and conductive STFs (C-STFs) as well. A novel C-STF incorporated with MWCNTs is developed, and its rheological behavior and electrical properties are discussed in detail. This chapter provides recent developments and ideas for further research on the properties of C-STFs.

2.2 Shear Thickening Classifications

Granular suspension, cross-linked polymer, micelle, and insoluble polymer systems are the most common shear thickening systems (Fig. 2.1). Shear thickening is commonly observed in high-concentration granular solutions. Because of the shear thickening effect, the viscosity increases greatly in the shear thickening range, and then the phenomenon of the fluid transitioning into a solid-like condition is evident by making it appropriate for applications involving anti-impact and vibration

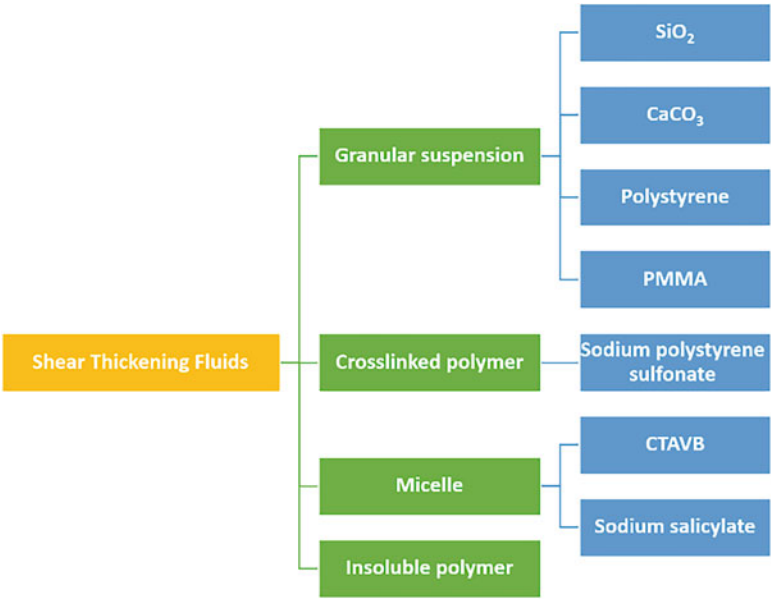

Fig. 2.1 Classification of different shear thickening systems

damping systems. As a result, this type of fluids has become the most commonly used STF [13]. Dispersion phase in granular suspensions often consists of gel particles from inorganic materials [14, 15] such as SiO_2, $CaCO_3$ and certain metal oxide gels or organic polymer particles such as polystyrene (PS) and PMMA submicron particles [16, 17]. Cross-linked polymer systems are mostly dispersions formed by hydrophobic polymers with ionic groups or water-soluble polymers with hydrophobic groups dispersed in water such as sodium polystyrene sulfonate dispersion in water [18]. The dispersion of these cross-linked polymers in water displays shear thickening effect because the cross-linking time of the polymers is smaller than the relaxing time at a given shear rate. The polymers can also be cross-linked to generate a network structure with shear thickening characteristics [19]. The shear thickening impact of cross-linked polymer dispersions is studied for coatings, papermaking, and oil transportation. To create the micelle system, anionic and cationic surfactants are mixed in deionized water in a certain ratio such as 0.1 wt% cetyltrimethylammonium benzoate and sodium salicylate solution [20]. The micellar rods readily spread in the aqueous phase in the absence of shear. Because micelle rods are stacked in layers along the flow direction, micelle dispersions show shear thinning behavior when the external shear rate is low. In contrast, the micelle rods merge in the micelle dispersion to create a bigger micelle network when the shear rate exceeds a specific critical value. At the end, the viscosity of micelle dispersions increases while showing shear thickening behavior. Micelle dispersions get shear thicken similarly to granular suspensions with the distinction that rod micelles are generated by tiny molecules and have limited strength. As a result, it can only exhibit

modest shear thickening behavior, making it suitable for vibration control. An insoluble polymer system is a dispersion made by combining certain high molecular weight polymers with a solvent that is unable to dissolve the polymer such as PS in decahydronaphthalene or polyethylene oxide in ethanol [18]. The polymer in the dispersion aggregates and, therefore, creates a polymer-rich phase in response to a certain external shear rate. In turn, this causes the dispersion gel to develop, which has a shear thickening effect. The gel network has very high strength due to the polymer's substantial strength, which exhibits a strong shear thickening phenomenon. This kind of fluids is extensively used in the coatings industry. Determining its shear thickening effect is critical for the coating and spraying processes as well as the advancement of coating construction technology [21, 22].

2.3 Shear Thickening Mechanism

As non-Newtonian fluids, STFs are often distinguished by a considerable rise in viscosity when the applied shear rate approaches a critical threshold. Figure 2.2 depicts a simplified illustration of shear thickening behavior. Particles in media are well-dispersed in the equilibrium condition. At shear rates less than a threshold value, the STF exhibits low viscosity. Because of the chaotic nature of the particles under the applied stress, layers of particles are formed as the shear rate increases. By increasing shear rate, hydroclusters are developed, thereby causing the particles to

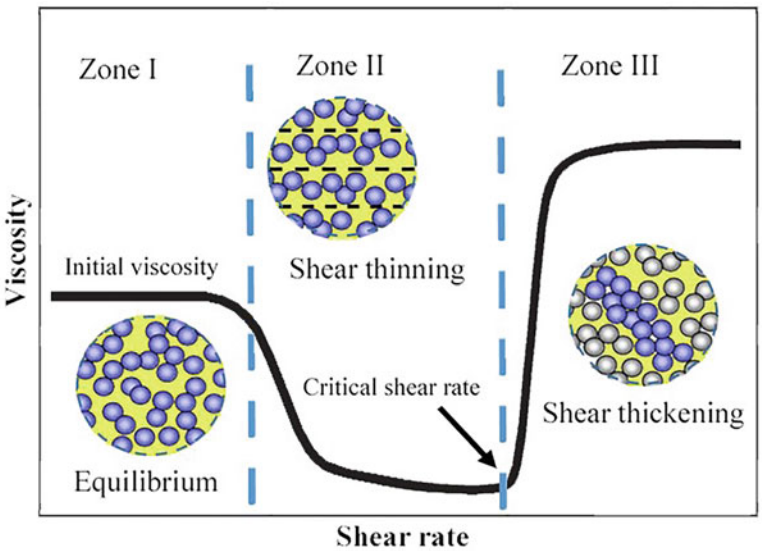

Fig. 2.2 Typical viscosity curve of a STF showing shear thinning and shear thickening behavior of colloidal suspensions

agglomerate. After the stress is removed, the suspensions return to an easy-flowing condition, and therefore, the flow shows regular fluidic texture. During this transition, the shear thinning is completely reversible. According to the literature, researchers have put forth several ideas to account for the fundamental reasons behind shear thickening behavior. The "order-disorder transition" (ODT) [23–27] and the "hydrocluster" mechanism [28, 29] provide a more comprehensive explanation of this behavior than the other ideas. The ODT explains how the application of shear rate causes the particle arrangements to break down, increasing the drag forces between the particles. Based on this expertise, Hoffman [26], one of the first researchers to thoroughly study shear thickening, developed a micromechanical model of shear thickening as a flow-induced ODT. He hypothesized that a transition from a layer ordered and easily flowing condition to a disordered one caused the shear thickening propensity. He suggested that this transition is caused by the van der Walls and London interactions, electric double layer, and shear stress forces acting on a cluster of particles. Furthermore, it was postulated that the particles inside the moving layers are subjected to hydrodynamically generated forces that cause the particles to be pushed out of their layer, disrupting the ordered flow. When the shear rate reaches a critical threshold, a quick rise in viscosity occurs. The hydrocluster mechanism is based on particle interactions in a liquid medium. Consequently, it is possible to deduce that the shear thickening behavior in concentrated colloidal suspensions is caused by hydrodynamic lubricating forces between the particles. When shear force is applied and particles suspended in a fluid collide, the hydrodynamic pressure rises. The drag forces between particles are enhanced because of the development of clusters under shear force. Experimental evidence for the hydrocluster process is provided by rheological, rheo-optical, and flow-SANS experiments as well as computer simulations [30]. Although both microscopic explanations for the shear thinning phenomena have been put forth, the "hydrocluster" explanation is more precise and all encompassing.

Although shear thinning is more prevalent than shear thickening, it has been postulated that under the correct conditions, shear thickening may occur in any dense suspension [31]. One of the most difficult problems is determining why not all dense suspensions display shear thickening behavior. One of the more confusing concerns is why soft particle suspensions, which may readily bend to shear past one other, do not shear thicken yet tightly packed hard particle suspensions do. Due to strong coulombic, charge-dipole, dipole-dipole, and van der Waals interactions, the behavior of nanoparticles differs dramatically for hard spheres. In such systems, interactions between nanoparticles and nanoparticles and liquid medium alter the state of the nanoparticles. According to the literature, lubricating and frictional forces play a significant part in the shear thickening process. Lin et al. [32] investigated the shear thickening behavior in the interface of micron-sized silica and latex particles to determine the hydrodynamic and contact force contributions to the shear thickening process. They observed that raising the strain rate causes the contact contribution to increase, while the hydrodynamic contribution remains constant as the suspension deepens. This phenomenon demonstrates how contact forces influence the shear thickening of dense colloidal suspensions. According to contact rheology models

[32, 33], hydrodynamic lubrication forces induce Newtonian behavior or shear thinning at low shear rates (Zone I) due to minimal particle interactions. When the shear rate (Zone II) is raised, lubrication breaks down. Because of frictional forces, force chains form, causing discontinuous shear thickening [34]. As the shear rate increases (Zone III), the force network tightens, finally becoming entirely shear jammed. When shear rearranges particles into anisotropic patterns, large clusters emerge. Instead of the quick and irreversible increase in viscosity associated with strong and discontinuous shear thickening, frictional hydrodynamic interactions between suspended particles create the smooth and reversible viscosity increase associated with continuous shear thickening [35].

2.4 Conductive Shear Thickening Fluids (C-STFs)

For many applications, the electrical conductivity of STFs is the most significant rheological parameter. The capacity of charged particles in a suspension to transport charges toward respective electrodes when an electric potential is introduced determines the electrical conductivity of an STF. For example, the next generation of soft body armor will need to be sensitive to outside stimuli in addition to being able to withstand mechanical impact. Multi-component Kevlar textiles with mechano-electric coupling properties are urgently needed in soft body armor as a crucial component of smart wearable systems. Previous studies have shown how adding conductive fillers to fabrics could produce electronic fabrics with good electrical characteristics [36]. Additionally, multifunctional STFs and shear stiffening gels (SSGs) with magnetic or electric characteristics might be made simply because of their gel-like structure [37, 38]. The electrical conductivity of STFs can be greatly enhanced by inserting some metal, metal oxide, or nanomaterials in them. C-STFs offer several technical and commercial applications, including colloidal dispersion field-induced pattern creation, sensors, and electrically conductive adhesive technology. Several studies on the electrical conductivity of STF have been published. Figure 2.3 depicts the increase of conductive STF related publications during the last decade.

Due to their high fundamental electrical conductivity and low density compared to metals or metal oxides, C-STFs comprising electrically conductive elements including carbon nanotubes (CNTs), diamond nanoparticles, and graphene have received a lot of attention. For instance, Wei et al. [39] investigated the rheological characteristics of suspensions containing varied concentrations of MWCNT and silica, and according to this research, introducing CNT resulted in substantial shear thinning and thickening phenomena. The STFs showed the largest shear thickening effects when the mass fraction was 0.8%. Nakonieczna et al. [40] achieved the highest viscosity in STF by using 55% silica and 0.25% CNTs. Hasanzadeh et al. [40] found that STF/MWCNT in PEG200 with 44% fumed silica and 0.8% CNT produced the best results when used to evaluate the puncture resistance performance of woven high modulus polypropylene (HMPP) textiles.

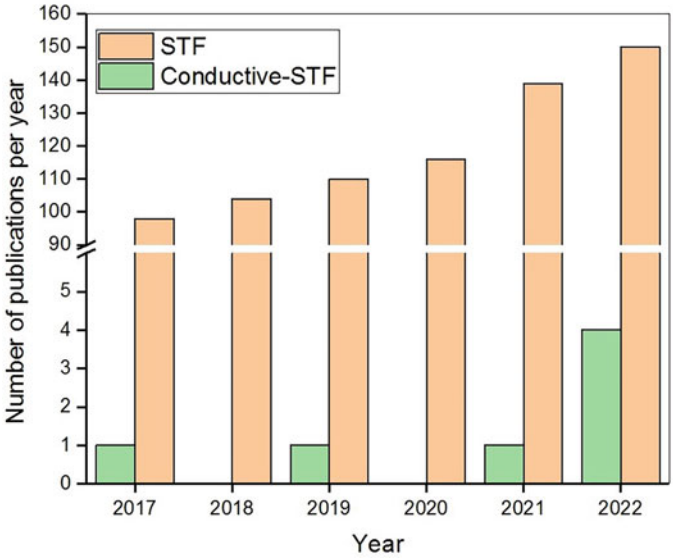

Fig. 2.3 The number of STF and C-STF related publications. The Scopus database was used to obtain the data

Chen et al. [41] developed conductive STF by dispersing CNTs in a silica based STF, and they discovered that as the CNT concentration grew, so did the shear thickening effect of STF. They discovered that resistance changes may be seen and that the R/R value might reach as high as 90%. Both initial and final resistance might be easily modified by changing the CNT mass percentage. Liu et al. [41] created a CNT/STF/Kevlar based wearable electronic textile composites in another work. The stab resistance tests on them revealed that the addition of CNT fillers to STF significantly improves impact resistance. The best sample was a CNT/STF-55%/Kevlar based electronic textile. Li et al. [42] investigated how temperature, plate spacing, and poly(vinylpyrrolidone) (PVP) mass fraction influenced the rheological performance of MWCNT-PVP/silica based STF systems. This study revealed that PVP improves MWCNT dispersibility and adhesion. Furthermore, shear thickening performance is shown to be the most effective when the PVP mass fraction reaches 0.15%. They also noted that the temperature sensitivity of the MWCNT-PVP/silica based STF system is equal to that of the MWCNT/STF system and that PVP may significantly improve the shear thickening performance without changing the temperature sensitivity. Nakonieczna et al. [43] studied silica based STFs containing polypropylene glycol and different nanofillers such as MWCNTs, RGO, GO, and carbon black. They discovered that the MWCNT produces the most significant alterations in the rheological properties of the STF, resulting in the highest peak viscosity in the rheological investigation. Ghosh et al. [44] investigated the effect of cellulose nanofibers on the rheological behavior of silica based STFs. The dynamic rheological research revealed that even at low shear rates, a modest concentration of

cellulose nanofibers may improve the elastic behavior of the whole solution. Additionally, Li et al. [45] discovered that adding MWCNTs to STFs improves the rheological behavior and quasi-static stab performance of Kevlar fabrics.

2.5 A Case of C-STF: MWCNT in STF

2.5.1 Experimental Details

Fumed silica (SiO_2) particles with an average size of 20 μm were obtained from Evonik (Germany). MWCNTs (D × L: 6–9 nm × 5 μm), polyethylene glycol (PEG, 400 g/mol), ethanol (Et-OH), and acetone were purchased from Sigma-Aldrich (USA).

Using a high-speed homogenizer, the fumed silica particles were progressively added to PEG and distributed in the liquid medium. To ensure a homogenous and steady dispersion, the mixing procedure was prolonged for an additional hour. After fabricating the STF (20 wt% SiO_2), different amounts of MWCNTs (0.20, 0.50, 1.00, 1.50, 2.50, 3.00, and 3.50 wt%) were added to the as-prepared STF and then stirred again for 30 min using a homogenizer. The suspensions were rested at room temperature overnight after the dispersion stage to get the removal of air bubbles. After 2 hours of the preparation procedure, rheological and electrical resistance measurements were carried out with the suspensions. The design of samples in the rheological and electrical resistance measurements is shown in Table 2.1.

A standard parallel plate system was used in the rheological measurements with an Anton Paar MCR 302 modular compact rheometer. The gap between the plates was fixed at 1 mm. The shear rates used in the studies ranged from 0 to 1000 s^{-1}. To prevent the loading effects, a pre-shear of 1 s^{-1} was applied to the samples for 60 s before each measurement. A multimeter (Uni-T UT71E with 1 Ω to 40 MΩ measurement accuracy) was used to obtain the electrical resistance of the samples. Each electrical resistance measurement was carried out using 50 g of samples with a

Table 2.1 Samples design in rheological and electrical resistance testing

Sample	Description
STF	STF (20 wt% SiO_2)
C-STF 1	STF + 0.20 wt% MWCNT
C-STF 2	STF + 0.50 wt% MWCNT
C-STF 3	STF + 0.70 wt% MWCNT
C-STF 4	STF + 1.00 wt% MWCNT
C-STF 5	STF + 1.50 wt% MWCNT
C-STF 6	STF + 2.00 wt% MWCNT
C-STF 7	STF + 2.50 wt% MWCNT
C-STF 8	STF + 3.00 wt% MWCNT
C-STF 9	STF + 3.50 wt% MWCNT

30 mm spacing between the probes and a 5 mm depth of penetration into the samples. All the samples were fixed and tested under identical conditions.

2.5.2 *Electrical Conductivity of C-STFs*

The electrical conductivity of C-STFs was studied in terms of electrical resistance. Figure 2.4 shows the variation of electrical resistance as a function of MWCNT weight fraction. It can be seen that the electrical resistance of C-STF decreases with increasing MWCNT content. The electrical resistance of C-STF drastically decreases at the MWCNT content of 0.5 wt%. This is the percolation threshold of C-STF, which is considered as one of the most important factors influencing the suspension properties. The intrinsic conductivity of MWCNTs and their aspect ratio have a significant effect on enhancing the electrical conductivity at the percolation threshold. Two distinct regions are observed in this plot: (i) high electrical resistance between 0.1 and about 0.5 wt% MWCNT, in which the electrical resistance of C-STF is very sensitive to the MWCNT content and decreases over several orders of magnitude when the MWCNT content reaches the percolation, and (ii) low electrical resistance after 0.5 wt% MWCNT content, in which the electrical resistance changes insignificant to the MWCNT concentration. At MWCNT content of 0.2 wt%, the electrical resistance is in the order of 2760 kΩ, while at 0.5 wt%, it steeply decreased to 1780 kΩ. Table 2.2 gives the electrical resistance of various C-STFs.

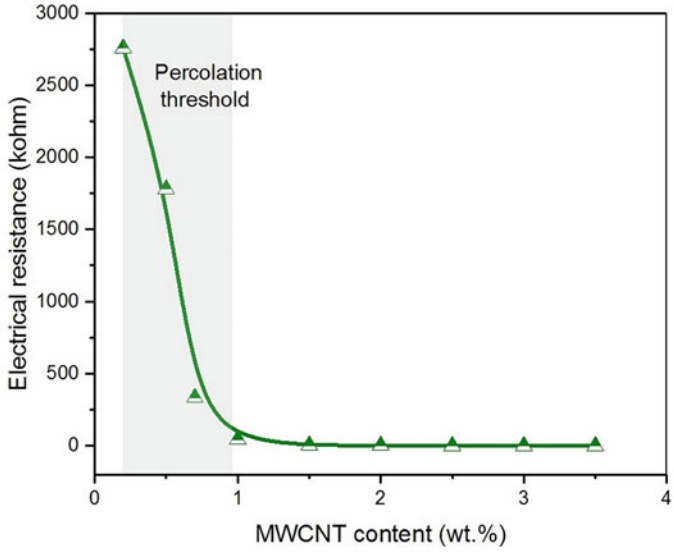

Fig. 2.4 Electrical resistance of C-STFs as a function of MWCNT content

Table 2.2 Electrical resistance of the samples

Sample	Details of samples	Electrical resistance (kΩ)
STF	STF (20 wt% SiO_2)	3890
C-STF 1	STF + 0.20 wt% MWCNT	2760
C-STF 2	STF + 0.50 wt% MWCNT	1780
C-STF 3	STF + 0.70 wt% MWCNT	335
C-STF 4	STF + 1.00 wt% MWCNT	45
C-STF 5	STF + 1.50 wt% MWCNT	3.680
C-STF 6	STF + 2.00 wt% MWCNT	1.650
C-STF 7	STF + 2.50 wt% MWCNT	0.565
C-STF 8	STF + 3.00 wt% MWCNT	0.245
C-STF 9	STF + 3.50 wt% MWCNT	0.128

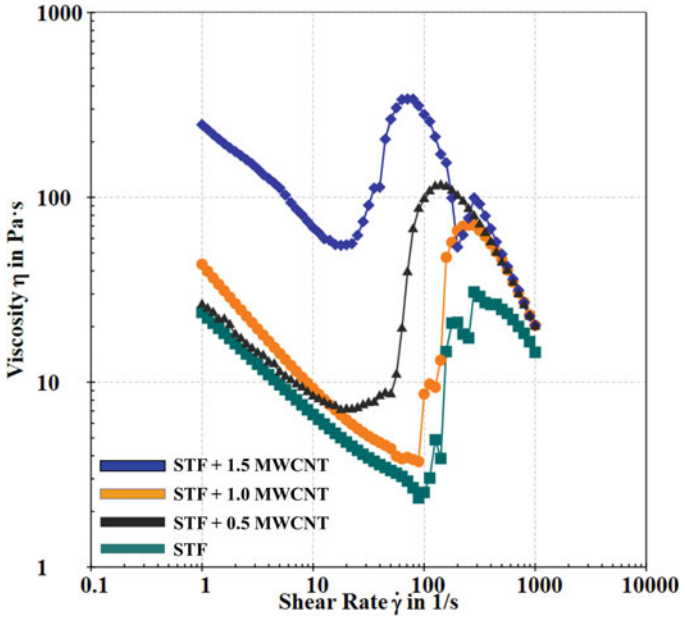

Fig. 2.5 Rheological behavior of C-STFs at different MWCNT content

2.5.3 Rheological Behavior of C-STFs

Figure 2.5 shows the rheological behavior of C-STFs containing 0.20, 0.50, 1.00, and 1.50 wt% of MWCNT at room temperature. The graph shows the variation of viscosity vs. shear rate in three different regions. The first region is about shear thinning behavior, which occurs at low shear rates. The second region corresponds to the abrupt increase in viscosity upon applying a shear rate at about critical point. The third region shows shear thinning at high shear rates. It can be found that increasing

Table 2.3 Electrical and rheological properties of C-STFs

Sample	Electrical resistance (kΩ)	Rheological properties		
		Initial viscosity (Pa. s)	Critical shear rate (1/s)	Peak viscosity (Pa. s)
STF	3890	25.9	89.1	30.77
C-STF 2 (STF + 0.50 wt % MWCNT)	1780	26.1	50.1	115.75
C-STF 4 (STF + 1.00 wt % MWCNT)	45	43.8	56.2	97.16
C-STF 5 (STF + 1.50 wt % MWCNT)	3.68	247.36	17.8	340.44

the MWCNT content to 1.5 wt% leads to the significant increase in initial and peak viscosity values of C-STF. Moreover, the critical shear rate decreases considerably by indicating a strong shear thickening behavior. Table 2.3 gives the rheological properties of various C-STFs such as critical shear rate, initial viscosity, and peak viscosity.

2.6 Conclusions

In this chapter, the electrical and rheological properties of C-STFs, consisting of fumed silica, polyethylene glycol (PEG), and multiwalled carbon nanotubes (MWCNTs), were discussed. Introduction to STF, classification of STF, and STF mechanism are discussed. Moreover, C-STFs and their behavior are discussed. For better understanding in this context, C-STF samples based on STF (20 wt% silica) and MWCNTs were produced. The electrical and rheological properties of these samples were discussed. The results show that the addition of MWCNTs increases the electrical conductivity of STF and improves the rheological properties of STF. It has been demonstrated that the electrical resistance of C-STFs is highly dependent on the MWCNT content. When the MWCNT content gets closer to the percolation threshold, the electrical resistance decreases by several orders of magnitude.

References

1. Brown E, Jaeger HM. Shear thickening in concentrated suspensions: Phenomenology, mechanisms and relations to jamming. Rep Prog Phys. 2014;77(4):046602.
2. Amoo LM, Fagbenle RL. Overview of non-newtonian boundary layer flows and heat transfer. Applications of Heat, Mass and Fluid Boundary Layers: Elsevier; 2020. p. 413–35.
3. Gürgen S, Kuşhan MC, Li W. Shear thickening fluids in protective applications: A review. Prog Polym Sci. 2017;75:48–72.

4. Wei M, Lin K, Sun L. Shear thickening fluids and their applications. Mater Des. 2022;110570: 110570.
5. Gates LE Jr. Evaluation and development of fluid armor systems. Hughes Aircraft Co Culver City CA Aerospace Groups; 1968.
6. Gong X, Xu Y, Zhu W, Xuan S, Jiang W, Jiang W. Study of the knife stab and puncture-resistant performance for shear thickening fluid enhanced fabric. J Compos Mater. 2014;48(6): 641–57.
7. Majumdar A, Butola BS, Srivastava A. Optimal designing of soft body Armour materials using shear thickening fluid. Mater Des. 2013;46:191–8.
8. Wei R, Dong B, Wang F, Yang J, Jiang Y, Zhai W, et al. Effects of silica morphology on the shear-thickening behavior of shear thickening fluids and stabbing resistance of fabric composites. J Appl Polym Sci. 2020;137(24):48809.
9. Gürgen S, Kuşhan MC. The stab resistance of fabrics impregnated with shear thickening fluids including various particle size of additives. Compos A: Appl Sci Manuf. 2017;94:50–60.
10. Taş H, Soykok IF. Investigation of the low velocity impact behaviour of shear thickening fluid impregnated Kevlar, hybrid (Kevlar/carbon) and carbon fabrics. Fibers Polymers. 2021;22(9): 2626–34.
11. Yeh F-Y, Chang K-C, Chen T-W, Yu C-H. The dynamic performance of a shear thickening fluid viscous damper. J Chin Inst Eng. 2014;37(8):983–94.
12. Freya R, Senthil R. Optimal evaluation of the rheological parameters for STF dampers in semi-rigid joints of steel structures using response surface method. Adv Civil Eng. 2022;2022:1.
13. Lim AS, Lopatnikov SL, Wagner NJ, Gillespie JW. Investigating the transient response of a shear thickening fluid using the split Hopkinson pressure bar technique. Rheol Acta. 2010;49 (8):879–90.
14. Yang H-l, J-m R, J-p Z, Wu Q-m, Z-c Z, Xie Y-y. Non-linear viscoelastic rheological properties of PCC/PEG suspensions. Chin J Chem Phys. 2013;22(1):46.
15. Khandavalli S, Rothstein JP. Large amplitude oscillatory shear rheology of three different shear-thickening particle dispersions. Rheol Acta. 2015;54(7):601–18.
16. Jiang W, Sun Y, Xu Y, Peng C, Gong X, Zhang Z. Shear-thickening behavior of polymethylmethacrylate particles suspensions in glycerine–water mixtures. Rheol Acta. 2010;49(11): 1157–63.
17. Zhou Z, Hollingsworth JV, Hong S, Wei G, Shi Y, Lu X, et al. Effects of particle softness on shear thickening of microgel suspensions. Soft Matter. 2014;10(33):6286–93.
18. van Egmond JW. Shear-thickening in suspensions, associating polymers, worm-like micelles, and poor polymer solutions. Curr Opin Colloid Interface Sci. 1998;3(4):385–90.
19. Wang SQ. Transient network theory for shear-thickening fluids and physically crosslinked networks. Macromolecules. 1992;25(25):7003–10.
20. Bautista F, Tepale N, Fernández V, Landázuri G, Hernández E, Macías E, et al. A master dynamic flow diagram for the shear thickening transition in micellar solutions. Soft Matter. 2016;12(1):165–70.
21. Elliott PT, Mahli DM, Glass JE. Spray applications: Part IV. Compositional influences of HEUR thickeners on the spray and velocity profiles of waterborne latex coatings. J Coat Technol Res. 2007;4(4):351–74.
22. Kim Y, Kumar SKS, Park Y, Kwon H, Kim C-G. High-velocity impact onto a high-frictional fabric treated with adhesive spray coating and shear thickening fluid impregnation. Compos Part B. 2020;185:107742.
23. Hoffman RL. Explanations for the cause of shear thickening in concentrated colloidal suspensions. J Rheol. 1998;42(1):111–23.
24. Boersma WH, Laven J, Stein HN. Viscoelastic properties of concentrated shear-thickening dispersions. J Colloid Interface Sci. 1992;149(1):10–22.
25. Laun H, Bung R, Hess S, Loose W, Hess O, Hahn K, et al. Rheological and small angle neutron scattering investigation of shear-induced particle structures of concentrated polymer dispersions submitted to plane Poiseuille and Couette flow a. J Rheol. 1992;36(4):743–87.

26. Hoffman R. Discontinuous and dilatant viscosity behavior in concentrated suspensions. II. Theory and experimental tests. J Colloid Interface Sci. 1974;46(3):491–506.
27. Della Valle G, Buleon A, Carreau P, Lavoie P-A, Vergnes B. Relationship between structure and viscoelastic behavior of plasticized starch. J Rheol. 1998;42(3):507–25.
28. Bender JW, Wagner NJ. Optical measurement of the contributions of colloidal forces to the rheology of concentrated suspensions. J Colloid Interface Sci. 1995;172(1):171–84.
29. Bender J, Wagner NJ. Reversible shear thickening in monodisperse and bidisperse colloidal dispersions. J Rheol. 1996;40(5):899–916.
30. Maranzano BJ, Wagner NJ. Flow-small angle neutron scattering measurements of colloidal dispersion microstructure evolution through the shear thickening transition. J Chem Phys. 2002;117(22):10291–302.
31. Barnes H. Shear-thickening ("Dilatancy") in suspensions of nonaggregating solid particles dispersed in Newtonian liquids. J Rheol. 1989;33(2):329–66.
32. Lin NY, Guy BM, Hermes M, Ness C, Sun J, Poon WC, et al. Hydrodynamic and contact contributions to continuous shear thickening in colloidal suspensions. Phys Rev Lett. 2015;115 (22):228304.
33. Peters IR, Majumdar S, Jaeger HM. Direct observation of dynamic shear jamming in dense suspensions. Nature. 2016;532(7598):214–7.
34. Wyart M, Cates ME. Discontinuous shear thickening without inertia in dense non-Brownian suspensions. Phys Rev Lett. 2014;112(9):098302.
35. Zarei M, Aalaie J. Application of shear thickening fluids in material development. J Mater Res Technol. 2020;9(5):10411–33.
36. Makowski T, Grala M, Fortuniak W, Kowalczyk D, Brzezinski S. Electrical properties of hydrophobic polyester and woven fabrics with conducting 3D network of multiwall carbon nanotubes. Mater Des. 2016;90:1026–33.
37. Grammatikos S, Kordatos E, Matikas T, David C, Paipetis A. Current injection phase thermography for low-velocity impact damage identification in composite laminates. Mater Des. 2014;55:429–41.
38. White KL, Yao H, Zhang X, Sue H-J. Rheology of electrostatically tethered nanoplatelets and multi-walled carbon nanotubes in epoxy. Polymer. 2016;84:223–33.
39. Wei M, Lv Y, Sun L, Sun H. Rheological properties of multi-walled carbon nanotubes/silica shear thickening fluid suspensions. Colloid Polym Sci. 2020;298(3):243–50.
40. Nakonieczna P, Wierzbicki Ł, Wróblewski R, Płociński T, Leonowicz M. The influence of carbon nanotube addition on the properties of shear thickening fluid. Bull Mater Sci. 2019;42 (4):1–4.
41. Chen Q, Liu M, Xuan S, Jiang W, Cao S, Gong X. Shear dependent electrical property of conductive shear thickening fluid. Mater Des. 2017;121:92–100.
42. Sun L, Wang G, Zhang C, Jin Q, Song Y. On the rheological properties of multi-walled carbon nano-polyvinylpyrrolidone/silicon-based shear thickening fluid. Nanotechnol Rev. 2021;10(1): 1339–48.
43. Nakonieczna-Dąbrowska P, Wróblewski R, Płocińska M, Leonowicz M. Impact of the carbon Nanofillers addition on rheology and absorption ability of composite shear thickening fluids. Materials. 2020;13(17):3870.
44. Ghosh A, Chauhan I, Majumdar A, Butola BS. Influence of cellulose nanofibers on the rheological behavior of silica-based shear-thickening fluid. Cellulose. 2017;24(10):4163–71.
45. Li D, Wang R, Liu X, Fang S, Sun Y. Shear-thickening fluid using oxygen-plasma-modified multi-walled carbon nanotubes to improve the quasi-static stab resistance of Kevlar fabrics. Polymers. 2018;10(12):1356.

Chapter 3
Shear Thickening Fluid Integrated Sandwich Structures for Vibration Isolation

Mohammad Rauf Sheikhi, Mehmet Alper Sofuoğlu, and Zhenmao Chen

3.1 Shear Thickening Fluid

Shear thickening fluid (STF) is a type of non-Newtonian material in which the viscosity rises as a function of shear rate or shear stress at a key parameter range as shown in Fig. 3.1. In many concentrated suspensions, a particularly disturbing version defined as shear thickening happens. When combined slowly, these suspensions are like a thin liquid; however, it is very thick like a solid when churned faster and then thin again when the loading is removed from the liquid [1, 2]. STF has been the subject of study throughout time to comprehend its rheological behavior and make use of it in engineering applications. Shear thickening was initially identified as a challenge in industrial processes like coating and mixing because it jams in tight spaces and overloads mixers, consequently reducing the process rate. However, more recently, smart materials and structures have been developed using the special property of these fluids. The rheology of an STF is determined by particle size, particle shape, size distribution, particle density, charge, particle roughness, and, in

M. R. Sheikhi
Key Laboratory of Traffic Safety on Track of Ministry of Education, School of Traffic & Transportation Engineering, Central South University, Changsha, China

State Key Laboratory for Strength and Vibration of Mechanical Structures, Shaanxi ERC of NDT and Structural Integrity Evaluation, School of Aerospace Engineering, Xi'an Jiaotong University, Xi'an, China
e-mail: mohammadraufsheikhi@csu.edu.cn

M. A. Sofuoğlu
Department of Mechanical Engineering, Eskişehir Osmangazi University, Eskişehir, Turkey

Z. Chen (✉)
State Key Laboratory for Strength and Vibration of Mechanical Structures, Shaanxi ERC of NDT and Structural Integrity Evaluation, School of Aerospace Engineering, Xi'an Jiaotong University, Xi'an, China

S. Gürgen (ed.), *Shear Thickening Fluid*, https://doi.org/10.1007/978-3-031-35521-9_3

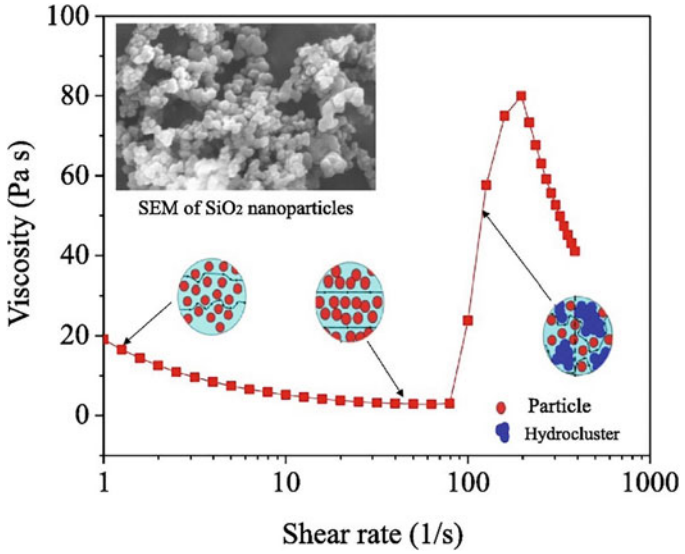

Fig. 3.1 Rheological properties of STF [6]. (Reprinted by permission from Elsevier)

certain situations, chemical interaction between the particle surface and carrier fluid [3, 4]. The initiation of reversible shear thickening at critical stress is affected by particle size, concentration, polydispersity, and interparticle interactions of dispersion [5].

Hence, STF, a soft material with intelligent properties, is more resistant to external force than a liquid and thereby displays variable properties unlike solids. As a result, STF has several application possibilities in the fields of surface polishing [7], human body protection [8–10], shock absorption [11–13], energy suppression [14], and vibration damping [15–18] in engineering structures. Although extensive studies have been conducted in recent years for the use of STF in engineering structures, the potential of these materials in integrating with new systems and transforming them into intelligent structures can still be considered, and their capacities can be studied.

3.2 Sandwich Structures

Sandwich structured composites are a specific type of composite materials with characteristics including low weight, high stiffness, and high strength. Sandwich structures are created by laminating two lightweight, moderately thick cores to two strong and rigid laminated facesheets [19]. The sandwich is like an endless I-beam in that when it bends, the flanges carry compression and tension loads in-plane (as do the sandwich facesheets), while the web bears shear loads (as does the structural

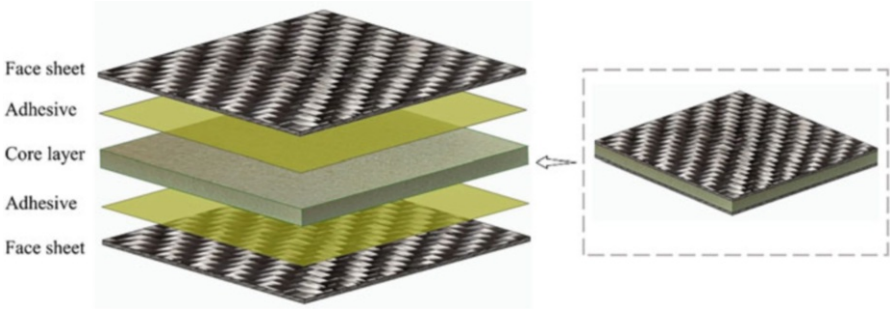

Fig. 3.2 Components in a conventional sandwich structure

sandwich core). Like a conventional I-beam, the structure becomes proportionally stiffer the farther away the flanges (facesheets) are from one another. The same result is achieved by a thicker core, but it also offers a low overall density, leading to a high stiffness-to-weight ratio. The potential for weight savings from utilizing a sandwich is demonstrated by a comparison of a steel panel and a composite sandwich panel. When the same deflection requirements are used, the weight reduction with sandwich design is close to 90% [20]. Thermal insulation, acoustic dampening, buoyancy, noncorrosiveness, and enhanced impact resistance are further advantages of sandwich structures. The stiffness of any beam or panel is inversely proportional to its thickness. The little weight penalty and higher yields in thickness are two significant differences between designs using traditional materials and those using a sandwich composite solution [21, 22]. A typical sandwich is composed of upper and lower facesheets with a significantly thicker core in between as shown in Fig. 3.2.

The tensile and compressive stresses in the sandwich structures are carried by the facesheets. Because the local flexural stiffness is so tiny, it is frequently neglected. Facesheets are commonly produced of conventional materials such as steel, stainless steel, and aluminum. In several applications, fiber- or glass-reinforced polymers can also be used as face materials. These materials are simple to use. Reinforced plastics may be designed to meet a variety of requirements such as anisotropic mechanical qualities, design freedom, high surface polish, and so on. Local pressure is also carried by the faces. Facesheets have to be measured for the shear forces related to them when the local pressure is high [23].

The role of core material is to hold the thin facesheets and keep them in relative position to each other so that they do not bend or deform inward or externally. To do this, the core material needs to possess several critical qualities. It needs to be stiff enough to maintain a continuous spacing between the faces. It must also be shear stiff enough to prevent the facesheets from sliding over one other. The shear stiffness pushes the facesheets to work together. If the shear strength of the core is low, the facesheets will not cooperate, and the sandwich will decrease rigidity [24]. To keep

the facesheets and the core layer interacting, the adhesive between them has to be capable of transferring shear forces between them. Moreover, the adhesive has to withstand the shear and tensile loads. The pressures on the joints are difficult to describe. The adhesive should be able to withstand the same shear stress as the core, according to a simple criterion [25].

3.3 Shear Thickening Fluid Integrated Sandwich Structures for Vibration Isolation

Vibration is generally an undesired phenomenon because of its negative effects on structural stability, position control, material performance, fatigue life, and noise reduction. Vibration dampening has been the subject of specific study to suppress vibrations that impact structures. It is preferable to increase structural stiffness and damping capability in vibration damping investigations. Materials should generally possess viscoelastic properties. For this reason, rubber and plastics are widely used in vibration damping applications. Vibrational energy is attenuated by heat loss because of the viscoelastic characteristics in the materials. In addition to viscoelasticity, microstructural defects in metal alloys, such as dislocations, grain boundaries, and secondary phases, are advantageous for vibration damping purposes. Zhang et al. [26] created a single-rod STF damper for the use of STF in the field of vibration control and supplied the hysteretic curve of the damping force versus displacement when the loading frequency varied. Due to the shear thickening mechanism of STF to offer a damper with a larger stiffness or damping, the curve demonstrates that the damper's capability to dissipate energy under high dynamic loading greatly exceeds that under low dynamic loading. To prevent the negative impacts of single-ended dampers on the thickening performance of STF, Zhou et al. [27] presented an STF double-rod damper. Higher damping or shock resistance is displayed by the damper packed with a denser STF because it dissipates more energy during each cycle. Zhao et al. [28] investigated the damping force vs. displacement and the damping force vs. velocity curve to analyze the dynamic performance of an STF damper. The maximum damping force in the STF damper, however, was less than 30 N because of the extremely constrained physical characteristics of the device. Given the scale effect of the test findings, the damper's applicability in vibration control is restricted. Comprehensive experimental research of STF dampers was carried out by Yeh et al. [29]. Even though the study showed how different harmonic loads affected the damp-velocity curve's hysteretic performance, only three sets of damp-velocity curve data were produced under low displacement and low loading frequency circumstances. Fischer et al. [30] created a sandwich beam structure based on STF to meet the goal of controlling the structural stiffness and damping under dynamic deformation. The stiffness and damping characteristics of the sandwich beam varied simultaneously as the loading amplitude changed. Due to the shear thickening effect in the core layer, the stiffness of the sandwich beam considerably reduced as the loading amplitude increased.

3.4 Damping and Vibration Isolation

Vibration is a frequently occurring phenomenon. Everything vibrates; it is only the degree of the vibration and its impact on machines, systems, and the environment that are of importance to humankind. Vibration is described as a particle's time-dependent movement around its equilibrium state. The dynamic (time-dependent) displacement is either uniform (harmonic) or nonuniform in timeframe (nonharmonic). The distinction between oscillation and vibration is that in oscillation, matter travels repeatedly about an equilibrium point without deforming the body, but in vibration, periodic deformation of a structure is also involved. Another effect of vibrations is a wave known as "sound," which is merely a mechanical pressure wave that may travel through a variety of media including gas, liquid, and solid. Within the range of 16–20,000 Hz, airborne sounds are detectable to the human ear. Vehicle horns, vocal cords, and all musical instruments are typical illustrations of vibration produced sound.

The dissipation of vibrational energy through time and distance in solid mediums and structures is known as damping. Like how sound is absorbed by air, damping happens wherever there is friction that lessens motion and disperses energy. The loss factor or ratio between the energy dissipated and the energy still present in the system throughout each cycle is referred to as each material's damping capability. In construction, dampening is crucial for preventing vibrations and maintaining the security and comfort of infrastructure and buildings. Friction is an instance of a dynamic damping system. Another example is the resistance that an automobile faces. The air resistance and the rolling friction of its tires are that cause the resistance. Viscous damping is the damping effect that occurs in liquid situations. Consider rolling a ball with a given amount of initial force on the floor. If there is nothing to stop this movement, the ball will continue to roll eternally. However, the ball eventually comes to rest due to friction between the ground and the ball, which counteracts the ball's movement, causing it to lose speed and eventually come to a stop. Damping is a technique for reducing vibrations and is crucial for the system's safety. When a door or drawer is opened or closed, damping prevents a significant impact, conserving the spring hinges and safeguarding the system. A similar function is served by bridge deck damping devices on a big scale. Assuming that a structure or building is being affected by dynamic energy at a frequency that is like (or close to) its natural frequency, in theory, the overlapping frequencies of the exciting force (disturbing frequency) and natural frequency lead to increasing vibration amplitudes. Various solutions have been researched to prevent resonance effects, and two key measures are included in the vibration isolation concept:

- Changing the natural frequency of the structure, adjusting the load and its distribution, and establishing a suitable gap between the structure's natural frequency and the exciting disturbing frequency. Dynamic loads and wind effects are two examples of incoming dynamic forces that can cause unpleasant frequencies.

- The stability of the structure is ensured even in resonance situations by the addition of dampening properties. When in resonance, it helps with energy loss.

It's a popular misunderstanding that vibration isolation of the structure may be accomplished "simply by adding some rubber" to the system. A resilient component can, however, have the opposite effect and increase displacements if it is introduced without considering the characteristics of the system (environmental atmosphere, temperature, material's rigidity, contact area, material transmissibility, material form factor, excitation frequency, etc.). The performance of an insulation system is defined by its transmissibility, which is the ratio of energy injected into the system to energy exiting the system. The vibration control material is chosen with the system's disruptive frequency in the insulating area in mind. Furthermore, the damping volume of the insulation system will define the system's maximal transmissibility level. The peak value drops as dampening rises.

A structure's dynamic responsiveness and transmissibility are primarily influenced by its mass and stiffness qualities, which are responsible for the energy remaining in the system and, by damping, which affects energy loss in the system. Damping is the least known and most difficult to forecast and quantify of these three properties. Because mass and stiffness can be established using static measures, they are easier to understand and quantify. The transmissibility curves for various damping factors are shown in Fig. 3.3 as functions of the frequency ratio. Using different damping factors of 0.05, 0.1, and 0.15, the decrease in transmissibility beyond $\omega = \sqrt{2}\omega_0$ occurs considerably more quickly with frequency for the low damping factor than it does for the larger damping factor. The system's dampening ability determines how transmissibility is reduced. For example, when a machine is placed on a shock and vibration damping platform apparently constructed of an elastomer, the damping, which is a dynamic viscoelastic loss feature of the elastomer, is highly dependent on the frequency and temperature of the environment. Dampers composed of STF would exhibit similar behavior. As a result, the amount of loss in transmissibility may differ from a theoretical curve derived as shown in Fig. 3.3, because it is assumed in this case that the damping factor is the same over the whole frequency range. The following equation reflects the vibration's amplitude when a machine vibrates because of base excitation with a viscoelastic damping mount:

In the situation of automotive suspension design, Fig. 3.3 might be evaluated to lower vibration intensity. If we can achieve $\omega/\omega_0 \gg 1$ by decreasing the suspension spring stiffness (soft spring) and increasing mass, the natural frequency (ω_0) of the unit is reduced, and the vibration attenuation is improved at the working frequency (ω). Lower stiffness, on the other hand, may increase the likelihood of transverse deflection in a rubber-based mount, resulting in additional vibrations in other directions. A reduced damping factor can also result in a considerable reduction in vibration amplitude beyond resonance. The low damping factor, on the other hand, has two important drawbacks: first, with any extra transient force, which is quite common for automobiles, the natural decay will take a long time, and second, at the resonance frequency, the vehicle may be damaged owing to the excessive amplitude

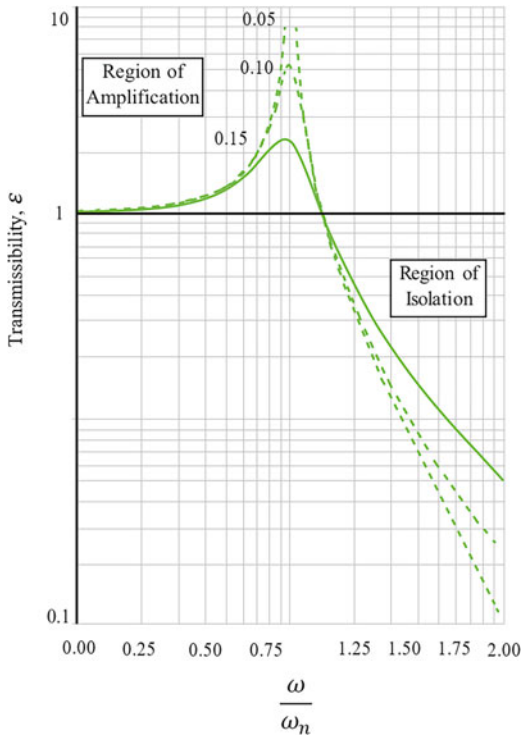

Fig. 3.3 Degree of transmission for a single degree of freedom (SDOF) damped forced vibration with different damping factors (0.05, 0.1, and 0.15)

of vibration. A third issue would be transmitted noise at higher frequencies. As a result, a suspension design is a balanced combination of spring and damper that necessitates an optimal viscoelastic material design. Equation 3.1 reflects the vibration's amplitude when a machine vibrates because of base excitation with a viscoelastic damping mount:

$$u(t) = \frac{\frac{F}{k}}{\sqrt{\left(1 - \frac{\omega^2}{\omega_n{}^2}\right)^2 + 4\xi^2\left(\frac{\omega}{\omega_n}\right)^2}} \tag{3.1}$$

where F/k is the mount's static deflection. This formula compares the amplitude of vibration at each frequency point to the static deflection. The amplitude reduction is affected by two parameters: the frequency ratio and the damping factor. The greater the frequency ratio, the greater the amplitude decrease. However, in the absence of a damper mount, the intensity at resonance ($\omega = \omega_0$) is infinite.

3.5 A Case of Vibration Isolation by an STF Integrated Sandwich Structure

3.5.1 Experimental Details

Using a high-speed homogenizer, fumed silica particles (20 wt% and 40 wt%) were progressively added and distributed in a polyethylene glycol (PEG) pool. To ensure a homogenous and steady dispersion, the mixing procedure was prolonged for an additional hour. The suspensions were maintained at room temperature overnight after the dispersion stage to get the removal of air bubbles. Within 2 hours of the preparation procedure, rheological experiments were conducted with the suspensions.

In the sandwich structures, the core material was a cork agglomerate supplied by Ducork, Inc., which has a density of 170–190 kg/m^3. Cork is a kind of wooden product that is stripped from the outer layer of a cork oak tree. Cork microstructure includes several closed cells. Because the big part of the cork includes air inside the cells, the cork floats on water, which means that it has a very low density. In addition to lightweight properties, cork shows good mechanical properties, and therefore, it can be adapted to energy absorbing and vibration damping systems. Sandwich composites were manufactured by scaling the cork core layers into 50 mm × 50 mm × 10 mm. Two 1.0-mm-thick glass fiber reinforced polymer (GFRP) (fabricated by hand-layup method) sheets were bonded to the cork core layers with powerful double-sided tape adhesive (supplied from Beta Kimya, Turkey). To integrate the fabricated sandwich structure with STFs, 3-mm-wide grooves in the cork core layers machined by a Miller FF 500/BL-CNC (Proxxon, Germany) and filled with STF. Figure 3.4 shows the machined design of the cork core layers for STF injection. Three different designs were considered to show the effect of STF. In Config-1, a neat sandwich structure was considered. In Config-2, the grooves were filled with STF with 20 wt% SiO_2. In Config-3, STF with 40 wt% SiO_2 was injected. Figure 3.5 shows the final form of a sandwich structure.

The study of a system's dynamic characteristics, which are defined apart from the pressures exerted on the system and its reaction, is known as modal analysis. Modal analysis may be used to investigate the vibration properties of mechanical constructions. It converts difficult-to-perceive vibration signals of excitation and response detected on a complex structure into a set of easily predicted modal properties. Structures vibrate or take on mode forms when stimulated at their natural frequencies. Under typical working conditions, a structure will vibrate in a complex combination of all mode configurations. The modal analysis transforms a complex and difficult-to-understand structure into a collection of unconnected single-degree freedom systems. An impact hammer is a specialized measurement tool that creates a short duration of excitation levels by hitting a specified place on the structure. Facesheets and sandwich structure specimens were clamped to a bench clamp and vibrated with a hammer to propagate vibrations on the structures during vibration testing in this study. An accelerometer placed on the opposite face of the impact location was used to assess the structural damping ratio of the specimens. Figure 3.6 shows the experimental setup in the vibration testing.

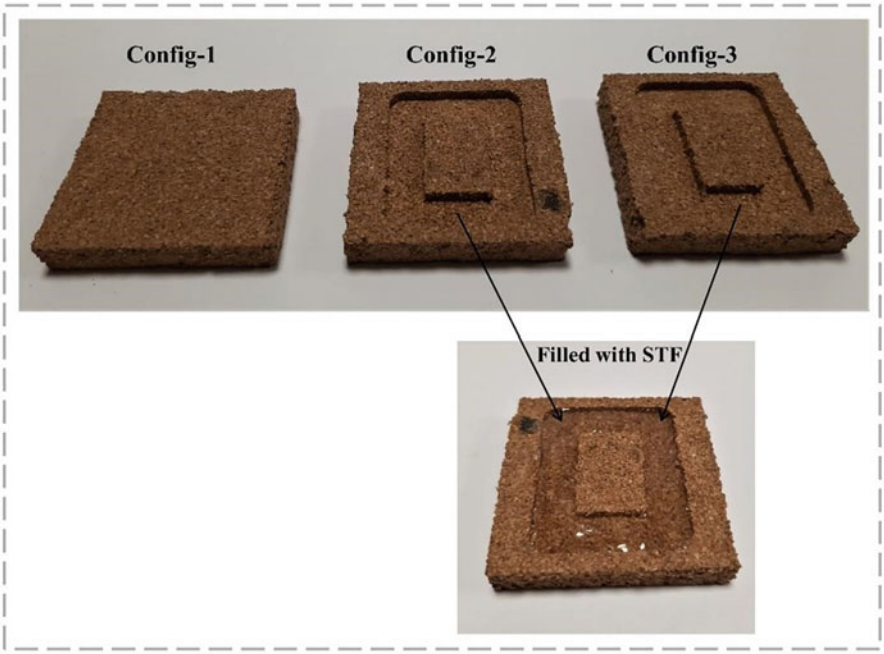

Fig. 3.4 Core layer design of sandwich structures

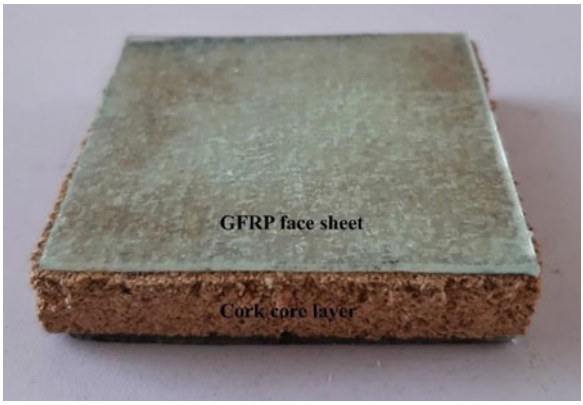

Fig. 3.5 Fabricated sandwich structure

3.5.2 Results and Discussion

Standard parallel plate system was used in the rheological measurements. The distance between the plates was fixed at 1 mm. The shear rates used in the studies ranged from 0 to 1000 s^{-1}. To prevent loading effects, a pre-shear of 1 s^{-1} was applied to the samples for 60 s before the measurements. Figure 3.7 shows the rheological behavior of STFs with 20 wt% and 40 wt% SiO_2.

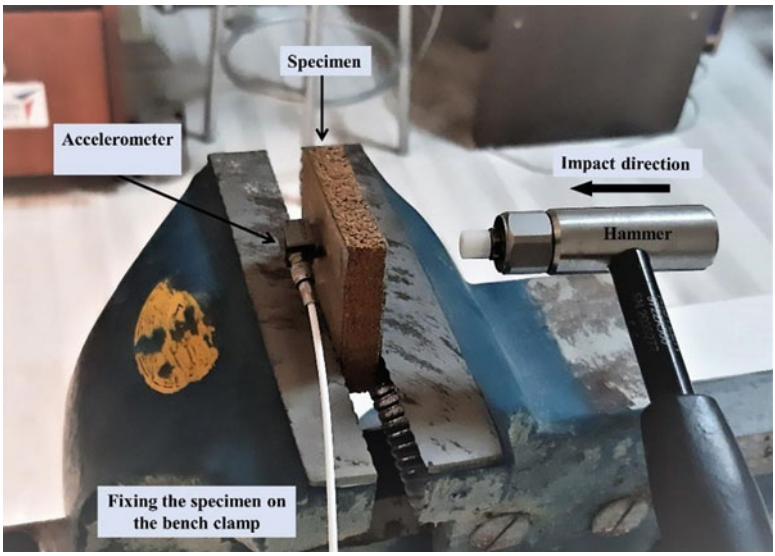

Fig. 3.6 Experimental setup in the vibration testing

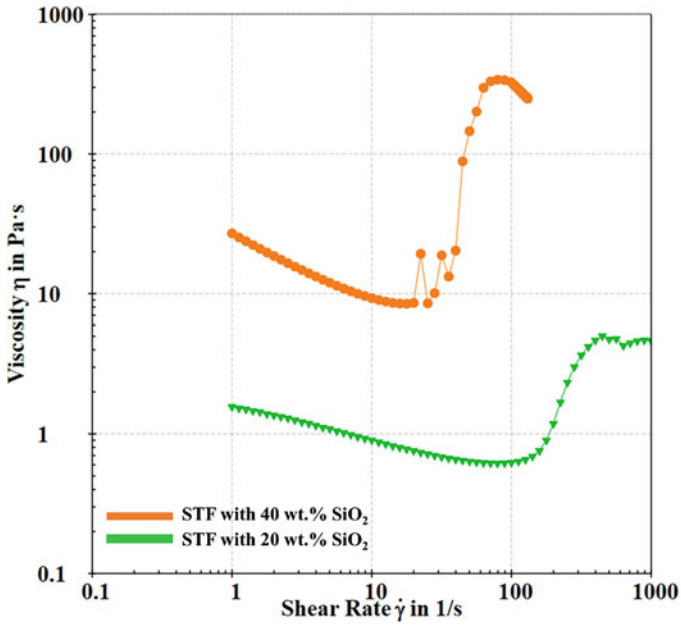

Fig. 3.7 Rheological behavior of STFs with 20 wt% and 40 wt% SiO_2

In Fig. 3.8, frequency response functions are shown for three different configurations. When the configurations are investigated, one or two peaks can be observed. Accordingly, these structures can be modeled as single or double degrees of freedom structures. Modeling these configurations as single degree of freedom reveals that

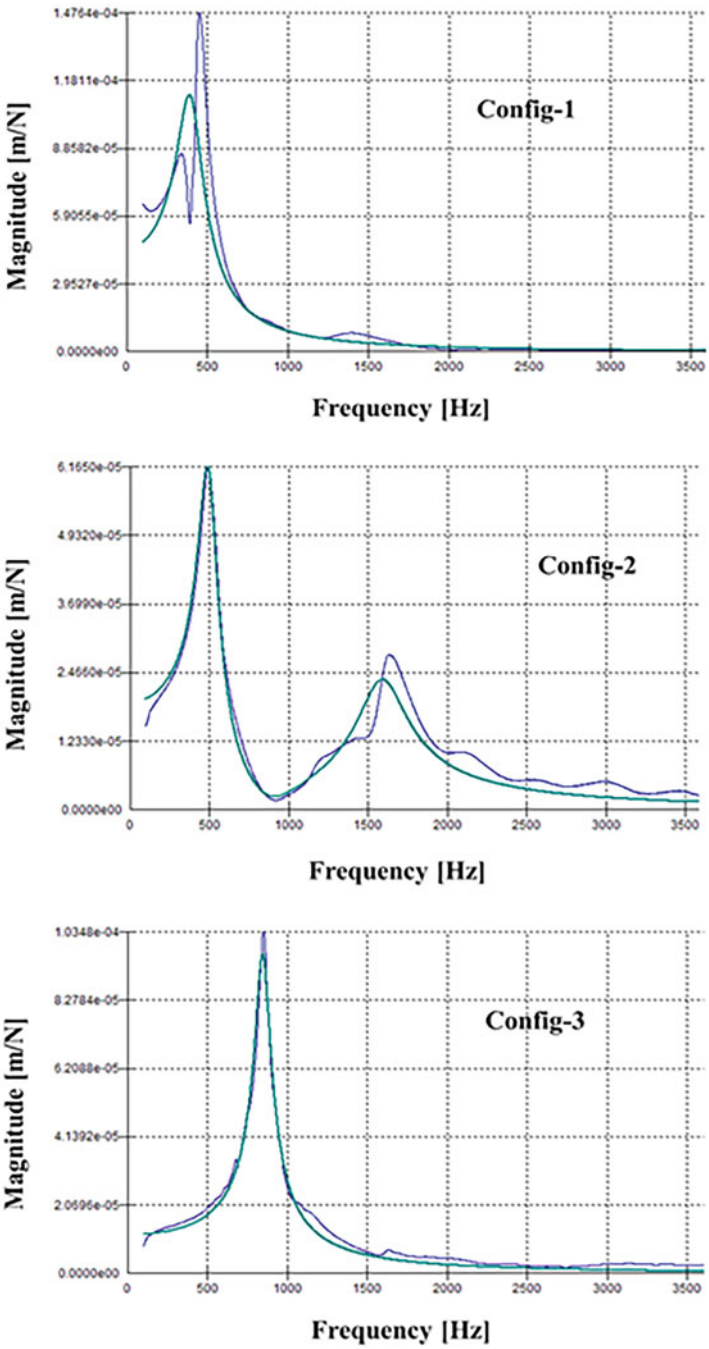

Fig. 3.8 The frequency response function graphs of sandwich structures

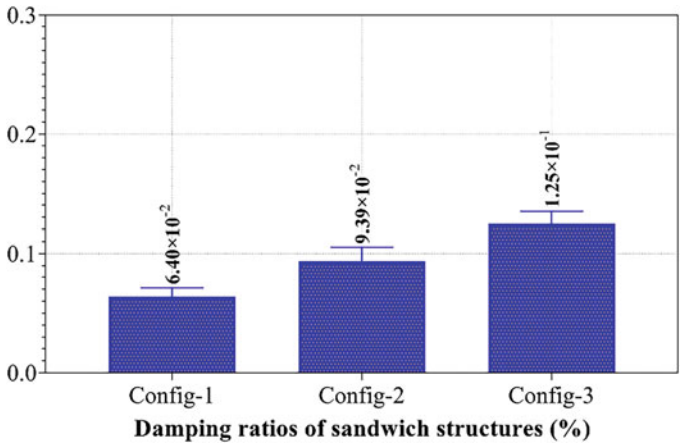

Fig. 3.9 Damping ratios for the sandwich structures

the natural frequency varies between 400 and 800 Hz. In general, the presence of silica can increase the stiffness of a material, which can lead to an increase in the natural frequency of a system. This is because the stiffness of a material determines how much it resists to deformation under loading and a stiffer material will have a higher natural frequency.

Figure 3.9 shows the damping ratios for the three different configurations. The vibration damping ratio is a measure of how effectively a material absorbs and dissipates energy when it is subjected to vibrations. It is defined as the ratio of the energy dissipated in the material to the energy input to the material. Materials with a high damping ratio can absorb and dissipate a greater amount of energy, making them more effective at reducing the amplitude of vibrations. The damping rate is increased by two times or more in the structure with STF and silica. When STFs are used as a damping medium in vibration control applications, they can have a positive effect on the damping ratio of the system. By increasing viscosity under shear stress, STFs can absorb and dissipate more energy, making them more effective at reducing the amplitude of vibrations. Silica can have a positive effect on the vibration damping ratio of a material when it is used as a filler. By increasing the stiffness and reducing the hysteresis of the material, silica can help to reduce the transmission of vibrations through the material and increase its damping ratio.

3.6 Conclusions

STF is used as an intelligent material that responds to high shear loads due to the beneficial attribute of excellent energy dissipation. This chapter investigates the possibility of using STF as a smart fluid with unique rheological properties in

vibration damping of sandwich structures. First, an introduction to STF, sandwich structures, and vibration isolation were discussed, and then, as a case study, sandwich structures consisting of GFRP facesheets and cork cores were designed. Two types of STFs (20 wt% and 40 wt% silica contents) with different rheological properties were added to the cork core, and then a hammer-based forced vibration testing was carried out with the sandwich composites. The results of the case study show that adding STF to the cork core significantly increases the damping capability of the sandwich structures. It can be stated that STF is a good candidate material for vibration control applications due to its intelligent properties.

References

1. Lee YS, Wagner NJ. Rheological properties and small-angle neutron scattering of a shear thickening, nanoparticle dispersion at high shear rates. Ind Eng Chem Res. 2006;45(21): 7015–24.
2. Gürgen S, Kuşhan MC, Li W. Shear thickening fluids in protective applications: a review. Prog Polym Sci. 2017;75:48–72.
3. Barnes H. Shear-thickening ("Dilatancy") in suspensions of nonaggregating solid particles dispersed in Newtonian liquids. J Rheol. 1989;33(2):329–66.
4. Gürgen S, Li W, Kuşhan MC. The rheology of shear thickening fluids with various ceramic particle additives. Mater Des. 2016;104:312–9.
5. Maranzano BJ, Wagner NJ. The effects of particle size on reversible shear thickening of concentrated colloidal dispersions. J Chem Phys. 2001;114(23):10514–27.
6. Wei M, Lin K, Sun L. Shear thickening fluids and their applications. Mater Des. 2022;110570: 110570.
7. Sun P, Li J, Zhang L, Wang Z, Zhou T, Ke R, editors. Investigation on the performance of fluid jet polishing using shear thickening slurry. Optical Manufacturing and Testing XII; 2018: SPIE
8. Gürgen S, Kuşhan MC. The ballistic performance of aramid based fabrics impregnated with multi-phase shear thickening fluids. Polym Test. 2017;64:296–306.
9. Sahoo SK, Mishra S, Islam E, Nebhani L. Tuning shear thickening behavior via synthesis of organically modified silica to improve impact resistance of Kevlar fabric. Mater Today Commun. 2020;23:100892.
10. Liu L, Yang Z, Liu X, Chen W, Zhao Z, Luo G. Yarn dynamic tensile behavior and meso-scale numerical simulation method for STF-Kevlar fabrics. Thin-Walled Struct. 2021;159:107319.
11. Tian T, Nakano M. Design and testing of a rotational brake with shear thickening fluids. Smart Mater Struct. 2017;26(3):035038.
12. Liu B, Du C, Wang L, Fu Y, Song L. The rheological properties of multifunctional shear thickening materials and their application in vehicle shock absorbers. Smart Mater Struct. 2021;30(8):085028.
13. Gürgen S, Fernandes FA, de Sousa RJA, Kuşhan MC. Development of eco-friendly shock-absorbing cork composites enhanced by a non-Newtonian fluid. Appl Compos Mater. 2021;28 (1):165–79.
14. Sheikhi MR, Gürgen S. Anti-impact design of multi-layer composites enhanced by shear thickening fluid. Compos Struct. 2022;279:114797.
15. Gürgen S, Sofuoğlu MA. Smart polymer integrated cork composites for enhanced vibration damping properties. Compos Struct. 2021;258:113200.
16. Gürgen S, Sofuoğlu MA. Integration of shear thickening fluid into cutting tools for improved turning operations. J Manuf Process. 2020;56:1146–54.

17. Gürgen S, Sofuoğlu MA. Vibration attenuation of sandwich structures filled with shear thickening fluids. Compos Part B. 2020;186:107831.
18. Gürgen S, Sofuoğlu MA. Experimental investigation on vibration characteristics of shear thickening fluid filled CFRP tubes. Compos Struct. 2019;226:111236.
19. Heimbs S. Foldcore sandwich structures and their impact behaviour: an overview. Dynam Fail Comp Sandwich Struct. 2013:491–544.
20. Davies JM. Lightweight sandwich construction. John Wiley & Sons; 2008.
21. Li Z, Crocker MJ. A review on vibration damping in sandwich composite structures. Int J Acoust Vib. 2005;10(4):159–69.
22. Vinson JR. Sandwich structures: past, present, and future. Sandwich structures 7: advancing with sandwich structures and materials. Springer; 2005. p. 3–12.
23. Gundberg TA. Face sheet materials for sandwich composites. Sandwich Structural Composites: CRC Press; 2021. p. 85–123.
24. Ma W, Elkin R. Sandwich structural core materials and properties. Sandwich Structural Composites: CRC Press; 2021. p. 1–72.
25. Ma W, Elkin R. Sandwich structural composites: theory and practice. CRC Press; 2021.
26. Zhang X, Li W, Gong X. The rheology of shear thickening fluid (STF) and the dynamic performance of an STF-filled damper. Smart Mater Struct. 2008;17(3):035027.
27. Zhou H, Yan L, Jiang W, Xuan S, Gong X. Shear thickening fluid–based energy-free damper: design and dynamic characteristics. J Intell Mater Syst Struct. 2016;27(2):208–20.
28. Zhao Q, He Y, Yao H, Wen B. Dynamic performance and mechanical model analysis of a shear thickening fluid damper. Smart Mater Struct. 2018;27(7):075021.
29. Yeh F-Y, Chang K-C, Chen T-W, Yu C-H. The dynamic performance of a shear thickening fluid viscous damper. J Chin Inst Eng. 2014;37(8):983–94.
30. Fischer C, Braun S, Bourban P, Michaud V, Plummer C, Månson JE. Dynamic properties of sandwich structures with integrated shear-thickening fluids. Smart Mater Struct. 2006;15(5): 1467.

Chapter 4
Shear Thickening Fluid/Cork Composites Against Blunt Impacts in Football Shin Guards Applications

Francisco J. Galindo-Rosales

Nomenclature

dpi	Dots per inch
EN	European Norm
EPP	Expanded polypropylene
EPS	Expanded polystyrene
EVA	Ethylene-vinyl acetate
FIFA	Fédération Internationale de Football Association
NOCSAE	National Operating Committee on Standards for Athletic Equipment
PMMA	Poly(methyl methacrylate)
PPE	Personal protective equipment
PPG	Polypropylene glycol
PVC	Poly(vinyl chloride)
STF	Shear thickening fluid
%v/v	Percentage in volume
%w/w	Percentage in weight

F. J. Galindo-Rosales (✉)
Transport Phenomena Research Center, Department of Chemical Engineering, Faculty of Engineering, University of Porto, Porto, Portugal

ALiCE—Associate Laboratory in Chemical Engineering, Faculty of Engineering, University of Porto, Porto, Portugal
e-mail: galindo@fe.up.pt

S. Gürgen (ed.), *Shear Thickening Fluid*, https://doi.org/10.1007/978-3-031-35521-9_4

4.1 Introduction

According to the Occupational Safety and Health Administration of the US Department of Labor [4], personal protective equipment (PPE) is equipment worn to minimize serious workplace injuries and illnesses which may result from contact with chemical, radiological, physical, electrical, mechanical, or other workplace hazards. Personal protective equipment may include gloves, safety glasses and shoes, earplugs or muffs, hard hats, respirators, or vests and body pads.

Shin guards, also known as shin pads, can be considered a kind of PPE [3]. It is a piece of equipment worn on the front of the shin to protect it from injury. Commonly used nowadays in many sports, such as football and cricket, as well as in military vests, modern shin guards have evolved from the metal counterpart greaves used in body armor to provide warriors with protection on the battlefield, dating back to the Bronze Age [7] (Fig. 4.1). Although many athletes wear them voluntarily for protective measures, others are forced to do so by means of a particular sports legislation, and the shin pads must accomplish specific standards of quality.

In this book chapter, the attention will be focused on the shin guards used in football or soccer. They have to satisfy the general requirements defined in the current European Norm [3] such as ergonomics, innocuousness, sizing, coverage, and cleaning but also performance against two kinds of impact tests, i.e., stud and blunt impacts, which will be described in more detail in Sect. 4.2.3. In the USA, the NOCSAE (National Operating Committee on Standards for Athletic Equipment) defines the standard regarding the test method and performance specification of soccer shin guards [8]. The Fédération Internationale de Football Association (FIFA), the sport's international governing body, has introduced the shin guard law in 1990, which made the wearing of shin guards compulsory during match in

Fig. 4.1 (**a**) Bronze greaves from the Archaeological Museum of Vergina (Royal Tombs) [5] and (**b**) modern shin guards used by professionals in Muay Thai fights [6]

order to prevent lower leg impact abrasions, contusions, and fractures [9]. The effectiveness of shin guards in reducing the incidence of lower leg football injuries has already been demonstrated [10], and its use is strongly recommended not only in matches but also in training sessions; however, the use of shin guards may not prevent fractures [11, 12].

The appropriate shape of the shin guard and the selection of the optimal materials are of paramount importance in determining the level of protection. Currently, shin guards consist of an outer shell made of a thick (1–4 mm) and rigid material (propylene, carbon fiber, etc.) providing energy absorption and protection against penetration and a liner (3–7 mm) made of soft material (EVA, Neoprene, etc.) to reduce the peak impact force [13]. Carbon fiber would provide better protection against high-impact forces because its reduced flexibility would reduce the time the force stays on the tibia; moreover, they also concluded that "choosing the right padding material requires as much care as the selection of a shell" [35].

Shear thickening fluids (STFs) are very popular among the scientific and technological community developing energy dissipative systems, particularly in protective applications [14], because of its unusual mechanical properties [15]. This kind of non-Newtonian fluids suddenly increases its viscosity upon the application of an external load that results in either inducing the hydrocluster formation [16] or jamming [17] of the particles dispersed in the carrier fluid [18]. The increase in viscosity can be engineered by choosing the formulation of the STF [19]. This has led to considerable interest in incorporating STFs into other materials, either porous materials, like fabrics and foams, by means of impregnation [20–22], or nonporous materials by means of multilayered structures consisting of solid laminates with STF as the interfacial element [23–25], to enhance their mechanical properties for a specific application. The major limitations of a STF composite developed either by impregnation or by multilayered structures are as follows:

- Large amount of fluid, which is detrimental for applications in which lightweight is of paramount importance, as in personal protective equipment such as helmets, helmet liners, bulletproof equipment, clothing, cushioning bodies, and shin guards.
- There is no room for optimization in the energy dissipated by the STF.
- The rheological response of the STFs cannot be enhanced due to the lack of confinement [26].

These limitations can be overcome by incorporating the STF into the solid material by means of embedded microfluidic patterns [1]. The microfluidic channels will ensure the confinement of the STF, as well as the reduced amounts of fluid sample needed and the possibility of producing highly integrated devices able to mimic porous media. Moreover, the geometric features of the microchannels can be numerically optimized to get the intended flow characteristics [27]. Additionally, many STFs also exhibit viscoelastic features [16], and the small length scales significantly increase the relevance of fluid elasticity, and, therefore, the flow resistance can be significantly different from those of their Newtonian counterparts at low Reynolds number, particularly if the microchannels are designed specifically

for that purpose, as it is the case of the microfluidic rectifiers [28]. Thus, using computational techniques is possible to optimize the fluidic microchannels to maximize the amount of energy dissipated by the composite [29]. This technology can be implemented in any resilient nonporous solid material, such as EPS, EPP, EVA, or cork, and it has already demonstrated its potential almost a decade ago in combination with micro-agglomerated cork pads [2], but it has never been validated in personal protective equipment. In this chapter, the usefulness of Rheinforce cork composites to be used in football shin guards has been assessed for the very first time.

4.2 Materials and Method

4.2.1 Rheinforce Cork Composites

Rheinforce cork composites, formerly known as CorkSTFμfluidics composites [2], consist of two micro-agglomerated cork pads; the bottom one is laser engraved [2] with microfluidic channels and filled with an STF, and one on top is a self-adhesive micro-agglomerated cork lamina. The open parameters for the design of the composites can be classified as follows:

- *Cork pads.* The mechanical properties of the reinforced cork composite will depend on each lamina's thickness, the cork granules' size, and the glue binding them.
- *STF.* The rheological properties of the STF will depend on the chosen formulation, i.e., the size and shape of the dispersed particles, the concentration of solids, the particle-particle and particle-fluid interactions, the viscosity of the carrier fluid, etc., and will affect the mechanical performance of the composite.
- *Microchannels.* The fluid-structure interaction is another critical aspect in the composite design, as the microchannels' shape will determine the energy dissipated by the fluid upon the impact force. Moreover, the number of microchannels and their dimensions (width -W- and depth -h0-) are also open parameters in the design of the composites, as they will affect the weight and their mechanical properties against impact loads.

Figure 4.2 shows the design process for the optimization of the Rheinforce cork composites, once the corks pads have been already selected.

Cork shows very little lateral expansion under compression (Poisson's ratio is close to 0); thus, under impact loads, the compressing deformation imposes a squeeze flow to the fluid in the microchannels, and the liquid is expelled out of the impact zone in both directions of the microchannel. In this way, the energy of the impact will be dissipated simultaneously by the STF and by the plasticity of the cork; additionally, another portion will be stored by the elasticity of the cork (Fig. 4.3).

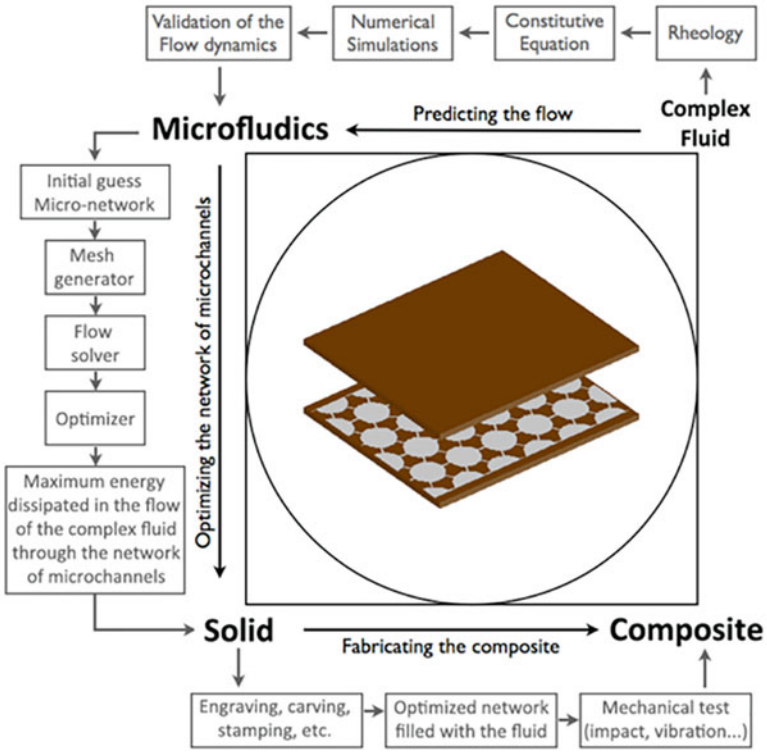

Fig. 4.2 The design process for the optimized Rheinforce cork composites

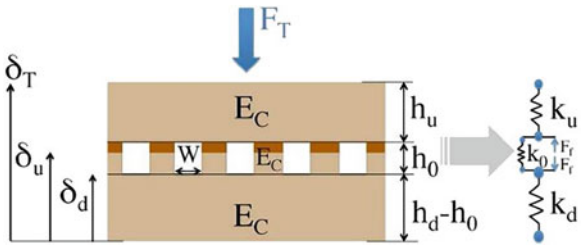

Fig. 4.3 Reduced model of the experimental device using nonlinear springs to simulate the cork layers, which allows to obtain the force exerted by the fluid inside the microchannels. (Reprinted from Ref. [2], with permission from Elsevier)

In this study, we have chosen a micro-agglomerated cork pad with $h_d = 4$ mm for the bottom layer of the composite and one self-adhesive micro-agglomerated cork pad for the top layer ($h_u = 1.2$ mm). Their properties are summarized in Table 4.1.

Apart from pure cork pads, four different Rheinforce cork composites were considered in this study to determine the influence of the microfluidic pattern in their performance against impact loads and their potential application for shin

Table 4.1 Properties of the cork pads

Layer	Density [kg/m^3]	Thickness [mm]	Compressibility [%]	Recovery [%]	Granule size [mm]	Binder	Self-adhesive
Bottom	170–220	4	25–50	⩾75	0.5	Polyurethane	No
Top	170–220	1.2	25–50	⩾75	0.5	Polyurethane	Yes

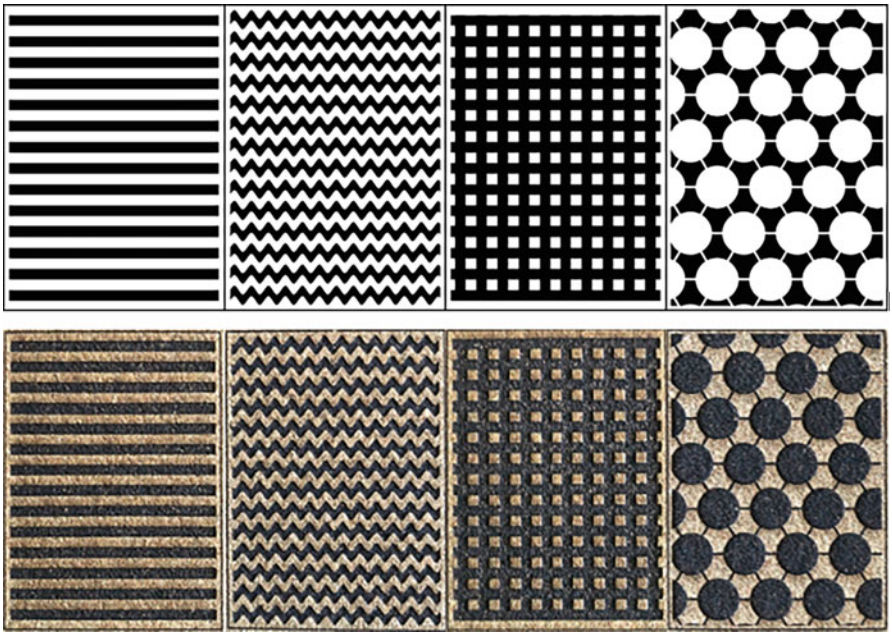

Fig. 4.4 Microfluidic patterns designed by CAD (top row). The microfluidic patterns are laser engraved on the bottom cork lamina (bottom row). As mentioned earlier, those from left to right are straight, splines, grid, and honeycomb channels

guards. Thus, four microfluidic patterns were designed using computer-aided design software, hereafter known as straight, splines, grid, and honeycomb (Fig. 4.4). The microfluidic patterns were engraved into the bottom cork layer (4 mm thickness) employing a laser engraving machine (LaserPro® Spirit GX 40 W with a resolution of 600 dpi) as in previous works [2, 29]. The depth of the microfluidic networks can be set by controlling the power of the laser beam (P) and the speed of the carriage (S); thus, according to preliminary studies [2], working with 40% of the total power and 40% of the speed one should get $h_0 \sim 750$um depth channels. As expected, the accuracy of the laser engraving technique was much higher in the XY plane, ensuring an error below 2% in the width of the channels, whereas the error in the depth was raised to 17% (Fig. 4.5). The nominal width of the straight, spline, and grid channels was 2500 μm (W), and each channel was separated by a cork wall of $E_C \sim 2500$ μm. The honeycomb patterns were replicated from our previous work [2]. Table 4.2 shows the content of STF in each cork composite and an estimation of the density.

The shear thickening used in this study consisted of a concentrated suspension (27.5%w/w) of fumed silica nanoparticles provided by Sigma-Aldrich (S5130) dispersed in polypropylene glycol (PPG 400). The average primary particle diameter is 7 nm although, at the end of the flame hydrolysis process, they fuse forming indivisible fractal aggregates that can be considered as fumed silica primary

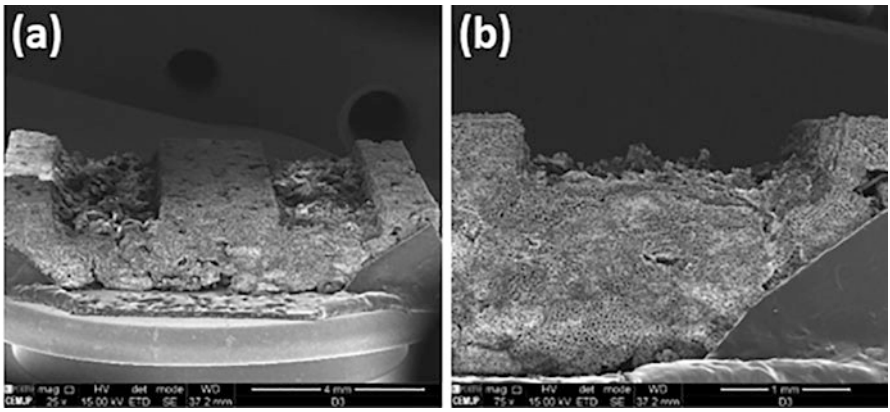

Fig. 4.5 Scanning electron microscopy of a portion of the straight microfluidic patterns engraved in the cork pads at different magnifications: (**a**) 25× and (**b**) 75×

Table 4.2 Density and fluid content of the different cork composites

	Pure cork	Rheinforce straight	Rheinforce spline	Rheinforce grid	Rheinforce honeycomb
Density [kg/m^3]	195	274	288	316	296
Fluid content [%v/v]	0	7	8	10	8

structure, having a characteristic size of 0.1–0.2 μm [30]; moreover, the surface area and density were of 395 ± 25 m^2/g and 36.84 kg/m^3, respectively. PPG 400 is a Newtonian polymeric liquid with a molecular weight of 400 g/mol having a viscosity of approximately 0.1 Pa·s and a density of 1010 kg/m^3 at 20 °C. The fumed silica was dried at 120 °C for 24 h [31] in a convection oven to remove moisture before mixing with PPG 400 in a blender (Robot Kenwood KVC5010T equipped with a dough hook) at room temperature for 11 h and sonicated in an ultrasonic bath for 4 h (Sonorex Super RK106 35 kHz) [2]. The viscosity curve was measured at 20 °C in a stress controlled rotational rheometer (Anton Paar MCR301) equipped with 50-mm-diameter parallel plates geometries with grooved surfaces to avoid slip. The steady shear viscosity measurements were performed using a gap of 750 μm, considering 20 s for each measurement point. The results (Fig. 4.6) show a marked shear thinning at low shear rates (below 10 s^{-1}) followed by a steep shear thickening response.

4.2.2 Commercial Shin Guards

In order to validate the usefulness of the Rheinforce cork composites for their use in football shin guards, the same blunt impact tests were developed with three recreational shin guards available at a local retailer (Table 4.3).

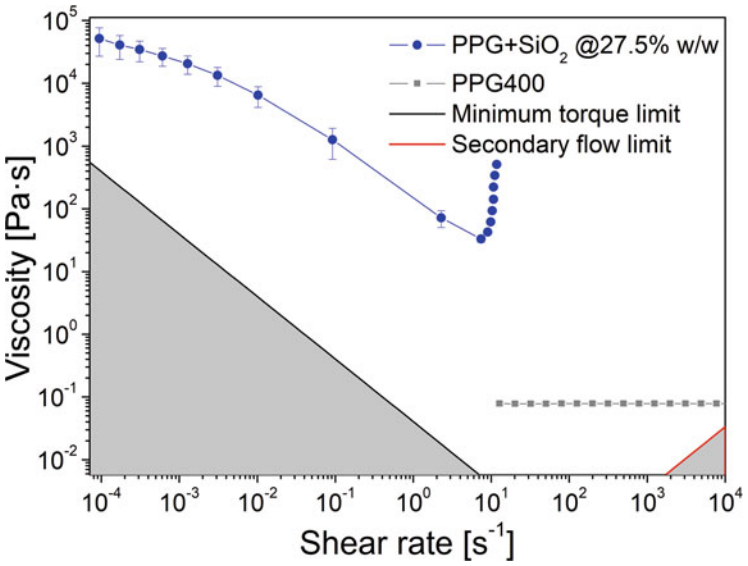

Fig. 4.6 Steady state viscosity curve of the STF compared with the viscosity of the carrier fluid

4.2.3 Low-Velocity Impact Tests

In this study, we focus on the performance of the Rheinforce cork composites against the blunt impact tests [3]. This impact is responsible for concussion or bruise, an injury in which the skin is not broken. Still, the underlying soft tissue is damaged by compression and shearing forces resulting in the damage of fine blood vessels leading to bleeding, discoloration, and swelling.

The drop weight testing machine (ROSAND Instrument Falling Weight) used in previous studies [2] was adapted to meet some of the features defined by the standards [3], which can be summarized in the following points:

- A guided falling mass with a striking face oriented at 90° ± 2°.
- The striking face has a width of 14 ± 0.5 mm and a length of 65 mm with the long edges rounded with a radius of 2 ± 0.1 mm.
- A strap system holds the shin guard in place during the impact tests.

However, as the minimum mass allowed by the ROSAND Instrument Falling Weight was limited to 3.986 kg (approximately four times larger than the mass defined in the EN 13061:2009 [3]), the velocity of the impact was reduced to the minimum affordable for that instrument (1.12 m/s) to reach 2.5 J, which is slightly above to the energy impact defined in the European standard (2 J). Under these circumstances, the transmitted force of the three single impacts to the same point on three shin guards shall not exceed 2.0 kN.

Regarding the force sensor, a Kistler Type 9031A was mounted on the falling mass. This sensor could measure forces up to 60 kN with an accuracy of 0.1 N,

Table 4.3 Main features of the commercial shin guards

Brand name	Model	Size	Hard shell	Hard shell thickness	Foam	Foam thickness	EN13061
Nike	SP2079 702 EWG092016	L	Polypropylene	4 mm	Neoprene	5.5 mm	Yes
Team Quest (TQ)	SKU5294103	L	Polypropylene	4 mm	EVA	4.5 mm	Yes
SAK	Shape	–	PMMA/PVC	2 mm	EVA	4 mm	Yes

having the lowest natural frequency of 65 kHz, meeting all the standard requirements for the load cell. All the experiments were performed at a temperature of 20 °C ± 2 °C and a relative humidity of 65% ± 5%.

4.3 Results and Discussion

In this study, four different Rheinforce cork composites are considered, whose differences lie in the microfluidic patterns, in which their geometric features were not numerically optimized but manually defined. Their performance against blunt impact tests is compared to the response given by a neat cork pad without engraved microchannels embedding the STF.

Figure 4.7 shows the time vs. force curves measured by the load cell for the cork composites under three consecutive impacts. The pure cork shows a smoother response than the Rheinforce counterparts, which provide a wavier signal due to the lack of internal cohesivity and the presence of the fluid. In general, for all cases considered, the maximum peak force remains below 2.0 kN required by the European standard [3]; moreover, the first impact (black square symbols) curve exhibits a lower force peak value than the two subsequent impacts.

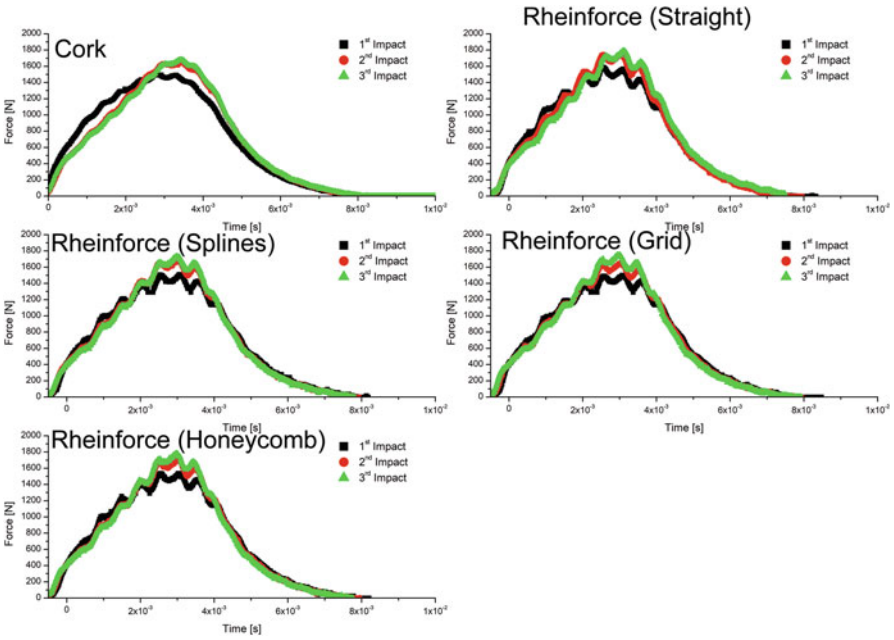

Fig. 4.7 Force vs. time curves measured for the pure cork pads and the different Rheinforce cork composites

Even though micro-agglomerated cork can recover more than 75%, the blunt impact will induce some plastic deformation. Cork is a cellular material, and unlike dense solids, it compacts when compressed. Suppose the linear limit of deformation is exceeded. In that case, a portion of the cells beneath the impact zone will crash, resulting in the densification of the zone and a permanent deformation when the load is removed [32]. This last consequence was observed in the time vs. force curve for the pure cork case, where after the crushing of the cells in the first impact, the two subsequent responses do not follow the first one; they exhibit a more prominent peak value due to the new denser structure generated after the first impact; moreover, these second impacts show overlapping curves, because the subsequent impacts do not result in further plastic deformation/densification beneath the impacted zone.

In the case of the Rheinforce cork composites, the volume occupied by the microchannels modifies the shape of the force vs. time curve compared to the pure cork. As part of the solid is replaced by a liquid, the remaining solid structure (walls of the microchannels) exhibits lower stiffness against the compression; the fluid beneath the impact zone is squeezed out after the first impact, and as it does not fully return to its position, the subsequent impacts result in higher and practically equal peak forces. This lack of restoration of the fluid can be understood from the shape of the viscosity curve provided by the STF formulation considered in this study (Fig. 4.6). The fluid exhibits yield stress and a marked shear thinning behavior below shear rates of the order of 10 s^{-1}; thus, if the applied pressure overcomes the yield stress value, the fluid will start to flow with a lower resistance with increasing shear rates; when the shear thickening is triggered, its viscosity rises again, and it will keep on flowing like a dough, probably slipping on the walls of the channels; when the deformation rate stops, the microstructure will be regenerated, the yield stress is restored, and the fluid will hold its position again and will not return to its original position, similar to what we observe in the toothpaste when it is squeezed out from the tube onto the toothbrush.

A more inside mechanical analysis will allow to determine the energy dissipation from the force vs. time curves. In an ideal case in which no energy was dissipated ($E = \frac{1}{2}mV^2, E_1 = E_2$), the impactor before and after the impact will have the same velocity but with different directions; consequently, the linear momentum ($\vec{p} = m\vec{V}$) of the mass strike before and after the impact will be the same, but with different sign, i.e., $\vec{p}_2 = -\vec{p}_1$ (Fig. 4.8). The presence of the composite introduces a loss of momentum in the striking mass ($\left|\vec{V}_2\right| < \left|\vec{V}_1\right|$) and is therefore, $\left|\vec{p}_2\right| < \left|\vec{p}_1\right|$, represented by the impulse $\vec{I} = \Delta\vec{p} = \vec{p}_2 - \vec{p}_1$ (Eq. 4.1):

$$\Delta\vec{p} = \vec{p}_2 - \vec{p}_1 = mV_2\vec{k} - \left(-mV_1\vec{k}\right) = m(V_2 + V_1)\vec{k}. \tag{4.1}$$

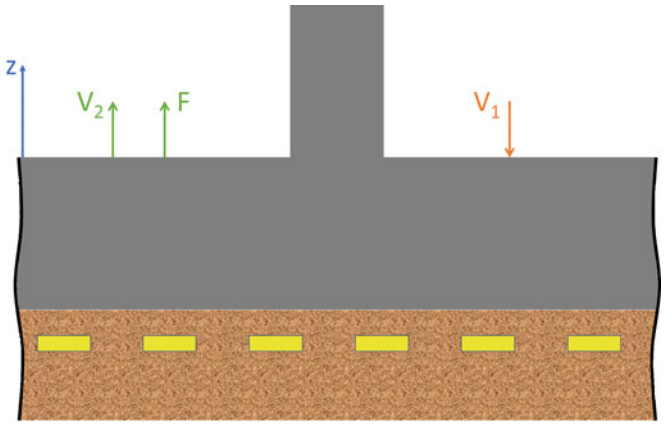

Fig. 4.8 Sketch of the force measured by the load cell during the impact time and the exchange in the impulse

That impulse ($\vec{I}$) can be calculated by integrating the force vs. time curve obtained from the experiments (Eq. 4.2):

$$\vec{I} = \Delta\vec{p} = \int_0^{\Delta t} F dt\, \vec{k} \tag{4.2}$$

As $\Delta\vec{p}$ from Eqs. 4.1 and 4.2 is the same, the velocity after the impact can be determined as follows (Eq. 4.3):

$$V_2\,\vec{k} = \left(\frac{\int_0^{\Delta t} F dt}{m} - V_1 \right) \vec{k} \tag{4.3}$$

Since the energy of the striking mass is constant for all the experiments ($V_1 = \sqrt{\frac{2E_1}{m}}$), lower values of velocity at the end of the impact indicate larger amount of energy dissipated: $E_{Diss} = \frac{1}{2}m\left(V_1^2 - V_2^2\right) = I\left(\sqrt{\frac{2E_1}{m}} - \frac{I}{m}\right)$. The maximum energy dissipated will be reached when $\frac{dE_{\text{Diss}}}{dI} = 0$, and that happens when the impulse is equal to the linear momentum of the striking mass at the beginning of the impact, i.e., $I = mV_1$. Moreover, the larger the impulse and the shorter the duration of the impact, the larger the force transmitted to the shin.

Figure 4.9 compares the accumulated impulse for the different cork composites for the three consecutive impacts. Their inset graphs represent a zoom into the last two milliseconds of the impact. As discussed above, the lower the accumulated

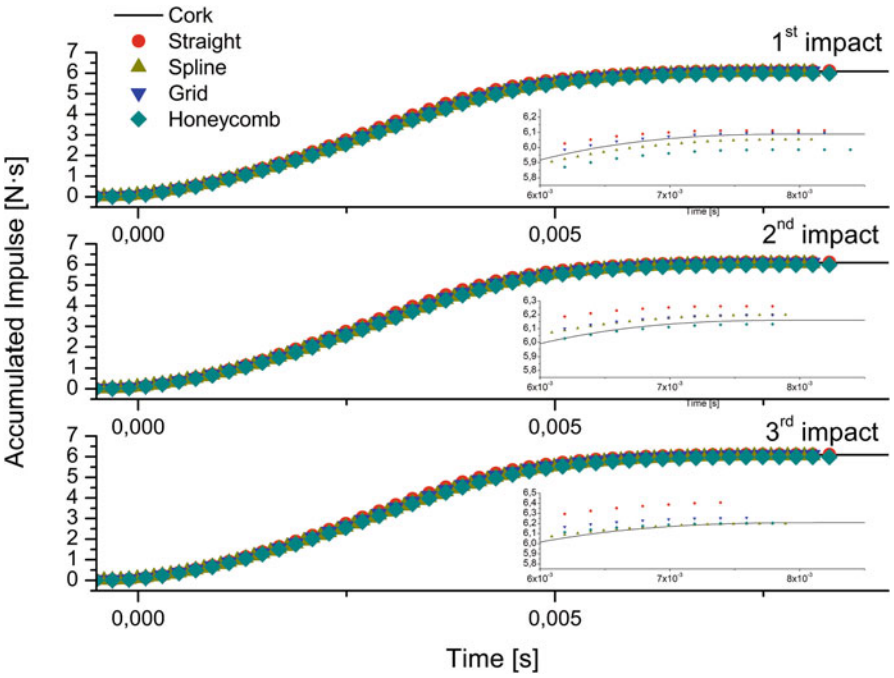

Fig. 4.9 Comparison of the accumulated impulse for the different cork composites and its evolution with the number of consecutive impacts

impulse at the end of the impact, the larger the energy will be dissipated by the composite. Different shapes in the microfluidic patterns result in significant changes in dissipated energy.

The solid line represents the reference given by the response of the pure cork composite. For the first impact, the Rheinforce cork composites having the spline and honeycomb patterns exhibited lower accumulated impulse than the grid and the straight channels. One would expect a larger dissipated energy for those composites containing more amount of fluid, and therefore, the Rheinforce cork composite having the grid pattern should provide the lowest accumulated impulse; however, as conceptualized in Fig. 4.2, it becomes evident the importance of the shape of the design in the dissipation of energy. Consecutive impacts onto the same position result in empty channels and densified cork microstructure. Besides providing more energy dissipation, even exceeding the performance of pure cork in every impact (Table 4.4), the honeycomb Rheinforce cork composite can also offer higher mechanical strength against impact when compared with the other patterns.

It can then be concluded that there is no direct correlation between the amount of fluid embedded and the energy dissipated by the cork composite, and the shape of the microfluidic pattern has a major role in the energy dissipation process, as it is

Table 4.4 Damping performance of the cork composites

Composite	First impact Energy dissipated [%]	Second impact Energy dissipated [%]	Third impact Energy dissipated [%]
Cork	86.71 ± 0.05	85.52 ± 0.05	84.67 ± 0.05
Rheinforce straight	86.32 ± 0.05	83.72 ± 0.05	80.94 ± 0.05
Rheinforce spline	87.27 ± 0.05	84.83 ± 0.05	84.52 ± 0.05
Rheinforce grid	86.56 ± 0.05	84.84 ± 0.05	83.82 ± 0.05
Rheinforce honeycomb	88.34 ± 0.05	85.99 ± 0.05	84.75 ± 0.05

responsible for the pressure drop. It is important to highlight here that none of the four microfluidic patterns considered in this study were numerically optimized. The application of a topological optimization process, similar to those included in our previous work [33], will provide the pattern leading to the maximum energy dissipation and mechanical strength, whereas the amount of fluid is kept minimal.

The performance of the Rheinforce cork composite with the honeycomb microfluidic pattern will be compared with the performance of the three commercial shin guards already qualified for the European standard [3] to assess the real potential of this technology for this application. It must be noticed two significant differences between the commercial shin guards and the Rheinforce composite: first, the Rheinforce cork composite does not have any hard shell, and second, the total thickness of the cork composite is roughly half of the thickness of the commercial shin guards (Table 4.3).

Figure 4.10 shows the force vs. time curves measured in the three consecutive impacts and the calculated accumulated impulse for the four shin guards. It can be observed that the Rheinforce cork composite exhibited the largest peak values for the force, but also the lowest impulse, whereas the Team Quest shin guard provided the lowest peak force.

In terms of energy dissipation, the SAK shin guard offered the lowest value (Fig. 4.11). This is due to the combination of two contributions: first, the reduced thickness and, second, the fact of having a stiffer shell (PMMA+PVC) than the polypropylene used in the Nike and Team Quest shin guards. For the same thickness, the stiffer the shell, the lower the deformation allowed, which results in larger peak values for the force and lower values in the energy dissipation. In the case of the Rheinforce cork composite, the reduced thickness allows for higher peak values in the force, whereas the lack of hard shell facilitated larger values in the energy dissipation.

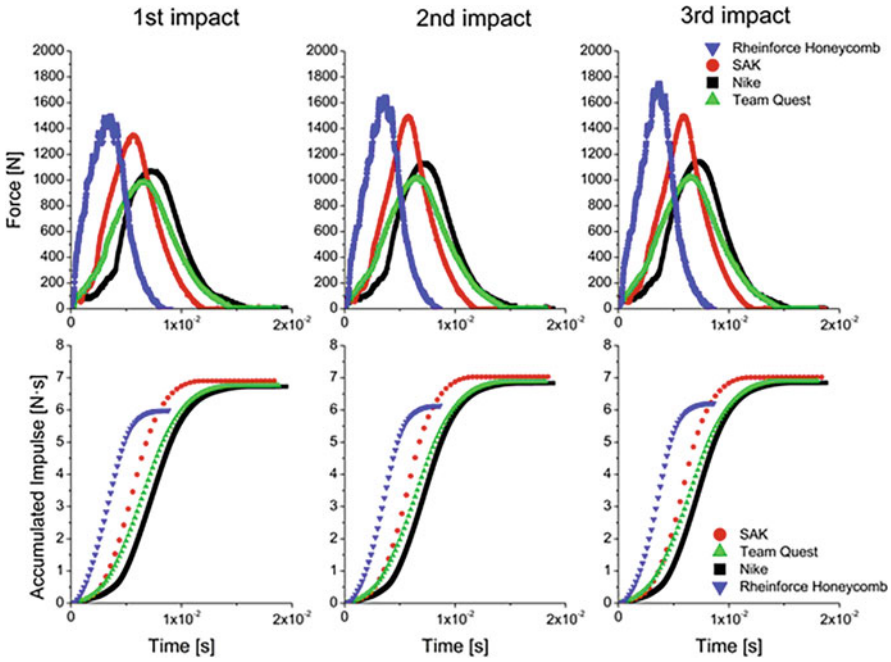

Fig. 4.10 Comparison of the force vs. time curves measured for the different shin guards and its evolution with the number of consecutive impacts (top row). Accumulated impulse for the different cork composites and its evolution with the number of consecutive impacts (bottom row)

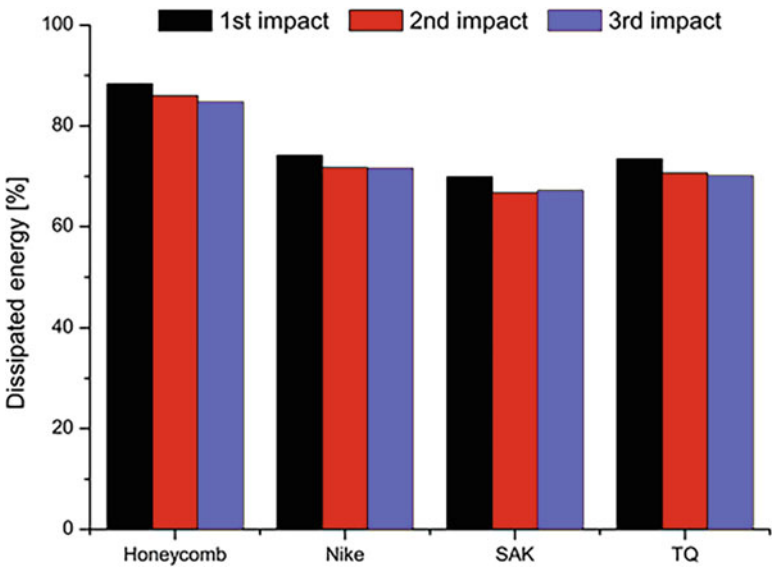

Fig. 4.11 Comparison of the percentage of the impact energy dissipated by the different shin guards and its evolution with the number of consecutive impacts

4.4 Conclusions and Remarks

In this study, the mechanical response of cork-STF composites, which were designed with the Rheinforce technology [1], has been assessed against low-velocity impacts. The aim was to assess the technology for its application in football shin guards. The composites consisted of a sandwich of two micro-agglomerated cork pads having a total thickness of 5.2 mm, and different microfluidic patterns were considered. For the STF, a concentrated suspension of fumed silica in polypropylene glycol of 400 g/mol has been considered. The results of the blunt impact tests evidenced the microfluidic pattern's importance in the mechanical performance of the composites against impact loads.

Moreover, it was also observed that the formulation of the STF is paramount in that performance. In this sense, it is recommended to define a new formulation to remove the yield stress behavior, as it prevents the fluid from returning to the impacted zone once the load is released. Moreover, because cork is a natural material, an eco-friendlier design using Rheinforce cork composite as a core material will require for an eco-friendlier formulation of the STF. Among the four microfluidic patterns, the one with the honeycomb design provided the best result for this formulation of STF, providing a force peak below 2.0 kN and the most significant amount of energy dissipated, exceeding the performance of the pure cork.

Compared with the commercial shin guards, it can be highlighted that due to the reduction in the thickness between 13.3% and 45.3%, the Rheinforce cork composite provided the most significant peak values in the force and the shortest impact time. However, the amount of energy dissipated exceeded the ones from the commercial shin guards. Table 4.5 summarizes and compares these main features.

The impact resistance was not analyzed in this study. However, as shear thickening materials are typically used in more demanding anti-penetration applications, such as bulletproof vests [34] or stab-resistant materials [21], it is expected that the Rheinforce cork composites will also satisfy the requirements for stud impact tests. In a previous work using the same honeycomb microfluidic pattern [2], it was observed that the STF prevents the cork from being perforated and cracked. Nevertheless, if required, we could also use the Rheinforce cork composite as the liner of the shin guard, having an external hard shell (Fig. 4.12).

The conclusion of this study is that, even though there is still room for topological optimization, Rheinforce technology can be used to design football shin guards. Moreover, it also opens the door to applying this technology for many other PPE. Finally, thanks to a large number of unrestricted designing parameters, this technology offers the possibility of tweaking the mechanical performance to the required needs in many other applications such as baby chairs, helmets, etc.

Table 4.5 Summary of the key features in the design and performance of the different shin guards, considering the average values of the three consecutive impacts of 2.5 J with a striking mass of 3.982 kg

Shin guard	Hard shell	Total thickness [mm]	Energy dissipated [%]	Total impact time [ms]	Peak force [kN]	Time peak force [ms]	Impulse [N·s]
Nike	Polypropylene	9.5 ± 0.5	72 ± 1	15.9 ± 0.3	1114 ± 39	7.3 ± 0.4	6.8 ± 0.1
SAK	PMMA+PVC	6.0 ± 0.5	68 ± 2	12.2 ± 0.4	1444 ± 92	5.8 ± 0.1	7.0 ± 0.1
Team Quest	Polypropylene	8.5 ± 0.5	71 ± 2	14.6 ± 0.1	988 ± 5	6.5 ± 0.2	6.8 ± 0.1
Rheinforce honeycomb	–	5.2 ± 0.1	86 ± 2	8.3 ± 0.1	1557 ± 181	3.0 ± 0.4	6.1 ± 0.1

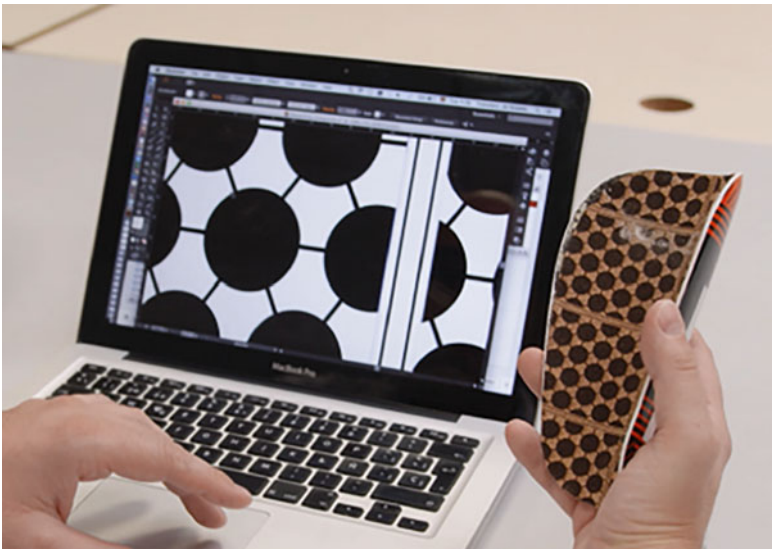

Fig. 4.12 Prototype of a shin guard using Rheinforce cork composite as inner liner and an outer hard shell

Acknowledgments The author would like to acknowledge the financial support from FEDER funds through COMPETE2020-Programa Operacional Competitividade e Internacionalização (POCI) and FCT/MCTES LA/P/0045/2020 (ALiCE) and UIDP/00532/2020 (CEFT), funded by national funds through FCT/MCTES (PIDDAC).

References

1. Galindo-Rosales FJ, Campo-Deaño L. Composite layer material for dampening external load, obtaining process, and uses thereof. Patent WO2016051320A1
2. Galindo-Rosales FJ, Martínez-Aranda S, Campo-Deaño L. CorkSTFμfluidics – A novel concept for the development of eco-friendly light-weight energy absorbing composites. Mater Des. 2015;82:326–34. https://doi.org/10.1016/j.matdes.2014.12.025.
3. Protective clothing — Shin guards for association football players — Requirements and test methods. EN 13061:2009EN 13061:2009
4. United States Department of Labor. Occupational safety and health administration. Personal protective equipment. Available from: https://www.osha.gov/personal-protective-equipment
5. Delides GS. The royal tombs at Vergina Macedonia, Greece, revisited a forensic review. Int J Forensic Sci Pathol. 2016;4(4):234–9. https://doi.org/10.19070/2332-287X-1600056.
6. Muay Thai Fight Us Vs Burma (80668065) – Muay Thai – Available from: https://es.wikipedia.org/wiki/Muay_thai#/media/Archivo:Muay_Thai_Fight_Us_Vs_Burma_(80668065).jpeg
7. Alexander C. How do we know what ancient Greek warriors wore for battle? It's in 'The Iliad. National Geographic. Published 19/2/2021. Availabel from: https://www.nationalgeographic.com/history/history-magazine/article/arms-armor-ancient-greece-full-display-the-iliad
8. Standard test method and performance specification for newly manufactured soccer shin guards. National Operating Committee On Standards For Athletic Equipment. NOCSAE DOC (ND) 090-06m18. February, 2018. Available from: https://nocsae.org/wp-content/uploads/2018/05/ND090-06m18MfrdSoccerShinGuardsStdperformance-1.pdf

9. The history of the laws of the game Fédération Internationale de Football Association. 2014 Available from: http://www.fifa.com/classicfootball/history/the-laws/from-1863-to-present.html
10. Vriend I, Valkenberg H, Schoots W, Goudswaard GJ, van der Meulen Wout J, Backx FJG. Shinguards effective in preventing lower leg injuries in football: Population-based trend analyses over 25 years. J Sci Med Sport. 2015;18(5):518–22. https://doi.org/10.1016/j.jsams.2014.07.002.
11. Barrey PB, John HL, James AN, William EG. Tibia and fibula fractures in soccer players. Knee Surg Sports Traumatol Arthrosc. 1999;7:262–6.
12. Ankrah S, Mills NJ. Performance of football shin guardsfor direct stud impacts. Sports Eng. 2003;6:207–20.
13. Francisco A, Nightingale RW, Guilak F, Glisson RR, Garret WE. Comparison of soccer shin guards in preventing ti-bia fracture. Am J Sports Med. 2000;28:227–33.
14. Gürgen S, Kuşhan MC, Li W. Shear thickening fluids in protective applications: A review. Prog Polym Sci. 2017;75:48–72. https://www.sciencedirect.com/science/article/pii/S0079670017300035
15. Galindo-Rosales FJ. Complex Fluids in Energy Dissipating Systems. Appl Sci. 2016;6(8):206. https://doi.org/10.3390/app6080206.
16. Galindo-Rosales FJ, Rubio-Hernández FJ, Velázquez-Navarro JF. Shear-thickening behavior of Aerosil® R816 nanoparticles suspensions in polar organic liquids. Rheol Acta. 2009;48:699–708. https://doi.org/10.1007/s00397-009-0367-7.
17. Ricardo J, Andrade E, Jacob AR, Galindo-Rosales FJ, Campo-Deaño L, Huang Q, Hassager O, Petekidis G. Dilatancy in dense suspensions of model hard-sphere-like colloids under shear and extensional flow. J Rheol. 2020;64:1179–96. https://doi.org/10.1122/1.5143653.
18. Brown E, Jaeger HM. Through Thick and Thin. Science. 2011;333(6047):1230–1. https://doi.org/10.1126/science.1211155.
19. Barnes HA. Shear-thickening ("dilatancy") in suspensions of nonaggregating solid particles dispersed in newtonian liquids. J Rheol. 1989;33(2):329–66. https://sor.scitation.org/doi/abs/10.1122/1.550017
20. Dawson MA. Composite plates with a layer of fluid-filled, reticulated foam for blast protection of infrastructure. Int J Impact Eng. 2009;36(10):1288–95.
21. Feng X, et al. Effects of different silica particles on quasi-static stab resistant properties of fabrics impregnated with shear thickening fluids. Mater Des. 2014;64:456–61. https://doi.org/10.1016/j.matdes.2014.06.060
22. Lomakin EV, Mossakovsky PA, Bragov AM, et al. Investigation of impact resistance of multilayered woven composite barrier impregnated with the shear thickening fluid. Arch Appl Mech. 2011;81:2007–20. https://doi.org/10.1007/s00419-011-0533-0.
23. Gürgen S, Fernandes FAO, de Sousa RJA, et al. Development of Eco-friendly Shock-absorbing Cork Composites Enhanced by a Non-Newtonian Fluid. Appl Compos Mater. 2021;28:165–79. https://doi.org/10.1007/s10443-020-09859-7.
24. Rizzo F, Pinto F, Meo M. Investigation of Silica-Based Shear Thickening Fluid in Enhancing Composite Impact Resistance. Appl Compos Mater. 2020;27:209–29. https://doi.org/10.1007/s10443-020-09805-7.
25. Myronidis K, Thielke M, Kopeć M, Meo M, Pinto F. Polyborosiloxane-based, dynamic shear stiffening multilayer coating for the protection of composite laminates under low velocity impact. Comput Sci Technol. 2022;222 https://doi.org/10.1016/j.compscitech.2022.109395.
26. Brown E, Jaeger HM. The role of dilation and confining stresses in shear thickening of dense suspensions. J Rheol. 2012;56:875–923. https://doi.org/10.1122/1.4709423.
27. Galindo-Rosales FJ, Oliveira, M.S.N. And Alves M.A. Optimized cross-slot microdevices for homogeneous extension. RSC Adv. 2014;4:7799–804.
28. Galindo-Rosales FJ, Campo-Deaño L, Sousa PC, Ribeiro VM, Oliveira MSN, Alves MA, Pinho FT, et al. Exp Thermal Fluid Sci. 2014;59:128–39. https://doi.org/10.1016/j.expthermflusci.2014.03.004.

29. Parras L, Galindo-Rosales FJ. Modelling the fluid-flow inside a microchannel under impact loads. J Fluids Struct. 2020;97:103069. https://doi.org/10.1016/j.jfluidstructs.2020.103069.
30. Sánchez A. Colloidal gels of fumed silica: microstructure, surface interactions and temperature effects. PhD thesis. North Carolina State University; 2006.
31. Raghavan SR, Walls HJ, Khan SA. Rheology of Silica Dispersions in Organic Liquids: New Evidence for Solvation Forces Dictated by Hydrogen Bonding. Langmuir. 2000;16(21): 7920–30.
32. Bonfanti A, Bhaskar A, Ashby MF. Plastic deformation of cellular materials, Reference module in materials science and materials engineering. Elsevier; 2016. https://doi.org/10.1016/B978-0-12-803581-8.03009-5.
33. Galindo-Rosales FJ, Oliveira MSN, Alves MA. Optimized cross-slot microdevices for homogeneous extension. RSC Adv. 2014;4(15):7799–804.
34. Lee B-W, et al. The influence of the particle size of silica on the ballistic performance of fabrics impregnated with silica colloidal suspension. J Compos Mater. 2009;43(23):2679–98.
35. Tatar Y, Ramazanoglu N, Camliguney AF, Saygi EK, Cotuk HB. The effectiveness of shin guards used by football players. J Sports Sci Med. 2014;13(1):120–7. PMID: 24570615; PMCID: PMC3918547

Chapter 5
Stab Resistance of Shear Thickening Fluid Treated High-Performance Textiles

Thiago F. Santos, Caroliny M. Santos, M. R. Sanjay, Suchart Siengchin, Emad Kamil Hussein, Ivan Medeiros, and Marcos Aquino

5.1 Introduction

High-performance fiber-based lightweight armor is used to provide protection against low velocity to ballistic threats. For this purpose, high-performance fibers made from ultrahigh molecular weight polyethylene (UHMWPE), polyp-phenylene benzobisoxazole (PBO), polyhydroquinone-di imidazopyridine, and p-aramid are widely used in the protective applications. Textiles made from p-aramid fibers, such as Kevlar, provide several advantages over the others. Lightweight, high toughness, increased tensile strength, advance impact/shock resistance, and excellent thermal stability are some of key factors that make the p-aramid based textiles suitable for protective applications [1–5]. In recent years, researchers have shown great interest in shear thickening fluid (STF) with high-performance fabrics to have enhanced protection performance against impacting threats. When engineering textiles are impregnated with STF, a considerable increase is observed in protective performance without compromising the flexibility and lightweight of the structures [6, 7].

Polyparaphenylene terephthalamide based yarns are considered as a substrate of chemical origin in which the fiber-forming substance is a long-chain synthetic polyamide. At least 85% of the amide bonds are directly linked and combined

T. F. Santos (✉) · C. M. Santos · I. Medeiros · M. Aquino
Textile Engineering Post Graduation Program (PPGET), Federal University of Rio Grande do Norte, Natal, Rio Grande do Norte, Brazil

M. R. Sanjay · S. Siengchin
Natural Composites Research Group Lab, Department of Materials and Production Engineering, The Sirindhorn International Thai-German Graduate School of Engineering (TGGS), King Mongkut's University of Technology North Bangkok (KMUTNB), Bangkok, Thailand

E. K. Hussein
Mechanical Power Engineering Department, Al Mussaib Technical College, Al Furat Al Awsat Technical University, Al Mussaib, Babil, Iraq

S. Gürgen (ed.), *Shear Thickening Fluid*, https://doi.org/10.1007/978-3-031-35521-9_5

with amide groups and benzene rings in polyamide molecules. These aromatic polyamide fibers (p-aramid) have been widely used in the development of lightweight reinforcing materials due to their high strength-to-weight ratio [8]. The p-aramid was developed by a Polish chemist, Stephanie Kwolek, while working for DuPont. She was researching, together with her group, poly-p-phenylene-terephthalate and polybenzamide, aiming to obtain a new lightweight and strong fiber to apply in tires. The fiber was discovered accidentally, and a few years later in the 1970s, the modern p-aramid was introduced to the market [9]. The p-aramid fibers have high tenacity and resistance to stretching in various chemical and high temperature conditions. Some of the physical and mechanical properties are density of 1.44 g/cm^3, toughness of 2.03 N/Tex, and tensile modulus of 70.3 GPa. Because the p-aramid yarns are more flexible than the other high-performance textile materials such as glass, they are also easier to be used in fabric manufacturing processes such as weaving, knitting, or braiding [10, 11]. Currently, the requirements of the protective textiles are mostly about high tenacity, lightweight, and flexibility. Although much progress has been made in improving the functionality in the protective textiles, they still adversely affect the user comfort and mobility, thereby still needing more comfortable solutions. To meet this requirement, many researchers have studied the relationship between material, manufacture, and protective properties [1, 4, 12]. Therefore, the great challenges for the researchers in this field are weight reduction, flexibility gain, and impact resistance improvement. For this purpose, different approaches have been made in recent years. One of these approaches is integrating the high-performance textiles with STF to enhance the protection with less numbers of fabric layers in the structures and thereby improve the flexibility as well [4, 13, 14].

The energy of impacting threats has to be dissipated on the protective systems without producing a penetration. Hence, protective structures are designed to resist to sharp penetrations and thereby avoid internal damages. However, non-penetrating impacts may induce blunt trauma or biomechanical injuries on the user bodies. There is little data that conclusively defines the limits of energy that the human body can safely support. Therefore, currently personal shielding does not adequately secure the body against problems such as brain or neck injuries caused by non-penetrating impacts [15, 16]. Even dealing with a non-penetrating threat, protective structures should lower the traumas on the bodies. At this point, kinetic energy of impacting threats has great importance to reduce the traumas. During the impacting process of a threat, some part of the kinetic energy is dissipated over an area on the target while some is absorbed. Yet, the remaining energy leads to deformations in the target. To enhance the protection, the dissipated and absorbed amounts of energy should be enhanced by designing proper structures. Multiple layers of p-aramid based textiles are efficiently used in flexible protective solutions. High tensile strength of fabric layers promotes distortions in impacting threats while dissipating the kinetic energy over an extended area [17, 18]. STF applications contribute to the protective capabilities of p-aramid layers providing a coupling effect between the yarns and thereby enhancing energy dissipation on the structures.

5.2 Shear Thickening Fluid and Protective Applications

If shear stress in a fluid is not directly proportional to shear rate, the fluid is called non-Newtonian [19, 20]. In that case, the fluid exhibits nonlinear behavior between shear stress and shear rate as shown in Fig. 5.1. The relationship between shear stress and shear rate is defined by Eq. 5.1:

$$\tau = \eta(\dot{\gamma})\dot{\gamma} \tag{5.1}$$

where τ is shear stress, η is viscosity, and $\dot{\gamma}$ is shear rate. In Newtonian fluids, viscosity is independent from shear rate and thereby becoming a constant. However, in non-Newtonian fluids, viscosity is dependent on shear rate and shows variable values at different shear rates [21].

Shear thickening behavior is seen in suspensions generally at high particle volume fractions and high shear rates. Viscosity increases drastically upon shearing the suspension. Shear stress increases accordingly in the suspension [22, 23]. The thickening is so severe and instantaneous that the suspension shows a solid-like behavior under high shear rates [24]. After removing the shear rate, relaxation occurs within a few seconds, which is rapid but not instantaneous as in the thickening process [25, 26].

Composite materials have been successfully introduced in protective applications. The concept of formulation is very broad that develops intermediates or finished products by mixing different raw materials. However, formulation can be defined as all the knowledge and operations implemented when mixing, combining, or molding ingredients of natural or synthetic origin in order to obtain a commercial product characterized by its function of use and its ability to satisfy a predetermined specification. In this way, they are formed by combining two or more individual materials in a defined proportion to have a desirable set of mechanical and physical

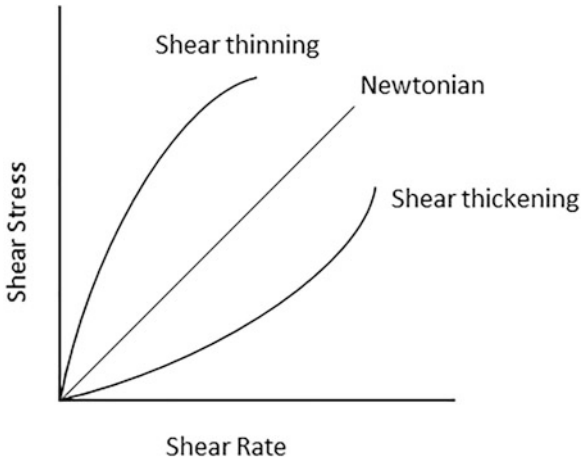

Fig. 5.1 Shear rate vs. shear stress for Newtonian and non-Newtonian fluids

properties of their components. The matrix, also called the continuous phase, ensures cohesion and orientation of the load, which is the discontinuous phase or reinforcement. They are combined in such a way that their physical and mechanical properties are complementary. The advantage of composites with polymeric matrix, in relation to metals, is to obtain a lower density. It is important to emphasize that the nature of the matrix and the filler, the shape and proportion of the filler, the quality of the interface, and the production process used are parameters that can influence the properties of the composite material. This results in high strength, low weight, high rigidity, and high impact resistance. Textile composites, in turn, have special properties due to their better draping ability and greater resistance to dynamic and out-of-plane loads. They are manufactured using fabrics inside the dies, which can result in superior mechanical and ballistic behavior with a very reduced weight [27–30]. STF in textile based composites is used as the matrix and thereby provides a continuous phase on the structures. Moreover, flexible behavior of textiles remains in STF-based composites since it is a fluidic material on the fabrics. In addition to these advantages, STF contributes to the protective properties by the effect of shear thickening mechanism, which leads to a solid-like texture upon introducing to the impact conditions.

5.3 A Case of Protective Applications Based on STF Treated Textiles

5.3.1 Experimental Details

In this work, a high-performance textile made from p-aramid was treated with an STF. The areal density of the textile was 497 ± 25 g/m^2, while the weaving details were 7 weft/cm and 7 warp/cm for the principal directions. The yarn counts were 1.73Ne ± 0.02 and 1.72Ne ±0.01 for weft and warp, respectively. The STF was fabricated by ultrasonically distributing the colloidal silica nanoparticles (7 nm, from Evonik) in a polyethylene glycol (PEG) 400 g/mol medium while adding ethanol and silane coupling agent chemically called aminopropyltrimethoxysilane (APTES, from Sigma Aldrich). After the mixing stage, ethanol was removed from the suspension, and the final content was 28% silica and 72% PEG while including 2% APTES with respect to the suspension.

The fabrics were cut in squares with the dimensions of 8 cm × 8 cm. The layers were immersed in the suspension for 15 min. Then, the layers were squeezed at 0.5 bar by a pair of rollers with the velocity of 3 m/min. After the padding process, fabric layers were rested at 75 °C to remove the ethanol. Figure 5.2 shows the macroscopic images of the fabric before and after the STF treatment. Finally, each target was assembled with three layers of fabrics with different plying angles such as (0°/0°/0°) and (0°/30°/60°) as shown in Fig. 5.3. Table 5.1 gives the details of the targets.

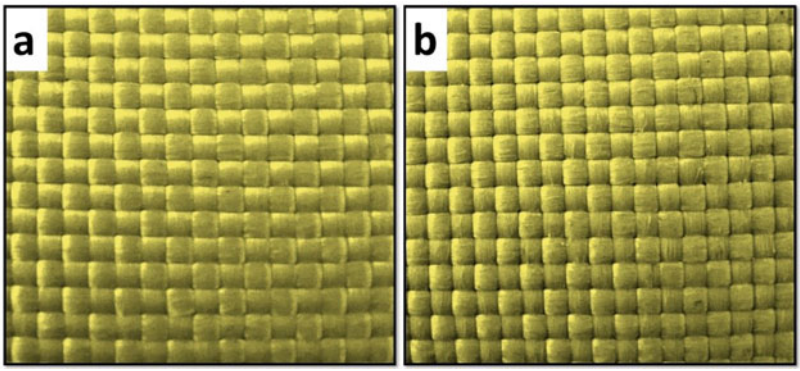

Fig. 5.2 Fabric (**a**) before and (**b**) after STF treatment

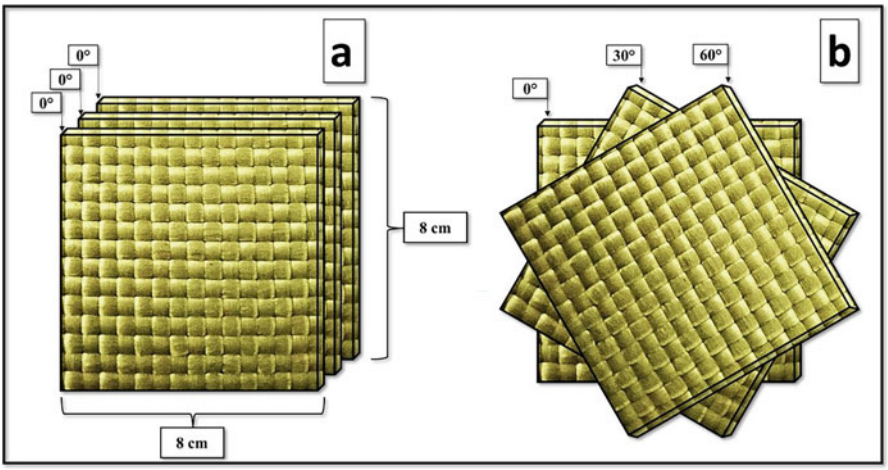

Fig. 5.3 Target configurations: (**a**) p-Ar-NOR and (**b**) p-Ar-OR

Table 5.1 Details of the targets

Specimen	Description
p-Ar-NOR	Neat fabrics with (0°/0°/0°) orientation
p-Ar-OR	Neat fabrics with (0°/30°/60°) orientation
p-Ar + STF-NOR	STF treated fabrics with (0°/0°/0°) orientation
p-Ar + STF-OR	STF treated fabrics with (0°/30°/60°) orientation

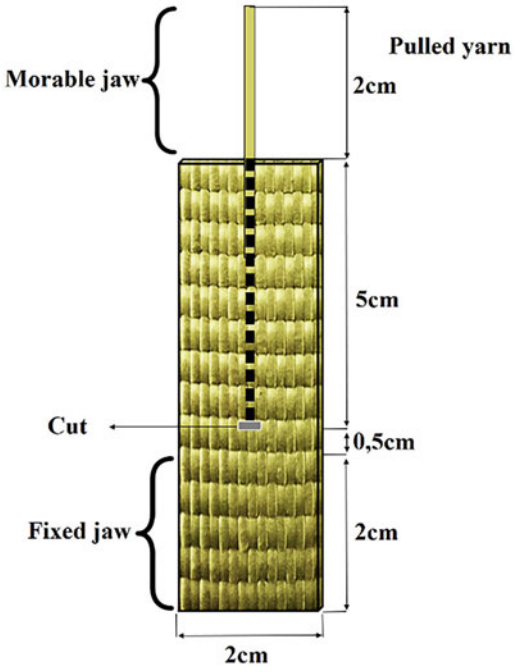

Fig. 5.4 Specimen details in pull-out testing

Pull-out test is a simple characterization method when trying to describe the friction behavior between the yarns in textiles [31]. Pull-out test was carried out in a Mesdan Tensolab 3000 tensile testing system [32]. An intentional cut was initially made at the lower end of the pulled yarn as shown in Fig. 5.4. The upper end of the yarn was pulled at the speed of 100 mm/min, and the pull-out forces were recorded [33].

The targets were also investigated under stab conditions. For this purpose, the targets were subjected to stabbing tests as shown in Fig. 5.5. The tests were conducted as per the NIJ Standard 0115.0 [34] by using the P1 coded knife in the same standard. The details of the P1 knife are shown in Fig. 5.5a. The knife was loaded with 3.34 kg before the tests, and therefore, the targets were stabbed with an impact energy of 27 J. The targets were located on a backing material that consists of a layer-by-layer staked pack having five witness papers and four neoprene sponges as shown in Fig. 5.5c. The stab results were evaluated in terms of penetration depth considering the witness papers in the backing material [35].

In order to evaluate the flexibility of the targets, specimens were investigated in bending angle test as shown in Fig. 5.6**.** The fabrics were sized into 51 mm × 51 mm in this testing. After fixing one of the edges by a distance of 13 mm, the other edge was loaded by a mass of 20 g and the bending angle was measured for each specimen [36]. This test has been widely applied to determine the flexibility of textiles impregnated with STF [37].

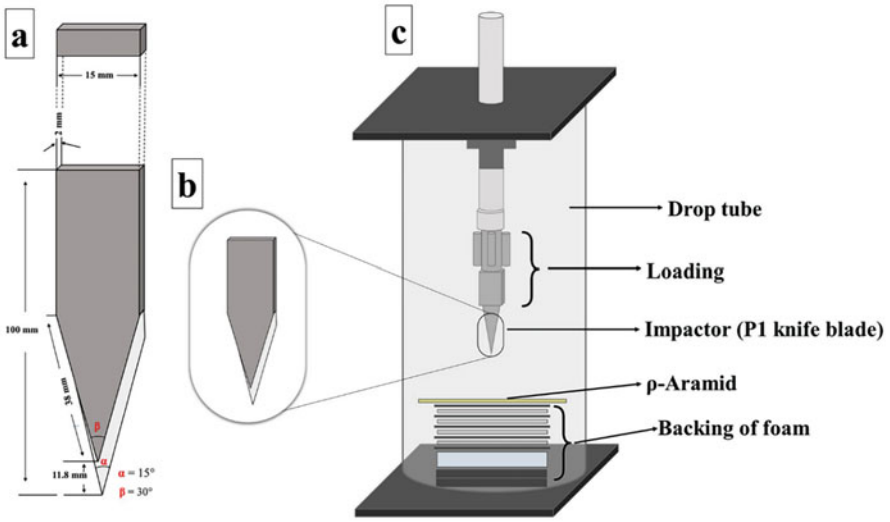

Fig. 5.5 Schematic illustration of stab testing system: (**a**) geometrical details of P1 knife, **(b**) P1 knife at impactor end, and (**c**) stab dropping tower

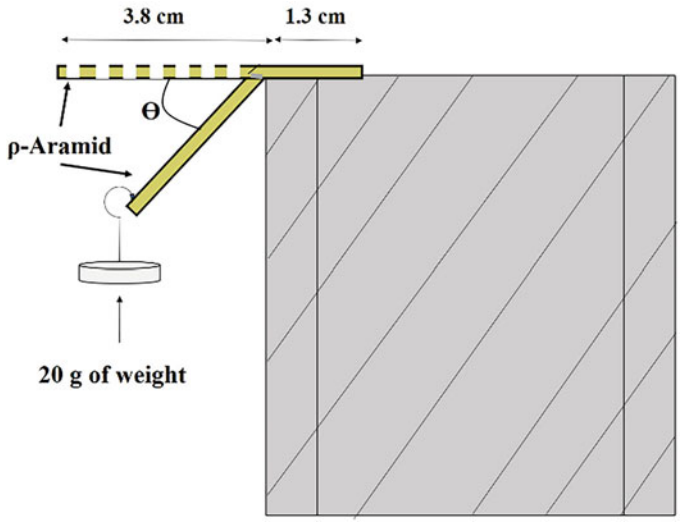

Fig. 5.6 Schematic illustration of bending angle test

In addition to the protective properties, photooxidation behavior of the targets was investigated in this study. Since the textile based protective structures are used in open-to-atmosphere conditions, ultraviolet (UV) exposure is one of the common problems for these materials. For this purpose, the specimens were characterized by

Fourier-transform infrared spectroscopy (FTIR) analysis in a Shimadzu IR Tracer 100 system to verify the new peak formations after the photooxidation exposure in an accelerated aging equipment (QUV). The analysis focused on the change in the intensity of the normalized wavenumber (820 cm^{-1}), which corresponds to the vibration outside the plane of the C–H bond of the benzene ring used as a reference, because it is the only peak that unchanged during UV exposure. The specimens with the dimensions of 25 mm × 220 mm were subjected to photooxidation by the UV lamps having a wavelength of 340 nm (equivalent to UVA light – daytime) with a condensation cycle (equivalent to night). Each complete cycle lasted 8 h of UV exposure at 60 °C (irradiance of 0.68 W/m^2) and followed by 4 h of condensation at 50 °C. The total testing period was 180 h for the specimens [38]. The characterization for reflectance spectrophotometer (RSP) was carried out before and after photooxidation with the standard illuminant CIE D65. The color system, CIELAB, was used for the quantitative determination of color variation and the total color difference [39].

The chemical treatment commenced with a solution comprising 98% ethanol, which served to reduce the surface tension and facilitate the dispersion of silica particles in polyethylene glycol (PEG) by weight. A 2% aqueous solution was also incorporated. APTES was then introduced into the mixture through ultra-sonication for 5 min to enable hydrolysis and the formation of Silanol. Subsequently, the silica particles, comprising 28% of the total mass, were mixed with the solution using ultra-sonication for approximately 15 min to accomplish the functionalization of the silica nanoparticles. Following this, a mixture of polyethylene glycol was added, and the solution was stirred for 3 min to complete the preparation of the suspension, with a pH ranging from 10.4 to 11.2. These steps were carried out in accordance with established guidelines found in the existing literature. To further proceed, the ethanol was evaporated using a laboratory stenter machine at 75 °C for 90 s, resulting in the formation of an STF composition comprising 28% silica and 72% PEG.

5.3.2 Results and Discussion

Figure 5.7 shows the scanning electron micrographs for the neat and STF treated fabrics. As shown in the images, a thin layer of silica nanoparticles covers the surface of the fibers within the STF treated fabric. A good dispersion of silica is observed in this specimen. The fabric benefits from the mechanical properties of silica nanoparticles such as high rigidity on the fibers. Moreover, coupling between the fibers is enhanced by the effect of silica nanoparticles. Hence, energy dissipation mechanism is improved in the structure as well as growing the friction between the yarns [40, 41]. Due to higher energy dissipation capabilities, impact performance of textiles is greatly enhanced after STF treatment [42, 43]. This change is also related to the friction between the yarns, which also grows up by the effect of STF treatment in the textiles [23, 35].

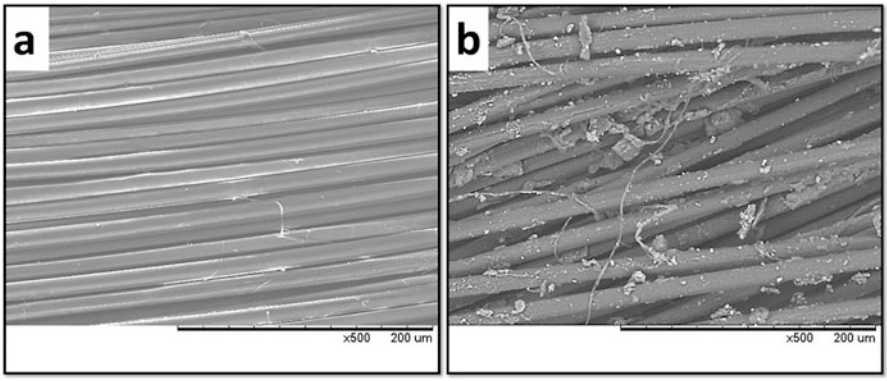

Fig. 5.7 Scanning electron micrographs for (**a**) neat and (**b**) STF treated fabrics

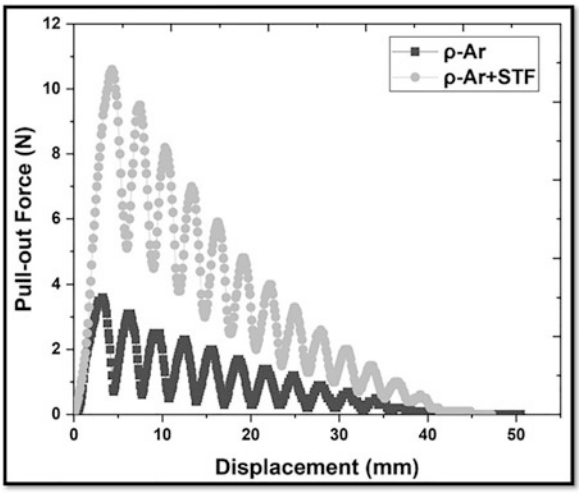

Fig. 5.8 Pull-out force vs. displacement curves for the specimens

Yarn pull-out test is widely used for evaluating the impact performance of textile based structures [44, 45]. Figure 5.8 shows the relationship between force and displacement for the neat and STF treated fabrics in the yarn pull-out testing. The pull-out force is associated with the yarn-to-yarn friction within the textiles so that the higher pull-out force, the higher friction in the structure [46]. In general, higher frictions between the yarns provide enhanced anti-impact properties in the textiles because the frictional interactions act as an additional energy absorbing mechanism during the impact process [47]. From this aspect, STF treated fabric is much more suitable for designing the anti-impact systems compared to the neat one. The peak yarn pull-out force is about 10.5 N in the STF treated fabric, whereas it is only 3.8 N in the neat fabric. From this result, it is obvious that the STF treatment provides about 2.76 times higher frictional increase within the textile. Higher friction in the

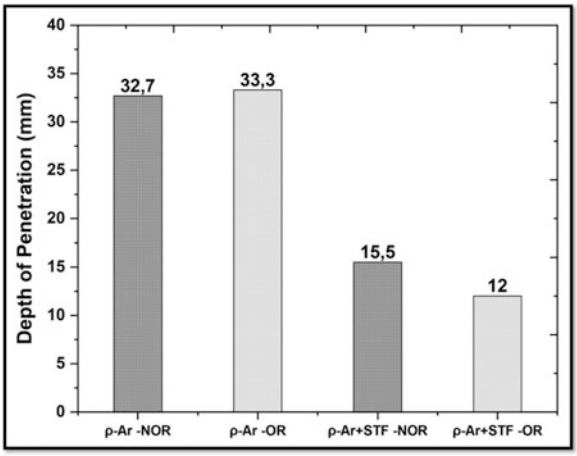

Fig. 5.9 Penetration depth results for the specimens

textiles promotes the anti-slip mechanism in the yarns and thereby prevents the yarn opening effect at the impact zone [48]. For this reason, penetration of the impacting threat is avoided in the structure [49, 50]. Moreover, yarn interlocking is enhanced by the effect of STF treatment in the structure [51, 52]. STF acts as a continuous matrix on the yarns, and therefore, coupling effect is observed in the textile [53–55]. In addition to the increased pull-out force by the effect of increasing frictional interactions between the yarns, tenacity of the yarns has to withstand the impacting threat for enhanced protection. In this case, the impacted yarns are strained and tensile stresses prevail over the yarns. For this reason, the yarns have to sustain their integrity without rupturing during the impact process [56].

Figure 5.9 shows the depth of penetration results for the specimens. Depth of penetration exhibits the protective performance of the textiles. According to the results, different orientations of the fabric layers has a minor effect on the penetration depth since the results are quite close to each other: 32.7 mm and 33.3 mm for the orientations of (0°/0°/0°) and (0°/30°/60°), respectively. However, penetration depth is heavily changed by the effect of SSTF treatment on the fabrics. After the STF treatments, penetration depth is lowered to 15.5 mm and 12 mm for the orientations of (0°/0°/0°) and (0°/30°/60°), respectively. The reductions in the penetration depths are significant when the fabrics are treated with STF. The results can be associated with the frictional interactions within the fabrics by the effect of STF application. During the stabbing process, impact energy is dissipated over a wider area due to the coupling effect between the STF treated yarns [43]. Hence, secondary yarns also contribute to the energy dissipation mechanism and, therefore, energy absorbing capacity of the structure is enhanced by STF treatment. For this reason, penetration depth is considerable reduced, which means that STF treated fabrics provide a great protective performance for their users.

Figure 5.10 shows the stabbing deformations on the witness papers layered in the backing material. The knife cuts are larger in dimension on the first witness papers and gradually get smaller to the fourth witness paper. This is because of the geometry of the knife blade used in the testing. The blade has a sharp point at the tip and an

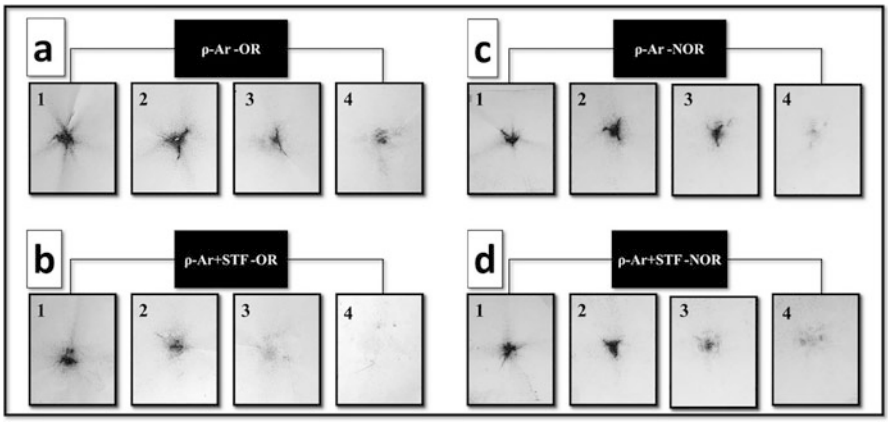

Fig. 5.10 Deformations on the witness papers for (**a**) p-Ar-OR, (**b**) p-Ar + STF-OR, (**c**) p-Ar-NOR, and (**d**) p-Ar + STF-NOR

extending shank to the knife root. Comparing the neat and STF treated fabrics, there are significantly different deformations on the witness papers. The knife cuts are more obvious on the last witness papers for the targets packed with neat fabrics. However, the cuts are hardly visible on the last layer of the witness papers for the STF treated targets. Despite the same stabbing energies both for the neat and STF treated fabrics, impact energies are distributed over larger areas on the STF treated targets and thereby lower the depth of penetrations. The main mechanism in this phenomenon is reduce the mobility of the yarns within the textiles and thereby hinder the yarn openings at the impact point [57, 58]. Furthermore, the contribution of the secondary yarns enhances the energy absorbing capabilities in the structures. Straining of far-fields is observed by this way. Consequently, impact energy is greatly attenuated by dissipating the large part of it at in-plane directions so that depth of penetration is significantly lowered.

Regarding the flexibility of the targets, it can be stated that STF treatment does not deteriorate the soft texture of the textiles. Both the neat and STF treated specimens show the bending angles of about 55° in the flexibility tests. Due to the fluidic characteristics of the STF, STF treated textiles keep their flexible properties. For this reason, STF application in textile based protective structures can be easily used without compromising the advantages of soft armor.

About the photooxidation and color change behavior, it is necessary to understand the vibration peaks of the functional groups that correspond to a specific wavenumber in the specimens exposed to QUV testing. The wavenumber at 3317 cm^{-1} corresponds to N–H stretching, which occurs when the carbonyl and amine groups are in trans configuration. On the other hand, the wavenumber vibrations at 2916 cm^{-1} and 2819 cm^{-1} are attributed to the stretching of C–H groups as well as aldehyde groups, and still, the peak at 1639 cm^{-1} corresponds to the stretching of the CO group (amide I) [59, 60]. The vibration peaks of the

functional groups at 1307 cm^{-1} are related to a combination in the flexing and stretching of N–H groups, while at 1539 cm^{-1}, there is a combination in the flexing and stretching of C–N groups (amide III and II) [59, 61]. Figure 5.11a shows the normalized intensity with percentage increase (+%) or percentage decrease (−%) of the bands corresponding to the specimens at the peaks of 3317 cm^{-1}, 2916 cm^{-1}, 2819 cm^{-1}, 1639 cm^{-1}, 1539 cm^{-1}, and 1307 cm^{-1}. Hence, amide band of the neat fabric at 3317 cm^{-1} does not exhibit a significant increase (+0.8%) after exposure to QUV compared to the STF treated fabric, as the STF applied fabric shows an increase of about +15.7% in wave number intensity at this peak. During UV exposure, photooxidation promotes the scission of C–N bonds in the main chain of the macromolecule in neat fabric by forming oxidized species. Due to this, the neat fabric suffers less oxidation in comparison with the STF treated one at the peak of 2916 cm^{-1}. Moreover, a positive increase in the wavenumber intensity is observed at 2916 cm^{-1} in the neat fabric (14.8%), while the STF treated fabric has just opposite progress (−0.7%) as shown in the chart. At 2819 cm^{-1}, STF treated fabric has a negative change (−9.1%) in the wavenumber intensity, while the neat fabric shows a positive increase of 5.9% after the UV exposure [62, 63]. However, the peaks at 1639 cm^{-1} and 1539 cm^{-1} show that the intensity of the normalized wavenumber has the same trend. At 1639 cm^{-1} (amide I), it decreases (−5.1%) for the neat fabric, whereas an increase about 10.3% is observed for the STF treated fabric. Regarding the amide II at 1539 cm^{-1}, the neat fabric shows a reduction of 3.5%, while the STF treated fabric shows an increase of 6.5%. This can be associated with the main chain scission and reduction of functional groups after UV exposure. The peak intensity normalized at 1307 cm^{-1} (amide III) increases after UV exposure both for the neat and STF treated fabrics. The rates of the increments are 2.8% and 6.6%, respectively. Comparing the specimens, it is clear that the increase for the STF treated fabric is larger at this peak. This indicates that there is a partial scission of the chain, generating amide (N–H groups) in the STF treated fabric more than the neat one. Considering the color change results as shown in Fig. 5.11b, the color index of

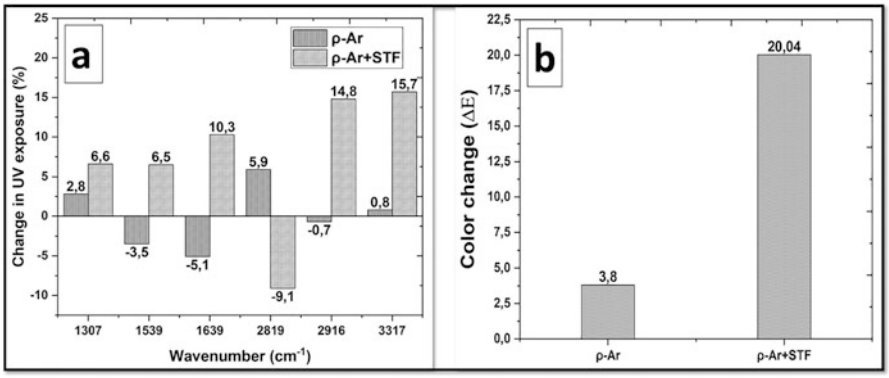

Fig. 5.11 (**a**) Change in the intensity of FTIR peaks after UV exposure and (**b**) color change index for the specimens

ΔE is considerably higher in the STF treated fabric. The color index is 20.04 for the STF treated fabric, while it is only 3.8 for the neat fabric. According to these results, it is possible to state that STF treated fabric is much more susceptible to the UV exposure so that this specimen shows visible changes in its appearance. In order to protect the STF treated fabrics from the UV degradation, various fillers having high photooxidation resistance can be included in the STF content [64–68]. The macromolecular degradation as well as color change in the structure can be hindered by this way.

5.4 Conclusions and Future Perspectives

This chapter shows that researches like the one presented promotes a significant expansion of the frontiers of knowledge. However, continued development of new STFs with new carrier fluids and/or particles, optimized conditions, or new manufacturing techniques are underway to meet new and more demanding requirements in the field of application. Additionally, there is a growing demand for research in the development of new STFs based on new nanoparticles that have adjustable properties as they have wide application potential. Other recent researches have indicated that shear thickening can be controlled by altering particle surface properties (e.g. hydrophilic or hydrophobic), roughness, and geometric shapes. Further investigations will provoke discoveries that open possibilities for new studies of shear thickening with control of the properties of absorbing/dissipation and pull-out force, producing specific STFs for different applications and certainly expanding the potential of applications of STFs based on nanoparticles. Looking at the future perspectives from our margin, it is clear that there are still some problems that need to be solved for nanoparticle-based STFs, including stability problems, absorbing/dissipate mechanism, phenomenon of absorbing kinetic energy, and widening the impact protection capacity in future applications. There are some studies focusing on the use of other textile structures to improve the kinetic mechanism of nanoparticle-based STFs. However, observing the current literature, little has been devoted to applying structures using hybrid knitting technology. In the coming years, the focus of research on impact protection will be devoted to studying hybrid knitted fabric/woven fabric structures with interspersed nanoparticle-based STFs. Thus, we will prove that the impact protection performance is improved with the help of STFs based on nanoparticles applied in 2D and 3D hybrid textile structures promoting new statistical, experimental, and depth investigations in the field of energy absorbing/dissipation mechanism in composites of hybrid textile fabrics treated with nanoparticle-based STFs. Thus, the fabrication of nanoparticle-based STFs with bold structural, rheological features opens up new possibilities to design efficient STF-based material for application in different fields of safety and security science and engineering.

Acknowledgments This research is supported by our Lord. Authors would like to thank their colleagues at the Textile Engineering Post Graduation Program-PPgET, the Federal University of Rio Grande do Norte.

References

1. Mawkhlieng U, Majumdar A, Laha A. A review of fibrous materials for soft body Armour applications. RSC Adv. 2020;10(2):1066–86.
2. Woo S-C, Kim T-W. High-strain-rate impact in Kevlar-woven composites and fracture analysis using acoustic emission. Compos Part B Eng. 2014 Apr;60:125–36.
3. Na W, Ahn H, Han S, Harrison P, Park JK, Jeong E, et al. Shear behavior of a shear thickening fluid-impregnated aramid fabrics at high shear rate. Compos Part B [Internet]. 2016, 97:162–75. Available from: http://ac-els-cdn-com.ez18.periodicos.capes.gov.br/S135983681630600X/1-s2.0-S135983681630600X-main.pdf?_tid=a1b751de-60fa-11e7-9da3-00000aab0f01&acdnat=1499201703_4b8b959506d96cb8ec07f84a4da7b9ca
4. Laha A, Majumdar A. Shear thickening fluids using silica-halloysite nanotubes to improve the impact resistance of p-aramid fabrics. Appl Clay Sci. 2016 Nov;132–133:468–74.
5. Priyanka P, Dixit A, Mali HS. High strength Kevlar fiber reinforced advanced textile composites. Iran Polym J. 2019 Jul;28(7):621–38.
6. Baharvandi HR, Khaksari P, Alebouyeh M, Alizadeh M, Khojasteh J, Kordani N. Investigating the quasi-static puncture resistance of p-aramid nanocomposite impregnated with the shear thickening fluid. J Reinf Plast Compos. 2014 Nov;33(22):2064–72.
7. Majumdar A, Butola BS, Srivastava A, Bhattacharjee D, Biswas I, Laha A, et al. Improving the impact resistance of p-aramid fabrics by sequential impregnation with shear thickening fluid. Fibers Polym. 2016 Feb;17(2):199–204.
8. Chen X, Zhou Y. Technical textiles for ballistic protection. In: Handbook of technical textiles [Internet]. Woodhead Publishing; 2016. [cited 2018 Jul 19]. p. 169–92. Available from: https://www.sciencedirect.com/science/article/pii/B9781782424659000069.
9. Tam T, Bhatnagar A. High-performance ballistic fibers and tapes. In: Lightweight ballistic composites [Internet]. Woodhead Publishing; 2016. [cited 2018 Jul 19]. p. 1–39. Available from: https://www.sciencedirect.com/science/article/pii/B9780081004067000015.
10. Rebouillat S. ARAMIDS: 'Disruptive', open and continuous innovation. Adv Fibrous Compos Mater Ballist Prot [Internet]. 2016 Jan 1 [cited 2018 Jul 20];11–70. Available from: https://www.sciencedirect.com/science/article/pii/B9781782424611000029
11. Chen X. Introduction. In: Advanced Fibrous Composite Materials for Ballistic Protection [Internet]. Woodhead Publishing; 2016 [cited 2018 Jul 20]. p. 1–10. Available from: https://www.sciencedirect.com/science/article/pii/B9781782424611000017
12. Gürgen S, Yıldız T. Stab resistance of smart polymer coated textiles reinforced with particle additives. Comput Struct. 2020;235:111812.
13. Chen X, Zhu F, Wells G. An analytical model for ballistic impact on textile based body Armour. Compos Part B Eng. 2013 Feb;45(1):1508–14.
14. Wei M, Lin K, Sun L. Shear thickening fluids and their applications. Mater Des [Internet]. 2022 Apr;216:110570. Available from: https://linkinghub.elsevier.com/retrieve/pii/S0264127522001915
15. Sheikhi MR, Gürgen S. Deceleration behavior of multi-layer cork composites intercalated with a non-Newtonian material. Arch Civil Mech Eng. 2023;23(1):2.
16. Lewis E, Carr DJ. Personal armour. Light Ballist Compos [Internet]. 2016 Jan 1 [cited 2018 Jul 20];217–29. Available from: https://www.sciencedirect.com/science/article/pii/B9780081004067000076

17. Shahkarami A, Cepus E, Vaziri R, Poursartip A. Material responses to ballistic impact. Light Ballist Compos [Internet]. 2006 Jan 1 [cited 2018 Jul 20];72–100. Available from: https://www.sciencedirect.com/science/article/pii/B9781855739413500037
18. Sinclair R. Understanding textile fibres and their properties: what is a textile fibre? In: Textiles and fashion [Internet]. Woodhead Publishing; 2015 [cited 2018 Jul 20]. p. 3–27. Available from: https://www.sciencedirect.com/science/article/pii/B9781845699314000015
19. Chhabra RP. Non-Newtonian fluid behavior. In: Bubbles, drops, and particles in non-newtonian fluids. 2nd ed. CRC Press; 2006. p. 9–47.
20. Sheikhi MR, Gürgen S. Anti-impact design of multi-layer composites enhanced by shear thickening fluid. Compos Struct [Internet]. 2022;279:114797. Available from: https://linkinghub.elsevier.com/retrieve/pii/S0263822321012447
21. Irgens F. Classification of fluids. In: Rheology and Non-Newtonian Fluids [Internet]. Cham: Springer International Publishing; 2014. p. 1–16. Available from: http://link.springer.com/10.1007/978-3-319-01053-3_1.
22. Gürgen S, Sousa RJA. Rheological and deformation behavior of natural smart suspensions exhibiting shear thickening properties. Arch Civil Mech Eng. 2020;20:1–8.
23. Gürgen S, Kuşhan MC. Improvement of spall liner performance with smart fluid applications. Thin-Walled Struct [Internet]. 2022;180:109854. Available from: https://linkinghub.elsevier.com/retrieve/pii/S0263823122005249
24. Nakanishi H, Nagahiro SI, Mitarai N. Fluid dynamics of dilatant fluids. Phys Rev E – Stat Nonlinear, Soft Matter Phys. 2012;85(1):1–11.
25. Gürgen S. Tuning the rheology of nano-sized silica suspensions with silicon nitride particles. J Nano Res. 2019;56:63–70.
26. Gürgen S, Sofuoğlu MA, Kuşhan MC. Rheological compatibility of multi-phase shear thickening fluid with a phenomenological model. Smart Mater Struct. 2019;28:035027.
27. Hsissou R, Seghiri R, Benzekri Z, Hilali M, Rafik M, Elharfi A. Polymer composite materials: A comprehensive review. Compos Struct. 2021 Apr;262:113640.
28. Priyanka P, Dixit A, Mali HS. High-strength hybrid textile composites with carbon, Kevlar, and E-glass fibers for impact-resistant structures. A Review. Mech Compos Mater. 2017;53(5):685–704.
29. Sevenois RDB, Van Paepegem W. Fatigue damage modeling techniques for textile composites: review and comparison with unidirectional composite modeling techniques. Appl Mech Rev. 2015;67(2):020802.
30. Ding J, Tracey PJ, Li W, Peng G, Whitten PG. Review on shear thickening fluids and applications. Text Light Ind Sci Technol. 2013;2(4):161–73.
31. Gürgen S. An investigation on composite laminates including shear thickening fluid under stab condition. J Compos Mater [Internet]. 2019;53(8):1111–22. Available from: http://journals.sagepub.com/doi/10.1177/0021998318796158
32. Santos TF, Santos CM, Fonseca RT, Melo KM, Aquino MS, Oliveira FR, et al. Experimental analysis of the impact protection properties for Kevlar® fabrics under different orientation layers and non-Newtonian fluid compositions. J Compos Mater [Internet]. 2020; Available from: http://journals.sagepub.com/doi/10.1177/0021998320916231
33. Santos TF, Santos CM, Aquino MS, Oliveira FR, Medeiros JI. Statistical study of performance properties to impact of Kevlar® woven impregnated with Non-Newtonian Fluid (NNF). J Mater Res Technol [Internet]. 2020; Available from: https://linkinghub.elsevier.com/retrieve/pii/S2238785419314668
34. National Institute of Justice. Stab Resistance of Personal Body Armor, NIJ Standard-0115.00. Stab Resist Pers Body Armor, NIJ Stand [Internet]. 2000;JR000235. Available from: https://ezp.lib.unimelb.edu.au/login?url=https://search.ebscohost.com/login.aspx?direct=true&db=ncj&AN=SM183652&scope=site
35. Feng X, Li S, Wang Y, Wang Y, Liu J. Effects of different silica particles on quasi-static stab resistant properties of fabrics impregnated with shear thickening fluids. Mater Des [Internet].

2014;64:456–61. Available from: https://linkinghub.elsevier.com/retrieve/pii/S0261306914005159
36. Lee YS, Wetzel ED, Wagner NJ. The ballistic impact characteristics of Kevlar R woven fabrics impregnated with a colloidal shear thickening fluid. J Mater Sci [Internet]. 2003 [cited 2017 May 5];33(1):2825–33. Available from: http://download.springer.com/static/pdf/59/art%253A10.1023%252FA%253A1024424200221.pdf?originUrl=http%3A%2F%2Flink.springer.com%2Farticle%2F10.1023%2FA%3A1024424200221&token2=exp=1493994734~acl=%2Fstatic%2Fpdf%2F59%2Fart%25253A10.1023%25252FA%25253A102442
37. Hassan TA, Rangari VK, Jeelani S. Synthesis, processing and characterization of shear thickening fluid (STF) impregnated fabric composites. Mater Sci Eng A [Internet]. 2010 May 15 [cited 2019 Aug 6];527(12):2892–9. Available from: https://www.sciencedirect.com/science/article/abs/pii/S092150931000033X
38. ASTM G154–16. Standard Practice for Operating Fluorescent Ultraviolet (UV) Lamp Apparatus for Exposure of Nonmetallic Materials [Internet]. West Conshohocken, PA; 2016 [cited 2019 Aug 3]. Available from: https://www.astm.org/Standards/G154
39. Blum P. Reflectance spectrophotometry and colorimetry. In: Physical properties handbook. 1997. p. 1–11
40. Santos T, Santos C, Jose HO, do Nascimento AM, Medeiros I. Influence of silane coupling agent on shear thickening fluids (STF). In: Fangueiro R, editor. 1st world conference on advanced materials for defense [Internet]. Lisboa: TECMINHO; 2018. [cited 2020 Feb 24]. p. 223–4. Available from: https://www.researchgate.net/publication/329988638_Influence_of_Silane_Coupling_Agent_on_Shear_Thickening_Fluids_STF.
41. Santos TF, Santos CMS, Aquino MS, Ionesi D, Medeiros JI. Influence of silane coupling agent on shear thickening fluids (STF) for personal protection. J Mater Res Technol [Internet]. 2019; Available from: https://linkinghub.elsevier.com/retrieve/pii/S2238785419302315
42. Gürgen S. Numerical modeling of fabrics treated with multi-phase shear thickening fluids under high velocity impacts. Thin-Walled Struct [Internet]. 2020;148:106573. Available from: https://linkinghub.elsevier.com/retrieve/pii/S0263823119310122
43. Wang X, Zhang J, Bao L, Yang W, Zhou F, Liu W. Enhancement of the ballistic performance of aramid fabric with polyurethane and shear thickening fluid. Mater Des [Internet]. 2020;196:109015. Available from: https://linkinghub.elsevier.com/retrieve/pii/S0264127520305505
44. Li D, Wang R, Guan F, Zhu Y, You F. Enhancement of the quasi-static stab resistance of Kevlar fabrics impregnated with shear thickening fluid. J Mater Res Technol [Internet]. 2022;18:3673–83. Available from: https://linkinghub.elsevier.com/retrieve/pii/S223878542200552X
45. Zhou Y, Yao W, Zhang Z, Lin Y, Xiong Z, Zhao Y, et al. Ballistic performance of the structure-modified plain weaves with the improved constraint on yarn mobility: Experimental investigation. Compos Struct [Internet]. 2022;280:114913. Available from: https://linkinghub.elsevier.com/retrieve/pii/S0263822321013477
46. Tan Z, Li W, Huang W. The effect of graphene on the yarn pull-out force and ballistic performance of Kevlar fabrics impregnated with shear thickening fluids. Smart Mater Struct [Internet]. 2018;27(7):075048. Available from: https://iopscience.iop.org/article/10.1088/1361-665X/aaca4b
47. Gürgen S, Kuşhan MC, Li W. Shear thickening fluids in protective applications: A review. Prog Polym Sci [Internet]. 2017;75:48–72. Available from: https://linkinghub.elsevier.com/retrieve/pii/S0079670017300035
48. Wang L, Du Z, Fu W, Wang P. Study of mechanical property of shear thickening fluid (STF) for soft body-armor. Mater Res Express [Internet]. 2021;8(4):045021. Available from: https://iopscience.iop.org/article/10.1088/2053-1591/abf76a
49. Zhu D, Soranakom C, Mobasher B, Rajan SD. Experimental study and modeling of single yarn pull-out behavior of kevlar® 49 fabric. Compos Part A Appl Sci Manuf [Internet]. 2011 [cited 2018 Sep 29];42(7):868–79. Available from: https://www.sciencedirect.com/science/article/pii/S1359835X1100087X#f0005

50. Javaid MU, Jabbar A, Irfan M, Javed Z, Naeem MS, Militký J. Investigation of the stab resistance mechanism and performance of uncoated and SiO 2 coated high-performance aramid fabrics. J Text Inst [Internet]. 2021. 2;1–16. Available from: https://www.tandfonline.com/doi/full/10.1080/00405000.2021.1972630
51. Arora S, Majumdar A, Butola BS. Structure induced effectiveness of shear thickening fluid for modulating impact resistance of UHMWPE fabrics. Compos Struct [Internet]. 2019;210:41–8. Available from: https://linkinghub.elsevier.com/retrieve/pii/S0263822318321743
52. Hasanzadeh M, Mottaghitalab V. The role of shear-thickening fluids (STFs) in ballistic and stab-resistance improvement of flexible armor. J Mater Eng Perform [Internet]. 2014;23(4):1182–96. Available from: http://download.springer.com/static/pdf/647/art%253A10.1007%252Fs11665-014-0870-6.pdf?originUrl=http%3A%2F%2Flink.springer.com%2Farticle%2F10.1007%2Fs11665-014-0870-6&token2=exp=1493745372~acl=%2Fstatic%2Fpdf%2F647%2Fart%25253A10.1007%25252Fs11665-014-087
53. Gürgen S, Kuşhan MC. High performance fabrics in body protective systems. Mater Sci Forum. 2017;880:132–5.
54. Feng Y, Ma Y, Lei Z, Cao S, Fang Q, Li W, et al. Experimental study on yarn pullout test of STF modified fabric. IOP Conf Ser Mater Sci Eng [Internet]. 2018 [cited 2018 Sep 28];381(1):1–6. Available from: http://stacks.iop.org/1757-899X/381/i=1/a=012111?key=crossref.f3ffe30897d1c20a8a97160f9104ad17
55. Zarei M, Aalaie J. Application of shear thickening fluids in material development. J Mater Res Technol [Internet]. 2020 Sep;9(5):10411–33. Available from: https://linkinghub.elsevier.com/retrieve/pii/S2238785420315489
56. Molnár K, Virág ÁD, Halász M. Shear and yarn pull-out grip for testing flexible sheets by universal load machines. Polym Test [Internet]. 2020;82:106345. Available from: https://linkinghub.elsevier.com/retrieve/pii/S0142941819312796
57. Tian T, Nakano M, Li W. Applications of shear thickening fluids: a review. Int J Hydromechatronics [Internet]. 2018;1(2):238. Available from: http://www.inderscience.com/link.php?id=92733
58. Zhang X, Yan R, Zhang Q, Jia L. The numerical simulation of the mechanical failure behavior of shear thickening fluid/fiber composites: A review. Polym Adv Technol. 2022 Jan 1;33(1):20–33.
59. Silva AO da, Monsores KG de C, Oliveira S de SA, Weber RP, Monteiro SN, Vital H de C. Influence of gamma and ultraviolet radiation on the mechanical behavior of a hybrid polyester composite reinforced with curaua mat and aramid fabric. J Mater Res Technol [Internet]. 2020;9(1):394–403. Available from: https://linkinghub.elsevier.com/retrieve/pii/S2238785419305745
60. Monsores KG de C, Silva AO da, Oliveira S de SA, Rodrigues JGP, Weber RP. Influence of ultraviolet radiation on polymethylmethacrylate (PMMA). J Mater Res Technol [Internet]. 2019;8(5):3713–8. Available from: https://linkinghub.elsevier.com/retrieve/pii/S2238785419305861
61. Silva AO da, Monsores KG de C, Oliveira S de SA, Weber RP, Monteiro SN. Ballistic behavior of a hybrid composite reinforced with curaua and aramid fabric subjected to ultraviolet radiation. J Mater Res Technol [Internet]. 2018 [cited 2019 Aug 8];7(4):584–91. Available from: https://linkinghub.elsevier.com/retrieve/pii/S2238785418302163
62. Tang C, Li X, Li Z, Tian W, Zhou Q. Molecular Simulation on the Thermal Stability of Meta-Aramid Insulation Paper Fiber at Transformer Operating Temperature. Polymers (Basel) [Internet]. 2018;10(12):1348. Available from: http://www.mdpi.com/2073-4360/10/12/1348
63. Davis R, Chin J, Lin C-C, Petit S. Accelerated weathering of polyaramid and polybenzimidazole firefighter protective clothing fabrics. Polym Degrad Stab [Internet]. 2010 Sep;95(9):1642–54. Available from: https://linkinghub.elsevier.com/retrieve/pii/S0141391010002314

64. Żurowski R, Tryznowski M, Gürgen S, Szafran M, Świderska A. The Influence of UV Radiation Aging on Degradation of Shear Thickening Fluids. Materials (Basel) [Internet]. 2022;15(9):3269. Available from: https://www.mdpi.com/1996-1944/15/9/3269
65. Zhang Y, Wu Y, Chen M, Wu L. Fabrication method of TiO2–SiO2 hybrid capsules and their UV-protective property. Colloids Surfaces A Physicochem Eng Asp [Internet]. 2010 [cited 2018 Nov 5];353(2–3):216–25. Available from: https://www.sciencedirect.com/science/article/pii/S0927775709006669
66. Pechyen C, Atong D, Aht-Ong D. Effect of additives on mechanical properties and photo-stability of filament-wound glass fiber reinforced epoxy pipes. Polym Polym Compos [Internet]. 2011 [cited 2019 Oct 1];19(2–3):161–70. Available from: http://journals.sagepub.com/doi/10.1177/0967391111019002-317
67. Wang H, Xie H, Hu Z, Wu D, Chen P. The influence of UV radiation and moisture on the mechanical properties and micro-structure of single Kevlar fi bre using optical methods. Polym Degrad Stab. 2012;97:1755–61.
68. Chen C-Y, Yu C-A, Hong T-F, Chung Y-L, Li W-L. Contact and frictional properties of stratum corneum of human skin. Biosurf Biotribol [Internet]. 2015 [cited 2019 Aug 30];1(1):62–70. Available from: https://www.sciencedirect.com/science/article/pii/S2405451815000021

Chapter 6
Dynamic Compressive Behavior of Shear Thickening Fluid Based Composites

Z. P. Gu, X. Q. Wu, and C. G. Huang

6.1 Introduction

Materials with impact and explosive protection have drawn much interest. Numerous materials have been shown to exhibit good high impact resistance and energy absorption characteristics at high pressures and high strain rates, including porous foam metals [1, 2], ceramics [3], and granular materials [4, 5]. Due to their reversibly sensitive reactivity to external impact loadings, shear thickening materials, a subset of intelligent materials, have received considerable interest [6, 7]. Currently, shear thickening gel (STG) and shear thickening fluid (STF) are the two main categories of shear thickening materials [8, 9]. The STF and STG both exhibit excellent potential as impact resistant materials [10, 11]. STF is made from a high mass fraction of dispersed nanoparticles in liquid media; however, STG is a kind of gel-like boron siloxane polymer composite with a low cross-linking degree. In most cases, STF displays a fluid-to-solid transition in response to an external transient loading with a slightly low starting viscosity [12]. STF is hence typically more flexible at the original conditions [13, 14]. Moreover, it is appropriate for impact conditions since the dispersed nanoparticles are often rigid inorganic materials [15].

To explain the thickening characteristics of STF, various mechanisms have been proposed. Hoffman is the one who initially discovered the order-to-disorder transformation mechanism [16]. The hydro-cluster of STF particles is typically thought to cause the shear thickening that occurs during shear loading [17–19]. Dynamic

Z. P. Gu · X. Q. Wu (✉)
Key Laboratory of Mechanics in Fluid Solid Coupling Systems, Institute of Mechanics, Chinese Academy of Sciences, Beijing, China

School of Engineering Science, University of Chinese Academy of Sciences, Beijing, China
e-mail: wuxianqian@imech.ac.cn

C. G. Huang
Hefei Institutes of Physical Science, Chinese Academy of Sciences, Hefei, China

S. Gürgen (ed.), *Shear Thickening Fluid*, https://doi.org/10.1007/978-3-031-35521-9_6

solidification occurs under compression at high loading strain rates [15, 20]. During the thickening, a tremendous amount of energy is lost [21–25]. More significantly, STF exhibits reversible energy absorption characteristics and quickly returns to its initial state if loadings are removed [22, 26, 27]. The unique characteristics of STF have led to its widespread applications in shock absorbers, dampers, control mechanisms, etc. [28–30]. Due to the fluidic nature and sensitivity to the environment, STF should be adequately encapsulated in actual uses. Fabric composites were treated with STF by Gürgen et al. [30, 31] to increase their impact and stab resistance while maintaining their flexibility. The research by Gürgen et al. [32, 33] also demonstrated that the impact behavior of cork composites with STF joints was enhanced. In another work [34], researchers designed composite tubes with STF to suppress the vibrational loadings. To increase the dynamic impact protection capability of SPLTC, various fillers, including low-density polymers and ceramics, have been considered [35, 36]. Gürgen et al. [6], Fischer et al. [37], and Tan et al. [38] have investigated the vibration attenuation and penetration protection capabilities of sandwich constructions filled with STF. The findings demonstrated that the addition of STF significantly increased the structural capacity for shock absorption and penetration resistance.

SPLTC has attracted a lot of interest in the scientific community as one of advanced structural materials [39–41]. Numerous articles on the mechanical characteristics of SPLTC demonstrate that the device can release dynamic energy through various deformation patterns [42–47]. The use of SPLTC as a protective construction is, however, still constrained by its inadequate dynamic energy absorption capacity and rapid stiffness loss upon impact [40, 48]. Filling the SPLTC with lightweight materials has shown to be a realistic method for improving impact resistance and energy absorption. To increase the capacity of SPLTC's shock absorption ability, filling with STF has been studied [49]. The results revealed that the dynamic compressive strength of the SPLTC-STF is much higher than that of the SPLTC. To increase the impact resistance of SPLTC-STF, more research into the coupling processes of energy dissipation between SPLTC and STF under impact loadings is required. As a result, it is critical to model the SPLTC-STF's compression behavior. The parameters of the hydrodynamic constitutive model for STF are determined in this study. Analytically and numerically, the coupling energy dissipation mechanisms of the SPLTC-STF under dynamic compression are explored. Investigations are also conducted on how the STF rheology affects the impact response of SPLTC-STF.

This chapter is organized as follows: Sect. 6.2 presents the dynamic response of STF exposed to laser-induced impact in relation to temperature, pressure, and stress conditions. Section 6.3 presents the dynamic compressive performance of STF experimentally and numerically. The compressive behavior of SPLTC-STF at high strain rates is discussed experimentally and numerically in Sect. 6.4.

6.2 Dynamic Shock Response of STF

This section discusses the dynamic behavior of a spherical nanoparticle silica and polyethylene glycol based STF at high pressure loading by measuring the back-free surface velocities of targets made of aluminum and STF assembled structures. An experimental setup is used to have laser generated shock impact loadings. The dynamic characteristics of STF at various shock pressure loadings and temperatures are compared, and a discussion related to the experimental results is provided.

6.2.1 Experimental Method

As shown in Fig. 6.1, laser-induced shock experiments were used to study the dynamic responses of STF at high pressure loadings. These experiments included an in situ shock diagnostic system for measuring back-free surface velocities of samples. An absorption layer that has been bonded to a metallic target is exposed to a high power density laser beam in a standard laser generated shock process after passing through a transparent overlay sheet. Thin surface layer on the metallic target is heated. It quickly changes into a plasma state with high electron and ion densities that are contained between the transparent overlay and the remaining portion of the target [50–52]. The plasma pressure typically rises to several GPa in tens of nanoseconds before rapidly falling once the laser turns off due to its swift adiabatic expansion [51–55]. The laser power density can be changed to generate different peak pressures. While the laser-induced shock pressure spreads through the sample,

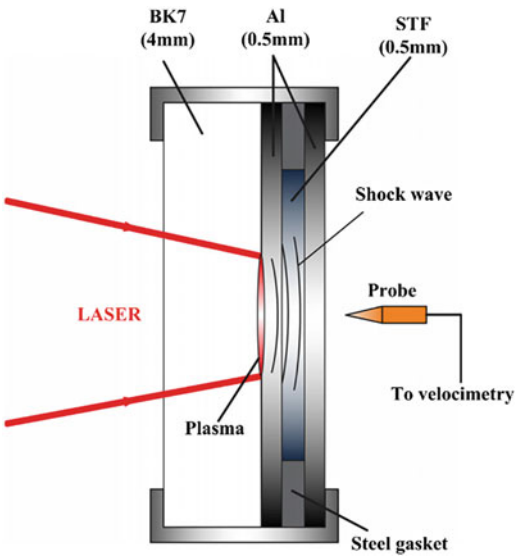

Fig. 6.1 Experiment setup in the laser-induced shock loading tests Ref. [21]

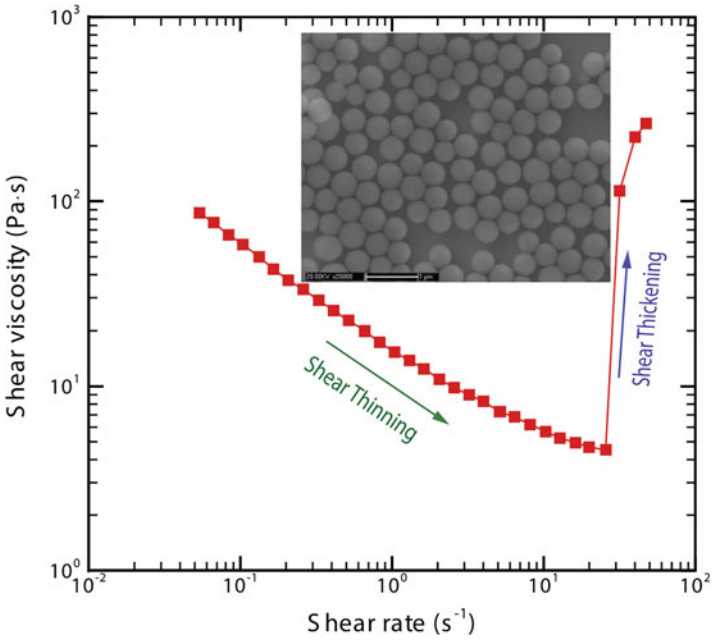

Fig. 6.2 Viscosity flow curve of the STF Ref. [24]

a PDV velocimeter measures the back-free surface velocity, which can be used to investigate the dynamic behavior of STF under different pressures, stress states, and temperatures. Laser and material interaction produces a pulse-loading wave with an amplitude of several GPa and a lifetime of tens of nanoseconds.

Spherical silica nanoparticle and polyethylene glycol suspension were used in the STF by keeping the particle volume fraction at 57 vol%. By using a hand mixer and an ultrasonic disperser, the silica nanoparticles were dispersed in the carrier liquid. The densities of polyethylene glycol and silica nanoparticles were 1.13 g/cm^3 and 1.95 g/cm^3, respectively. The silica nanoparticles had a sound velocity of 5870 m/s, while the bulk modulus of polyethylene glycol is 3.05 GPa, thereby resulting in a sound velocity of 1650 m/s. Plotted in Fig. 6.2 was the steady state shear viscosity of the STF at shear rates from 0.5 s^{-1} to 50 s^{-1} determined by a Kinexus Pro+ rheometer with a 40 mm and 4° cone and plate apparatus. As seen by the abrupt increase in shear viscosity, the STF displayed a shear thinning regime followed by a drastic shear thickening behavior at a shear rate of roughly 25 s^{-1}.

The target was assembled with two AA2024 plates having a diameter of 25.4 mm while containing a layer of STF between the plates. Each laser irradiated surface on the targets was adhered with 40 μm of aluminum foil as an absorption film and tightly contained by 4 mm of BK7 glass. A Q-switched high power Nd:YAG pulse laser operating at a wavelength of 1064 nm was employed in the tests. A two-step amplification system was utilized to generate the maximum output energy of 2.5 J per laser shot. The laser pulse has a near Gaussian temporal profile with a full width

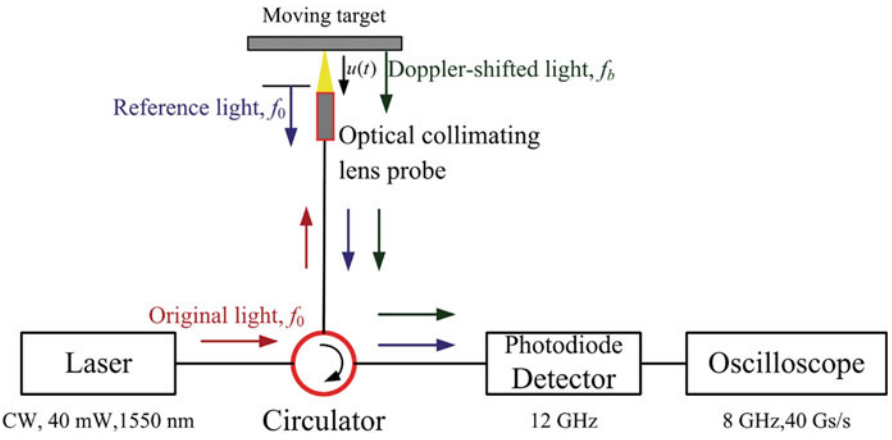

Fig. 6.3 PDV configuration: red, blue, and green arrows indicate the original, reference, and Doppler-shifted lights, respectively Ref. [24]

at half maximum (FWHM) of roughly 10 ns. The spatial pattern of the laser pulse is modified to have a basically flat shape. The incident laser beam was concentrated using a 600 mm optical focusing lens to create the necessary shock diameter. As shown in Fig. 6.3, the back-free surface velocity of the constructed target was measured using a photonic Doppler velocimetry (PDV) setup that essentially matches with the study by Strand et al. [56]. The PDV comprises an oscilloscope (WaveMast), an optical collimating lens probe with back reflection (−13 dB), and a work distance of 16 mm. The PDV also includes a high power 1550 nm CW distributed feedback laser (CQF938 series, provided by JDS Uniphase Corporation) with a polarization-maintaining fiber that operates at a maximum power of 0.04 W with a linewidth of about 0.2 MHz. The probe gives the reference light with frequency f_0 and collects the Doppler-shifted light with frequency f_b reflected from the moving surface of interest. The probe is linked to the first port of the circulator, while the laser and detector are connected to the circulator's second and third ports.

The difference between two frequencies, $f_{beat} - f_0$, represented by f_b yields the velocity of the observed surface of the target, denoted by $v(t)$ as given in Eq. 6.1:

$$v(t) = \frac{\lambda_0}{2} f_b(t) \tag{6.1}$$

where λ_0 represents the original wavelength of the CW laser (in the present study, λ_0=1550 nm). The temporal domain of the Nd:YAG laser coupled to a Si-biased detector initiates the observations in laser-induced shock investigations. As seen in Fig. 6.4, a shock wave with a maximum pressure of p_m propagates through a sample, with a proportion of the shock wave reflecting as a consequence of the impedance mismatch between the plate and the STF. The remaining wave eventually passes through the whole sample and reaches the back surface of the plate at the right side, where it generates the first peak velocity v_m. Due to the

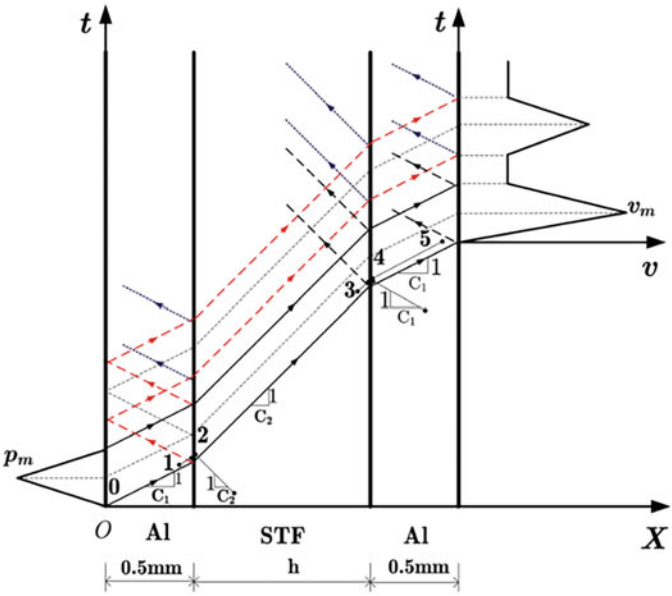

Fig. 6.4 Wave reflections in the target Ref. [24]

numerous wave reflections in the target, the subsequent peak velocities that are distinct from the first peak will also reach the rear-free surface. To demonstrate the analysis approach, simply the elastic waves of the aluminum plates, represented by a wave speed C_1, and a constant wave speed of the STF, denoted by C_2, are provided in Fig. 6.4. When the stress surpasses the Hugoniot elastic limit (HEL) of the AA2024 plate, the actual investigation employs the plastic wave speed. With the first peak velocity measurement data, the dynamic behavior of the STF was examined using a characteristic analysis [24]. Following is a description of the experimental process and analytic steps. First, the back-free surface velocity, v_{free1}, is measured to determine the stress at the point 1, designated by σ_1. The Rankin-Hugoniot relations [24] show that while σ_1 is less than HEL,

$$\sigma_1 = -\frac{1}{2}\rho_0 C_e v_{\text{free1}} \tag{6.2}$$

While σ_1 is higher than HEL,

$$\sigma_1 = \rho_0\left(C_0 + S\cdot\frac{1}{2}v_{\text{free1}}\right)\cdot\frac{1}{2}v_{\text{free1}} + \frac{2}{3}Y_0 \tag{6.3}$$

where $\rho_0 = 2.77$ g/cm^3 is the initial density of the plate, $C_e = 6.41$ km/s is the velocity of the elastic wave in the plate, $C_0 = 5.33$ *km/s* is sound velocity at zero pressure, $S = 1.34$ is empirical material parameter, $Y_0 = 265$ MPa is yield stress, and

$H_0 = (1 - v)Y_0/(1 - 2v) = 547$ MPa [24]. The stress of the STF near the left plate (point 2) was estimated as

$$\sigma_2 = -\frac{(\rho c)_{\mathrm{STF}} \cdot (\rho c)_{\mathrm{Al}}}{(\rho c)_{\mathrm{Al}} + (\rho c)_{\mathrm{STF}}} v_{\mathrm{free1}} \tag{6.4}$$

where $(\rho c)_{\mathrm{STF}}$ and $(\rho c)_{\mathrm{Al}}$ denote the STF and AA2024 wave impedances, respectively.

The surface velocity of the assembled target, which includes a thin layer of STF and the right AA2024 plate, is then measured and is represented by the notation v_{free2}. While the stress is smaller than HEL, point 5 stress is calculated as

$$\sigma_5 = -\frac{1}{2}\rho_0 C_e v_{\mathrm{free2}}. \tag{6.5}$$

While σ_5 exceeds HEL,

$$\sigma_5 = \rho_0 \left(C_0 + S \cdot \frac{1}{2} v_{\mathrm{free2}}\right) \cdot \frac{1}{2} v_{\mathrm{free2}} + \frac{2}{3} Y_0 \tag{6.6}$$

The stress at point 4 is determined using an empirical attenuation law of stress in AA2024 plate [51] because the wave will decay in the correct plate. Stress at point 4 is indicated by σ_5:

$$\frac{\sigma_5}{\sigma_4} = 0.67 \exp\left(-\frac{H/2R}{0.71}\right) + 0.25 \exp\left(-\frac{H/2R}{0.12}\right) + 0.09 \tag{6.7}$$

The stress at point 3 is determined as

$$\sigma_3 = -\frac{(\rho c)_{\mathrm{Al}} + (\rho c)_{\mathrm{STF}}}{2} v_4 \tag{6.8}$$

The thickness of STF between AA2024 plates was adjusted as 0.5 mm for shock studies. In order to generate the different laser power densities and, therefore, different shock pressures, radius and incident energy of the Nd:YAG laser were varied. It should be noted that the 2D effect, in which the shock wave changed from a uniaxial strain condition to a dilatation state while propagating through the STF layer, would be apparent for a tiny laser shock radius [57, 58]. The measured back-free surface velocities of targets in this research included the bulk compressive response and the shear effect of the STF during laser produced shock waves. Furthermore, on the result of the PDV measurements, studying the shock wave impact resistance of STF is possible. Therefore, the shock wave impact resistance of STF was estimated using the nominal impact resistance, IR_{STF}, which was described as

$$IR_{\mathrm{STF}} = \frac{\sigma_{1\_\mathrm{Peak}} - \sigma_{4\_\mathrm{Peak}}}{\sigma_{1\_\mathrm{Peak}}} \times 100\% \tag{6.9}$$

where σ_{1_Peak} is the peak stress of σ_1 at the left side of AA2024 surface and σ_{4_Peak} is the peak stress of σ_4 at the right side of AA2024 surface.

6.2.2 Experimental Results

First, without using the STF specimen and the right side of AA2024 plate, the back-free surface velocities, v_{free1}, of the left side AA2024 plate at various shock pressures were directly measured to determine the stress, σ_1, at point 1, as shown in Fig. 6.4. The measured observations for the shock diameter of 3.62 mm at varied shock pressures are shown in Fig. 6.5. With increasing shock pressure, it was found that the peak velocity raised and the shock duration dropped. It was found that when shock pressure increased, the peak velocity raised, and the shock duration fell. The initial peak velocity quickly climbed from approximately 122 m/s to 372 m/s with a rise in shock pressure from 2.59 GPa to 3.82 GPa, but the shock duration – defined as the increasing duration, T, as shown in Fig. 6.5 – declined from 53.2 ns to 23.6 ns. It should be noted that the shock loading pressures for various laser power densities were computed using a previously published coupling model [51] in which the laser-

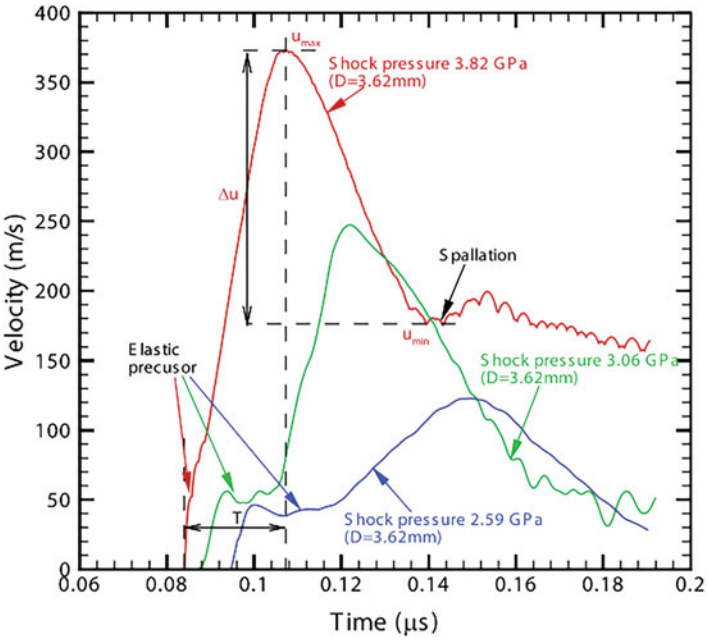

Fig. 6.5 Measured observations for shock pressures of 2.59 GPa, 3.06 GPa, and 3.82 GPa Ref. [24]

induced heat plasma's rapid expansion and the sample's dynamic deformation were examined. Additionally, it was found that the elastic precursor wave induced plateau's duration grew as shock pressure decreased, indicating that the velocity of the plastic wave decreased as shock pressure decreased. The initial AA2024 plate experienced back-free velocities from the elastic predecessors of around 58 m/s. The maximum velocity induced by the elastic precursor, u_{H_max}, could be calculated for the uniaxial strain state using the Rankin-Hugoniot relations [24] as

$$u_{H\_\max} = \frac{\sigma_{\mathrm{HEL}}}{\rho_0 C_e} \tag{6.10}$$

where σ_{HEL} is the HEL for AA2024 plate. According to Eq. 6.10, the highest velocity induced by the elastic precursor wave is approximately 30.8 m/s, which is almost half of the experimentally observed speeds induced by the elastic precursor wave at the free surface of AA2024 plate. Additionally, upon being shocked at a pressure of 3.82 GPa, the spallation of the plate was seen. The following formula 6.is employed to calculate the spall strength:

$$\sigma_{\mathrm{spall}} = \frac{1}{2}\rho_0 C_0 \Delta u \tag{6.11}$$

where $C_0 = \sqrt{E/3(1-2v)\rho_0}$ denotes bulk wave velocity and Δu denotes pullback speed, as seen in Fig. 6.5, specified as the difference between the greatest and minimum velocities of the spallation signal. According to Eq. 6.11, AA2024 has a spall strength of roughly 1.40 GPa, similar to the results of Rosenberg et al. [59].

The back-free surface velocity of the right side AA2024 plate, v_{free2}, was measured at temperature of 21 °C, as shown in Fig. 6.6. The thickness of STF between the plates is around 0.5 mm. Various shock pressures were achieved with a shock diameter of 3.62 mm by varying the input laser intensity. Be aware that the unfinished interfering fringes caused by the elastic predecessors should be attributed to the modest initial variation in the observed values at a shock loading pressure of 3.82 GPa. A full interference fringe will be produced for the PDV measurement, as shown in Fig. 6.3, once the observed surface has moved half the wavelength of the CW laser. However, under some circumstances, a complete interference fringe cannot be acquired while measuring low velocity with a short duration such as elastic precursor. This complicates the interpretation of measured data when determining the frequency of the uncompleted interfered fringes and introduces some mistakes in testing the elastic precursor. The PDV system performed effectively in measuring the particle velocity profiles. A tiny variation in measured results with a shock pressure of 3.06 GPa should be attributed to the slight variation in STF layer thicknesses brought on by uncontrolled elastic deformation of the stainless steel gasket while tightly clamping the constructed samples, as was the case in the prior investigation. The shock wave velocity decreased with the lowering of shock pressure and the arrival time increased [21]. The similar Grüneisen equation of state (EOS), $U_S = C_0 + SU_p$, could be used to explain the link between

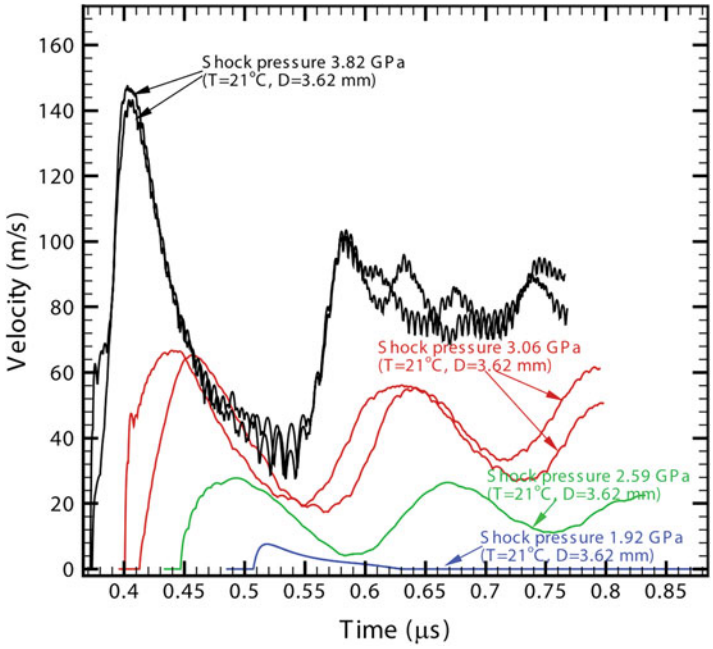

Fig. 6.6 Back-free surface velocity of the right side AA2024 plate Ref. [24]

particle velocity and shock velocity in STF [24]. The shock response of STF at temperatures around 21 °C can be described by the Grüneisen EOS parameters of $C_0 = 2.05$ mm/μs and $S = 5.324$, which results in a higher shock velocity at a higher shock pressure as seen in Fig. 6.6. Additionally, with the shock pressure dropping from 3.82 GPa to 1.92 GPa, the first peak velocities rapidly reduced from around 145 m/s to about 8 m/s.

Figure 6.7 shows the measured v_{free2} with a layer of STF with a thickness of 0.5 mm at 21 °C and varying shock pressures by altering the focused laser radius and maintaining nearly identical maximum incident laser energies. As the shock pressure climbed from 3.82 GPa to 4.70 GPa, and the shock loading diameter decreased from 3.62 mm to 2.94 mm, it was evident that the first peak velocity marginally increased from 145 m/s to 150 m/s. Nevertheless, the initial peak velocity quickly dropped to 82 m/s as the shock pressure increased to 5.38 GPa and the shock diameter reduced to 2.56 mm. It should be observed that while propagating through a relatively thick STF specimen, the shock wave will change from a one-dimensional condition (a uniaxial strain stress wave) to a three-dimensional state (a dilatational stress wave) [58].

When the aforementioned uniaxial strain and the dilatational stress waves propagate in the STF layer, the bulk viscosity during compression and the shear viscosity during dilatation could clearly have dragging effects. The stress wave may be regarded as a uniaxial strain stress wave for shock diameters of 3.62 mm and

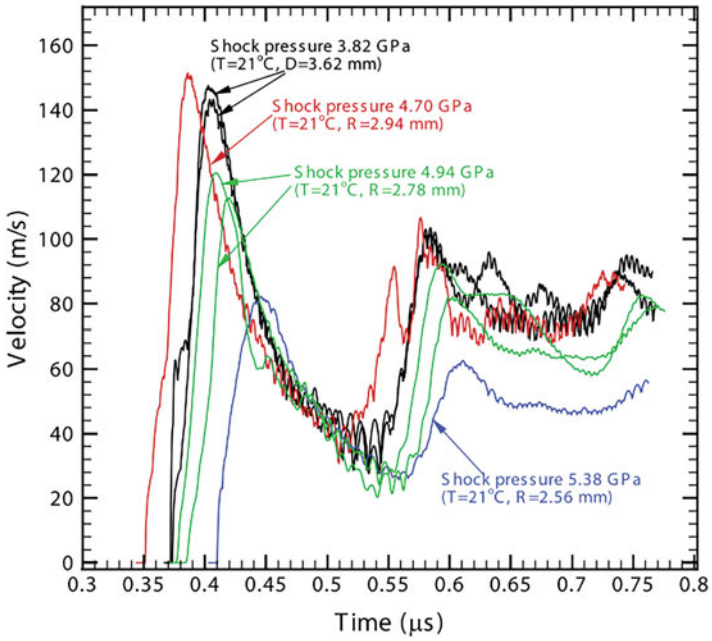

Fig. 6.7 Measured back-free surface velocities of the right side plate with a layer of STF at 21 °C Ref. [24]

2.94 mm since those shock radii were almost equivalent to or larger than the integrated Al-STF-Al thicknesses of samples of 1.50 mm. As a result, only the bulk viscosity served as a dragging mechanism while shock waves propagated, which caused the initial peak velocity to increase as shock pressure increased from 3.82 GPa to 4.70 GPa as seen in Fig. 6.7. However, in addition to the bulk viscosity, the shear viscosity also contributed to the dragging effect during the propagation of shock waves with a 2.56 mm starting shock diameter. When comparing the results at a shock pressure of 4.70 GPa and a shock diameter of 2.94 mm, the initial peak velocity declined dramatically, leading one to hypothesize that the shear viscosity-induced dragging effect in the STF was stronger than the bulk viscosity-induced dragging effect.

In Fig. 6.8, the measured velocities, v_{free2}, for various STF thicknesses is displayed at 21.0 °C and 27.2 °C. With an increase in STF layer thickness from 0.12 to 1.5 mm, the initial peak velocity quickly fell from around 207 m/s to almost 38 m/s. The slight variation in back-free velocity for the same STF thickness testing was attributed to the sample's uncontrolled elastic deformation during the constructed clamping. As the STF layer thickness was increased while exceeding 1.5 mm, the initial peak velocity decreased relatively gradually. Additionally, the results of the tests conducted at 21.0 °C and 27.2 °C did not obviously differ from one another, save from the tests with a thickness of roughly 2 mm. The steel gasket's

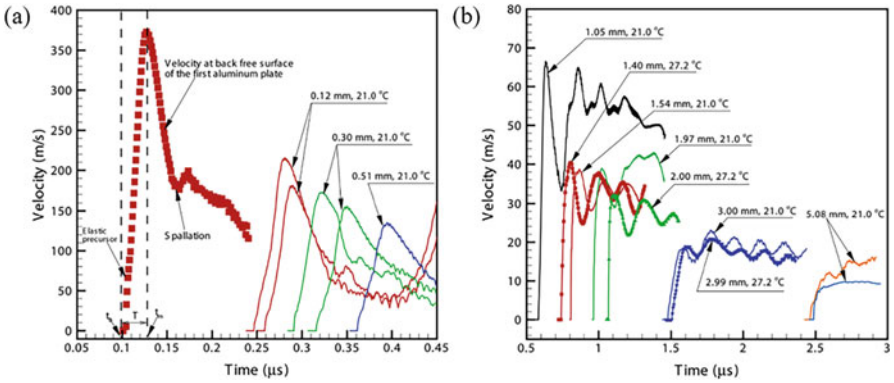

Fig. 6.8 (**a**) Particle velocities at the left side single AA2024 plate's back-free surface and particle velocities at the right side AA2024 plate's back-free surface for a thin layer coating of STF varied in thickness from 0.12 to 0.51 mm at 21.0 °C and (**b**) particle velocities for layers of STF with thicknesses ranging from 1.0 mm to 5.0 mm at 21.0 °C and 27.2 °C Ref. [21]

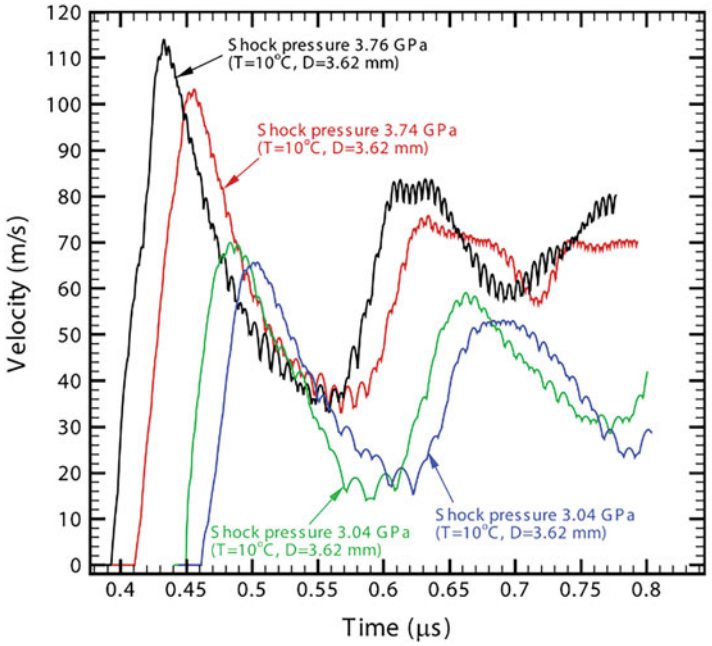

Fig. 6.9 Back-free surface velocities with a layer of STF having a thickness of 0.5 mm at 10 °C Ref. [24]

elastic deformation during the assembly of the target is likely the cause of the relatively high peak velocity seen for the STF layer thickness of 1.97 mm at 21.0 °C.

Figure 6.9 shows the measured v_{free2} with a layer of STF having a thickness of 0.5 mm at 10 °C and varying shock pressures at the focused laser diameter of 3.62 mm by altering maximum incident laser energies. The modest variation in

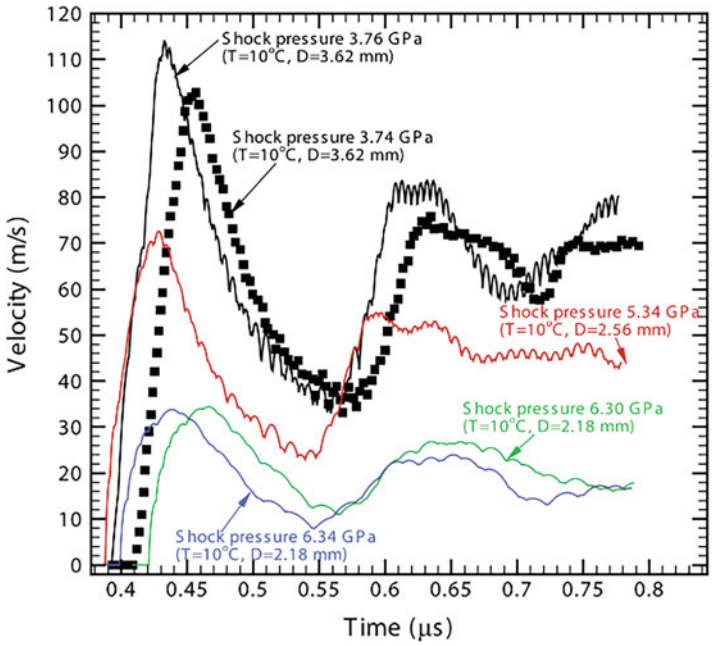

Fig. 6.10 Back-free surface velocities of the layer of STF having a thickness of 0.5 mm at 10 °C Ref. [24]

experiment results at the same shock pressure was also attributed to the slight variation in STF targets brought on by the uncontrolled elastic deformation of the gasket when clamping the constructed specimens [21]. Similar to the experimental results at 21 °C, when shock pressure declined, the arriving time increased, and the shock wave velocity reduced. Additionally, with the shock pressure dropping from 3.76 GPa to 3.04 GPa, the first initial velocity dropped quickly from around 108 m/s to approximately 68 m/s.

Figure 6.10 shows the recorded v_{free2} with a layer of STF having a thickness of 0.5 mm at 10 °C and varying shock pressures by altering the focused laser radius and maintaining nearly identical maximum incident laser energies. The arrival time of the shock wave depended on shock pressures and radius because the bulk viscosity effect and shear viscosity effect existed in the STF layer when shocked at a relatively small initial shock radius. The unclear trend of arriving time while raising shock pressure and decreasing shock diameter resulted from the influences of bulk viscosity and shear viscosity. As shock pressure increased from 3.75 GPa to 6.30 GPa and shock diameter fell from 3.62 mm to 2.18 mm, it was also noticed that the initial peak velocity rapidly decreased from around 110 m/s to approximately 34 m/s. The rapid drop in particle velocities for relatively small shock diameters may be attributed to the shear viscosity-induced dragging effect during the propagation of shock waves, as the shear viscosity was evident for the experiments with shock diameters of 2.18 mm and 2.56 mm.

6.2.3 Discussion and Summary

By measuring the back-free surface particle velocities of the targets, the current work studied the dynamic behavior of STF under laser produced shock at varying temperatures, shock pressures, and stress states. The summary of velocities of the right side AA2024 plate with a 0.5-mm-thick layer of STF at 10 °C and 21 °C and varying shock pressures and radius are shown in Fig. 6.11. Except for the tests that were done at shock pressures of roughly 3.05 GPa and shock diameters of 3.62 mm, an apparent temperature effect was seen in the studies. Commonly, Arrhenius's law governs the relationship between temperature, T, and the viscosity of a fluid, η as,

$$\eta(T) = \eta_{\text{int}} \exp\left(\frac{E}{RT}\right) \tag{6.12}$$

where η_{int}, R, and E are variables linked to material viscosity [24]. Assume that the STF's temperature-viscosity relationship likewise matches with the Arrhenius law. The viscosity of STF decreases with decreasing temperature according to Eq. 6.12. The initial peak velocity increases dramatically with increasing temperature from 10 °C to 21 °C at a shock diameter of 3.62 mm and shock pressures in the region of 3.74 GPa to 3.82 GPa. However, when the shock pressure is reduced to roughly 3.05 GPa, the measurements at 21 °C and 10 °C at the same shock diameter of

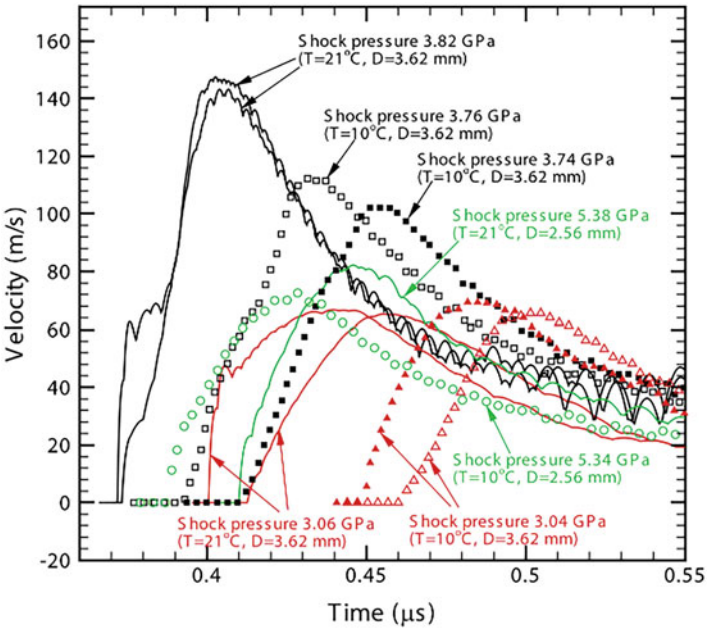

Fig. 6.11 Velocities in the right side AA2024 plate with a 0.5-mm-thick layer of STF at 10 °C and 21 °C Ref. [24]

3.62 mm are nearly identical to one another. It is the bulk viscosity of STF that principally contributes to the attenuation response of shock waves, particularly when shock waves are subjected to a shock incident at a diameter of 3.62 mm. The bulk viscosity of the STF is significantly higher at test temperatures of 10 °C than 21 °C for shock pressures in the region of 3.74 GPa to 3.82 GPa. The shock pressure is nearly the same as the test temperature of 21 °C at pressures of roughly 3.05 GPa. The response of STF during the laser-induced shock that causes compression induced thickening should be attributed to the explanation. According to the research of Waitukaitis and Jaeger [20], when a rod directly strikes the STF, the suspended nanoparticles are driven to cross the jamming transient, resulting in a quickly developing impact-jammed solid by the compression of the particle matrix. The laser-induced shock might also cause an impact-induced jamming response, which would then quickly reduce the stress by defeating the short range hydrodynamic lubricating force between the nanoparticles in STF. The thickening responses would result in an enormous increase in the bulk viscosity of STF. Suppose that the impact-induced thickening exhibits a response for shear thickening that is comparable as

$$\eta_{\text{compression}} = \eta_0^{\text{bulk}}(T)\dot{\varepsilon}^{\alpha}. \tag{6.13}$$

At temperature T, the initial bulk viscosity is $\eta_0^{\text{bulk}}(T)$. The strain rate of compression is $\dot{\varepsilon}$. The exponent of impact-induced thickening is α. According to Eq. 6.13, after the occurrence of the thickening responses caused by the shock loading, the temperature influence on the STF's bulk viscosity would have been magnified by several orders of magnitude. The compression induced thickening characteristic of the STF only becomes apparent at shock pressures higher than 3.74 GPa and not at shock pressures lower than 3.06 GPa, according to this study. The earlier research [20, 60–64] showed that essential features, like a minimum strain, were necessary for the thickening characteristic in STF. When particle velocities are at relatively low values, it is possible that a minimum strain will not be attained in several tens of nanoseconds to cause the impact-induced jamming characteristic of the STF. For example, the experiments at test temperatures of 10 °C and 21 °C, with shock pressures of approximately 3.05 GPa and a shock diameter of 3.62 mm, produced nearly comparable test results.

Additionally, it has been found that the stress state greatly influences the dynamic behavior of the STF at various shock diameters, which results in a reduction in initial peak velocity while concurrently dropping shock diameter and raising shock pressure. The shock attenuation response of STF is dependent on both the shear viscosity and the bulk viscosity for tiny shock diameters. Typically, the shear thickening characteristic of STF could well be defined as

$$\eta_{\text{shear}} = \eta_0^{\text{shear}}(T)\dot{\gamma}^{\beta} \tag{6.14}$$

At temperature T, the initial bulk viscosity is $\eta_0^{\text{shear}}(T)$. The strain rate of shear is $\dot{\gamma}$. The exponent of shear induced thickening is β. As a result, once the shear

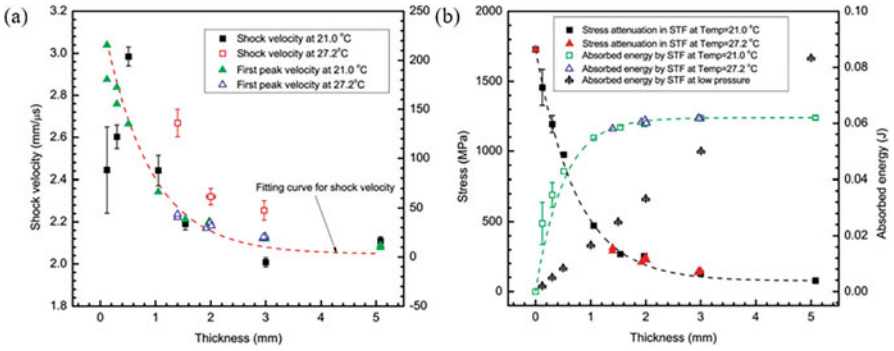

Fig. 6.12 (**a**) Average shock velocities along the STF at 21 °C and 27.2 °C and (**b**) energy absorbed in the STF Ref. [21]

thickening response begins, the shear viscosity of STF increases dramatically. This increase can be enhanced by several orders of magnitude due to the temperature effect. Therefore, at a relatively modest shock diameter of 2.56 mm, the initial peak velocities abruptly decreased, and an apparent temperature effect was observed. The experiments, which were conducted at 21 °C and 27.2 °C while the STF layer thickness was thicker than 1.5 mm, revealed that the observed back-free particle velocities of the target were nearly equal. The shock wave would change from a uniaxial strain stress wave to a dilatation wave after traveling a given distance in the STF targets as thick layers of STF were obtained. As a result, the impact-induced jamming effect would be seen around the shock surface, followed by the shear induced thickening effect once the shock wave has transmitted into a specific thickness in STF. Nevertheless, the impact and shear induced thickening characteristic ought to diminish once the shock waves have traveled a reasonable distance due to the conditions that generate thickening. The inability to meet requirements, such as minimal stress and strain, resulted in a stress and energy absorption response that was almost saturation-like and had negligible effect on temperatures [21].

Figure 6.12a shows the average shock velocities at 21 °C and 27.2 °C along the thickness of the STF. With increasing the thickness of the STF layer, the average shock velocities fell dramatically. The peak stress reduced dramatically when the STF thickness was increased from 1.73 GPa to roughly 68 MPa. Figure 6.12b shows the corresponding energy absorption characteristic of STF and the energy absorption performance at pressures between 36 MPa and 48 MPa. The average absorbed energy per unit volume calculated by Jiang et al. [22] was used to estimate the equivalent absorbed energy with varied STF thicknesses. When the STF thickness was increased for a layer of STF smaller than 1 mm, the absorbed energy increased quickly compared to the energy absorption characteristic at relatively low pressure. Energy absorption and stress attenuation saturation were seen when the STF was thicker than 2 mm.

There are three causes for the quick rise in energy absorption in the thin STF layer. One illustration is how the STF responds to shock by jamming on impact.

According to the research of Waitukaitis and Jaeger [20], when a rod directly strikes the STF, the suspended nanoparticles are driven to cross the jamming transient, resulting in a quickly developing impact-jammed solid by the compression of the nanoparticle matrix. During laser shock, the impact-induced jamming phenomenon might also occur, which would cause energy to be lost by defeating the short range hydrodynamic lubricating force between the nanoparticles in the STF. The second possibility is the deformation or cracking of hard-sphere nanoparticles after impact following jamming development. The third factor would be the volume compressibility of polyethylene glycol and hard spherical nanoparticles under high pressure, which causes additional energy loss. The shock pressure and particle velocity drop relatively low once the shock wave has traveled a specified sum through the STF. By defeating the short range hydrodynamic lubricating force between the particles, energy dissipation moves considerably more slowly. Additionally, the volume compressibility of the nanoparticles and the polyethylene glycol in STF and the deformation or crack of the hard-sphere nanoparticles might be disregarded.

With a constant shock diameter of 3.62 mm and test temperatures of 10 °C and 21 °C, Fig. 6.13 shows the relationship between incident peak stress, denoted by $\sigma_{1\ \_\ Peak}$, and matching transmitted peak stress, denoted by $\sigma_{2\ \_\ Peak}$. It has been found that for both temperatures of 10 °C and 21 °C, the transmitted peak stress rises as the incident peak stress rises. Nevertheless, compared to incident peak stress, the growing velocity of transmitted peak stress at 10 °C is substantially slower than at 21 °C. At the greatest incident peak stress, i.e., at a shock pressure of around 3.80 GPa, the transmitted peak stress at 10 °C is substantially lower than that at 21 °C due to the reduced bulk viscosity of the STF layer at the lower temperature after the occurrence of impact-induced thickening response. The transmitted peak stresses are practically the same for tests conducted at experimental temperatures of 10 °C and 21 °C because the compression induced thickening characteristic of STF may not occur at a shock pressure of roughly 3.05 GPa. The relationship between the incident and transmitted peak stresses for the experiments at temperatures of 10 °C and 21 °C should follow the same tendency even if the shock pressure is less than 3.05 GPa. According to Eq. 6.9, the nominal impact resistances, IR_{STF}, of the STF layer with a thickness of 0.5 mm at the experimental temperature of 21 °C are 43.67%, 48.73%, and 50.46% for shock pressures of 2.59 GPa, 3.05 GPa, and 3.80 GPa, respectively. In comparison, at the experimental temperature of 10 °C, they are 44.24% and 53.02% for shock pressures of 3.05 GP. The STF layer, measuring 0.5 mm thick, demonstrated significant impact resistance at high shock pressure at both experimental temperatures of 10 °C and 21 °C. However, a relatively small temperature range was investigated to examine the impact of temperature on the dynamic response of STF under laser-induced shock. The dynamic mechanical properties of STF over a wider temperature range need more experiments to investigate. Furthermore, when shocked at relatively small diameters, both uniaxial and dilatational waves appeared in the tests, making it hard to separate the effects of temperature pressure and shear.

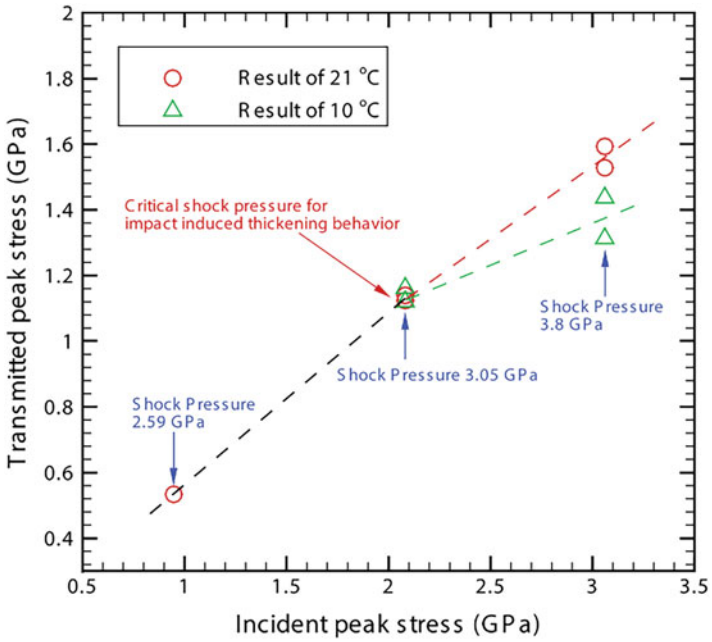

Fig. 6.13 Relationship between incident peak stress and transmitted peak stress at 10 °C and 21 °C Ref. [24]

6.3 Dynamic Compressive Behavior of STF

Understanding the dynamic behavior of STF is necessary to perform the modeling and simulation analysis on the compression performance of the STF. In this section, firstly, a hydrodynamic constitutive model and analytical model of STF are developed. Then, the dynamic compressive experiments of STF are performed. Finally, the numerical model representing the compressive behavior of the STF is constructed.

6.3.1 Hydrodynamic Constitutive and Analytical Model of STF

The hydrostatic behavior of STF under compression and the vicious behavior of STF under shear loads can both be explored via the dynamic constitutive equation. Here, the dynamic compressive and shearing response of the STF is described using a hydrodynamic constitutive model [21, 24, 49]. The squeezing characteristic of the STF is explored using the squeezing hydrological model for a non-Newtonian fluid layer. The hydrostatic behavior of STF under compression and the vicious behavior

of STF under shear loads can both be explored via the dynamic constitutive equation [65]. With an increase in shear strain rate, the STF's dynamic shear viscosity varies considerably. The hydrostatic pressure and the volumetric compressibility of STF are not linearly related. As a result, the stress, σ_{ij}, applied to the STF is divided into hydrostatic pressure, p, and deviatoric stress, S_{ij}:

$$\sigma_{ij} = -p\delta_{ij} + s_{ij}, \tag{6.15}$$

where δ_{ij} is the function of Kronecker.

The strain of STF, e_{ij} is

$$e_{ij} = \frac{1}{3}e_{ii}\delta_{ij} + \varepsilon_{ij}, \tag{6.16}$$

where e_{ii} is volumetric strain and ε_{ij} is deviatoric strain.

Therefore, the strain rate is

$$\frac{de_{ij}}{d\mathrm{t}} = \frac{1}{3V}\frac{dV}{dt}\delta_{ij} + \frac{d\varepsilon_{ij}}{dt}, \tag{6.17}$$

where the specific volume is V.

The shear strain rate, $\dot{\varepsilon}_{ij}$, determines the dynamic viscosity of the STF, μ_{ij}, [65]:

$$\mu_{ij} = m \cdot \dot{\varepsilon}_{ij}^{n-1}, \tag{6.18}$$

where m and n are material parameters of STF. The deviatoric stresses are then calculated using

$$s_{ij} = \mu_{ij} \cdot \dot{\varepsilon}_{ij} = m \cdot \dot{\varepsilon}_{ij}^{n}. \tag{6.19}$$

The Mie-Grüneisen equation of state [66, 67] is used to characterize the hydrostatic response of the STF.

Similar to Petel et al. [68, 69], the Mie-Grüneisen EOS [66, 67] is used to describe the hydrostatic behavior of the STF:

$$U_s = C_0 + S \cdot U_p, \tag{6.20}$$

where U_s is shock wave velocity and U_p is particle velocity, C_0 is shock wave velocity at zero stress state, and S is the material parameter [68, 69].

In the above studies, laser-induced shock tests were used to obtain the material parameters, C_0 and S, of STF:

$$U_s = 2.050 + 5.324U_p, \tag{6.21}$$

where the unit of U_s and U_p are km/s.

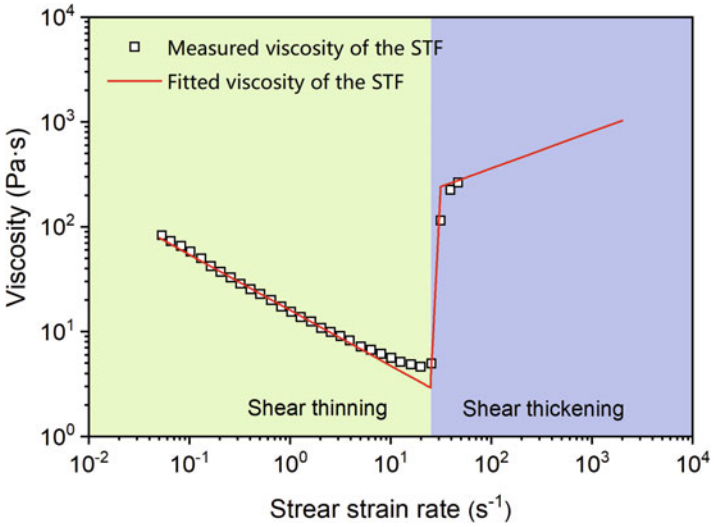

Fig. 6.14 Thinning and thickening characteristics of STF in numerical simulations Ref. [49]

It is possible to acquire the values of m and n in Eq. 6.18 by fitting the results of the experiments. The above study investigated the steady state shear viscosity of the 57% silica particle in polyethylene glycol based STF [49]. As shown in Fig. 6.14, the measured and fitted viscosity of the STF is performed. The viscosity of the STF initially declines gradually with an increase in shear strain rate, signifying the shear thinning regime. It is followed by a rapid increase, which marks the beginning of the shear thickening regime. It must be highlighted that the rotational rheometer's limitations prevent the complete measurement of the viscosities of the STF in the shear thickening regime at shear rates greater than 47 s^{-1}. According to Fig. 6.14, the shear thinning regime, where shear rates are less than 25 s^{-1}, has $m = 16$ and $n = 0.47$. When shear thickening occurs, the viscosity of the STF increases dramatically, making it challenging to obtain the viscosity of the STF in the shear thickening domain at a high shear rate. Based on the experimental findings and the fluid-structure interaction (FSI) simulation, the shear strain rate dependent viscosity of STF in the shear thickening domain is determined in the current work. The following modeling and numerical analysis sections explain the FSI simulation in more detail.

A non-Newtonian fluid layer squeezing flow model was formulated. As depicted in Fig. 6.15, assume that two circular plates with radii of R compress a non-Newtonian fluid layer with a thickness of h.

The fluid layer moves according to the following equations, which are based on the assumption that the flow is two-dimensional [70]:

$$\frac{\partial^2 u}{\partial y^2} = \frac{1}{\mu}\frac{\partial p}{\partial r} + \frac{\rho}{\mu}\left(\frac{\partial u_0}{\partial t} + u_0\frac{\partial u_0}{\partial r} + v_0\frac{\partial u_0}{\partial y}\right) - \left(\frac{\partial^2 u_0}{\partial r^2} + \frac{1}{r}\frac{\partial u_0}{\partial r} - \frac{u_0}{r^2}\right), \quad (6.22)$$

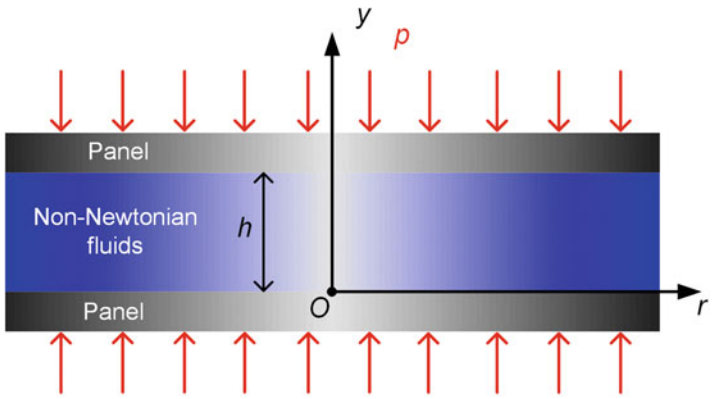

Fig. 6.15 Compressing flow mode of non-Newtonian fluid Ref. [70, 73]

where μ is the viscosity of the fluid, p is the pressure in y direction, u_0 is velocity solution in y direction, and v_0 is the velocity solution r direction. When the inertial influence of fluid is ignored,

$$u_0 = \frac{3r\dot{h}}{h^3}\left(y^2 - hy\right), v_0 = -\frac{\dot{h}}{h^3}\left(2y^3 - 3hy^2\right), \tag{6.23}$$

where the velocity of compressing is $\dot{h}$. Equation 6.23 is substituted into Eq. 6.22 to produce

$$\frac{\partial^2 u}{\partial y^2} = \frac{1}{\mu}\frac{\partial p}{\partial r} + \frac{\rho}{\mu}\left(\frac{3r\ddot{h}}{h^3}\left(y^2 - hy\right) + \frac{r\dot{h}^2}{h^2}\left(-\frac{3y^4}{h^4} + \frac{6y^3}{h^3} - \frac{9y^2}{h^2} + \frac{6y}{h}\right)\right). \tag{6.24}$$

The strain rate of the fluid can be expressed as

$$\dot{\varepsilon} = \frac{\partial u_0}{\partial y} + \frac{\partial v_0}{\partial r} = \frac{3r\dot{h}}{h^3}(2y - h). \tag{6.25}$$

The non-Newtonian fluid has a viscosity of $\mu = m\dot{\varepsilon}^{n-1}$, as calculated by Eq. 6.18. The shear thinning behavior of non-Newtonian fluid is denoted by $n < 1$. The shear thickening behavior of non-Newtonian fluid is denoted by $n > 1$.

According to Eq. 6.18, the viscosity of the non-Newtonian fluid is $\mu = m\dot{\varepsilon}^{n-1}$. $n < 1$ and $n > 1$ denote the shear thinning and shear thickening behavior of the fluid, respectively. Accordingly,

$$\frac{1}{\mu} = \frac{1}{m}\dot{\varepsilon}^{1-n} = \alpha\dot{\varepsilon}^{\beta} = \alpha\left(\frac{3r\dot{h}}{h^3}(2y - h)\right)^{\beta}, \tag{6.26}$$

where

$$\alpha = \frac{1}{m}, \beta = 1 - n. \tag{6.27}$$

Therefore, Eq. 6.24 can be written as

$$\begin{aligned} \frac{\partial^2 u}{\partial y^2} = & \frac{\partial p}{\partial r}\alpha\left(\frac{3r\dot{h}}{h^3}(2y-h)\right)^{\beta} + \rho\alpha\left(\frac{3r\dot{h}}{h^3}(2y-h)\right)^{\beta} \\ & \cdot\left(\frac{3r\ddot{h}}{h^3}\cdot\left(y^2-hy\right) + \frac{r\dot{h}^2}{h^2}\cdot\left(-\frac{3y^4}{h^4}+\frac{6y^3}{h^3}-\frac{9y^2}{h^2}+\frac{6y}{h}\right)\right) \end{aligned} \tag{6.28}$$

Define $2y - h = \xi$. Consequently, $\xi = 0$, $\mu = 0$; $\xi = h$, $\frac{1}{\mu} = \alpha\left(\frac{3r\dot{h}}{h^2}\right)^{\beta}$,

$$\frac{1}{\mu} = \alpha\left(\frac{3r\dot{h}}{h^3}(2y-h)\right)^{\beta} = \alpha\left(\frac{3r\dot{h}}{h^3}\xi\right)^{\beta}. \tag{6.29}$$

Consider boundary conditions $\xi = 0$, $\frac{\partial u}{\partial \xi} = 0$, and $\xi = h$, $u = 0$, and the integration of u for variable ξ. The derived equation is as follows:

$$\begin{aligned} 4u = & \alpha\left(\frac{3r\dot{h}}{h^3}\right)^{\beta}\frac{\partial p}{\partial r}\left(\frac{\xi^{2+\beta}}{(1+\beta)(2+\beta)} + C_1\right) \\ & +\rho\alpha\left(\frac{3r\dot{h}}{h^3}\right)^{\beta}\left(\begin{array}{l} \frac{3r\ddot{h}}{4h^3}\left(\frac{\xi^{4+\beta}}{(3+\beta)(4+\beta)} - h^2\frac{\xi^{2+\beta}}{(1+\beta)(2+\beta)} + C_2\right) \\ +\frac{3r\dot{h}^2}{16h^2}\left(-\frac{\xi^{6+\beta}}{h^4(5+\beta)(6+\beta)} - \frac{6\xi^{4+\beta}}{h^2(3+\beta)(4+\beta)} + \frac{7\xi^{2+\beta}}{(1+\beta)(2+\beta)} + C_3\right) \end{array}\right), \end{aligned} \tag{6.30}$$

where

$$\begin{aligned} C_1 &= -\frac{h^{2+\beta}}{(1+\beta)(2+\beta)} \\ C_2 &= \left(-\frac{1}{(3+\beta)(4+\beta)} + \frac{1}{(1+\beta)(2+\beta)}\right)h^{4+\beta} \\ C_3 &= \left(\frac{1}{(5+\beta)(6+\beta)}\frac{6}{h^2(3+\beta)(4+\beta)} - \frac{7}{(1+\beta)(2+\beta)}\right)h^{2+\beta} \end{aligned}.$$

Based on the continuity of deformation,

$$\int_0^h 4ud\xi = -r\dot{h}. \tag{6.31}$$

Integrating the function, Eq. 6.31, we obtain

$$\int_0^h 4ud\xi = \alpha\left(\frac{3r\dot{h}}{h^3}\right)^{\beta}\frac{\partial p}{\partial r}m_1h^{3+\beta} + \rho\alpha\left(\frac{3r\dot{h}}{h^3}\right)^{\beta}\left(\frac{3r\ddot{h}}{h^3}m_2h^{5+\beta} + \frac{3r\dot{h}^2}{16h^2}m_3h^{5+\beta}\right), \\ = -r\dot{h} \tag{6.32}$$

where

$$\begin{aligned} \mathrm{m}_1 &= -\frac{1}{(1+\beta)(3+\beta)} \\ m_2 &= \frac{1}{(1+\beta)(3+\beta)(5+\beta)} \\ m_3 &= \frac{1}{(5+\beta)(7+\beta)} + \frac{6}{(3+\beta)(5+\beta)} - \frac{7}{(1+\beta)(3+\beta)} \end{aligned}.$$

In Eq. 6.32, p can be integrated with respect to r to determine the pressure:

$$p = -\frac{\dot{h}}{a\left(3\dot{h}\right)^{\beta}m_1h^{3-2\beta}}\frac{r^{2-\beta}}{2-\beta} - \left(\frac{3m_2\rho\ddot{h}}{4m_1h} + \frac{3m_3\rho\dot{h}^2}{16m_1h^2}\right)\frac{r^2}{2} + C_4, \tag{6.33}$$

The constant C_4 is established with the boundary condition $p(R, t) = p_0$, where p_0 is the atmospheric pressure:

$$C_4 = p_0 + \frac{\dot{h}}{a\left(3\dot{h}\right)^{\beta}m_1h^{3-2\beta}}\frac{R^{2-\beta}}{2-\beta} - \left(\frac{3m_2\rho\ddot{h}}{4m_1h} + \frac{3m_3\rho\dot{h}^2}{16m_1h^2}\right)\frac{R^2}{2}. \tag{6.34}$$

Furthermore, the non-Newtonian fluid's squeezing force is determined by

$$F_{squeeze} = \int_0^R 2\pi r(p - p_0)dr \\ = \frac{\pi\dot{h}}{a\left(3\dot{h}\right)^{\beta}m_1h^{3-2\beta}}\frac{R^{4-\beta}}{4-\beta} + \left(\frac{3m_2\rho\ddot{h}}{4m_1h} + \frac{3m_3\rho\dot{h}^2}{16m_1h^2}\right)\frac{\pi R^4}{4} \tag{6.35}$$

At varying compressive strain rates, the nominal stress versus strain characteristics of the non-Newtonian fluid is calculated as follows:

$$\sigma_{\text{squeeze}} = \frac{F}{\pi R^2}, \tag{6.36}$$

$$\dot{\varepsilon}_{\text{squeeze}} = \frac{\dot{h}}{h}, \tag{6.37}$$

$$\varepsilon_{\text{squeeze}} = \int_0^t \dot{\varepsilon}_{\text{squeeze}} dt, \tag{6.38}$$

where $\sigma_{squeeze}$ is nominal stress, $\varepsilon_{\text{squeeze}}$ is compressive strain, and $\dot{\varepsilon}_{\text{squeeze}}$ is compressive strain rates.

6.3.2 Material Fabrication and Experimental Method

The colloidal particles used in this study are monodispersed silica nanospheres generated using Stöber's technique [71]. In conclusion, absolute ethanol and TEOS are dripped into each other's mixtures of ammonia and absolute ethanol throughout the duration. In order to prepare the silica microspheres for usage, they are centrifuged, cleaned with ethanol, and then dried in a vacuum oven at 80 °C. The silica nanospheres, polyethylene glycol, and ethanol are added to a round flask to produce the STF. Lastly, the mixed solution is rotary evaporated to yield the STF, which is then sealed in a bottle before usage. The density, bulk modulus, and sound velocity of polyethylene glycol are 1.127 g/cm^3, 3.05 GPa, and 1650 m/s, respectively. The density and sound velocity of silica nanoparticles are 1.950 g/cm^3 and 5869 m/s, respectively.

The SHPB equipment [72] is modified in the current study to examine the dynamic characteristics of the STF at nominal strain rates ranging from 500 to 1500 s^{-1}. The modified SHPB, as shown in Fig. 6.16, consists of a striker bar and an incident bar with a diameter of 19 mm. The striker bar and incident bar have lengths of about 0.7 m and 1.8 m, respectively. Both bars are manufactured of AA7075 with a nominal yield strength of about 500 MPa. Because STF samples are typically taken in relatively large sizes compared to the diameter of the incident bar, a loading end structure is used to reduce the size effect of the STF sample. The diameter of the loading end structure with a thickness of 15 mm, which is trumpet-shaped, ranges from 19 mm to a maximum of 80 mm. The trumpet-shaped loading end near the incident bar is also constructed of AA7075 to minimize the effect of the impedance mismatch between the trumpet-shaped structure and the incident bar. The STF samples separate the trumpet-shaped structure and a relatively sizable hard steel disk. The steel disk with a radius of 75 mm and thickness of 100 mm is rigid support made of Carpenter Hampden (CH) tool steel. A compressed gas gun accelerates the striker bar to impact velocities between 5 and 16 m/s. A digital oscilloscope, a Wheatstone bridge circuit, and a differential amplifier are utilized in conjunction with a pair of strain gages carefully positioned right in the middle of the incident bar to record the strain pulses in the incident bar during the SHPB experiments.

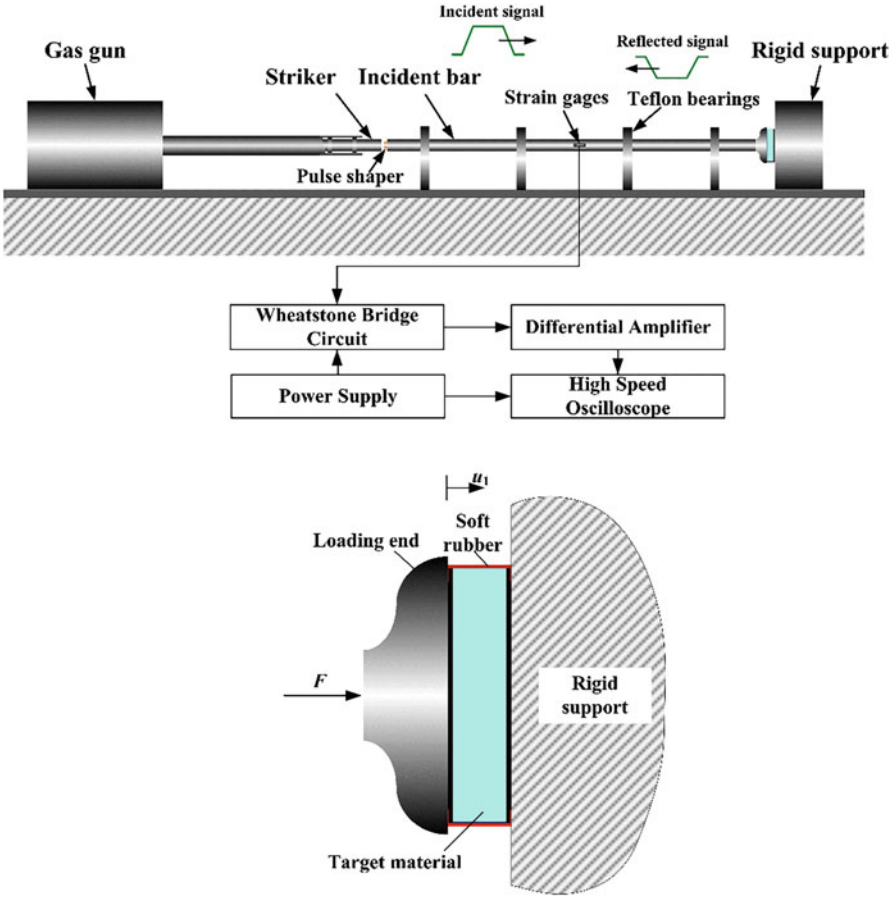

Fig. 6.16 Modified SHPB system Ref. [49]

In the SHPB experiment, the setup mentioned above, the gas gun accelerates the striker bar to strike the incident bar at various predetermined velocities. An elastic compression wave induced from the striker bar with a strain profile travels through the incident bar in the direction of the STF specimen and is represented by the symbol $\varepsilon_I(t)$. The incidence compressive wave is partially reflected into the incident bar, indicated by $\varepsilon_R(t)$, due to the mismatched impedances between the STF sample and the pressure bar. Moreover, the rest compressive wave is transmitted into the giant steel disk due to the mismatched impedances between the STF sample and the pressure bars. The steel disk is considered a rigid supporter since its impedance is significantly higher than the STF specimens. As a result, the contact end surface between the specimen and the steel disk is assumed to be stationary. The engineering strain rate $\dot{\varepsilon}_S(t)$, strain $\varepsilon_S(t)$, and stress $\sigma_S(t)$ in the specimen are calculated using

basic 1D elastic wave propagation formulas under the homogeneous deformation assumption:

$$\dot{\varepsilon}_S(t) = -2\frac{C_0}{h_S}\varepsilon_R(t), \tag{6.39}$$

$$\varepsilon_S(t) = \int_0^t \dot{\varepsilon}_S(t)dt. \tag{6.40}$$

$$\sigma_S(t) = E\frac{A_0}{A_S}[\varepsilon_I(t) + \varepsilon_R(t)], \tag{6.41}$$

In the relationships from Eq. 6.39 to 6.41, E is the modulus of elasticity, A_0 is the cross-sectional area of the incident bar, C_0 is longitudinal wave velocity of AA7075 bar, A_S is the original cross-sectional area of the specimen, and h_S is the original thickness of the specimen. By considering uniform and isochoric deformation conditions to exist within the specimen during the compression process, the relationship between the true strain and the true stress can be inferred from the relationship between the engineering strain and the engineering stress.

To apply pressure on the STF samples, the loading end in the experiment has a trumpet-like shape with a maximum radius of 40 mm. Although the trumpet-like shape end is made of the same material as the incident bar, studies have shown that irregular geometry of the trumpet-like shape loading end causes an impedance mismatch with the incident bar. As a result, the data reduction approach is used in conjunction with numerical simulation to reduce the inaccuracies caused by the impedance mismatch between the trumpet-like shape end and the incident bar. Each experiment uses a specimen to measure the incident wave and the reflected wave in the incident bar. Then, the free-end condition (without the specimen) is analyzed using the LS-DYNA [73], which has been verified for simulating SHPB experiments [74]. Then the incident bar and the trumpet-like shape loading end, which are supposed to be integrated rods, are simulated. The recorded incident stress wave is applied to the surface of the incident bar near the strike bar. Figure 6.17 shows the recorded and calculated stress waves at the middle surface of the incident bar. As can be observed, the simulated stress wave and the recorded stress wave from the incident bar coincide well before 840 μs. The boundary condition between the trumpet-like shape loading end and the incidence bar should be attributed to the difference between the recorded and simulated reflected stress waves after the time of 840 μs. In the SHPB tests, the incident bar contacts the trumpet-like shape loading end rather than integrating with it. Therefore, the incident bar and trumpet-like shape loading end will split when the unloading stress wave in the incident bar arrives at the surface of the trumpet-like shape loading end. Nevertheless, it is sufficient to measure the dynamic compressive response of the specimen. Figure 6.18 shows the produced simulated reflected stress wave with a free-end condition and a typical experimentally recorded reflected stress wave when compressing a specimen. The fact that the simulated and observed reflected waves are nearly identical at the beginning shows that an impedance mismatch between the trumpet-like shape

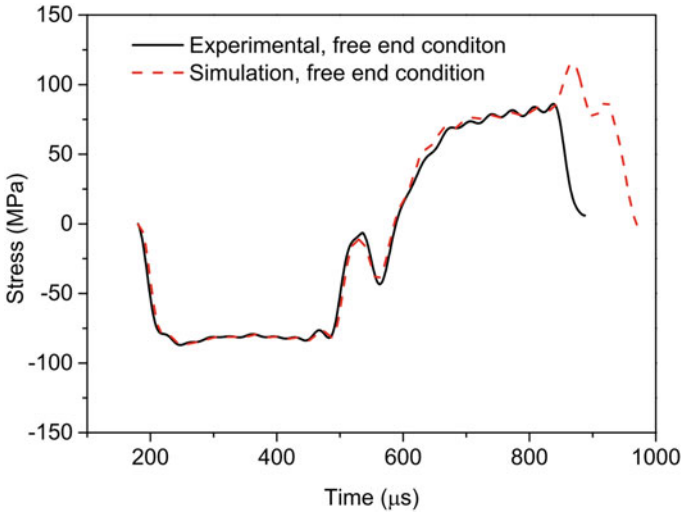

Fig. 6.17 Validation of numerical model with stress wave in the incident bar Ref. [49]

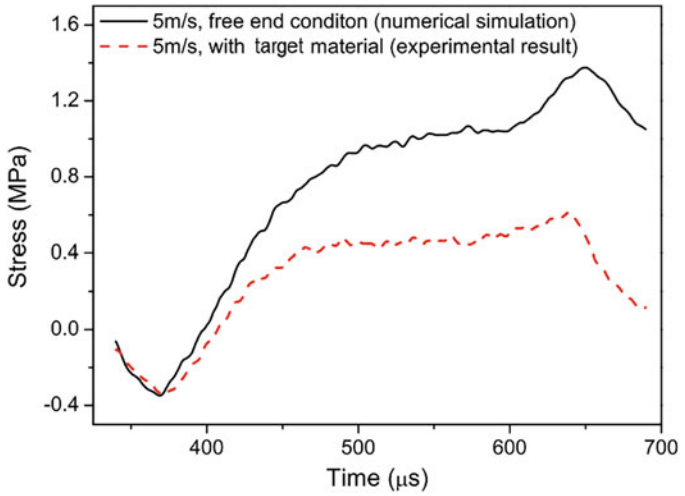

Fig. 6.18 Reflected stress wave with free-end condition in simulations and experiments Ref. [49]

loading end and the incident bar causes the reflected stress wave in this duration. The observed reflected stress wave is then lesser than the simulated wave. The actual stress wave applied to the specimen is calculated for each experiment by subtracting the measured wave from the simulated wave.

STF sample is used at varied impact velocities in the experiments. Table 6.1 gives a summary of the experimental settings for each test. In Fig. 6.19, the dynamic compressive response of the pure STF is depicted at impact velocities of

Table 6.1 Geometrical parameters of STF samples and test conditions in SHPB experiments

Test no.	Test specimen	Specimen radius (mm)	Impact velocity (m/s)	Strain rate (s^{-1})
1	STF-1	26.40	5	540
2	STF-2	26.37	8	920
3	STF-3	26.38	13	1500

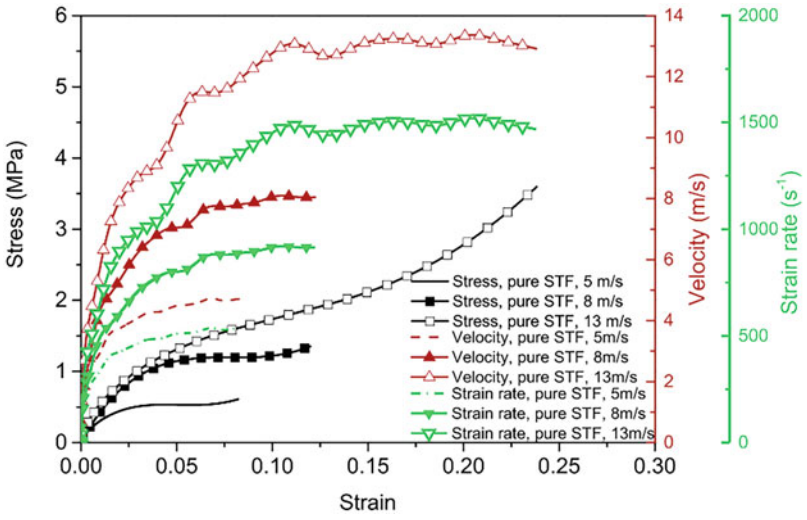

Fig. 6.19 Relationship between strain and stress for pure STF at various impact velocities Ref. [49]

approximately 5 m/s, 8 m/s, and 13 m/s. These impact velocities correspond to strain rates of approximately 540 s^{-1}, 920 s^{-1}, and 1500 s^{-1} respectively. For impacts with impact velocities of 5 m/s and 8 m/s, the stresses initially rise immediately with increases in strain with a plateau at around 0.5 MPa and 1.2 MPa, respectively. For a brief period, at impact velocities of 5 m/s and 8 m/s, stresses rise once more with continued loading. The compressive resistance of the STF continues to rise at the impact velocity of 13 m/s, and the stress plateau seen at the impact velocities of 5 m/s and 8 m/s is not well defined at 13 m/s; nevertheless, the stress rises a little bit with increasing strain.

6.3.3 Simulation of Compression Resistance of STF

The relationships between stress and strain at different shear strain rates for non-Newtonian fluids with just shear thinning or shear thickening behavior indicated by Eq. 6.18 could be determined by using the relationships given from Eq. 6.22 to 6.38. Nevertheless, it is challenging to integrate Eq. 6.31 with the complicated

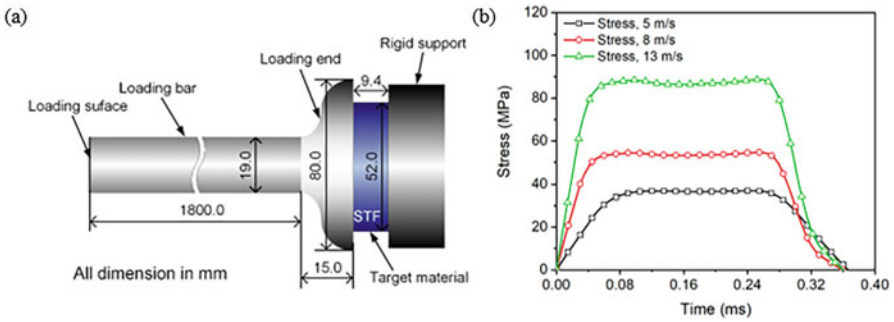

Fig. 6.20 (**a**) Numerical model and (**b**) loading stress wave histories at various impact velocities Ref. [73]

border between shear thinning and shear thickening, and the dynamic compression response of the STF cannot be analytically provided by the model. As illustrated in Fig. 6.14, this is especially true for non-Newtonian fluids whose deformation includes shear thinning and shear thickening regimes. In order to examine the dynamic compressive response of the STF, the coupled Eulerian-Lagrangian FSI simulation method is used, where the domain of Eulerian elements overlaps with the domain of the Lagrangian elements [75]. Figure 6.20 shows a schematic of the numerical simulation model based on the experimental setup. A trumpet-like shape loading end with a maximum radius of 40 mm and a maximum thickness of 15 mm is used to attach the loading bar, which has a size of Φ19 × 1800 mm. The STF specimen, which measures Φ52 × 9.4 mm and is enclosed in air, is positioned between a rigid body and a trumpet-like shape loading end. Additionally, the air domain is modeled to guarantee that the STF can be compressed into the surrounding atmosphere during the deformation. The interaction between the STF and the trumpet-like shape loading end is studied using the arbitrary Lagrangian-Eulerian (ALE) method [76, 77] utilizing the constrained model *CONSTRAINED LAGRANGE IN SOLID, which is implemented by LS-DYNA implements. The mechanical behavior of STF is simulated using the ALE model *ALE MULTI MATERIAL GROUP and the material model *MAT ALE VISCOUS. The mass, momentum, and energy formulas that control the ALE algorithm are given as

$$\left(\frac{\partial \rho}{\partial t}\right)_{\kappa} = -\rho \frac{\partial v_i}{\partial x_i} - c_i \frac{\partial \rho}{\partial x_i}, \tag{6.42}$$

$$\rho\left(\frac{\partial v_i}{\partial t}\right)_{\kappa} = \frac{\partial \sigma_{ij}}{\partial x_j} + \rho f_i - \rho c_i \frac{\partial v_i}{\partial x_j}, \tag{6.43}$$

$$\left(\rho \frac{\partial e}{\partial t}\right)_{\kappa} = \sigma_{ij} \frac{\partial v_i}{\partial x_j} - \frac{\partial q_i}{\partial x_i} - \rho c_i \frac{\partial e}{\partial x_i}, \tag{6.44}$$

Table 6.2 Constitutive parameters of STF using Mie-Grüneisen EOS Ref. [21, 24]

ρ_0 (kg/m^3)	C_0 (m/s)	S_1	S_2	S_3	γ_0	a
1600	2050	5.324	0	0	2	0

where v_i represents the velocity in Lagrange coordinate, ρ denotes the density of the ALE material, σ_{ij} indicates Cauchy stress tensor, f_i is the body force per mass, c_i indicates convection velocity, q_i denotes heat flux, and e represents internal energy [75–78].

On the coupling borders, the Eulerian elements' mesh sizes are relatively smaller than the Lagrangian elements' mesh sizes to avoid leaking in the FSI numerical simulation. The STF and the surrounding air are fine meshed with 203,776 hexahedral Eulerian elements. The loading part, consisting of the loading bar, the trumpet-like shaped loading end, and the rigid supported body, is meshed with 296,892 hexahedral Lagrangian elements. Two coupling points are employed within every Lagrangian element to improve the reliability of numerical simulation. To maintain the continuity of displacement, velocity, and acceleration between STF and air, the elements at the domain boundary of STF and air are co-nodal. There are constraints on acceleration and velocity at the boundary between the fluid and the structure. To simulate the sticky characteristic of the STF, the directions of compression, tension, and shear are coupled. The compressive characteristic of STF is analyzed using the Mie-Grüneisen EOS. It can be expressed as

$$P = \frac{\rho_0 C_0^2 \mu_0 \left(1 + \left(1 - \frac{\gamma_0}{2}\mu_0\right) - \frac{a}{2}\mu_0^2\right)}{\left(1 - (S_1 - 1)\mu_0 - S_2 \frac{\mu_0^2}{\mu_0 + 1} - S_3 \frac{\mu_0^3}{(\mu_0 + 1)^2}\right)^2} + (\gamma_0 + a\mu_0)E, \tag{6.45}$$

where $\mu_0 = \frac{\rho}{\rho_0} - 1$, C_0 denotes the intercept of the $U_S - U_P$ curve, S_1, S_2, S_3 are slope coefficients of the $U_S - U_P$ curve, γ_0 represents a constant of Mie-Grüneisen EOS, a represents the first-order volume correction to γ_0, ρ denotes current density, and ρ_0 is initial density [79]. Table 6.2 gives the STF constitutive parameters. It needs to be emphasized that the Mie-Grüneisen EOS does not explain how fluid cavitation bubbles arise and deflate. However, cavitation is exceedingly difficult to happen for fluids with exceptionally high viscosities such as the STF in the current work. Additionally, the STF will behave as a solid following the appearance of the shear thickening characteristic, allowing Mie-Grüneisen EOS to be used to describe the STF's compressibility responses.

The EOS of linear polynomial describes the hydrostatic characteristic of the air:

$$P = C_0 + C_1\mu_0 + C_2\mu_0^2 + C_3\mu_0^3 + \left(C_4 + C_5\mu_0 + C_6\mu_0^2\right)E, \tag{6.46}$$

where $\mu_0 = \frac{\rho}{\rho_0} - 1$, $C_0 \sim C_6$ are constants, E is internal energy, ρ is current density, and ρ_0 is initial density [80].

The relevant constitutive EOS parameters of the air are shown in Table 6.3.

Table 6.3 Constitutive parameters of air using linear polynomial EOS Ref. [80]

ρ_0 (kg/m^3)	C_0	C_1	C_2	C_3	C_4	C_5	C_6	E (J/m^3)
1.29	0	0	0	0	0.4	0.4	0	2.5×10^5

As determined by experiments [49], the loading stress wave histories at the impact velocities of 5, 8, and 13 m/s are applied to the loading surface of the incident bar as illustrated in Fig. 6.20b. The relationship between nominal engineering stress and engineering strain of the STF is obtained using the same data processing technique as in the above experiments.

The STF is modeled using the hydrodynamic constitutive model. In the numerical model, both shear thickening and thinning regimes of STF are considered. According to the rheological results given in Fig. 6.14, the numerical model fits the shear thinning behavior of the STF between the strain rates from 5×10^{-2} to 25 s^{-1}:

$$\mu_{ij} = 16 \cdot \dot{\varepsilon}_{ij}^{0.47-1}. \tag{6.47}$$

It was noted that the limitations in the rheometer prevented a complete measurement of the STF viscosity in the shear thickening domain when the strain rate exceeds a specific value. Therefore, by matching the numerical simulation results with various thickening values to the performance of the dynamic compression experiments, the shear thickening response of the STF is verified. It has been discovered that the simulation results best fit with the experimental results when the shear thickening equation is

$$\mu_{ij} = 72 \cdot \dot{\varepsilon}_{ij}^{1.35-1}. \tag{6.48}$$

The relationships between engineering strain and stress of the STF based on the FSI simulation results are slightly greater than their measured stresses when the strains are more than 2.2%, 4.1%, and 3.1% for impact velocities of 5 m/s, 8 m/s, and 13 m/s, respectively. After running several simulations with different shear thickening values, we have discovered that the shear thickening regime with $m = 72$ and $n = 1.35$ produces the best results. The compressive behavior of the SPLTC-STF, as predicted by numerical simulation with these shear thickening values, will also be demonstrated to agree with the experimental findings. Therefore, the shear thinning characteristics of the STF are used when the strain rates $\dot{\varepsilon}_{ij} < 25$ s^{-1}, as shown in Eq. 6.47, with $m = 16$ and $n = 0.47$. The shear thickening characteristics of the STF are used when the strain rates $\dot{\varepsilon}_{ij} < 25$ s^{-1}, as shown in Eq. 6.48, with $m = 72$ and $n = 1.35$. In order to maintain computation continuity, it is necessary to use the linear relationship between the strain rate logarithmic and viscosity logarithmic when

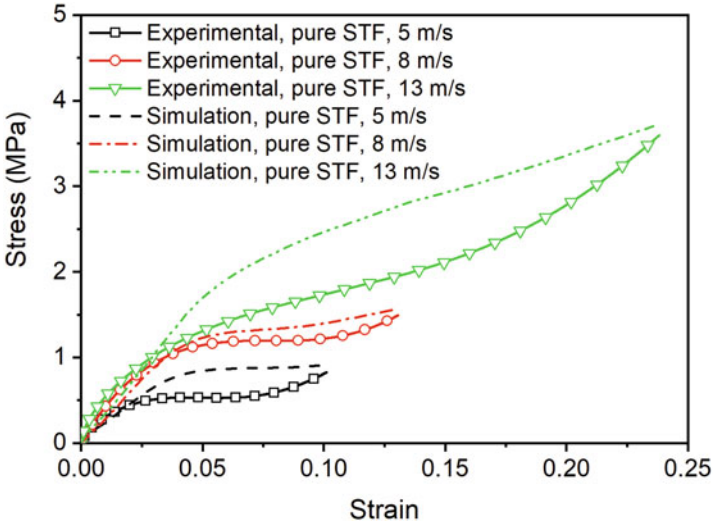

Fig. 6.21 Compressive relationship between strain and stress in STF at various impact velocities with the shear thinning equation, Eq. 6.47, and the shear thickening equation, Eq. 6.48 Ref. [73]

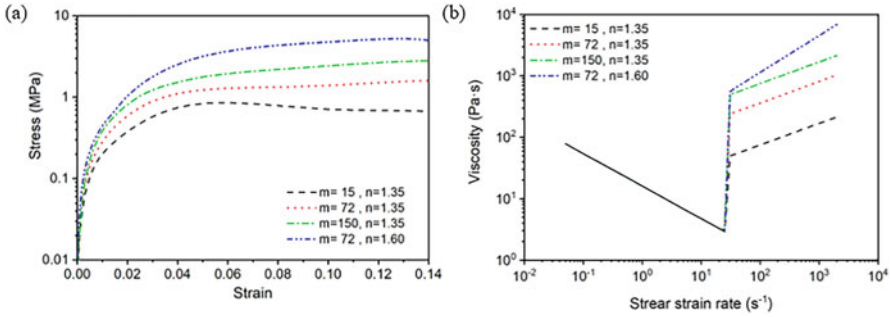

Fig. 6.22 (**a**) Compressive relationship between strain and stress in STF with shear thickening parameters of m and n. (**b**) Continuous transition from thinning to thickening characteristics with shear thickening values of m and n Ref. [73]

$25 < \dot{\varepsilon}_{ij} < 31\ \mathrm{s}^{-1}$. With the shear thinning regime equation, Eq. 6.47, and the shear thickening regime equation, Eq. 6.48, Fig. 6.21 shows the compressive relationship between the engineering strain and stress of the STF at various impact velocities. Under a squeezing velocity at 8 m/s, Fig. 6.22a shows the compressive relationship between the engineering strain and stress of the STF with various shear thickening parameters m and n. The continuous transition from shear thinning to shear thickening characteristics is seen in Fig. 6.22 with various shear thickening values of m and n. It is apparent that when viscosity increases at the shear thickening region, the compressive stress of the STF increases dramatically.

6.4 Dynamic Compressive Behavior of Sandwich Panels with Pyramidal Lattice Truss Core Filled by STF

This section discusses the dynamic compressive response of SPLTC-STF. Firstly, the detailed experimental approach is provided to prepare the SPLTC, water-filled SPLTC (SPLTC-WT), and STF-filled SPLTC (SPLTC-STF). Secondly, the experimental findings and corresponding discussions are given. Finally, the FSI method [73] is used to investigate the dynamic compressive behavior of the SPLTC-STF combining elastic bending and post-plastic buckling of the pyramidal lattice truss core structures of the SPLTC. The pyramidal lattice truss of SPLTC is produced by folding a 0.7-mm-thick perforated stainless steel sheet.

6.4.1 Fabrication of SPLTC and Experimental Method

The unit cell of the perforated steel sheet is rhombic with an acute angle of 60° and a length of 12 mm. A unit pyramidal lattice truss cell with dimensions of 16 mm in length, 9 mm in width, and 7 mm in height is formed by folding a steel plate 60°. SPLTCs are constructed with 3 mm broad flat surfaces at nodal regions to increase the welding quality between the pyramidal lattice truss cell and steel panels [81]. The truss core beams are slightly bent at the welding site as a result of the folding operation. 0.9-mm-thick panels and truss cores are joined using the brazing technique, which involves keeping the solder substance BNi-2 at 1040 ~ 1060 °C for about 15 min. The research of Yuan et al. [82] provides the details for establishing the SPLTC. As shown in Fig. 6.23a, the structure of a typical SPLTC for dynamic compression has three unit cells in length (roughly 48 mm) and four unit cells in width (roughly 36 mm). A soft rubber strip with a thickness of 0.1 mm and an elastic modulus of roughly 0.5 MPa is used to seal both open sides of an SPLTC while it is filled with water or STF. To investigate the dynamic response of SPLTC, SPLTC-

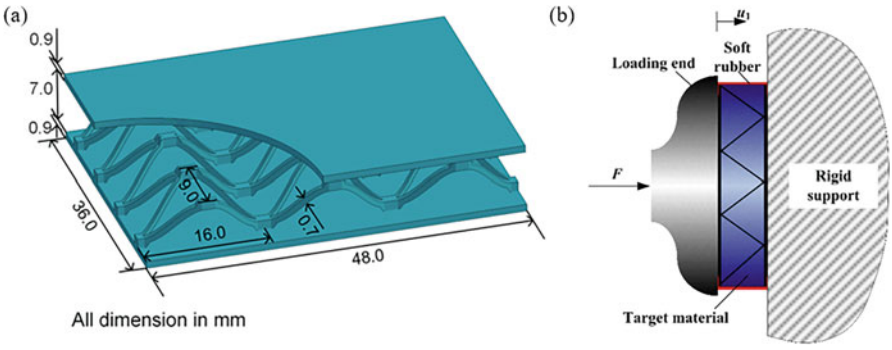

Fig. 6.23 (**a**) Geometrical details of SPLTC and (**b**) impact section in the modified SHPB system Ref. [73]

Table 6.4 Test parameters in the experiments

Test no.	Specimen	Specimen size (mm)	Unit cells	Impact velocity (m/s)	Strain rate (s^{-1})
1	SPLTC-1	100.1 × 100.1	6 × 11	3×10^{-5}	0.004
2	SPLTC-2	46.2 × 36.1	3 × 4	5	420
3	SPLTC-3	48.2 × 36.4	3 × 4	10	900
4	SPLTC-WT-1	49.1 × 37.1	3 × 4	16	1400
5	SPLTC-STF-1	46.8 × 37.1	3 × 4	5	430
6	SPLTC-STF-2	49.2 × 36.9	3 × 4	10	840
7	SPLTC-STF-3	46.2 × 37.0	3 × 4	16	1300

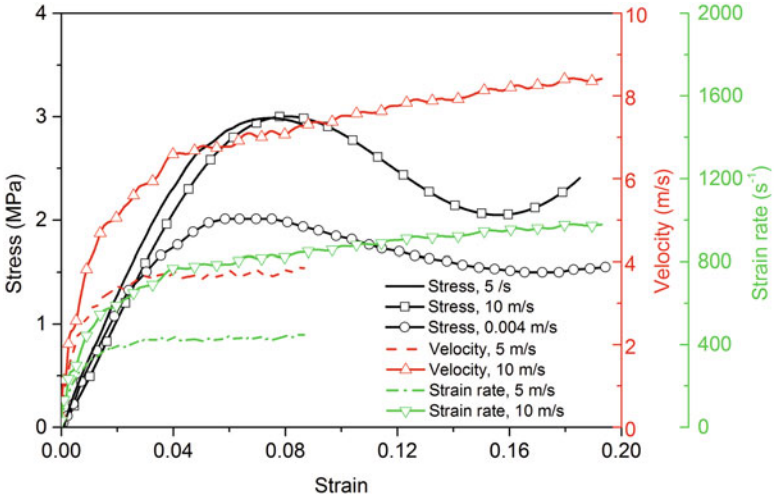

Fig. 6.24 Relationships between strain and stress in SPLTC Ref. [49]

WT, and SPLTC-STF at strain rates ranging from 300 to 1700 s^{-1}, the modified SHPB [72] has been used in the study. Similar to the experimental method for STF, the updated SHPB is depicted in Fig. 6.16. Figure 6.23b shows the loading part of the modified SHPB. The SPLTC, SPLTC-WT, and SPLTC-STF with relatively large section areas are compressed using a trumpet-like shaped loading end with a thickness of 15 mm and a maximum radius of 40 mm. Table 6.4 gives the experimental parameters of the tests. Unit cell dimensions slightly vary due to the nonuniform bending of the perforated steel sheet during manufacture.

6.4.2 *Experimental Results and Discussion*

In Fig. 6.24, the relationships between engineering strain and stress of the SPLTC are depicted for impact velocities of roughly 5 m/s and 10 m/s, respectively. The strain rate is approximately 420 s^{-1} at an impact velocity of 5 m/s while 900 s^{-1} at a

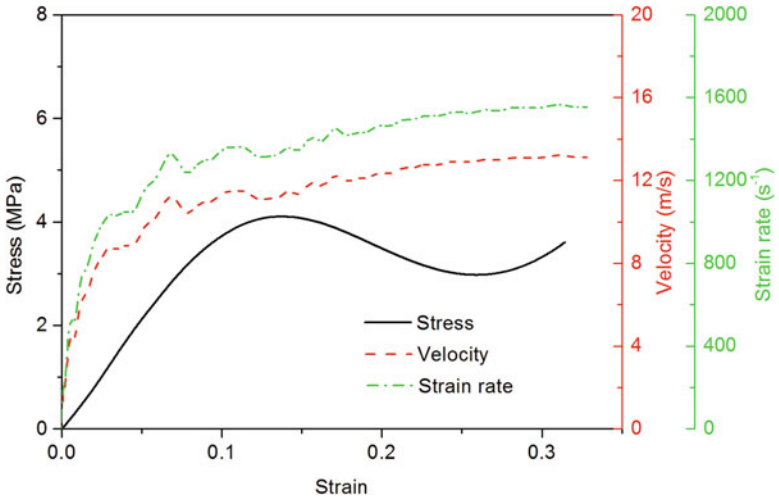

Fig. 6.25 Relationships between strain and stress in SPLTC-WT Ref. [49]

velocity of 10 m/s. As a comparison, the performance of SPLTC under quasi-static compression is also shown in the chart. As the strain increases, the stresses initially rise practically linearly. The maximal elastic engineering strain is about 0.058 for quasi-static and 0.078 for impact compression, respectively. The stresses then reduce with increased strain due to the buckling characteristic of the truss cores of SPLTC. After continued compression, the stresses immediately rise with increased strain as the panels or truss cores of SPLTC are in contact with each other. The findings produced at impact velocities of 5 m/s and 10 m/s are not apparent because the strain rates are approximately the same level. The initial peak stress of SPLTC is around 2.0 MPa during the quasi-static compression test. Because of lateral effects, as the research performed by Vaughn et al. [83], Lee et al. [84], and Tang et al. [85], the initial peak stress of SPLTC, which is about 50% higher than that achieved at quasi-static compression, is around 3.0 MPa at a strain rate of about 900 s^{-1} as opposed to 2.0 MPa during the quasi-static compression test.

Figure 6.25 shows the relationships between engineering strain and stress of the SPLTC-WT at an impact velocity of approximately 16 m/s, which corresponds to a strain rate of around 1400 s^{-1}. At the strain of 0.14, the stress of the SPLTC-WT quickly rises to an initial peak value of roughly 4.1 MPa. Due to the buckling and post-buckling characteristics of the truss core of SPLTC, the stress of the SPLTC-WT reduces to roughly 3.0 MPa at the strain of 0.26. Compared to the strengths of the SPLTC, the inertial effect of the filled water causes the initial peak stress of the SPLTC-WT to increase by roughly 36.7%.

In Fig. 6.24, the relationships between engineering strain and stress of the SPLTC-STF are depicted for impact velocities of roughly 5 m/s, 10 m/s, and 16 m/s, respectively. The strain rate is approximately 430 s^{-1} at an impact velocity of 5 m/s, 840 s^{-1} at 10 m/s, and 1300 s^{-1} at 16 m/s. The trends of the engineering

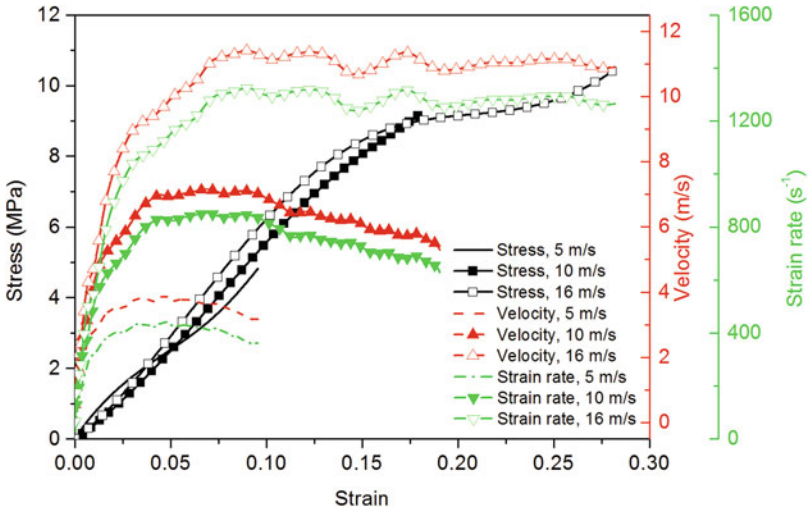

Fig. 6.26 Relationships between strain and stress in SPLTC-STF Ref. [49]

stress with increasing strain are not obvious after the loading engineering strain reaches 0.18 due to the limits of the loading pulse lengths at impact velocities of 5 m/s and 10 m/s. We assume that the relationships between engineering strain and stress of the SPLTC-STF obtained at impact velocities of 5 and 10 m/s are the same as those obtained at 16 m/s. Compared to the dynamic strengths of the SPLTC, the stresses increase practically linearly to roughly 9.0 MPa. The SPLTC demonstrates excellent energy absorption capabilities. As depicted in Figs. 6.24 and 6.25, the stress steadily rises with continued compression as opposed to rapidly falling caused by the buckling behavior of SPLTC and SPLTC-WT (Fig. 6.26).

The findings show that the buckling behavior of the truss core of SPLTC controls the peak stress of the SPLTC under quasi-static and dynamic compaction. The dynamic initial peak stress of SPLTC is more significant than that produced during quasi-static compression due to the inertial effect of the SPLTC, as demonstrated by investigations by Vaughn et al. [83], Lee et al. [84], and Tang et al. [85]. It is noteworthy to observe that SPLTC-STF strength increases when fluids are injected into the hollow areas of SPLTC. Figure 6.27 compares the relationships of nominal dynamic engineering stress and strain of the SPLTC, SPLTC-WT, and SPLTC-STF. The initial peak stress of the SPLTC rises from approximately 3.0 MPa to roughly 4.0 MPa after being filled with water, which should also be attributed to the inertial effect of the filled water during dynamic compression. Furthermore, the stress falls slowly after the initial peak stress is reached due to the post-buckling performance of the truss core of SPLTC-WT, which is identical to the dynamic compressive behavior of the SPLTC. Nevertheless, the stresses of the SPLTC-STF climb practically linear to about 9.0 MPa, which is about three times greater than the peak stress of the SPLTC, demonstrating the strong interaction between the STF and SPLTC. The stress then increases slightly with increased compressive strain, rather than gradually decreasing as illustrated by the SPLTC-STF.

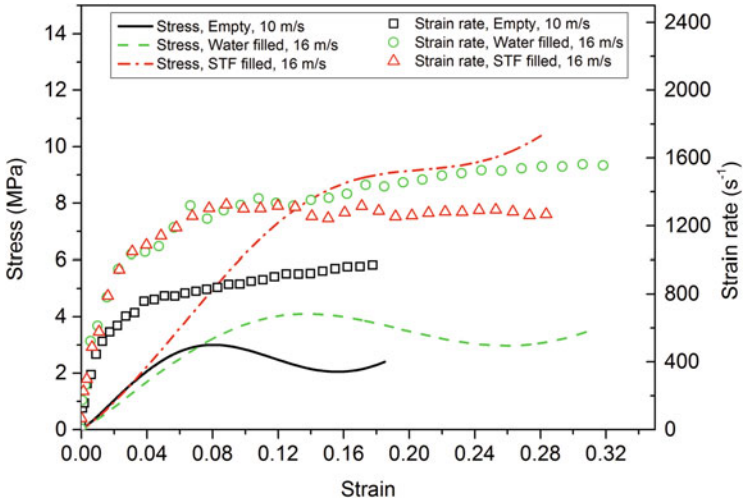

Fig. 6.27 Relationships between stress and strain in SPLTC, SPLTC-WT, and SPLTC-STF Ref. [49]

The interaction between the STF and the truss core of SPLTC could be used to understand the improved dynamic energy absorption performance of the SPLTC-STF. Figure 6.28 shows the post-compression deformation behavior of SPLTC and SPLTC-STF, respectively. As illustrated in Fig. 6.28a, the unit cell core of SPLTC undergoes elastic deformation during compression, which causes a rapid increase in stress at initial compression. After continuous compression, the maximum stress is reached when only one side of the beams buckles. Following that, the buckled beams exhibit post-buckling behavior, as seen by the substantial plastic deformation of the SPLTC, leading to a delayed stress drop after reaching the peak stress. With further compression after asymmetric flexion of the truss core, the upper panel of the SPLTC is tilted. The unbuckled beams start rotating around the welding points that serve as hinges and do not buckle during the subsequent compression. However, the deformation modes of the truss core of SPLTC-STF are altered due to intense interaction between the STF. As a result, the SPLTC-STF exhibits superior dynamic energy absorption performance. More research will be conducted to perfect the composite structural material's design and increase its capacity to absorb dynamic energy.

6.4.3 Plastic Buckling Behavior of SPLTC-STF

The same FSI as the compressive model of STF is used to study the dynamic compressive behavior of the core structures of the SPLTC-STF that involves elastic buckling and post-plastic buckling. The SPLTC, SPLTC-WT, and SPLTC-STF all

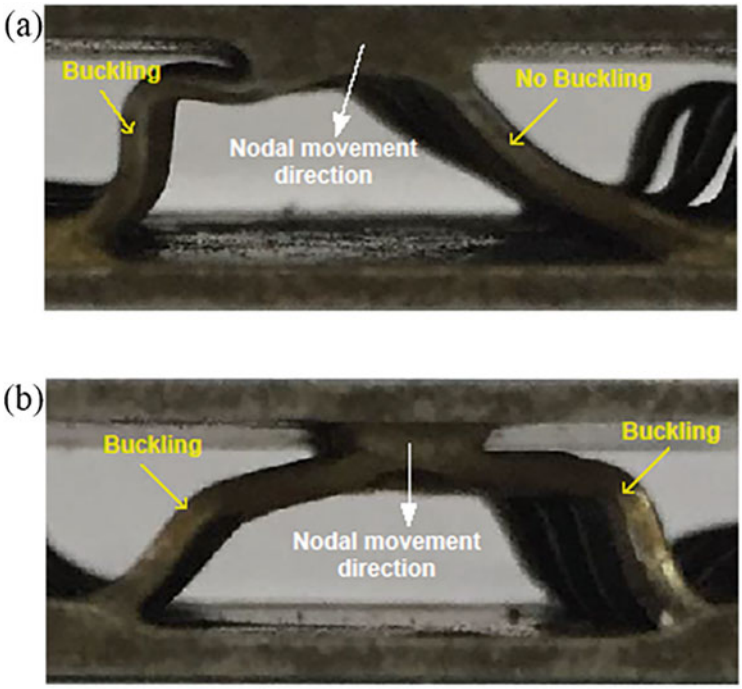

Fig. 6.28 Post-compression deformation behavior in (**a**) SPLTC and (**b**) SPLTC-STF Ref. [49]

use the same loading techniques and data processing steps as the compressive model of STF depicted in Fig. 6.20a. The pressure histories obtained in the SHPB tests at various loading velocities are applied to the left-end cross section of the incident bar. As illustrated in Fig. 6.23a, a numerical model of the SPLTC with the same size as the SHPB experiments is constructed. As illustrated in Fig. 6.29, the SPLTC-WT and SPLTC-STF FSI numerical models are created by including water or STF inside the inner space of the SPLTC model and air in the surrounding domain with a nonreflecting boundary. The same boundary conditions are used for the bottom surface and rest sides of the SPLTC-WT or SPLTC-STF as in the SPLTC model. The interaction between the SPLTC and the filler is examined using the ALE algorithm [76, 77]. To avoid fluid leakage, the Eulerian elements in the SPLTC-WT and SPLTC-STF models have smaller mesh sizes than the Lagrangian elements. There are 183,600 and 292,560 hexahedral Lagrangian elements meshing the SPLTC and the loading bar. The water and STF of SPLTC meshed with 549,280 hexahedral Eulerian elements. The surrounding air of SPLTC meshed with 1,472,480 hexahedral Eulerian elements. Two coupling points are employed in each Lagrangian element at the boundary between the Eulerian and Lagrangian domains to improve the simulation accuracy. The fluid boundary nodes are shared by the Eulerian elements of air and filled water or STF to maintain the continuity of

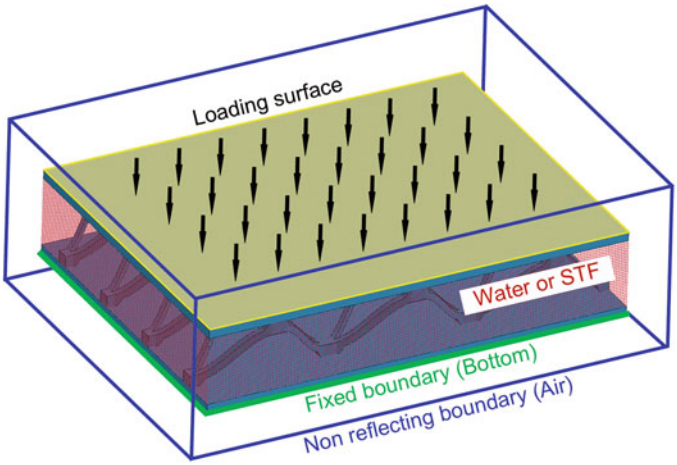

Fig. 6.29 FSI numerical models for SPLTC-WT or SPLTC-STF Ref. [73]

Table 6.5 The Johnson-Cook parameters for SS304 steel Ref. [84]

E (GPa)	Poisson's ratio	A (MPa)	B (MPa)	C	n
200	0.33	310	1000	0.064	0.34

Table 6.6 The Mie-Grüneisen EOS parameters for SS304 steel Ref. [84]

ρ_0 (kg/m^3)	C_0 (m/s^1)	S_1	S_2	S_3	γ_0	a
7800	4570	1.49	0	0	0.34	0.46

displacement, velocity, and acceleration. To imitate the sticky behavior of the STF, the compression, tension, and shear directions are coupled.

The Johnson-Cook constitutive model and the Mie-Grüneisen EOS describe the mechanical characteristics of SPLTC manufactured of stainless steel [20]. The effective stress of the Johnson-Cook constitutive model is defined as

$$\sigma_y = (A + B\overline{\varepsilon^p}^n)(1 + Cln\dot{\varepsilon}^*), \tag{6.49}$$

where A, B, and C are material constants, $\overline{\varepsilon^p}$ represents the equivalent plastic strain, $\dot{\varepsilon}^*$ indicates the normalized equivalent plastic strain rate, and n denotes the work hardening exponent. The Mie-Grüneisen EOS is used to characterize the STF, SPLTC, and water hydrostatic behavior [21, 24, 79, 84]. The linear polynomial EOS describes the hydrostatic behavior of air [80]. The EOS parameters of air and STF are shown in Table 6.2 and Table 6.3. The Johnson-Cook constitutive model and the Mie-Grüneisen EOS parameters of SS304 steel are given in Table 6.5 and Table 6.6, respectively. The Mie-Grüneisen EOS parameters of water are given in Table 6.7. The hydrostatic behavior of the STF, SPLTC, and water is described by

Table 6.7 The Mie-Grüneisen EOS parameters for water Ref. [79]

ρ_0 (kg·m^{-3})	C_0 (m·s^{-1})	S_1	S_2	S_3	γ_0	a
1000	1647	2.56	1.986	1.2268	0.5	0

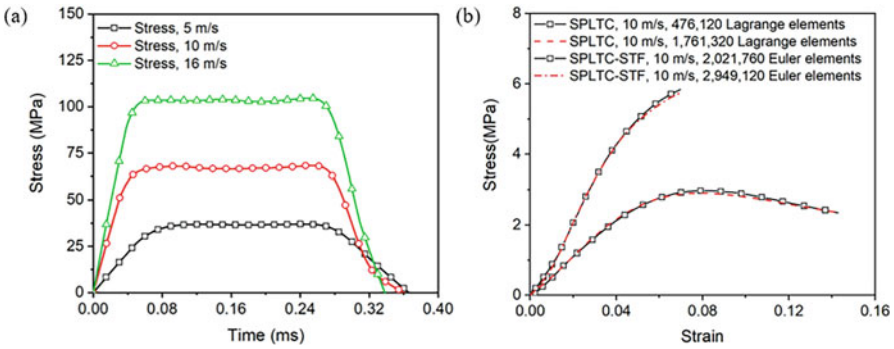

Fig. 6.30 (**a**) Stress histories on the free surface and (**b**) mesh sensitivity in the numerical models Ref. [73]

the Mie-Grüneisen EOS [21, 24, 79, 84], and the hydrostatic behavior of air is described by the linear polynomial EOS [80].

The stress histories determined in experiments at loading velocities of 5, 10, and 16 m/s are applied to the loading bar free-end cross section as shown in Fig. 6.30a. The mesh sensitivity in the numerical model of SPLTC and SPLTC-STF is verified first. At an impact velocity of 10 m/s, Fig. 6.30b shows the simulated relationships between nominal compressive engineering stress and strain for the SPLTC model and the SPLTC-STF model meshed with different element sizes. At an impact velocity of 10 m/s, the numerical simulation relationship between stress and strain of the SPLTC model meshed with 476,120 Lagrangian elements is nearly identical to that of the model meshed with 1,761,320 Lagrangian elements. Additionally, at an impact velocity of 10 m/s, the numerical simulation relationship between stress and strain of the SPLTC-STF model meshing 476,120 Lagrangian elements and 2,021,760 Eulerian elements is nearly identical to that meshing 476,120 Lagrangian elements and 2,949,120 Eulerian elements. The following numerical simulations use the SPLTC model with 476,120 Lagrangian elements and the SPLTC-STF model with 476,120 Lagrangian elements and 2,021,760 Eulerian elements as meshes because the mesh strategies of the numerical models satisfy the convergence criteria.

Figure 6.31a shows the relationships between engineering stress and strain in SPLTC at impact velocities of 5 and 10 m/s, as well as SPLTC-WT at 16 m/s. The experimental findings for SPLTC and SPLTC-WT are also provided for comparison purpose. The observation validates the numerical models of SPLTC and SPLTC-WT that the numerical results are closely matched with the experimental data. The deformation response of SPLTC after dynamic compression at an impact velocity of 5 m/s is depicted in Fig. 6.31b using simulation and experimental results. As seen

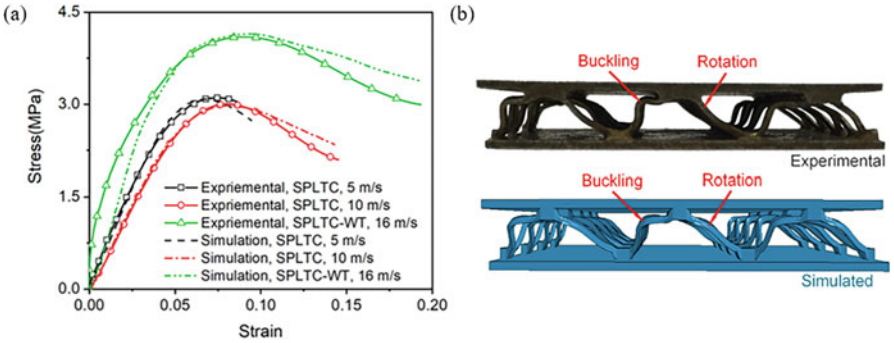

Fig. 6.31 (**a**) Relationships between stress and strain in SPLTC and SPLTC-WT and (**b**) deformation in SPLTC after dynamic compression at 5 m/s Ref. [73]

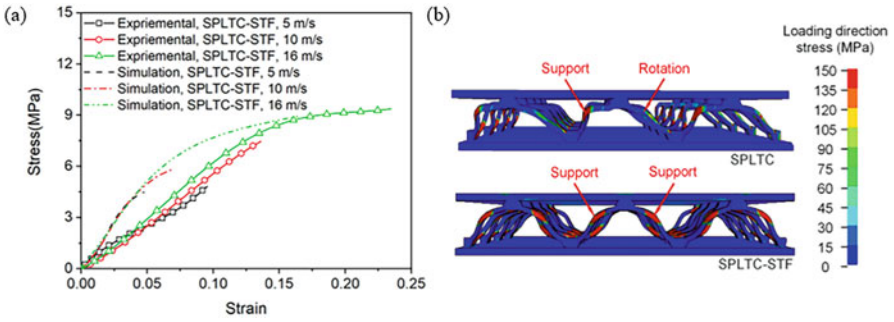

Fig. 6.32 (**a**) Relationships between stress and strain of the SPLTC-STF and (**b**) stress distributions in SPLTC and SPLTC-STF after 5 m/s impact Ref. [73]

in the images, numerical models could accurately predict the nonsymmetrical deformation characteristics in the targets.

Figure 6.32a shows the relationships between nominal compressive engineering stress and strain in SPLTC-STF at loading velocities of 5, 10, and 16 m/s according to the numerical and experimental results. Similar with the conducted experiments, the simulated nominal compressive engineering stress in SPLTC-STF initially increases practically linearly with strain increase. The stress then gradually increases with more compression, even once truss core beam buckling is achieved. Except for the increased stiffness of the simulated results, which could be attributable to the inaccuracy in calculating the viscosity of the STF in the shear thickening regime, the simulation results of the SPLTC-STF agree with the experimental data. At high shear strain rates, it is exceedingly challenging to quantify the viscosity of STF directly; this issue will be further researched in the near future. Figure 6.32b shows the simulated stress distributions in SPLTC and SPLTC-STF after impact loading at the velocity of 5 m/s. The truss at the left side of SPLTC begins to buckle after elastic deformation, and the truss at the right side rotates, thus reaching the peak stress. Only

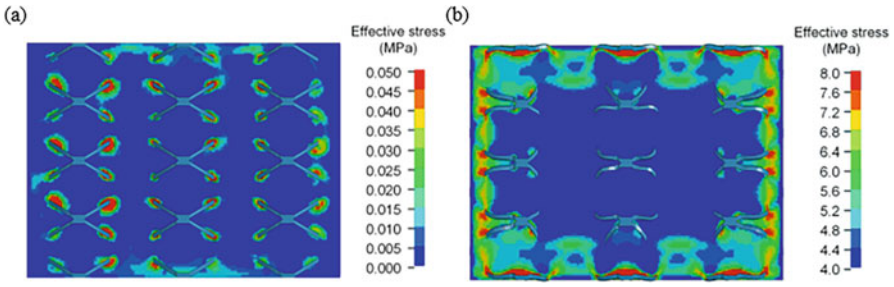

Fig. 6.33 Effective stress profiles for the strains of (**a**) 0.002% and (**b**) 13.6% in SPLTC-STF Ref. [73]

one side of SPLTC produces strong supporting forces throughout the buckling process. The truss at both sides of SPLTC-STF starts to buckle following the elastic deformation, and both sides produce significant supporting forces as illustrated in Fig. 6.32b.

The effective stress profiles for the strains of 0.002% and 13.6% are illustrated in Fig. 6.33. The images show the center region of STF in SPLTC-STF at the loading velocity of 16 m/s. As seen in Fig. 6.33a, as the truss in SPLTC deforms under impact loading, the lateral velocities of the truss increase and then the viscosity of the surrounding STF increases. In response, the STF offers restraining pressures to prevent the truss of SPLTC from moving laterally. As demonstrated in Fig. 6.33b, as the strain increases, the effective stress of the STF along the periphery of the SPLTC increases dramatically. As indicated in Fig. 6.31b, substantial symmetrically distributed counterforces are applied on the truss in the periphery of STF. The lateral restraint forces restrict the upper panel of the SPLTC from moving laterally due to asymmetrical deformation. As a result, the lattice truss in SPLTC-STF is compelled to deform symmetrically as depicted in Fig. 6.32b, increasing the ability to absorb the dynamic impact energy of SPLTC-STF. The significant outward counterforces given by the STF near the periphery of SPLTC-STF are generated by the significant interaction between the lattice truss and the fast-flow STF. As demonstrated in Fig. 6.34, the outward resultant flow velocities of the STF toward the edge of the SPLTC-STF increase rapidly as strain increases. When STF flows quickly across the lattice truss, the STF is sheared at high shear rates, resulting in shear thickening and huge magnitude counterforces on the lattice truss.

Figure 6.35 shows the simulated compressive performances for pure STF, SPLTC, SPLTC-WT, and SPLTC-STF. Additionally, shown in Fig. 6.35b is a "total" stress-strain relationship that was formed by simply adding the stress-strain curves for the pure STF and SPLTC at the loading velocity of 5 m/s. Figure 6.35b shows the numerically predicted relationships of engineering strain and specific energy absorption for SPLTC at 10 m/s loading velocity and SPLTC-STF and SPLTC-WT at 16 m/s loading velocity. The stress of SPLTC-STF at 4.5% strain is approximately 60% more than that of SPLTC at 5 m/s and 35% more than that of SPLTC-WT at 16 m/s. Additionally, compared to the combined strength of the pure STF and SPLTC at the loading velocity of 5 m/s, the numerically simulated peak

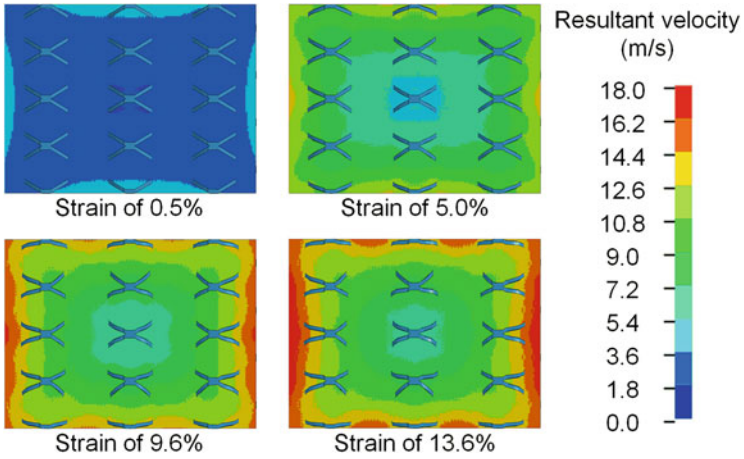

Fig. 6.34 Outward flow velocities in STF toward the edge of SPLTC-STF Ref. [73]

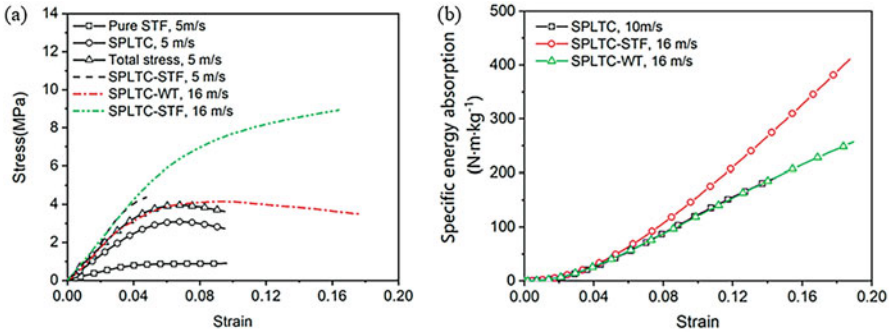

Fig. 6.35 (**a**) Relationships between stress and strain in pure STF, SPLTC, SPLTC-WT, and SPLTC-STF and (**b**) relationships between specific energy absorption and strain in SPLTC, SPLTC-WT, and SPLTC-STF Ref. [73]

strength in SPLTC-STF is substantially higher. After the engineering strain of 6.1%, the numerical energy absorption of SPLTC-STF is significantly larger than that of SPLTC and SPLTC-WT, demonstrating the improved impact energy absorption capability of the SPLTCSTF as seen in the experiments.

Figure 6.36 shows the compressive characteristics of SPLTC filled with non-Newtonian or Newtonian fluids at various viscosities at the loading velocity of 10 m/s. With increasing viscosity of the filler fluid, the stress at the same engineering strain of SPLTC increases. Unlike SPLTC or SPLTC-WT, the dynamic compressive engineering stresses in SPLTC-STF and SPLTC packed with fluids of constant high viscosity continued to increase after the viscosities above a specific threshold, allowing the energy absorption of capacity sandwich panels to be significantly improved. By filling fluids with various viscosity behaviors, the energy absorption capacity of the sandwich panels could be optimized.

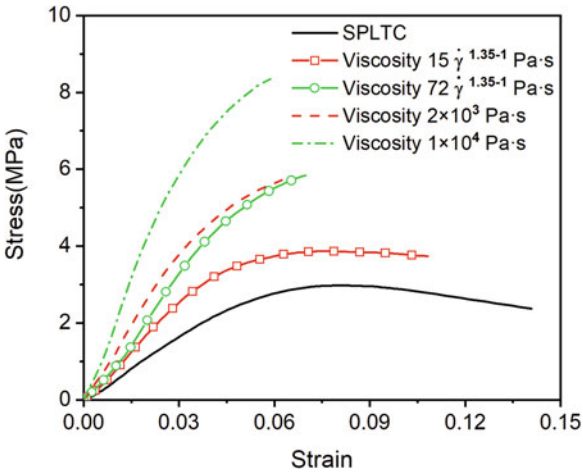

Fig. 6.36 Compressive characteristics of SPLTC filled with non-Newtonian or Newtonian fluids at the loading velocity of 10 m/s Ref. [73]

6.5 Summary

By evaluating the back-free surface velocities of targets designed with AA2024 plates and STF at various shock pressures, stress states, and temperatures, the dynamic behavior of the STF under laser-induced shock was investigated. The results indicated that shock pressure, stress state, and temperature are important about the shock wave attenuation in the STF. When shocked at the same temperature and shock diameter while under the same shock pressure, the measured back-free velocity of the sample and shock wave velocity in the STF both dropped. Additionally, for a high shock pressure of roughly 3.8 GPa and a shock diameter of 3.62 mm, the initial peak velocity dropped with decreasing temperature due to the impact-induced jamming behavior in the STF, which increased the bulk viscosity and significantly enhanced the temperature effect. However, there was no considerable difference between the tests conducted at 10 °C and 21 °C and at the same shock diameter of 3.62 mm while lowering shock pressure to about 3.0 GPa. The above suggests that the STF did not exhibit the bulk induced thickening behavior because the shock induced displacements of hard-sphere particles at such pressure and in tens of nanoseconds were insufficient to bridge the initial particle gap. It is also noteworthy that at the same temperature, shock pressure increased from roughly 3.8 GPa to roughly 5.4 GPa, and shock diameter decreased from 3.62 mm to 2.56 mm, significantly reducing particle velocity. It exhibits substantial dragging due to shear induced thickening behavior as the shock wave transitioned from a state of uniaxial strain to one of dilatation after a certain amount of time in the STF.

The modified SHPB setup is used to investigate the dynamic compressive response of SPLTC, SPLTC-WT, and SPLTC-STF at high strain rates. The high energy absorption capacity of SPLTC-STF is developed and exhibits the "1 + 1> > 2" phenomena as a result of the coupling effect between the truss core

beams of SPLTC and STF. Based on the studies of the experiments, a hydrodynamic constitutive model for the STF is established. A squeeze model for the STF is also established, which could accurately depict the STF's dynamic compressive behavior. Moreover, the FSI numerical model is built through LS-DYNA to analyze the coupling effect between the buckling and plastic post-buckling of truss core beams and the shear thinning and shear thickening in the STF. The buckling and post-buckling behavior of the truss core beams in the STF, as well as the influence of the STF with different shear thickening behavior, is obtained. The high energy absorption capacity of the sandwich panel and the "1 + 1> > 2" phenomenon after being filled with the STF are explained by using analytical and numerical methods.

Acknowledgments This research was supported by the National Natural Science Foundation of China (Grant Nos. 11772347, 12272391, and 12232020).

References

1. Karagiozova D, Langdon GS, Nurick GN. Propagation of compaction waves in metal foams exhibiting strain hardening. Int J Solids Struct. 2012;49(19–20):2763–77.
2. Lopatnikov SL, Gama BA, Haque MJ, Krauthauser C, Gillespie JW, Guden M, et al. Dynamics of metal foam deformation during Taylor cylinder-Hopkinson bar impact experiment. Compos Struct. 2003;61(1–2):61–71.
3. Lundberg P, Renstrom R, Lundberg B. Impact of metallic projectiles on ceramic targets: Transition between interface defeat and penetration. Int J Impact Eng. 2000;24(3):259–75.
4. Antonyuk S, Heinrich S, Tomas J, Deen NG, van Buijtenen MS, Kuipers JAM. Energy absorption during compression and impact of dry elastic-plastic spherical granules. Granul Matter. 2010;12(1):15–47.
5. Daraio C, Nesterenko VF, Herbold EB, Jin S. Energy trapping and shock disintegration in a composite granular medium. Phys Rev Lett. 2006;96(5):058002.
6. Gurgen S, Sofuoglu MA. Vibration attenuation of sandwich structures filled with shear thickening fluids. Compos Part B Eng. 2020;186:107831.
7. Zhao CY, Gong XL, Wang S, Jiang WQ, Xuan SH. Shear stiffening gels for intelligent anti-impact applications. Cell Rep Phys Sci. 2020;1(12):100266.
8. Zhang SS, Wang S, Hu T, Xuan SH, Jiang H, Gong XL. Study the safeguarding performance of shear thickening gel by the mechanoluminescence method. Compos Part B Eng. 2020;180:107564.
9. Wei MH, Lin K, Sun L. Shear thickening fluids and their applications. Mater Des. 2022;216:110570.
10. Fan T, Sun Z, Zhang YY, Li YQ, Chen ZK, Huang P, et al. Novel Kevlar fabric composite for multifunctional soft body armor. Compos Part B Eng. 2022;242:110106.
11. Zhang X, Wang PF, Kurkin A, Chen Q, Gong XL, Zhang Z, et al. Mechanical response of shear thickening fluid filled composite subjected to different strain rates. Int J Mech Sci. 2021;196:106304.
12. Yu KJ, Cao HJ, Qian K, Sha XF, Chen YP. Shear-thickening behavior of modified silica nanoparticles in polyethylene glycol. J Nanopart Res. 2012;14(3):747.
13. Lin GJ, Li JQ, Li F, Chen PW, Sun WF. Low-velocity impact response of sandwich composite panels with shear thickening gel filled honeycomb cores. Compos Commun. 2022;32:101136.

14. Khodadadi A, Liaghat G, Vahid S, Sabet AR, Hadavinia H. Ballistic performance of Kevlar fabric impregnated with nanosilica/PEG shear thickening fluid. Compos Part B Eng. 2019;162:643–52.
15. Fan T, Xue SS, Zhu WB, Zhang YY, Li YQ, Chen ZK, et al. Multifunctional polyurethane composite foam with outstanding anti-impact capacity for soft body armors. ACS Appl Mater Interfaces. 2022;14(11):13778–89.
16. Hoffman RL. Explanations for the cause of shear thickening in concentrated colloidal suspensions. J Rheol. 1998;42(1):111–23.
17. Cheng X, McCoy JH, Israelachvili JN, Cohen I. Imaging the microscopic structure of shear thinning and thickening colloidal suspensions. Science. 2011;333(6047):1276–9.
18. Brown E, Jaeger HM. Through thick and thin. Science. 2011;333(6047):1230–1.
19. Zhang JS, Wang Y, Deng HX, Zhou JY, Liu S, Wu JP, et al. A high anti-impact STF/Ecoflex composite structure with a sensing capacity for wearable design. Comp Part B-Eng. 2022;233:109656.
20. Waitukaitis SR, Jaeger HM. Impact-activated solidification of dense suspensions via dynamic jamming fronts. Nature. 2012;487(7406):205–9.
21. Wu X, Zhong F, Yin Q, Huang C. Dynamic response of shear thickening fluid under laser induced shock. Appl Phys Lett. 2015;106(7):071903.
22. Jiang WF, Gong XL, Xuan SH, Jiang WQ, Ye F, Li XF, et al. Stress pulse attenuation in shear thickening fluid. Appl Phys Lett. 2013;102(10):101901.
23. Hsu CP, Mandal J, Ramakrishna SN, Spencer ND, Isa L. Exploring the roles of roughness, friction and adhesion in discontinuous shear thickening by means of thermo-responsive particles. Nat Commun. 2021;12(1):1477.
24. Wu XQ, Yin QY, Huang CG. Experimental study on pressure, stress state, and temperature-dependent dynamic behavior of shear thickening fluid subjected to laser induced shock. J Appl Phys. 2015;118(17):173102.
25. Qin JB, Guo BR, Zhang L, Wang TW, Zhang GC, Shi XT. Soft armor materials constructed with Kevlar fabric and a novel shear thickening fluid. Compos Part B Eng. 2020;183:107686.
26. Qin JB, Zhang GC, Shi XT, Tao M. Study of a shear thickening fluid: the dispersions of silica nanoparticles in 1-butyl-3-methylimidazolium tetrafluoroborate. J Nanopart Res. 2015;17:17(8).
27. Peng GR, Li WH, Tian TF, Ding J, Nakano M. Experimental and modeling study of viscoelastic behaviors of magneto-rheological shear thickening fluids. Korea-Australia Rheol J. 2014;26(2):149–58.
28. Balali E, Kordani N, Vanini AS. Response of glass fiber-reinforced hybrid shear thickening fluid (STF) under low-velocity impact. J Text Inst. 2017;108(3):376–84.
29. Lin K, Zhou AN, Liu HJ, Liu Y, Huang CC. Shear thickening fluid damper and its application to vibration mitigation of stay cable. Structure. 2020;26:214–23.
30. Mawkhlieng U, Majumdar A. Deconstructing the role of shear thickening fluid in enhancing the impact resistance of high-performance fabrics. Compos Part B Eng. 2019;175:107167.
31. Arora S, Majumdar A, Butola BS. Structure induced effectiveness of shear thickening fluid for modulating impact resistance of UHMWPE fabrics. Compos Struct. 2019;210:41–8.
32. Gurgen S, Fernandes FAO, de Sousa RJA, Kushan MC. Development of eco-friendly shock-absorbing cork composites enhanced by a non-Newtonian fluid. Appl Compos Mater. 2021;28(1):165–79.
33. Gurgen S, Kushan MC, Li WH. Shear thickening fluids in protective applications: A review. Prog Polym Sci. 2017;75:48–72.
34. Gurgen S, Sofuoglu MA. Experimental investigation on vibration characteristics of shear thickening fluid filled CFRP tubes. Compos Struct. 2019;226:111236.
35. Yungwirth CJ, Radford DD, Aronson M, Wadley HNG. Experiment assessment of the ballistic response of composite pyramidal lattice truss structures. Compos Part B Eng. 2008;39(3):556–69.

36. Wadley HNG, Dharmasena KP, O'Masta MR, Wetzel JJ. Impact response of aluminum corrugated core sandwich panels. Int J Impact Eng. 2013;62:114–28.
37. Fischer C, Braun SA, Bourban PE, Michaud V, Plummer CJG, Manson JAE. Dynamic properties of sandwich structures with integrated shear-thickening fluids. Smart Mater Struct. 2006;15(5):1467–75.
38. Tan ZH, Zuo L, Li WH, Liu LS, Zhai PC. Dynamic response of symmetrical and asymmetrical sandwich plates with shear thickening fluid core subjected to penetration loading. Mater Des. 2016;94:105–10.
39. Evans AG, Hutchinson JW, Fleck NA, Ashby MF, Wadley HNG. The topological design of multifunctional cellular metals. Prog Mater Sci. 2001;46(3–4):309–27.
40. Hutchinson JW, Xue ZY. Metal sandwich plates optimized for pressure impulses. Int J Mech Sci. 2005;47(4–5):545–69.
41. Wadley HNG. Multifunctional periodic cellular metals. Philosophic Transact Royal Soc A Mathematic Phys Eng Sci. 2006;364(1838):31–68.
42. Deshpande VS, Fleck NA. One-dimensional response of sandwich plates to underwater shock loading. J Mech Phys Solids. 2005;53(11):2347–83.
43. McShane GJ, Deshpande VS, Fleck NA. Underwater blast response of free-standing sandwich plates with metallic lattice cores. Int J Impact Eng. 2010;37(11):1138–49.
44. Mohr D. Mechanism-based multi-surface plasticity model for ideal truss lattice materials. Int J Solids Struct. 2005;42(11–12):3235–60.
45. Wadley HNG, Borvik T, Olovsson L, Wetzel JJ, Dharmasena KP, Hopperstad OS, et al. Deformation and fracture of impulsively loaded sandwich panels. J Mech Phys Solids. 2013;61(2):674–99.
46. Xue ZY, Hutchinson JW. Constitutive model for quasi-static deformation of metallic sandwich cores. Int J Numer Methods Eng. 2004;61(13):2205–38.
47. Zhu F, Zhao LM, Lu GX, Gad E. A numerical simulation of the blast impact of square metallic sandwich panels. Int J Impact Eng. 2009;36(5):687–99.
48. Vaziri A, Xue Z, Hutchinson JW. Metal sandwich plates with polymer foam-filled cores. J Mech Mater Struct. 2006;1(1):97–127.
49. Wu XQ, Xiao KL, Yin QY, Zhong FC, Huang CG. Experimental study on dynamic compressive behaviour of sandwich panel with shear thickening fluid filled pyramidal lattice truss core. Int J Mech Sci. 2018;138:467–75.
50. Wu XQ, Tan QM, Huang CG. Geometrical scaling law for laser shock processing. J Appl Phys. 2013;114(4):043105.
51. Wu XQ, Duan ZP, Song HW, Wei YP, Wang X, Huang CG. Shock pressure induced by glass-confined laser shock peening: Experiments, modeling and simulation. J Appl Phys. 2011;110 (5):053112.
52. Wu XQ, Huang CG, Wang X, Song HW. A new effective method to estimate the effect of laser shock peening. Int J Impact Eng. 2011;38(5):322–9.
53. Fabbro R, Fournier J, Ballard P, Devaux D, Virmont J. Physical study of laser-produced plasma in confined geometry. J Appl Phys. 1990;68(2):775–84.
54. Fabbro R, Peyre P, Berthe L, Scherpereel X. Physics and applications of laser-shock processing. J Laser Appl. 1998;10(6):265–79.
55. Hong X, Wang SB, Guo DH, Wu HX, Wang J, Dai YS, et al. Confining medium and absorptive overlay: Their effects on a laser-induced shock wave. Opt Lasers Eng. 1998;29(6):447–55.
56. Strand OT, Goosman DR, Martinez C, Whitworth TL, Kuhlow WW. Compact system for high-speed velocimetry using heterodyne techniques. Rev Sci Instrum. 2006;77(8):083108.
57. Bolger JA, Montross CS, Rode AV. Shock waves in basalt rock generated with high-powered lasers in a confined geometry. J Appl Phys. 1999;86(10):5461–6.
58. Boustie M, Cuq-Lelandais JP, Bolis C, Berthe L, Barradas S, Arrigoni M, et al. Study of damage phenomena induced by edge effects into materials under laser driven shocks. J Phys D Appl Phys. 2007;40(22):7103–8.

59. Rosenberg Z, Luttwak G, Yeshurun Y, Partom Y. Spall studies of differently treated 2024Al specimens. J Appl Phys. 1983;54(5):2147–52.
60. Bender JW, Wagner NJ. Optical measurement of the contributions of colloidal forces to the rheology of concentrated suspensions. J Colloid Interface Sci. 1995;172(1):171–84.
61. Hoffman RL. Discontinuous and dilatant viscosity behavior in concentrated suspensions .2. theory and experimental tests. J Colloid Interface Sci. 1974;46(3):491–506.
62. Lim AS, Lopatnikov SL, Wagner NJ, Gillespie JW. Investigating the transient response of a shear thickening fluid using the split Hopkinson pressure bar technique. Rheol Acta. 2010;49 (8):879–90.
63. Maranzano BJ, Wagner NJ. The effects of interparticle interactions and particle size on reversible shear thickening: Hard-sphere colloidal dispersions. J Rheol. 2001;45(5):1205–22.
64. Maranzano BJ, Wagner NJ. The effects of particle-size on reversible shear thickening of concentrated colloidal dispersions. J Chem Phys. 2001;114(23):10514–27.
65. Kumar S, Tripathi PK, Upadhyay SN. On the mass-transfer in non-newtonian fluids .1. transfer from spheres to power law fluids. Lett Heat Mass Transfer. 1980;7(1):43–53.
66. Herrmann W. Constitutive equation for dynamic compaction of ductile porous materials. J Appl Phys. 1969;40(6):2490.
67. McQueen RG, Marsh SP. Shock-wave compression of iron-nickel alloys and earths core. J Geophys Res. 1966;71(6):1751.
68. Petel OE, Frost DL, Higgins AJ, Ouellet S. Formation of a disordered solid via a shock-induced transition in a dense particle suspension. Phys Rev E. 2012;85(2):021401.
69. Petel OE, Higgins AJ. Shock wave propagation in dense particle suspensions. J Appl Phys. 2010;108(11):114918.
70. Kuzma DC. Fluid inertia effects in squeeze films. Appl Sci Res. 1967;18(1):15.
71. Stober W, Fink A, Bohn E. Controlled growth of monodisperse silica spheres in micron size range. J Colloid Interface Sci. 1968;26(1):62–70.
72. Hopkinson B. A method of measuring the pressure produced in the detonation of high explosives or by the impact of bullets. Philosophic Transact Royal Soc London Series A Containing Papers of a Mathematical or Physical Character. 1914;213:437–56.
73. Gu ZP, Wu XQ, Li QM, Yin QY, Huang CG. Dynamic compressive behaviour of sandwich panels with lattice truss core filled by shear thickening fluid. Int J Impact Eng. 2020;143: 103616.
74. Wu XQ, Yin QY, Wei YP, Huang CG. Effects of imperfect experimental conditions on stress waves in SHPB experiments. Acta Mech Sinica. 2015;31(6):827–36.
75. Pi SJ, Cheng DS, Cheng HL, Li WC, Hung CW. Fluid-structure-interaction for a steel plate subjected to non-contact explosion. Theor Appl Fract Mech. 2012;59(1):1–7.
76. Barlow AJ, Maire PH, Rider WJ, Rieben RN, Shashkov MJ. Arbitrary Lagrangian-Eulerian methods for modeling high-speed compressible multimaterial flows. J Comput Phys. 2016;322: 603–65.
77. Souli M, Ouahsine A, Lewin L. ALE formulation for fluid-structure interaction problems. Comput Methods Appl Mech Eng. 2000;190(5–7):659–75.
78. Hu HH, Patankar NA, Zhu MY. Direct numerical simulations of fluid-solid systems using the arbitrary Lagrangian-Eulerian technique. J Comput Phys. 2001;169(2):427–62.
79. Panciroli R, Abrate S, Minak G, Zucchelli A. Hydroelasticity in water-entry problems: Comparison between experimental and SPH results. Compos Struct. 2012;94(2):532–9.
80. Wang ZL, Li YC, Shen RF. Numerical simulation of tensile damage and blast crater in brittle rock due to underground explosion. Int J Rock Mech Min Sci. 2007;44(5):730–8.
81. Kooistra GW, Deshpande VS, Wadley HNG. Compressive behavior of age hardenable tetrahedral lattice truss structures made from aluminium. Acta Mater. 2004;52(14):4229–37.
82. Yuan W, Song H, Wang X, Huang C. Experimental investigation on thermal buckling behavior of truss-Core Sandwich panels. AIAA J. 2015;53(4):948–57.
83. Vaughn DG, Canning JM, Hutchinson JW. Coupled plastic wave propagation and column buckling. J Appl Mech Transact Asme. 2005;72(1):139–46.

84. Lee S, Barthelat F, Hutchinson JW, Espinosa HD. Dynamic failure of metallic pyramidal truss core materials - experiments and modeling. Int J Plast. 2006;22(11):2118–45.
85. Tang X, Prakash V, Lewandowski JJ, Koolstra GW, Wadley HNG. Inertial stabilization of buckling at high rates of loading and low test temperatures: Implications for dynamic crush resistance of aluminum-alloy-based sandwich plates with lattice core. Acta Mater. 2007;55(8): 2829–40.

Chapter 7
Energy Dissipation in Shear Thickening Fluid Integrated Structures Under Ballistic Impacts

Victor Avisek Chatterjee, Seema Singh, and Swati Neogi

7.1 Introduction

Advanced composites are preferred over traditional materials in a variety of engineering domains [1–19] because of their high specific strength, ease of fabrication, customizability, and potential for property enhancement through the addition of fillers or other improvements [20]. Advanced composite materials have found use in various defense applications such as helmets, armor, gloves, and bomb blankets. These materials absorb the kinetic energy of the incident particle to enhance their effectiveness. Plastic deformation or fracture processes have the potential to dominantly absorb energy. However, high strength steels and other conventional materials are heavy, and they often fail due to a high concentration of plastic deformation coupled with extremely high adiabatic heat in a small number of shear planes, which strongly softens the material. In contrast, harder materials such as ceramics lack necessary toughness and typically require support from more ductile metals. Due to their high strength and low cost, composites are extensively used for better energy dissipation. However, many composites are fairly soft and ineffective against projectiles with hard surfaces. Composites, however, offer a viable option when combined with ceramics or laminates. The synthesis of shear thickening fluids (STFs) and their use in both soft and hard armor panels have recently garnered the attention of scientists and engineers.

V. A. Chatterjee · S. Neogi (✉)
Composites Applications and Testing Laboratory, Department of Chemical Engineering, Indian Institute of Technology, Kharagpur, West Bengal, India
e-mail: swati@che.iitkgp.ac.in

S. Singh
Department of Chemical Engineering, National Institute of Technology, Durgapur, West Bengal, India

S. Gürgen (ed.), *Shear Thickening Fluid*, https://doi.org/10.1007/978-3-031-35521-9_7

Advanced composites have the potential to be used in impact-resistant armor structures, which can be either soft or hard armor systems. However, for heavy armor applications, it is crucial to find materials that offer improved impact resistance without adding excessive weight. To achieve this, new composites can be developed with cores filled with high-performance rheologically tuned fluids, such as STFs. The rheology of these fluids can increase the impact resistance of advanced composites without significantly increasing their weight. Researchers have been exploring potential applications of STFs in body armor since the 1970s [14, 21]. STFs are non-Newtonian fluids that exhibit shear thickening properties, meaning their dynamic viscosities increase with increased shear rates or stresses. By applying STFs on armor panels, they can dissipate energy upon projectile impact. The properties of the fluid also make the materials lightweight and flexible.

The application of STFs in impact-resistant structures has opened up new horizons in materials research with enhanced energy dissipation. STF has the inherent property of undergoing a change from a liquid to a solid-like condition at high shear rates, causing enhanced energy dissipation when applied to textile materials. The application of STF on fabrics has also shown a significant increase in the yarn pull out energy in composites. The shear thickening behavior of the fluid is influenced by various factors such as particle size, volume fraction of the solid, shape of the particle, and particle size distribution. At lower shear rates, shear thickening can occur if the particle size is smaller, the solid volume fraction is higher, and the particle shape has a higher aspect ratio. Although researchers have explored the mechanism of shear thickening, there is still a need to gain a clearer understanding of the mechanism of energy absorption in textiles applied with STFs [22].

The plan to use STFs in advanced composites faces two main challenges. The first challenge is formulating viable STFs that combine desirable levels of post-transitional viscosity, significant shear thickening rheological characteristics, and relatively low viscosity at rest [23]. STFs exhibit clear thickening characteristics, making them useful as shock-absorbing and force-dampening materials in applications such as vehicles, sports equipment, and flexible armor [24]. The mechanism behind STFs providing additional impact resistance is due to the formation of nonequilibrium, self-organized hydroclusters [25–34], which cause shear thickening and give the fluid a solid-like character. The critical shear rate is one of the most important rheological properties of the STF and can be adjusted as per the requirements. Several researchers have conducted previous studies on STFs concerning various substrates and have discussed the impact of different factors on the rheological parameters [35–41]. However, there has not been a concentrated effort to demonstrate the shear thickening phenomenon for a single set of systems as a whole and move toward a fluid that can be customized based on particle size, carrier fluid viscosity, and particle loading fraction.

Another challenge is introducing the synthesized STF into the center of the composite. Hard armors are advanced composites created by consolidating reinforcement mats in thermosetting polymers. Although researchers have extended the idea of STF treatment to textiles and reinforcement mats in composite materials for better impact resistance properties [42–47], they have mostly limited themselves to

soft armor systems. Few attempts have been made to incorporate STFs in hard advanced composites, and there are major challenges in doing so using simple methods like soaking and drying, which work for soft armors. Sandwiching the STF between reinforcement mats has been tried but failed to produce positive results for impact resistance. Developing SCPs appears to be the most promising method for containing the STF within the reinforcement layer and providing energy dissipation upon impact. The literature lacks a comprehensive description of how sandwich composite structures behave under the effect of an impact [48]. Many researchers aim to develop SCPs that can effectively absorb the majority of energy from an incident object. To achieve greater energy dissipation in sandwich composite structures, a noncritical deceleration has to be accomplished [49]. To enhance energy dissipation, researchers have attempted numerous changes to the shape and geometry of the core materials [50–66].

Previous studies have extensively explored the energy dissipation of textiles and composites impregnated with STFs upon exposure to high-speed impacts [37–40, 61–67]. However, the impact of an STF-incorporated core in a SCP and its effect on energy absorption has been the subject of relatively few investigations.

Taking the above factors into consideration, this chapter focuses on three case studies related to the use of STF-impregnated advanced composites for energy dissipation. These case studies involve the incorporation of STFs into the cores of polymer-matrix composites using different configurations, which are described in detail in the following sections. While the composite designs differ in each case, similar manufacturing techniques such as hand layup (HLU) and vacuum assisted resin infusion molding (VARIM) have been employed. The incorporation of STFs within the composite structures is the main focus of this chapter. This chapter also provides detailed descriptions of the ballistic impact using projectiles of two different velocities and the resulting energy dissipation due to their impact.

7.2 Experimental Details

7.2.1 Fabrication of Shear Thickening Fluid

This study focuses on advanced composites incorporated with STF. The fabricated STF was used in all the case studies. The following three materials were used in the formulation of STF.

(a) Spherical silica nanoparticles having an average particle size of 600 nm were supplied from United Chemicals, India.
(b) Polyethylene glycol (PEG) with a molecular weight range of 200 g/mol was supplied from Merck Life Sciences, India.
(c) Ethanol was supplied from Honyon International Laboratories, China.

A silica loading of 65% was used to prepare the STF [68]. Two key terms were defined before proceeding: particle loading, which indicates the proportion of silica

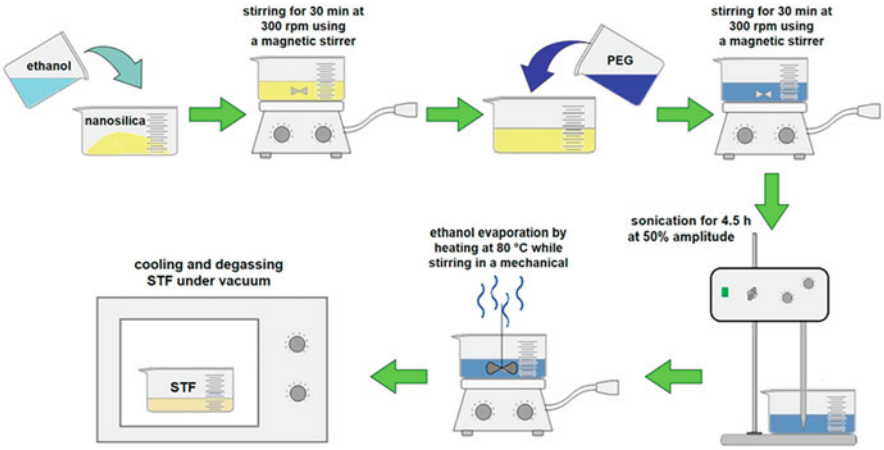

Fig. 7.1 STF fabrication Ref. [69]

by weight (w/w), and packing fraction (ϕ), which describes the percentage of silica in the prepared STF by volume (v/v). The packing fraction is calculated using Eq. 7.1. The densities for the silica and PEG at 25 °C are 2.01 g/cm^3 and 1.125 cm^3, respectively, resulting in a packing fraction of 0.51:

$$\phi = \frac{\left(m/\rho\right)_{\text{Silica}}}{\left(m/\rho\right)_{\text{Silica}} + \left(m/\rho\right)_{\text{PEG}}} \tag{7.1}$$

where $\left(m/\rho\right)_{\text{Silica}}$= mass-to-density ratio of silica and $\left(m/\rho\right)_{\text{PEG}}$= mass-to-density ratio of PEG base fluid. The product needs well-distributed silica particles in PEG so that ethanol is used for diluting the suspension for ease-of-distribution. The STF was produced using a procedure that combines mechanical mixing and ultrasonication. At the first step, silica particles were added in an excessive amount of ethanol. PEG was added to the suspension after the mechanical mixing at 300 rpm for 30 min. Then, another 30 min of mechanical mixing was applied to the suspension. Completing this step, the mixture was subjected to ultrasonication at 50% amplitude and 24 kHz for 4.5 h. In order to remove the ethanol from the suspension, the mixture was rested at 80 °C while blending it in a mechanical stirrer. After the cooling stage, the suspension was vacuumed to eliminate the air bubbles in the suspension. Figure 7.1 shows the procedures that were followed to fabricate the STF.

The rheological characteristics of the STF were evaluated in an Anton Paar MCR301 rheometer. The rheology measurements were carried out at 25 °C with a 50-mm-diameter parallel plate configuration having a 0.5 mm gap between the plates. Rheology results were evaluated in terms of two main parameters: critical shear rate ($\dot{\gamma}_c$) and peak viscosity (η_{peak}). Figure 7.2a shows the rheology flow curve for the STF. The apparent viscosity initially decreases (Region-1), and this trend continues until the shear thickening onset at the critical shear rate, where the

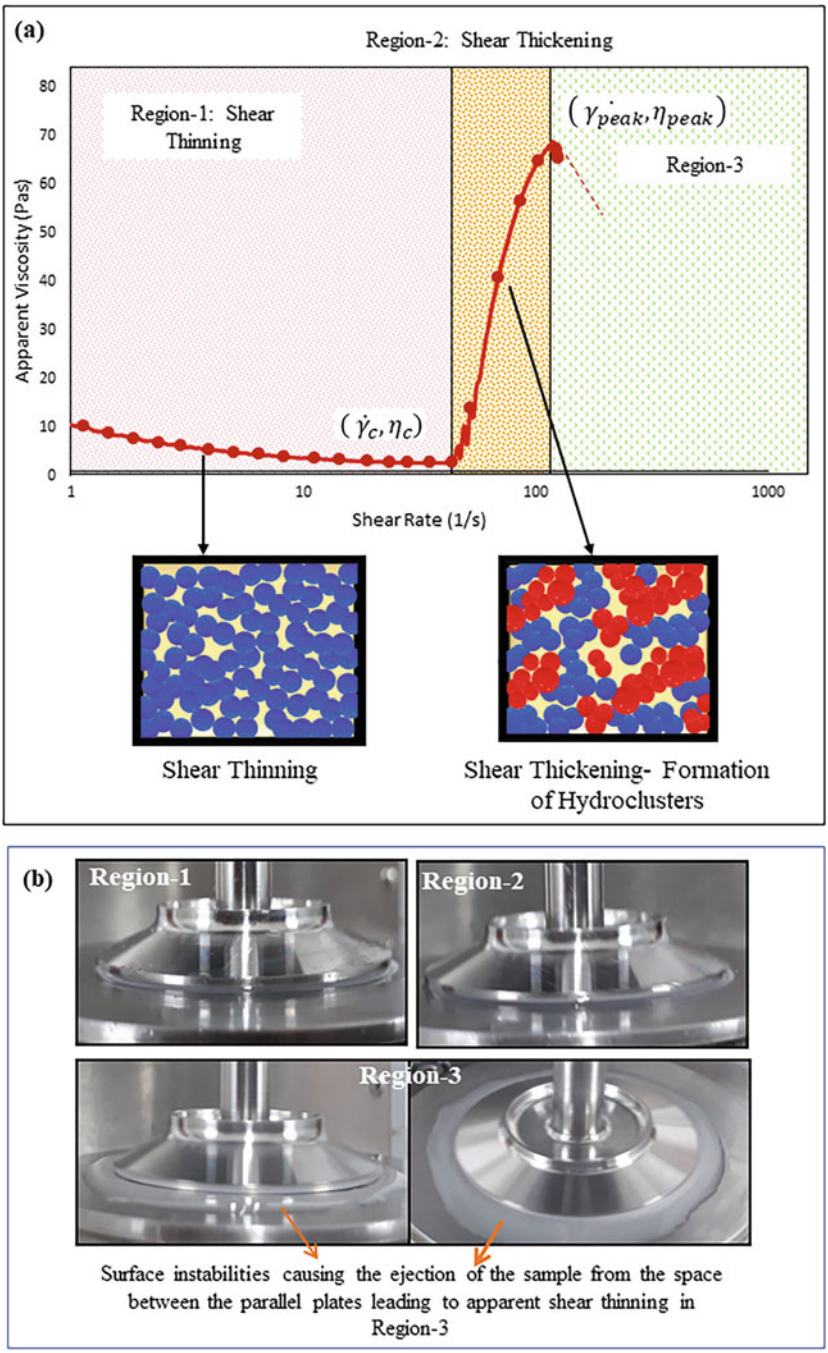

Fig. 7.2 (**a**) STF flow curve and (**b**) STF sample images during rheological measurements Ref. [74]

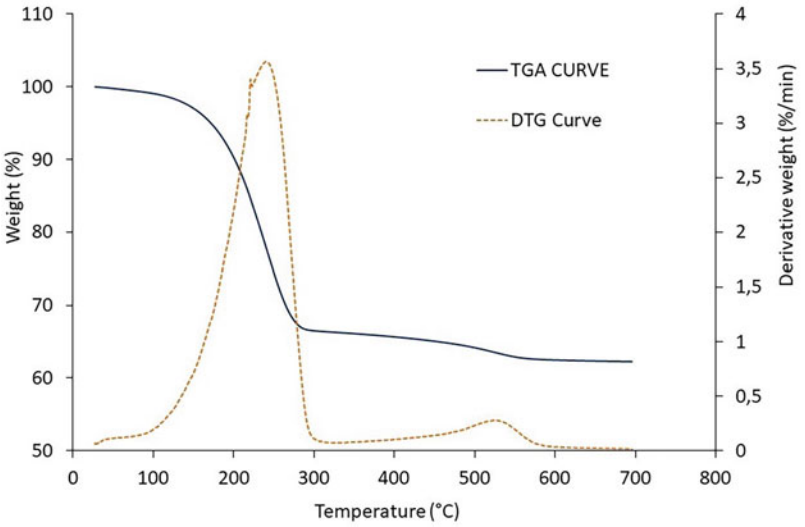

Fig. 7.3 TGA and DTG curves for STF

apparent viscosity is called critical viscosity (η_c). Beyond this point, the viscosity drastically increases to the peak viscosity (Region-2) [36]. The viscosity shows a reduction such as thinning only after the peak point (Region-3) [68, 70]. Figure 7.2b shows the STF samples at three different regions related to the rheological behavior. The apparent viscosity increases upon reaching out the critical shear rate and thereby generates surface instabilities, which lower the gap size as well as cause the spilling of some amount of sample between the plates. The reduced amount of sample leads to a reduction in the torque required to maintain the shear rate constant. Due to this, a lower magnitude of viscosity is observed in Region-3; however, this cannot be regarded as the actual flow curve for the STF at that region [32, 70]. The hydrocluster theory is attributed with providing a more comprehensive explanation for the shear thickening as seen in Region-2 [33]. Following the critical shear rate, the increase in the fluid viscosity results in the formation of hydroclusters, which are self-organized, nonequilibrium microstructures that form under strong flows. The particle motions get difficult as a result of hydroclustering, and viscosity increases by this way [71–73].

Thermogravimetric analysis (TGA) of the synthesized STF was conducted in an inert nitrogen environment. Figure 7.3 shows the TGA and derivative thermogravimetry (DTG) curves. From these curves, PEG shows a degradation at about 240 °C. Another change is observed at about 550 °C, which gives a minor peak in the DTG curve. This may arise from the decomposition of any bonded solvent that may have been present during the formation of the nanoparticles. A value of 62.5% was obtained for the silica loading percent from the TGA curves. With only a 2.5% manual handling variance, this figure is more of an expected value.

The additional percentage of 65% has therefore been mentioned throughout the chapter even though the real silica loading weight percentage is 62.5%.

7.2.2 *Manufacturing of STF Based Composites*

In order to achieve an enhanced energy dissipation under ballistic impact, three different case studies are discussed focusing more on the details of STF based composite manufacturing. The following materials were used for the fabrication of STF based composite panels:

(a) 3D E-glass fabrics with a silane finish (Paraglass/8) were supplied from Parabeam Industries, the Netherlands. The areal weight is 936 g/m^2. An exceptional feature as depicted in Fig. 7.4, these products have a 3D structure with interconnected passageways for fluid flow.
(b) Aramid mats (Kevlar-362S) with an areal weight of 185 and 400 g/m^2 and a layer of 30 g/m^2 E-glass surface mat were supplied from Owen Corning, India.
(c) Epoxy resin (Araldite CY-230-1) and hardener (Aradur HY-951) were supplied from Huntsman Advanced Materials, India.

Since the epoxy resin and hardener combination have a gel time of 160 min at room temperature, HLU and VARIM techniques had a sufficient time to successfully manufacture the composites. The composite panels were prepared using three different configurations as given in the next sections.

7.2.2.1 Case-I: Incorporation of STF in 3D-Mat composites with Kevlar Facesheets

The first step in this fabrication process is to manufacture the 3D-mat composites. To do so, the 3D-mat fabrics were first located on an aluminum mold with a mold-releasing agent application. The resin-hardener combination was then applied with a hardener to resin ratio of 1:10 by weight. A hand-roller was used for epoxy application on the 3D-mats. The composites were rested at room temperature for

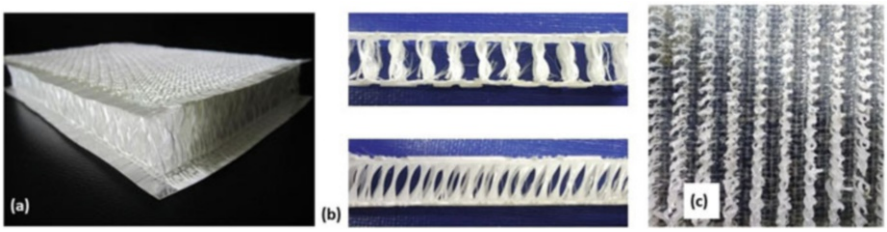

Fig. 7.4 (**a**) Virgin 3D-mat prior to curing, (**b**) cross sections of the cured 3D-mat composites, and (**c**) interconnected channels within 3D-mat as viewed after removal of the top surface Ref. [75]

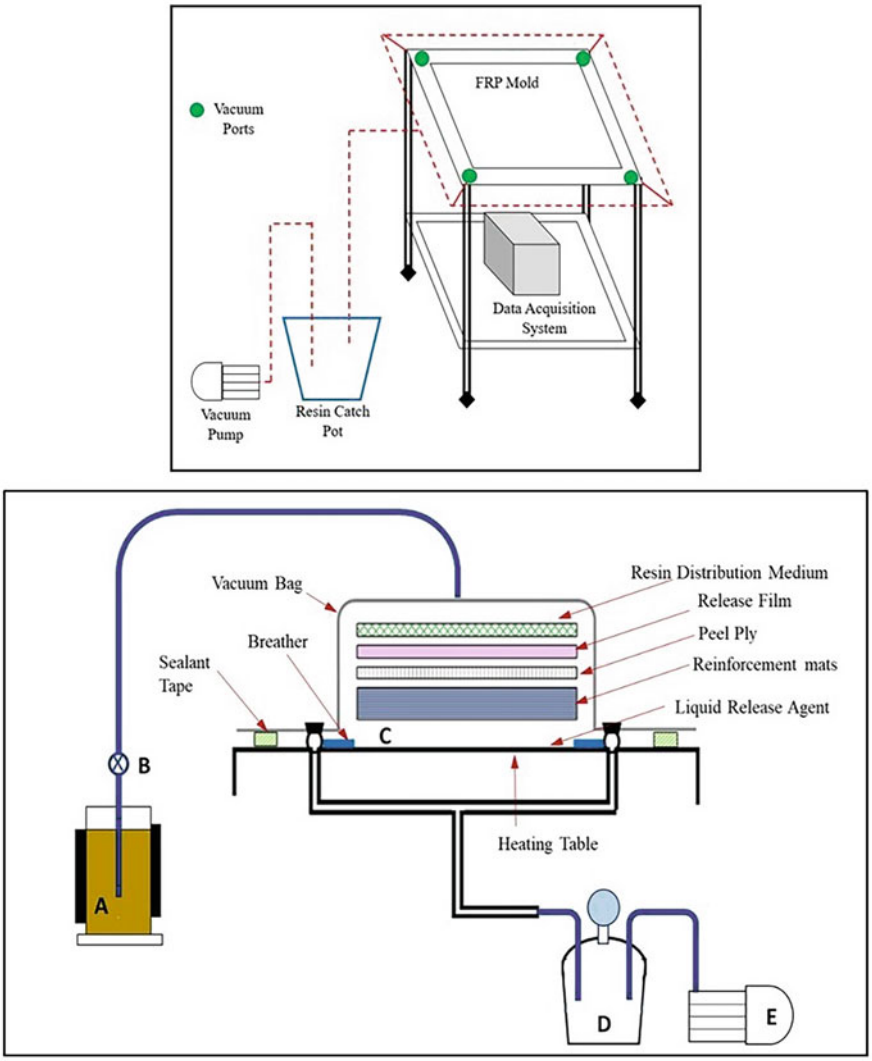

Fig. 7.5 Schematic diagram of VARIM system Ref. [74]

6 h and then undergone to a curing stage at 60 °C for 4 h. After this stage, the composites were sized into 10 cm × 10 cm specimens, and the edges were sealed with epoxy application. Three different configurations were designed for these composites: Type-1: kept pristine; Type-2: filled with PEG; and Type-3: filled with STF. PEG and STF were filled in the specimens by drilling tiny holes on the composites. Four layers of Kevlar fabrics were integrated with epoxy matrix by VARIM method to produce Kevlar facesheets as shown in Fig. 7.5 [76]. A composite mold was used to maintain the dimensional stability in the products. Table 7.1

Table 7.1 Details of the specimens in Case-I

Specimen	Configuration	Manufacturing method	Thickness (mm)	Mass (g)	Areal weight (kg/m^2)
(a) Reference 3D-Mat Composites					
Ref_3D1_H	1 layer of 3D-mat	HLU	9.41	52.8	5.280
Ref_3D1_PEG	1 layer of PEG filled 3D-mat		11.26	155.8	15.580
Ref_3D1_STF	1 layer of STF-filled 3D-mat		11.63	189.2	18.920
(b) 3D-Mat-Kevlar Composites					
KEV_3D1_H	1 layer of 3D-mat with 4 + 4 Kevlar facesheets	VARIM	11.43	195.58	5.417
KEV_3D1_PEG	1 layer of PEG filled 3D-mat with 4 + 4 Kevlar facesheets		12.66	308.14	8.535
KEV_3D1_STF	1 layer of STF-filled 3D-mat with 4 + 4 Kevlar facesheets		12.29	289.59	8.021

Table 7.2 Details of the VARIM process

Equipment Specifications	
Vacuum pump type	Rotary high vacuum pump
Pressure	5 mTorr
Mold dimension	609 mm × 609 mm × 4 mm
Injection location	Center of the mold
Mold filling time	20–50 min depending on thickness
Process specifications	
Resin system	Epoxy resin system
Curing	4 h at room temperature + 4 h at 60 °C
Post curing	7 h at 60 °C

gives the details of the specimens in Case-I. Table 7.2 gives the details of the VARIM process in the manufacturing of Kevlar facesheets.

As shown in Fig. 7.5, a delivery tube was dipped into a glass container (A) with a 2000 ml capacity that contained the resin/hardener system. A flow control valve (B) attached to the delivery tube was in charge of controlling the flow. The delivery tube was plugged in the middle of the mold (C). A catch pot (D) connected the vacuum pump (C) to the four corners and four ports of the mold. The catch pot had a suction pump (E) attached to it. First, in order to get the mold ready for demolding, it was cleaned, and a releasing agent was then used to coat it. At the bottom of the mold, the combined hybrid reinforcement was put in place. Peel plies were applied to the top to create a clean and untainted surface. These were then followed by a release film, which enabled a uniform distribution of resin and good heat resistance. A green mesh covering above it removed any trapped air or volatiles. In order to absorb the

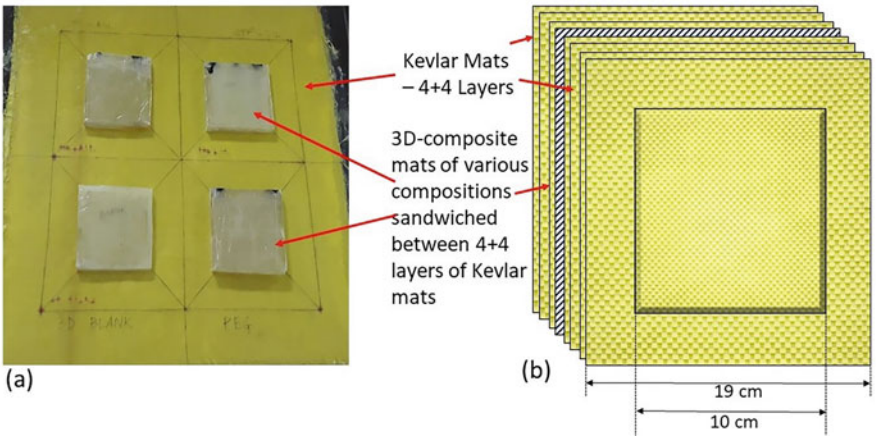

Fig. 7.6 (**a**) 3D-mat composites before being assembled with Kevlar facesheets and (**b**) design of composite in Case-I Ref. [75]

extra resin contained in the composite layup, bleeder textiles were positioned on the sides connecting with the reinforcing assembly. The use of vacuum bags and double-sided tape to seal the edges resulted in a closed system. The air was removed using a vacuum pump. The same resin/hardener system, which was combined in a 10:1 weight-to-weight ratio, was applied and injected through a supply line with a flow control valve (B) in the middle of the mold with the aid of vacuum created by the vacuum pump. Curing cycle consisted of specimens resting at room temperature for 6 h and at 60 °C for 4 h successively. The specimens were demolded, sized into 19 cm × 19 cm, and subjected to ballistic testing after curing. Figure 7.6 shows the 3D-mat composites before being assembled with Kevlar facesheets and the layers within the structure.

Figure 7.7 shows the SEM images of the 3D-mat composites having Kevlar facesheets. Before taking the SEM photos, the composites were divided into thin slices and dried at 100 °C to remove any potential moisture or solvent. Then the specimens were visualized using their strands. The figures clearly show that KEV_3D1_H has a clean and smooth strand because the mat has no fluid inside. On the other hand, heating the specimen KEV_3D1_PEG led to a porous surface on the fibers. In this perspective, KEV_3D1_STF is particularly significant since it clearly demonstrates the presence of silica nanoparticles on the fiber surfaces. The reliability of the SEM image results was confirmed by the EDX analyses from the specimens. It was expected that the EDX graphs for KEV_3D1_H would only show the carbon and oxygen peaks because the strands were cured with epoxy resins, which mostly contain these elements. KEV_3D1_PEG, on the other hand, exhibited peaks for carbon and oxygen as well, but with a greater proportion of oxygen due to the presence of PEG. There were peaks for silicon, carbon, and oxygen on the EDX curves for KEV_3D1_STF, indicating the presence of silica nanoparticles on the surface.

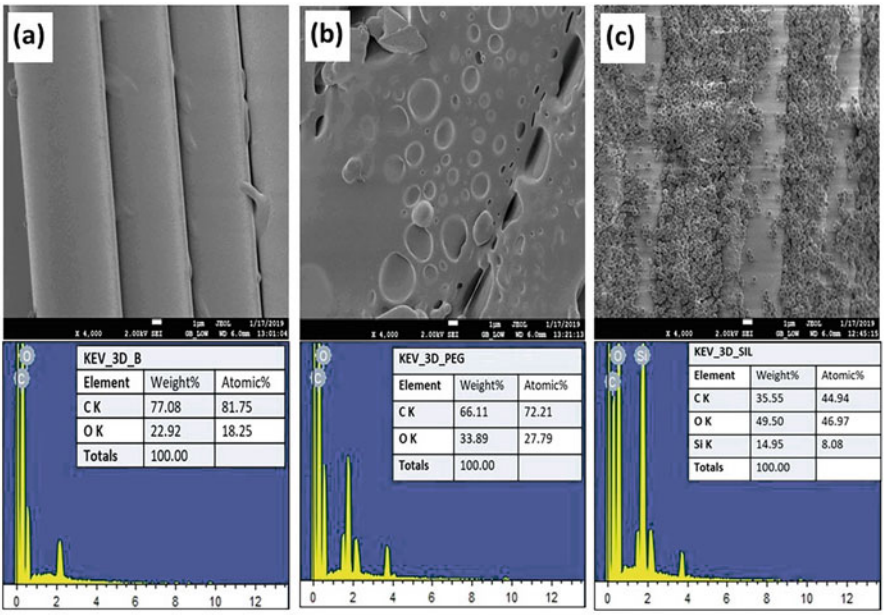

Fig. 7.7 SEM and EDX for (**a**) KEV_3D1_H, (**b**) KEV_3D1_PEG, and (**c**) KEV_3D1_STF Ref. [75]

7.2.2.2 Case-II: Incorporation of STF in 3D-mat composites with Glass-Kevlar hybrid facesheets

The process for the manufacture of the 3D-mat composites for this case was exactly same with Case-I. The difference was using hybrid facesheets that were combined with Glass and Kevlar layers. Similarly, the specimens were designed as Type-1: kept pristine; Type-2: filled with PEG; and Type-3: filled with STF. For the fabrication of the facesheets, four layers of Glass and Kevlar fabrics were alternately stacked and combined with epoxy matrix with the same resin/hardener system as described in Case-I. The specimens were cured, then demolded, and sized into 20 cm × 20 cm. Following that, the specimens were subjected to ballistic tests. Figure 7.8 shows the design of specimens. Table 7.3 gives the details of specimens in Case-II.

After drying the 3D-mat composites at 100 °C, the strands on the facesheets of the specimens were investigated with electron microscopy. Figure 7.9 shows the SEM images of the fibers. The images show that the fibers in Ref_3D2_H are smooth and liquid-free, whereas the fibers in Ref_3D2_PEG have a porous surface. The porous surface in this specimen may have developed by the PEG contact that was present during the heating process at 100 °C. On the other hand, fibers in Ref_3D2_STF are rougher than those in the neat fabric due to the adhesion of spherical silica nanoparticles. Additionally, these particles are seen to be scattered within the gaps

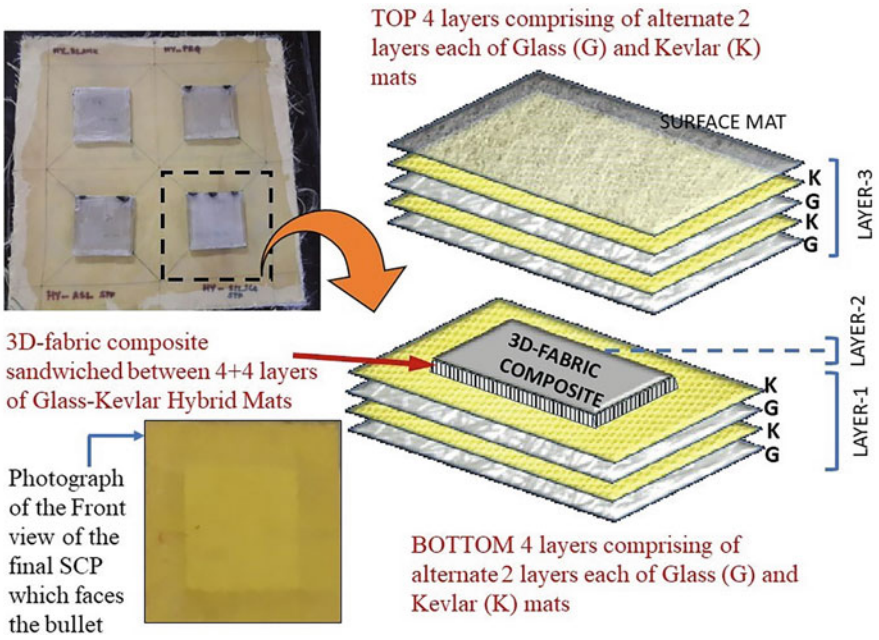

Fig. 7.8 Design of specimens in Case-II Ref. [74]

Table 7.3 Details of the specimens in Case-II

Specimen	Configuration	Manufacturing Process	Thickness (mm)	Mass (g)	Areal weight (kg/m^2)
(a) Reference 3D-Mat Composites					
Ref_3D2_H	1 layer of 3D-mat	HLU	9.98	51.45	5.15
Ref_3D2_PEG	1 layer of PEG filled 3D-mat		10.2	106.36	10.64
Ref_3D2_STF	1 layer of STF-filled 3D-mat		10.41	130.89	13.09
(b) Hybrid 3D-Mat-Glass-Kevlar Composites					
KGEV_3D2_H	1 layer of 3D-mat with 4 + 4 Glass-Kevlar facesheets	VARIM	12.54	282.9	7.07
KGEV_3D2_PEG	1 layer of PEG filled 3D-mat with 4 + 4 Glass-Kevlar facesheets		12.39	330.8	8.27
KGEV_3D2_STF	1 layer of STF-filled 3D-mat with 4 + 4 Glass-Kevlar facesheets		12.08	362.3	9.06

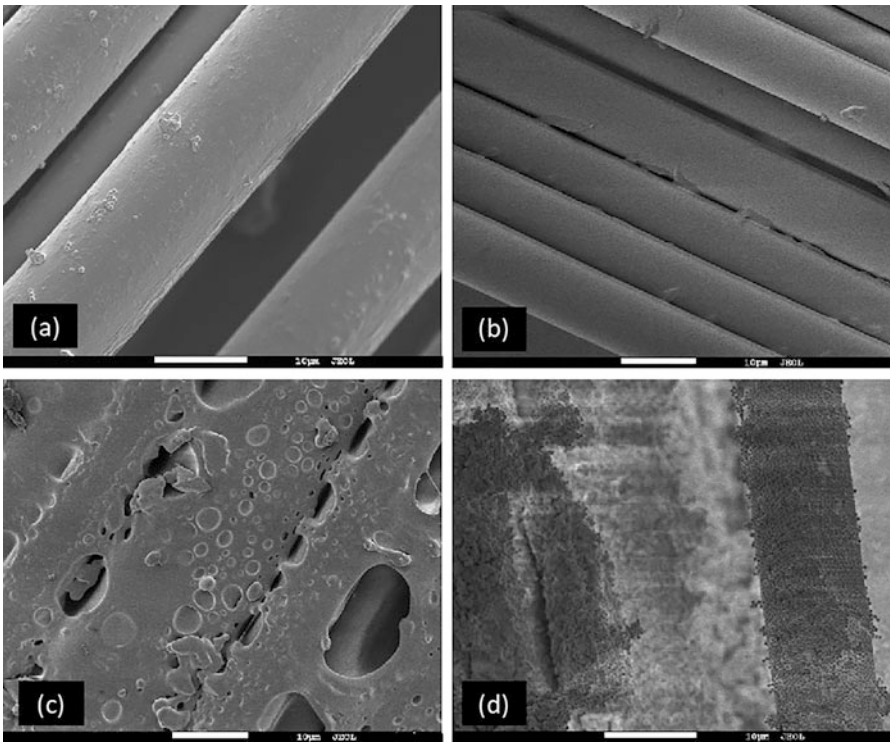

Fig. 7.9 SEM images of (**a**) 3D-mat before adding resin, (**b**) Ref_3D2_H, (**c**) Ref_3D2_PEG, and (**d**) Ref_3D2_STF Ref. [74]

between the fibers [73]. This can be explained by the fact that silica based STF previously filled in the annulus of the Ref_3D2_STF before the specimen was dried. We may infer from the microstructural images that during the VARIM method processing, the STF occupying the composite core did not dry out, did not deteriorate, or was not contaminated with the entering resin. The resin and hardener mixture recorded a glass-transition temperature of 99.9 °C according to the differential scanning calorimetry (DSC) results.

7.2.2.3 Case-III: Incorporation of STF in Double Core 3D-Mat Composites with Kevlar Facesheets

An aluminum mold with a coating of mold release agent was utilized to prepare the double 3D-mat core composites. Two layers of 3D-mat were piled one on top of the other and placed on the mold using the HLU method. A mixture of resin and hardener in a weight ratio of 10:1 served as the matrix for the composite. The excess matrix was then consolidated using a hand-roller as shown in Fig. 7.10a. Upon curing the matrix, the composites were cut into 10 cm × 10 cm sizes. The edges of

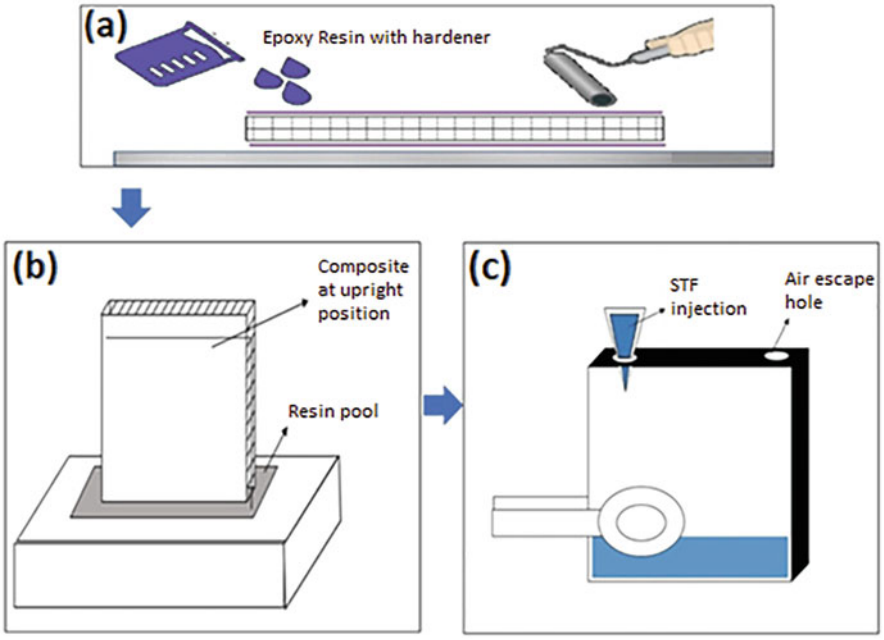

Fig. 7.10 Specimen preparation steps in Case-III Ref. [77]

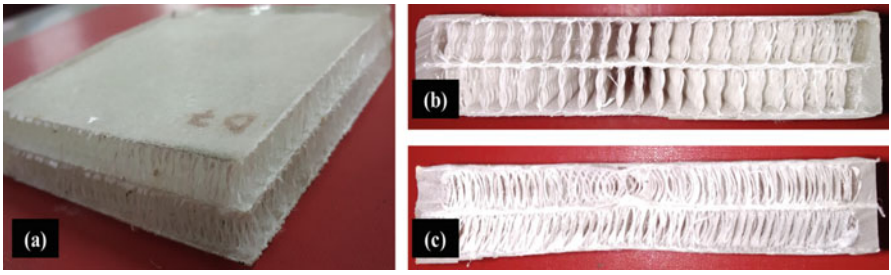

Fig. 7.11 (**a**) Double core 3D-mat and cross-sectional view of double core 3D-mat for (**b**) principal and (**c**) secondary directions Ref. [77]

the composites were sealed by dipping them into the resin/hardener system as shown in Fig. 7.10b. Similar to the other cases, the composites were designed as Type-1: kept pristine; Type-2: filled with PEG; and Type-3: filled with STF. For the PEG and STF-filled composites, a small hole was drilled on one of the edges, and then the filler liquids were injected into the composites as shown in Fig. 7.10c. Figure 7.11 shows the double core 3-D mat. The interconnected channels for PEG or STF fillers are obviously seen in the cross-sectional views. These images also exhibit how the cross-linking of the epoxy and double core 3D-mats resulted in a fusion at the interface.

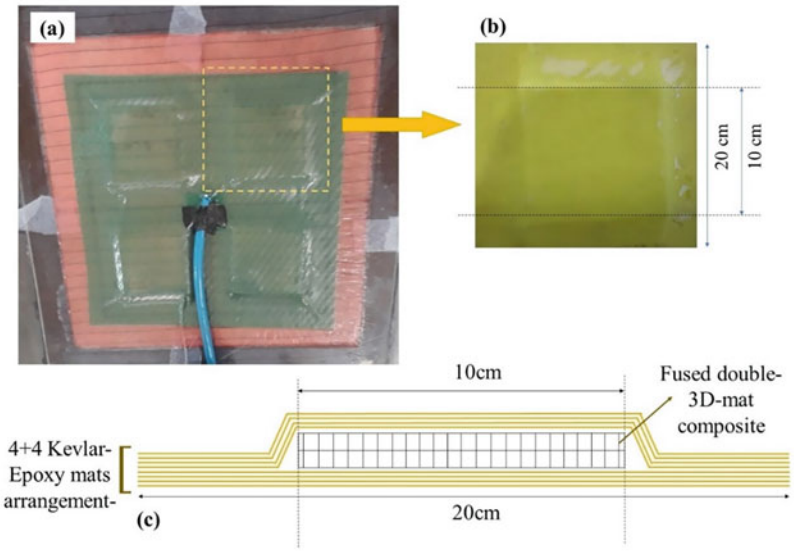

Fig. 7.12 (**a**) VARIM processing for the specimens, (**b**) specimen after demolding, (**c**) design of specimens in Case-III Ref. [77]

For the fabrication of facesheets, the matrix consisted of the resin/hardener mixture with a 10:1 weight-to-weight ratio. The VARIM process was employed to improve the fiber/volume fraction and the reproducibility of the product. The composites were demolded and cut into 20 cm × 20 cm sizes following the curing cycle as described in the previous cases. Ballistic tests were then carried out to investigate the impact properties of these specimens. Figure 7.12 shows the VARIM process along with the configuration and arrangement of the layers in the double core 3D-mat composites. Table 7.4 gives the details of specimens in Case-III.

Similar to the other cases, these specimens were also investigated with electron microscopy. The double core 3D-mat composites were cut and dried at 100 °C, and then a strand of fibers from the inner side facesheets was visualized with a microscope. Figure 7.13 shows the SEM images for each specimen. Due to the absence of fluids, the fiber surface in Ref_3D3_H is quite smooth. The fiber in Ref_3D3_PEG exhibits a relatively smooth surface and includes some porous characteristics due to the PEG effect on the fiber. Two different magnifications were used for Ref_3D3_STF. The fibers are covered by spherical silica nanoparticles as seen in both images. These photos exhibit that the fluid within the double core 3D-mat composites did not degrade or are not being contaminated with the incoming resin during the VARIM process.

Table 7.4 Details of the specimens in Case-III

Specimen	Configuration	Manufacturing process	Thickness (mm)	Mass (g)	Areal weight (kg/m^2)
(a) Reference Double Core 3D-Mat Composites					
Ref_3D3_H	2 layers of 3D-mat	HLU	17.63	69.34	0.693
Ref_3D3_PEG	2 layers of PEG filled 3D-mat		18.09	185.44	1.854
Ref_3D3_STF	2 layers of STF-filled 3D-mat		18.05	247.94	2.479
(b) Double Core 3D-Mat-Kevlar Composites					
KEV_3D3_H	2 layers of 3D-mat with 4 + 4 Kevlar facesheets	VARIM	20.53	277.4	0.694
KEV_3D3_PEG	2 layers of PEG filled 3D-mat with 4 + 4 Kevlar facesheets		20.31	374.6	0.937
KEV_3D3_STF	2 layers of STF-filled 3D-mat with 4 + 4 Kevlar facesheets		20.1	449.1	1.123

7.2.3 Ballistic Impact Testing

Ballistic tests were conducted to investigate the energy absorbing properties of the STF based composites upon high velocity impact. The tests were carried out at the Terminal Ballistics Research Laboratory (TBRL), Chandigarh, India. For Case-I and Case-II, the targets were impacted with 9 mm bullets having a lead core and an average weight of 15.6 g. Each target was tested for three repetitive impacts from 5 m distance. The impact velocities were measured with a laser chronograph system. According to the measurements, the impact velocities were varied from 140 to 170 m/s. In addition, another chronograph was located at the back side of the targets to measure the residual velocity of the bullets after perforating the targets as shown in Fig. 7.14. For Case-III, a 9 × 19 mm barrel piston was used for the same ballistic testing setup with the other cases. Because the barrel length was increased, impact velocities were about 400 m/s in the tests. Eq. 7.2 and Eq. 7.3 give the impact energy (E_i) and residual energy (E_R) based on the impact velocity (V_i) and residual velocity (V_R) of the bullets. The difference between the impact and residual energies is calculated as energy absorbing by the targets (E) as given in Eq. 7.4. Eq. 7.5 gives the percentage of absorbed energy by the targets. Percentage increase in the absorbed energies of the reference targets is calculated in Eq. 7.6 by comparing the PEG or STF included targets. E_{hc} gives the energy absorbed by the reference targets, while E_{fc} is the energy absorbed by the targets with a fluid (PEG or STF) included cores.

$$E_i = 0.5mV_i^2 \tag{7.2}$$

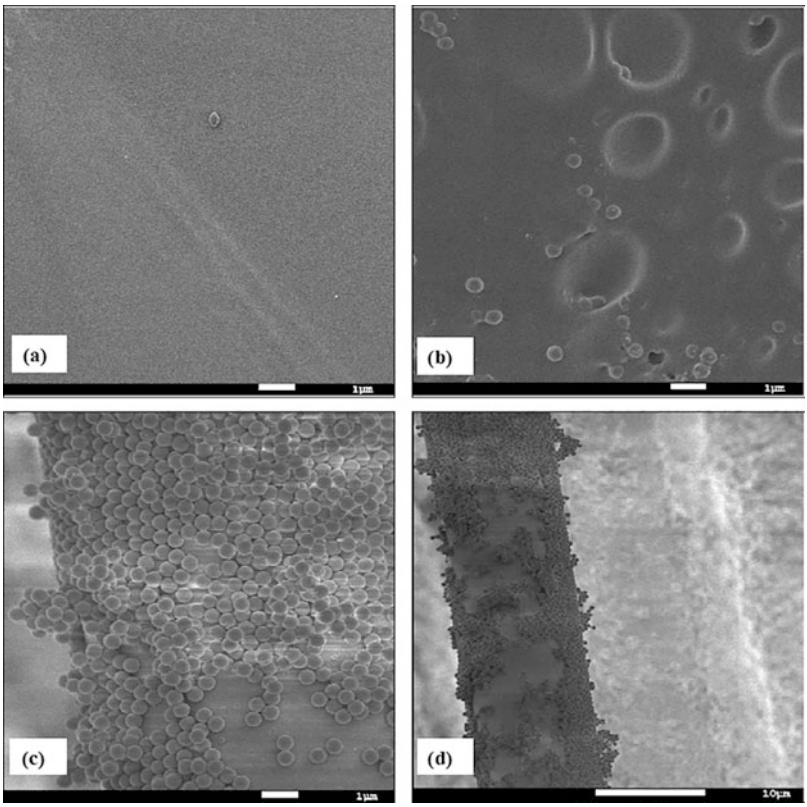

Fig. 7.13 SEM images of (**a**) Ref_3D3_H, (**b**) Ref_3D3_PEG, and (**c–d**) Ref_3D3_STF at different magnifications Ref. [77]

$$E_R = 0.5mV_R{}^2 \tag{7.3}$$

$$E = 0.5mV_i{}^2 - 0.5mV_R{}^2 \tag{7.4}$$

$$\%\ \text{Absorbed Energy} = \frac{E}{E_i} \times 100\% \tag{7.5}$$

$$\%\ \text{Increase in Absorbed Energy} = \frac{E_{fc} - E_{hc}}{E_{hc}} \times 100\% \tag{7.6}$$

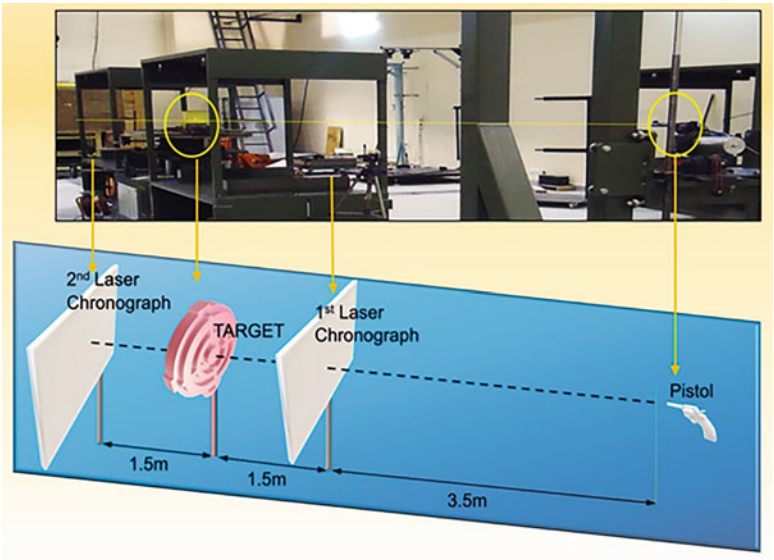

Fig. 7.14 Ballistic test setup Ref. [74]

7.3 Results and Discussion

7.3.1 Energy Absorbing Capacities

Table 7.5 shows the energy absorbing capabilities for the targets. By comparing the results, it is clear that the reference composites are substantially less effective in dissipating impact energy. The Hybrid-Kevlar-Glass layer facesheets in Case-II as well as the Kevlar facesheets in Case-I and Case-III enhance the protective performance of the 3D core materials by increasing the energy absorbing capabilities. The reference composites without any fluid reinforcement show significantly less energy absorbing than those incorporated with PEG or STF. Moreover, STF included composites provide higher energy absorbing capabilities than PEG included ones. Higher energy absorbing performances in the STF integrated composites stem from the shear thickening behavior, which is triggered when the characteristic shear rate of the bullet is higher than the critical shear rate of the STF. Figure 7.15 shows the energy absorbing capabilities for each case. The data given in the charts is based on the average values of the repetitive tests.

Considering Case-I, KEV_3D1_H is able to absorb 56.31% of the energy incident, while Ref_3D1_H is only able to do so for 5.68% of the impact energy. Similar to this, KGEV_3D2_H is able to absorb 49.06% of the energy incident, while Ref_3D2_H absorbs the energy of 6.63%. These results show that facesheets have a significant role in the energy absorbing performance. Despite an increase in the energy absorbing performance by using the facesheets in Case-III, the increase is not at higher levels as such in Case-I and Case-II. This could be due to the double layer

Table 7.5 Energy absorbing capabilities for the targets

Specimen	Impact velocity (m/s)	Residual velocity (m/s)	Impact energy (J)	Energy absorbed (J)	Energy absorbed (%)	Increase in energy absorbed (%)
Case-I						
(a) Reference 3D-Mat Composites						
Ref_3D1_H	168.90	164.03	167.32	9.504	5.680	–
Ref_3D1_PEG	157.63	145.73	146.95	21.190	14.420	122.95
Ref_3D1_STF	157.37	136.50	145.35	35.934	24.723	278.08
(a) Reference 3D-Mat-Kevlar Composites						
KEV_3D1_H	*160.73*	*105.80*	151.65	85.400	56.314	–
KEV_3D1_PEG	147.20	56.30	127.38	103.511	81.259	21.21
KEV_3D1_STF	157.53	20.60	148.51	142.988	96.280	67.43
Case-II						
(a) Reference 3D-Mat Composites						
Ref_3D2_H	178.10	171.95	186.05	12.63	6.63	–
Ref_3D2_PEG	176.77	168.87	187.60	15.96	8.79	26.42
Ref_3D2_STF	180.00	141.07	185.32	72.83	36.50	476.82
(b) Hybrid 3D-Mat-Glass-Kevlar Composites						
KGEV_3D2_H	181.95	128.80	194.86	96.24	49.06	–
KGEV_3D2_PEG	181.93	125.33	197.18	102.01	52.53	5.99
KGEV_3D2_STF	173.13	24.33	184.49	165.69	94.50	72.16
Case-III						
(a) Reference Double Core 3D-Mat Composites						
Ref_3D3_H	406.55	393.40	627.81	40.35	6.43	–
Ref_3D3_PEG	403.57	387.57	610.81	47.40	7.77	17.49
Ref_3D3_STF	409.80	384.40	629.77	75.65	12.01	87.49
(b) Double Core 3D-Mat-Kevlar Composites						
KEV_3D3_H	405.40	374.25	613.08	87.61	14.49	–
KEV_3D3_PEG	410.43	373.83	631.68	107.58	17.05	22.8
KEV_3D3_STF	407.70	364.07	623.33	126.12	20.24	43.96

of core material in Case-III that enhances the effect of core material in energy absorbing mechanism.

Considering the fluids in the core of the composites, there are obvious developments in the energy absorbing. PEG inclusion provides a viscous medium inside the core section so that producing increased forces making a difficult-to-penetrate environment for the bullets. On the other side, STF included composites show the highest energy absorbing capacities due to the shear thickening effect during the penetration process. The STF used in the composites show a thickening onset at about 40 s^{-1} (recalling Fig. 7.2). When the shear rate during the bullet penetration process exceeds the thickening onset point of 40 s^{-1}, hydroclustering develops in the suspension by forming microscale particle groups [29]. These formations lead to a solid-like behavior in the suspension and thereby provide an additional mechanism in the targets. It is anticipated that hydrogen bonds are developed when the polymer

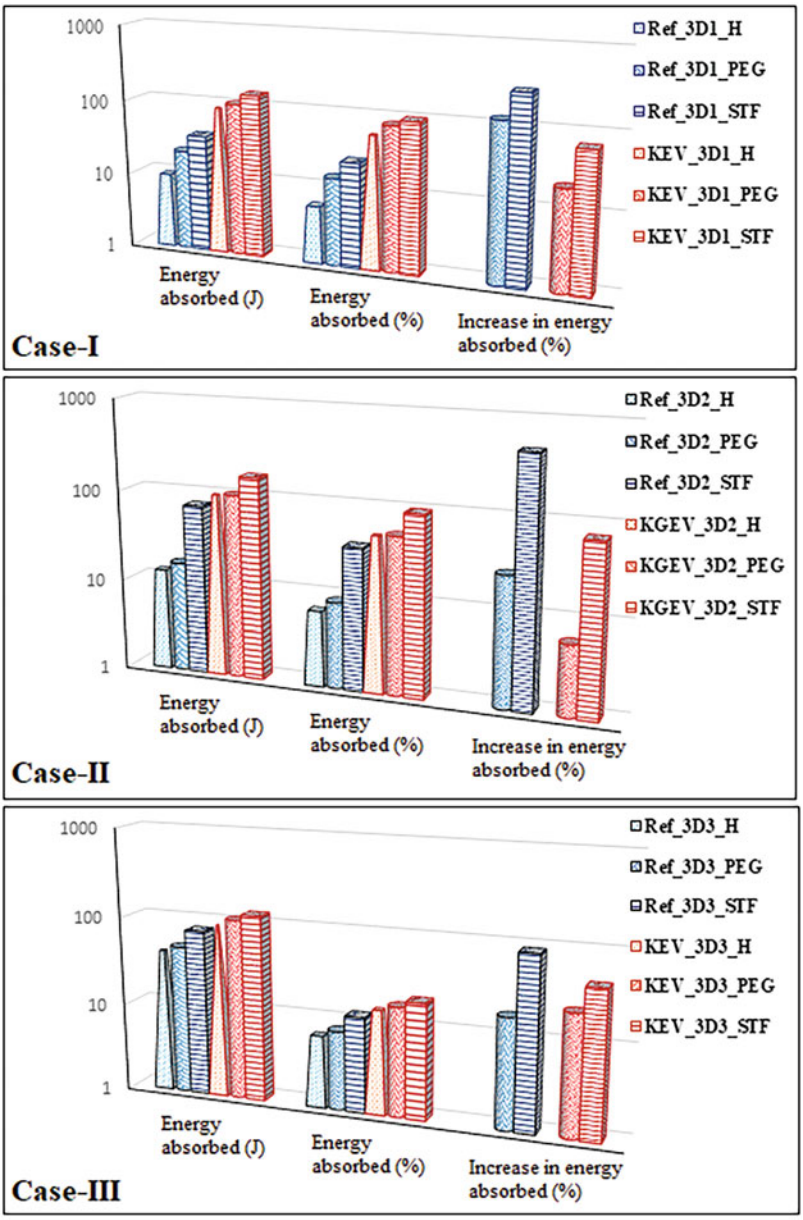

Fig. 7.15 Energy absorbing capabilities for the targets

chains in PEG interact with the surface hydroxyl groups of the silica. As a result, a polymer layer known as the solvation layer forms a surrounding envelop around the silica nanoparticles [78–80]. As shown in Fig. 7.16, intra- and inter-hydrogen

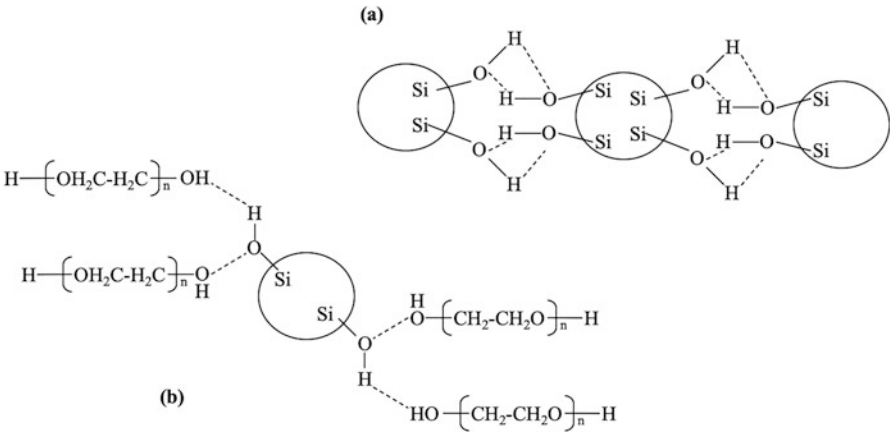

Fig. 7.16 (**a**) Intra-particular H-bonding within the isolated silanol groups and (**b**) inter-particular H-bonding between the hydroxyl groups on the surface of the silica nanoparticles and polyethylene glycol molecules Ref. [74]

bonding between the polymer chains and the surface hydroxyl groups leads to the solvation layer to be formed on the silica surface. The distance between the silica nanoparticles grows as a result of the solvation layers, increasing deflocculation and interparticle repulsion forces. If the STF is loaded with a large amount of silica nanoparticles, there will be larger surface areas resulting in an increased reactivity. Some carrier fluids do not react with the silanol groups to create the solvation layers that serve as lubricating layers between the nanoparticles. Due to the increased interparticle separation, the aggregated particles have more room to move as they rearrange from one to another [81]. The volume packing fraction is higher with a higher silica loading percentage, decreasing the lubricating effect of the layers between the particles and thereby resulting in a less interparticle separation. Because the particles move close to each other, hydroclusters can easily form at much lower shear rates, requiring less external forces to counteract the forces of attraction and repulsion between the particles. The number of nanoparticles per unit volume decreases as nanoparticle size increases, which also reduces the density of interparticle H-bonding and consequently lowering the critical shear rate in the suspension. This indicates that solvation forces of lower intensities may be adequate to cause shear thickening in the STF, showing lower values of critical shear rate and ultimately resulting in a quicker onset of shear thickening behavior with a larger silica nanoparticle size [82].

Weight of the targets should be considered to properly evaluate the energy absorbing capabilities of composites. For this purpose, specific energy absorbing is calculated by dividing the energy absorbing capacity of the composite by the weight of the composite. Hence, energy absorbing of unit weight in the composites is obtained. Table 7.6 gives the specific energy absorbing capabilities for the targets. Although there is an increasing trend in the energy absorbing capabilities of no-fluid,

Table 7.6 Specific energy absorbing capabilities for the targets

Specimen	Energy absorbing (J)	Specific energy absorbing (Jm^2/kg)
Case-I		
Ref_3D1_H	9.504	1.80
Ref_3D1_PEG	21.190	1.36
Ref_3D1_STF	35.934	1.90
KEV_3D1_H	85.400	15.76
KEV_3D1_PEG	103.511	12.13
KEV_3D1_STF	142.988	17.83
Case-II		
Ref_3D2_H	12.63	2.45
Ref_3D2_PEG	15.96	1.5
Ref_3D2_STF	72.83	5.56
KGEV_3D2_H	96.24	13.61
KGEV_3D2_PEG	102.01	12.33
KGEV_3D2_STF	165.69	18.29
Case-III		
Ref_3D3_H	40.35	5.82
Ref_3D3_PEG	47.40	2.56
Ref_3D3_STF	75.65	3.05
KEV_3D3_H	87.61	12.63
KEV_3D3_PEG	107.58	11.49
KEV_3D3_STF	126.12	11.23

PEG, and STF included composites, respectively, specific energy absorbing results are not with the same manner due to the weight effect in the composites. PEG inclusion enhances the energy absorbing capabilities for the targets; however, the weight increase due to the PEG addition is significantly high. For this reason, PEG integrated composites have lower specific energy absorbing capabilities than the targets without fluid application. STF leads to a weight gain similar to PEG in the composites. However, energy absorbing capacity of the composite is heavily increased after STF integration so that specific energy absorbing performance leaves behind those of the targets without any fluid addition for Case-I and Case-II. On the other hand, STF application does not show an efficient result in Case-III. Specific energy absorbing capacity is lower in STF included target than that with no-fluid application for Case-III. Figure 7.17 shows the specific energy absorbing capabilities for the targets.

7.3.2 Impact Damages

Figure 7.18 shows the impact damages on the composites for Case-II as a representative of all three cases mentioned in this study. As shown in the images, all the

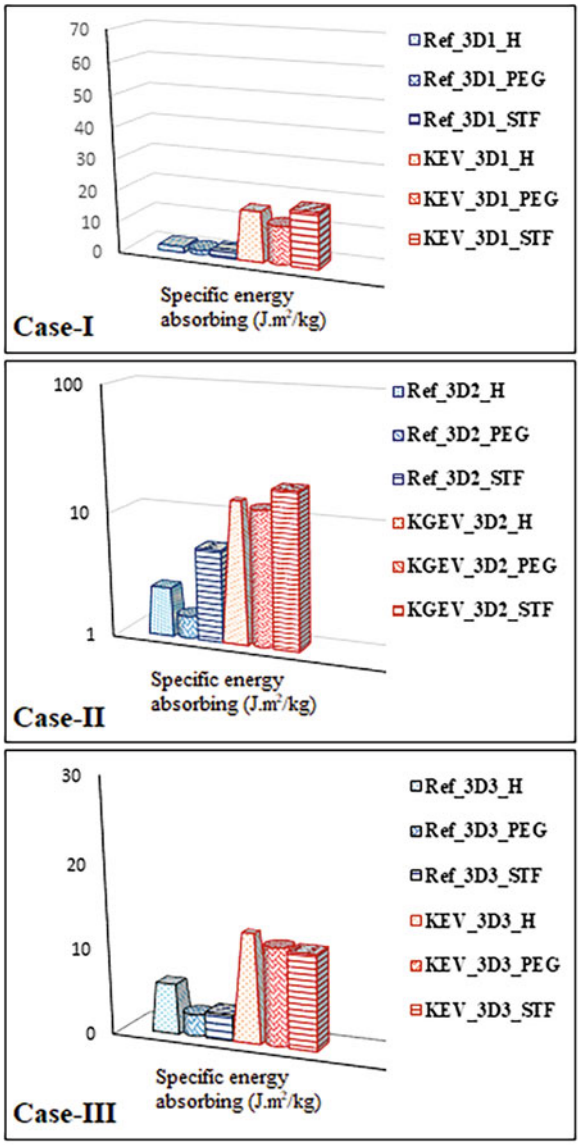

Fig. 7.17 Specific energy absorbing capabilities for the targets

targets show similar damages upon ballistic impact. Moreover, the targets in Case-I and Case-III have also the same impact damages on the surfaces. The fracture morphologies on the composites exhibit that each facesheet has a shear plug development on the front faces. Additionally, the thin surface mat on top of each panel is observed to be delaminating and breaking in each instance. Furthermore, the damages on the back faces generate cone-formation and petalling effect [83] as well as delamination and matrix cracking on the target surfaces [84]. Longitudinal and

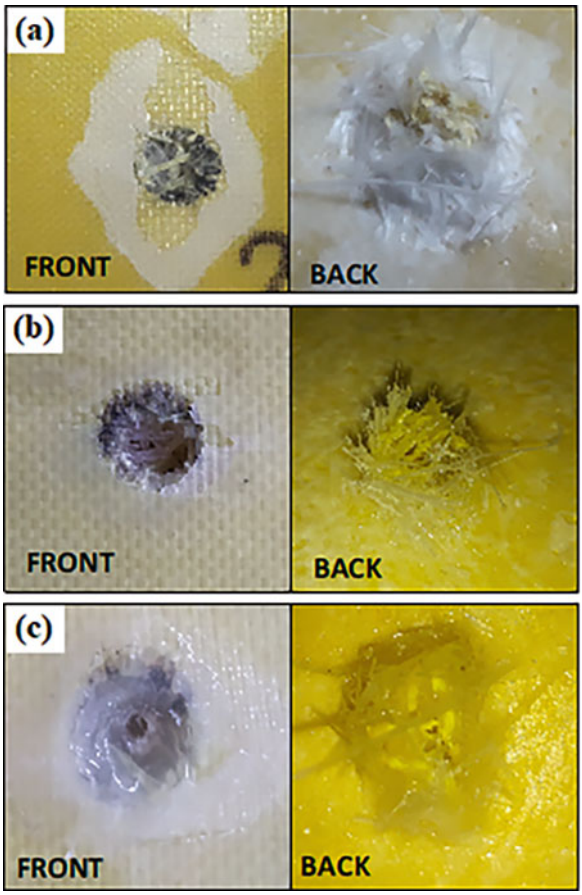

Fig. 7.18 Impact damages on the targets: (**a**) KGEV_3D2_H, (**b**) KGEV_3D2_PEG, and (**c**) KGEV_3D2_STF Ref. [74]

transverse waves are generated at the impact point when the composites are impacted [85]. Naik et al. [84] used the propagation of transverse waves during ballistic impact to explain how the impact cone formed. It is evident that the projectile transfers the kinetic energy to the composite. Primary and secondary yarn deformations, which also lead to shear plugging, are the main causes of energy absorption [86]. Transverse wave propagation during the impact process causes the conical deformation on the back face of the composites [84]. The back sides of the composites have a circular damage area having a conical eruption. The diameter of the damaged area is smaller than the diameter of the bullet due to the elastic recovery in the targets.

Figure 7.19 shows the cross-sectional views of the targets after impacts. The impact produces shear cutting deformations in the fibers due to high strain rate loading. Delamination is also visible at both front and back sides of the targets. High impact loading leads to large delamination damages at the interfaces between the facesheets and core sections. PEG provides a viscous medium for the core material and thereby contributes to the impact resistance of the composites during the impact

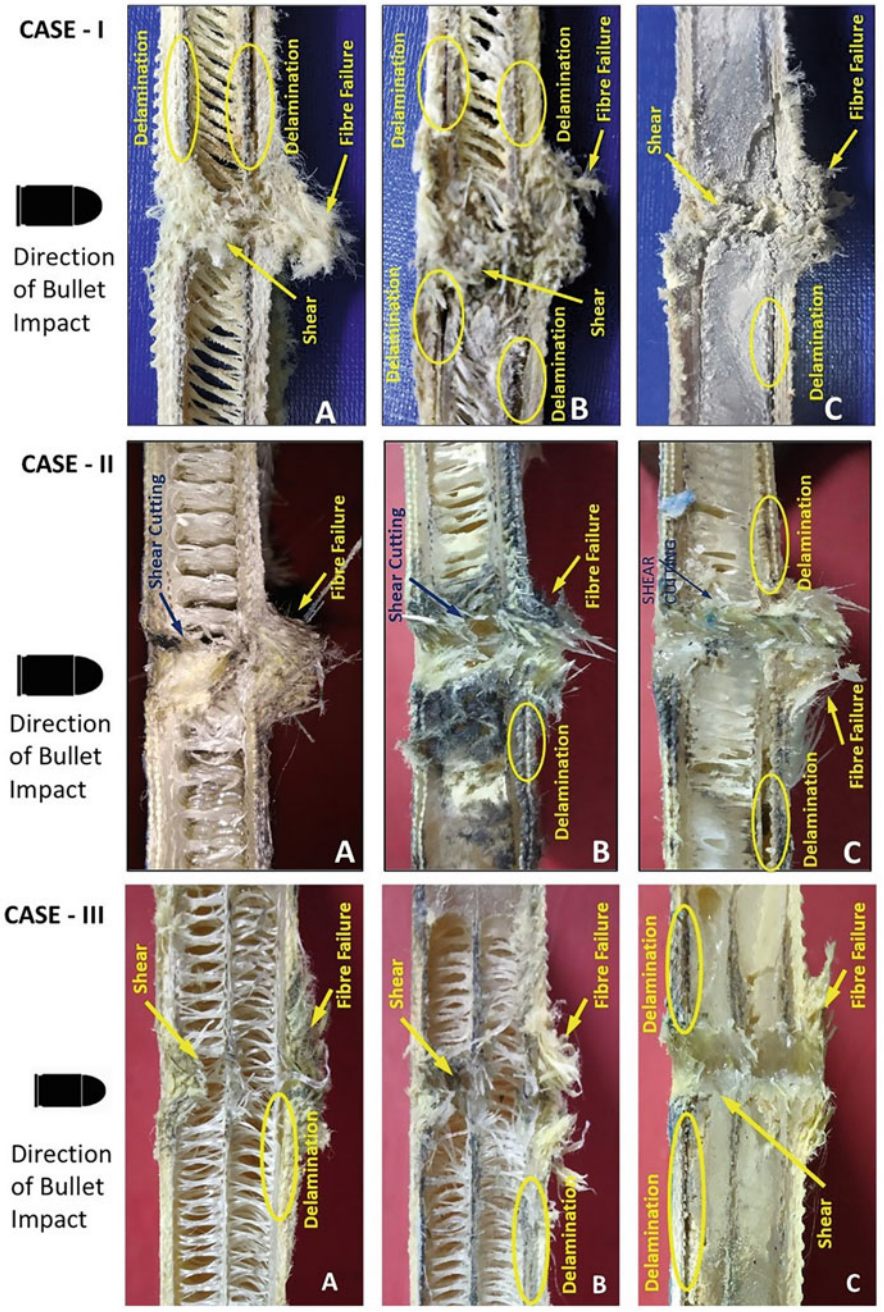

Fig. 7.19 Cross-sectional views of the targets with (**a**) no-fluid, (**b**) PEG, and (**c**) STF Ref. [74, 75, 77]

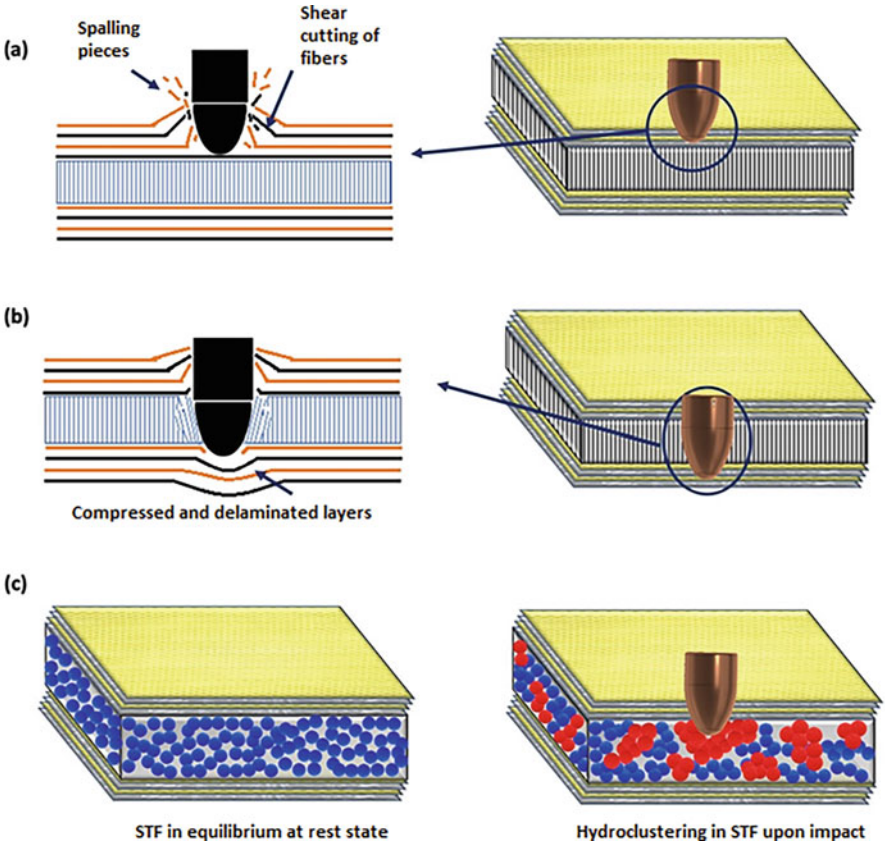

Fig. 7.20 (**a**) First contact, (**b**) penetration process, and (**c**) shear thickening formation during impact Ref. [74]

process. On the other hand, shear thickening rheology provides an additional energy absorbing mechanism during the projectile penetration into the STF-filled targets because the viscosity jump requires a certain amount of energy input and consequently provides a solid-like behavior in the suspension.

Composite materials primarily rely on brittle microfractures as a method for energy dissipation. The eventual energy absorption is thus significantly influenced by the strain at which the fibers fail. The composites collapse as a result of fiber ruptures with no further energy loss. When it comes to the sandwich type composites, there are two distinct phases in composite failures. When the structure is subjected to high velocity impact, there is no time to deflect in response to the impact. This will result in a compaction and shear failure mechanism as shown in Fig. 7.20a. In the second phase, the projectile penetrates into the composite with a deceleration and thereby leads to a gradual deformation mechanism in the remaining layers within the structure [87]. For this reason, remaining layers are compressed, stretched, and finally delaminated as shown in Fig. 7.20b. In STF-filled composites,

hydroclustering mechanism produces extending particle groups within the suspension as shown in Fig. 7.20c. This process results in a great amount of energy dissipation over the structure. Hence, the impact energy is spread over a large area, and consequently the impact accumulation is avoided in the composite. On the other hand, there is no shear thickening rheology in the PEG included composites; however, a viscous medium is provided by this fluid. PEG provides a certain amount of force against the projectile penetration that contributes to the impact resistance in the structure. Although this force is relatively weak, it is nonetheless able to attenuate some part of impact energy during the impact process.

7.4 Conclusions

In this chapter, STF included sandwich structures are investigated under high velocity impact conditions. Various composite designs are studied by using 3D-mat cores and high-performance textile based facesheets. According to the results, STF provides an additional energy absorbing mechanism in structures and thereby contributes to the anti-impact properties of the composites. Comparing to PEG, STF has a shear thickening rheology that leads to a sudden viscosity increase in the suspension. For this reason, thickening rheology provides solid-like behavior upon impact. The structures benefit from this quick change in the viscosity during impact processes. Although PEG has a certain amount of contribution to the energy attenuation, it provides only a viscous medium without viscosity increase for the composites. Despite their contributions to the energy absorbing capabilities, PEG and STF lead to a weight gain in the composites. To consider this effect, specific energy absorbing capabilities are calculated. Due to its significant energy absorbing properties, STF has a high specific energy absorbing capacity despite the weight gain in the structure. However, PEG is not efficient in terms of specific energy absorbing because the energy absorbing capacity of PEG is much behind that of STF. It can be concluded that STF is a promising component in protective composites to effectively enhance the energy absorbing properties of structures. However, the design of composites should be precisely tailored based on the impact conditions.

Acknowledgments The authors acknowledge the TBRL, Defense Research and Development Organization, Chandigarh, India, for supporting this research by supplying certain raw materials, providing relevant information into the research, and making it possible for the ballistic tests to be carried out in their facility. The authors express their gratitude to scientists Ms. I. Biswas, Dr. D. Bhattacharjee, and Dr. S. K. Verma for their unwavering support. The research associates, technicians, staff, and students of the Composite Application and Testing Laboratory, Indian Institute of Technology, Kharagpur, India, are also acknowledged for all of their generous assistance.

References

1. Laun HM. Rheology of extremely shear thickening polymer dispersionsa (passively viscosity switching fluids). J Rheol (N Y N Y). 1991;35:999. https://doi.org/10.1122/1.550257.
2. Zhang XZ, Li WH, Gong XL. The rheology of shear thickening fluid (STF) and the dynamic performance of anSTF-filled damper. Smart Mater Struct. 2008;17:035027. https://doi.org/10.1088/0964-1726/17/3/035027.
3. Fischer C, Braun SA, Bourban P-E, Michaud V, Plummer CJG, Månson JE, Manson J-AE. Dynamic properties of sandwich structures with integrated shear-thickening fluids. Smart Mater Struct. 2006;15:1467–75. https://doi.org/10.1088/0964-1726/15/5/036.
4. Hoffman RL. Discontinuous and dilatant viscosity behavior in concentrated suspensions .parti. Observation of a flow instability. Trans Soc Rheol. 16(1972):155–73. https://doi.org/10.1122/1.549250.
5. Chaffey CE. Mechanisms and equations for shear thinning and thickening in dispersions. Colloid Polym Sci. 1977;255:691–8. https://doi.org/10.1007/BF01550058.
6. Soutis C. Fibre reinforced composites in aircraft construction. Prog Aerosp Sci. 2005;41:143–51. https://doi.org/10.1016/j.paerosci.2005.02.004.
7. Friedrich K, Almajid AA. Manufacturing aspects of advanced polymer composites for automotive applications. Appl Compos Mater. 2013;20:107–28. https://doi.org/10.1007/s10443-012-9258-7.
8. Evans SL, Gregson PJ. Composite technology in load-bearing orthopaedic implants. Biomaterials. 1998;19:1329–42. https://doi.org/10.1016/S0142-9612(97)00217-2.
9. Zhao N, Ye R, Tian A, Cui J, Ren P, Wang M. Experimental and numerical investigation on the anti-penetration performance of metallic sandwich plates for marine applications. J Sandw Struct Mater. 2019;22:494–522. https://doi.org/10.1177/1099636219855335.
10. Zinno A, Fusco E, Prota A, Manfredi G. Multiscale approach for the design of composite sandwich structures for train application. Compos Struct. 2010;92:2208–19. https://doi.org/10.1016/j.compstruct.2009.08.044.
11. Birman V, Kardomateas GA. Review of current trends in research and applications of sandwich structures. Compos Part B Eng. 2018;142:221–40. https://doi.org/10.1016/j.compositesb.2018.01.027.
12. Shen W, Luo B, Yan R, Zeng H, Xu L. The mechanical behavior of sandwich composite joints for ship structures. Ocean Eng. 2017;144:78–89. https://doi.org/10.1016/j.oceaneng.2017.08.039.
13. Chróścielewski J, Miśkiewicz M, Pyrzowski Ł, Sobczyk B, Wilde K. A novel sandwich footbridge - Practical application of laminated composites in bridge design and in situ measurements of static response. Compos Part B Eng. 2017;126:153–61. https://doi.org/10.1016/j.compositesb.2017.06.009.
14. Bach MR, Chalivendra VB, Alves C, Depina E. Mechanical characterization of natural biodegradable sandwich materials. J Sandw Struct Mater. 2015;19:482–96. https://doi.org/10.1177/1099636215622143.
15. Choi HS, Jang YH. Bondline strength evaluation of cocure/precured honeycomb sandwich structures under aircraft hygro and repair environments. Compos Part A Appl Sci Manuf. 2010;41:1138–47. https://doi.org/10.1016/j.compositesa.2010.04.012.
16. Manteghi S, Mahboob Z, Fawaz Z, Bougherara H. Investigation of the mechanical properties and failure modes of hybrid natural fiber composites for potential bone fracture fixation plates. J Mech Behav Biomed Mater. 2017;65:306–16. https://doi.org/10.1016/j.jmbbm.2016.08.035.
17. Sakly A, Laksimi A, Kebir H, Benmedakhen S. Experimental and modelling study of low velocity impacts on composite sandwich structures for railway applications. Eng Fail Anal. 2016;68:22–31. https://doi.org/10.1016/j.engfailanal.2016.03.001.
18. Di Bella G, Calabrese L, Borsellino C. Mechanical characterisation of a glass/polyester sandwich structure for marine applications. Mater Des. 2012;42:486–94. https://doi.org/10.1016/j.matdes.2012.06.023.

19. Xu JL, Chen YW, Wang RH, Li FQ, Liu AY, Wei HZ, Wang DY, Li SH. Research progress in advanced polymer matrix composites for armor protection systems. J Phys Conf Ser. 2020;1507:62011. https://doi.org/10.1088/1742-6596/1507/6/062011.
20. Karbhari VM, Zhao L. Use of composites for 21st century civil infrastructure. Comput Methods Appl Mech Eng. 2000;185:433–54. https://doi.org/10.1016/S0045-7825(99)90270-0.
21. Hoffman RL. Discontinuous and dilatant viscosity behavior in concentrated suspensions, part II. Theory and experimental tests. J Colloid Interface Sci. 1974;46:491–506. file:///C:/Users/VICTOR/Desktop/NEW AND IMP PAPERS/hoffman 1974.pdf
22. Srivastava A, Majumdar A, Butola BS. Improving the impact resistance performance of Kevlar fabrics using silica based shear thickening fluid. Mater Sci Eng A. 2011;529:224–9. https://doi.org/10.1016/j.msea.2011.09.021.
23. Manukonda BH, Chatterjee VA, Verma SK, Bhattacharjee D, Biswas I, Neogi S. Rheology based design of shear thickening fluid for soft body armor applications. Period Polytech Chem Eng. 2019;64:1–10. https://doi.org/10.3311/ppch.13626.
24. Lee YS, Wagner NJ. Dynamic properties of shear thickening colloidal suspensions. Rheol Acta. 2003;42:199–208. https://doi.org/10.1007/s00397-002-0290-7.
25. Vermant J, Solomon MJ. Flow-induced structure in colloidal suspensions. J Phys Condens Matter. 2005;17 https://doi.org/10.1088/0953-8984/17/4/R02.
26. Maranzano BJ, Wagner NJ. The effects of particle size on reversible shear thickening of concentrated colloidal dispersions. J Chem Phys. 2001;114:10514. https://doi.org/10.1063/1.1373687.
27. Bender JW, Wagner NJ. Optical measurement of the contribution of colloidal forces to the rheology of concentrated suspensions. J Colloid Interface Sci. 1995;172:171–84.
28. Bender J, Wagner NJ. Reversible shear thickening in monodisperse and bidisperse colloidal dispersions. J Rheol (N Y N Y). 1996;40:899–916. https://doi.org/10.1122/1.550767.
29. Maranzano BJ, Wagner NJ. Flow-small angle neutron scattering measurements of colloidal dispersion microstructure evolution through the shear thickening transition. J Chem Phys. 2002;117:10291–302. https://doi.org/10.1063/1.1519253.
30. D'haene P, Mewis J, Fuller GG. Scattering dichroism measurements of flow-induced structure of a shear thickening suspension. J Colloid Interface Sci. 1993;156:350–8. https://doi.org/10.1006/jcis.1993.1122.
31. Kaffashi B, O'Brien VT, Mackay ME, Underwood SM. Elastic-Like and viscous-like components of the shear viscosity for nearly hard sphere, Brownian suspensions. J Colloid Interface Sci. 1997;187:22–8. https://doi.org/10.1006/jcis.1996.4611.
32. O'Brien VT, Mackay ME. Stress components and shear thickening of concentrated hard sphere suspensions. Langmuir. 2000;16:7931–8. https://doi.org/10.1021/la000050h.
33. Wagner NJ, Brady JF. Shear thickening in colloidal dispersions. Phys Today. 2009;62:27–32. https://doi.org/10.1063/1.3248476.
34. Afeshejani SHA, Sabet SAR, Zeynali ME, Atai M. Energy Absorption in a Shear-Thickening Fluid. J Mater Eng Perform. 2014;23:4289–97. https://doi.org/10.1007/s11665-014-1217-z.
35. Lee YS, Wagner NJ. Rheological properties and small-angle neutron scattering of a shear thickening, nanoparticle dispersion at high shear rates. Ind Eng Chem Res. 2006;45:7015–24. https://doi.org/10.1021/ie0512690.
36. K. Yu, H. Cao, K. Qian, X. Sha, Y. Chen, Shear-thickening behavior of modified silica nanoparticles in polyethylene glycol. J Nanoparticle Res. 14:2012. https://doi.org/10.1007/s11051-012-0747-2
37. Qin J, Zhang G, Shi X. Study of a shear thickening fluid: the suspensions of monodisperse polystyrene microspheres in polyethylene glycol. J Dispers Sci Technol. 2017;38:935–42. https://doi.org/10.1080/01932691.2016.1216435.
38. Eric NJW, Wetzel D, Lee YS, Egres RG, Kirkwood KM, Kirkwood JE. The effect of rheological parameters on the ballistic properties of shear thickening fluid (STF)-kevlar composites, NUMIFORM Proc; 2004. https://doi.org/10.1063/1.1766538.

39. Lee BWW, Kim IJJ, Kim CGG. The influence of the particle size of silica on the ballistic performance of fabrics impregnated with silica colloidal suspension. J Compos Mater. 2009;43:2679–98. https://doi.org/10.1177/0021998309345292.
40. Hasanzadeh M, Mottaghitalab V. The role of shear-thickening fluids (STFs) in ballistic and stab-resistance improvement of flexible armor. J Mater Eng Perform. 2014;23:1182–96. https://doi.org/10.1007/s11665-014-0870-6.
41. Wei M, Lin K, Sun L. Shear thickening fluids and their applications. Mater Des. 2022;216:110570. https://doi.org/10.1016/j.matdes.2022.110570.
42. Lee YS, Wetzel ED, Wagner NJ. The ballistic impact characteristics of Kevlar woven fabrics impregnated with a colloidal shear thickening fluid. J Mater Sci. 2003;38:2825–33. https://doi.org/10.1023/A
43. Hassan TA, Rangari VK, Jeelani S. Synthesis, processing and characterization of shear thickening fluid (STF) impregnated fabric composites. Mater Sci Eng A. 2010;527:2892–9. https://doi.org/10.1016/j.msea.2010.01.018.
44. Majumdar A, Butola BS, Srivastava A. Optimal designing of soft body armour materials using shear thickening fluid. Mater Des. 2013;46:191–8. https://doi.org/10.1016/j.matdes.2012.10.018.
45. Sun L-L, Xiong D-S, Xu C-Y. Application of shear thickening fluid in ultra high molecular weight polyethylene fabric. J App Poly Sc. 2013;129:1922–8. https://doi.org/10.1002/app.38844.
46. Mishra VD, Mishra A, Singh A, Verma L, Rajesh G. Ballistic impact performance of UHMWP fabric impregnated with shear thickening fluid nanocomposite. Compos Struct. 2022;281:114991. https://doi.org/10.1016/j.compstruct.2021.114991.
47. Bablu MA, Manimala JM. Mechanisms of ballistic performance enhancement in silica nanoparticle-treated kevlar fabric. J Compos Mater. 2022;56:2253–66. https://doi.org/10.1177/00219983221093717.
48. Asija N, Chouhan H, Amare S, Gebremeskel SA, Bhatnagar N. Impact response of shear thickening fluid (STF) treated high strength polymer composites – effect of STF intercalation method. Procedia Eng. 2016;00:1–8. https://doi.org/10.1016/j.proeng.2016.12.133.
49. Fu K, Wang H, Chang L, Foley M, Friedrich K, Ye L. Low-velocity impact behaviour of a shear thickening fluid (STF) and STF- filled sandwich composite panels. Compos Sci Technol. 2018;165:74–83. https://doi.org/10.1016/j.compscitech.2018.06.013.
50. Chen Y, Fu K, Hou S, Han X, Ye L. Multi-objective optimization for designing a composite sandwich structure under normal and 45 ° impact loadings. Compos Part B Eng. 2018;142:159–70.
51. Paz J, Díaz J, Romera L, Costas M. Crushing analysis and multi-objective crashworthiness optimization of GFRP honeycomb- fi lled energy absorption devices. Finite Elem Anal Des. 2014;91:30–9.
52. Fazilati J, Alisadeghi M. Multiobjective crashworthiness optimization of multi-layer honeycomb energy absorber panels under axial impact. Thin-Walled Struct. 2016;107:197–206.
53. Kalantari M, Nami MR, Kadivar MH. Optimization of composite sandwich panel against impact using genetic algorithm. Int J Impact Eng. 2010;37:599–604. https://doi.org/10.1016/j.ijimpeng.2009.12.002.
54. Li W, Sun F, Wang P, Fan H, Fang D. A novel carbon fiber reinforced lattice truss sandwich cylinder : Fabrication and experiments. Compos Part A. 2016;81:313–22.
55. Burlayenko VN, Sadowski T. Effective elastic properties of foam-filled honeycomb cores of sandwich panels. Compos Struct. 2010;92:2890–900. https://doi.org/10.1016/j.compstruct.2010.04.015.
56. M. V Hosur, M. Abdullah, S. Jeelani. Manufacturing and low-velocity impact characterization of foam filled 3-D integrated core sandwich composites with hybrid face sheets, Compos. Struct. 69:2005;167–181. https://doi.org/10.1016/j.compstruct.2004.06.008

57. Vaidya UK, Ulven C, Pillay S, Ricks H. Impact Damage of Partially Foam-filled Co-injected Honeycomb Core Sandwich Composites. J Compos Mater. 2003;37:611–26. https://doi.org/10.1177/0021998030297 24.
58. Zhang G, Wang B, Ma L, Wu L, Pan S, Yang J. Energy absorption and low velocity impact response of polyurethane foam filled pyramidal lattice core sandwich panels. Compos Struct. 2014;108:304–10. https://doi.org/10.1016/j.compstruct.2013.09.040.
59. Caliskan U, Apalak MK. Bending impact behaviour of sandwich beams with expanded polystyrene foam core: Analysis. J Sandw Struct Mater. 2019;21:230–59. https://doi.org/10.1177/1099636216689545.
60. Atas C, Potoğlu U. The effect of face-sheet thickness on low-velocity impact response of sandwich composites with foam cores. J Sandw Struct Mater. 2016;18:215–28. https://doi.org/10.1177/1099636215613775.
61. Islam MM, Kim HS. Sandwich composites made of syntactic foam core and paper skin: Manufacturing and mechanical behavior. J Sandw Struct Mater. 2011;14:111–27. https://doi.org/10.1177/1099636211413564.
62. Gupta N, Maharsia R. Enhancement of energy absorption in syntactic foams by nanoclay incorporation for sandwich core applications. Appl Compos Mater. 2005;12:247–61. https://doi.org/10.1007/s10443-005-1130-6.
63. Yang JS, Chen SY, Li S, Pang YZ, Schmidt R, Schröder KU, Qu J, Wu LZ. Dynamic responses of hybrid lightweight composite sandwich panels with aluminium pyramidal truss cores. J Sandw Struct Mater. 2020;23:2176. https://doi.org/10.1177/1099636220909816.
64. Tarlochan F, Ramesh S. Composite sandwich structures with nested inserts for energy absorption application. Compos Struct. 2012;94:904–16. https://doi.org/10.1016/j.compstruct.2011.10.010.
65. Mezeix L, Dols S, Bouvet C, Castanié B, Giavarini JP, Hongkarnjanakul N. Experimental analysis of impact and post-impact behaviour of inserts in Carbon sandwich structures. J Sandw Struct Mater. 2019;21:135–53. https://doi.org/10.1177/1099636216687582.
66. Crupi V, Kara E, Epasto G, Guglielmino E, Aykul H. Theoretical and experimental analysis for the impact response of glass fibre reinforced aluminium honeycomb sandwiches. J Sandw Struct Mater. 2016;20:42–69. https://doi.org/10.1177/1099636216629375.
67. Decker MJ, Halbach CJ, Nam CH, Wagner NJ, Wetzel ED. Stab resistance of shear thickening fluid (STF)-treated fabrics. Compos Sci Technol. 2007;67:565–78. https://doi.org/10.1016/j.compscitech.2006.08.007.
68. Chatterjee VA, Dey P, Verma SK, Bhattacharjee D, Biswas I, Neogi S. Probing the intensity of dilatancy of high performance shear-thickening fluids comprising silica in polyethylene glycol. Mater Res Express. 2019;6:1–22. https://doi.org/10.1088/2053-1591/ab1185.
69. K. Czech, R. Oliwa, D. Krajewski, K. Bulanda, M. Oleksy, G. Budzik, A. Mazurkow, Hybrid polymer composites used in the arms industry: A review, Materials (Basel). 14:2021. https://doi.org/10.3390/ma14113047
70. Warren J, Offenberger S, Toghiani H, Pittman CU, Lacy TE, Kundu S. Effect of Temperature on the Shear-Thickening Behavior of Fumed Silica Suspensions. ACS Appl Mater Interfaces. 2015;7:18650–61. https://doi.org/10.1021/acsami.5b05094.
71. Gürgen S, Kuşhan MC. The stab resistance of fabrics impregnated with shear thickening fluids including various particle size of additives. Compos Part A Appl Sci Manuf. 2017;94:50–60. https://doi.org/10.1016/j.compositesa.2016.12.019.
72. Maranzano BJ, Wagner NJ. The effects of interparticle interactions and particle size on reversible shear thickening: Hard-sphere colloidal dispersions. J Rheol (N Y N Y). 2001;45:1205–22. https://doi.org/10.1122/1.1392295.
73. Q. shi Wang, R. jun Sun, M. Yao, M. yu Chen, Y. Feng, The influence of temperature on inter-yarns fictional properties of shear thickening fluids treated Kevlar fabrics. Compos Part A Appl Sci Manuf 116 (2019) 46–53. https://doi.org/10.1016/j.compositesa.2018.10.020
74. V.A. Chatterjee, S.K. Verma, D. Bhattacharjee, I. Biswas, S. Neogi, Manufacturing of dilatant fluid embodied Kevlar-Glass-hybrid-3D-fabric sandwich composite panels for the enhancement

of ballistic impact resistance, Chem Eng J 406 (2021). https://doi.org/10.1016/j.cej.2020.127102
75. V.A. Chatterjee, S.K. Verma, D. Bhattacharjee, I. Biswas, S. Neogi, Enhancement of energy absorption by incorporation of shear thickening fluids in 3D-mat sandwich composite panels upon ballistic impact, Compos Struct. 225 (2019). https://doi.org/10.1016/j.compstruct.2019.111148
76. P.K. Mungamurugu, P. Marru, H.H. Sardar, S. Neogi, Long term performance study of glass reinforced composites with different resins under marine environment, 18 (2017) 122–130. https://doi.org/10.1007/s12221-017-6543-y
77. Chatterjee VA, Saraswat R, Verma SK, Bhattacharjee D, Biswas I, Neogi S. Embodiment of dilatant fluids in fused-double-3D-mat sandwich composite panels and its effect on energy-absorption when subjected to high-velocity ballistic impact. Compos Struct. 2020;249:112588. https://doi.org/10.1016/j.compstruct.2020.112588.
78. Liu X-Q, Bao R-Y, Wu X-J, Yang W, Xie B-H, Yang M-B. Temperature induced gelation transition of a fumed silica/PEG shear thickening fluid. RSC Adv. 2015;5:18367–74. https://doi.org/10.1039/C4RA16261G.
79. Raghavan S, Khan S. Shear-thickening response of fumed silica suspensions under steady and oscillatory shear. J Colloid Interface Sci. 1997;185:57–67. https://doi.org/10.1006/jcis.1996.4581.
80. Raghavan SR, Carolina N, Walls HJ, Khan SA. Rheology of silica dispersions in organic liquids : new evidence for solvation forces dictated by Hydrogen Bonding. Langmuir. 2000;16:7920–30. https://doi.org/10.1021/la991548q.
81. Moriana AD, Tian T, Sencadas V, Li W. Comparison of rheological behaviors with fumed silica-based shear thickening fluids. Korea-Australia Rheol J. 2016;28:197–205. https://doi.org/10.1007/s13367-016-0020-9.
82. Asija N, Chouhan H, Gebremeskel SA, Bhatnagar N. Influence of particle size on the low and high strain rate behavior of dense colloidal dispersions of nanosilica. J Nanopart Res. 2017;19:21. https://doi.org/10.1007/s11051-016-3723-4.
83. Wagner NJ, Lee YS. The Ballistic Impact Characteristics of Kevlar Woven Fabrics Impregnated with a Colloidal Shear Thickening Fluid. J Mater Sci. 2015;8:2825–33. https://doi.org/10.1023/A
84. Naik NK, Shrirao P. Composite structures under ballistic impact. Compos Struct. 2004;66:579–90. https://doi.org/10.1016/j.compstruct.2004.05.006.
85. Sheikh AH, Bull PH, Kepler JA. Behaviour of multiple composite plates subjected to ballistic impact. Compos Sci Technol. 2009;69:704–10. https://doi.org/10.1016/j.compscitech.2008.03.022.
86. Sorrentino L, Bellini C, Corrado A, Polini W, Aricò R. Ballistic performance evaluation of composite laminates in kevlar 29. Procedia Eng. 2015;88:255–62. https://doi.org/10.1016/j.proeng.2015.06.048.
87. Wambua P, Vangrimde B, Lomov S, Verpoest I. The response of natural fibre composites to ballistic impact by fragment simulating projectiles. Compos Struct. 2007;77:232–40. https://doi.org/10.1016/j.compstruct.2005.07.006.

Index

S. Gürgen (ed.), *Shear Thickening Fluid*, https://doi.org/10.1007/978-3-031-35521-9